

PEOPLE'S DEMOCRATIC REPUBLIC OF ALGERIA

Ministry of Higher Education and Scientific Research

BLIDA 1 UNIVERSITY

Faculty of Technology Department of Renewable Energies

DOCTORAL THESIS

Specialty: Renewable Energy in Mechanics

Parametric study of a desalination system powered by solar energy

By

Yasmine KACIMI

The thesis was defended before a jury composed of:

Djaffar SEMMAR	Full professor at Blida 1 University	Chair
Hacene MAHMOUDI	Full professor at the National High School of Nano-sciences and Nanotechnology, Algeria	Examiner
Rachid BOUKENOUI	Lecturer A at Blida 1 University	Examiner
Benamar CHEKNANE	Full professor at Blida 1 University	Thesis Supervisor
Abdelkader HAMID	Full professor at Blida 1 University	Co-supervisor
Noureddine SAID	Full professor at Blida 1 University	Guest

Blida, 2025/2026

ملخص

تمثل ندرة المياه تحديًا عالميًا متزايدًا، يتفاقم بفعل التغير المناخي والتوسع العمراني السريع والطلب المتزايد على المياه لأغراض الزراعة. تُعد تحلية المياه حلاً أساسيًا، إلا أن التقنيات التقليدية، تستهلك كميات كبيرة من الطاقة، حيث تمثل الكهرباء أكثر من نصف تكاليف الإنتاج. لذا، من الضروري تطوير عمليات تحلية أكثر كفاءة مندمجة مع مصادر الطاقة المتجددة.

تبحث هذه الدراسة في جدوى دمج الطاقة الشمسية الحرارية في أنظمة تحلية المياه باستخدام التقطير متعدد المراحل (MSF)بهدف تحسين استدامتها وتقليل استهلاكها للطاقة. يُقترح نظام هجين يجمع بين المجمعات الخطية من نوع فريسنل (LFC)، وتخزين الطاقة الحرارية، والدعم بالطاقة الأحفورية، وتكوين التقطير متعدد المراحل بتمرير واحد-MSF) (OT)، مما يضمن الحفاظ على درجة حرارة ثابتة للمحلول الملحي العلوي (TBT) عند 90 درجة مئوية مع تحسين استخدام المساحة المتاحة.

تم تطوير نموذج عددي باستخدام MATLAB لتقييم أداء النظام، مع الأخذ في الاعتبار الإشعاع الشمسي والتكوينات الهندسية وزوايا السقوط. بالإضافة إلى ذلك، تم تحليل تأثير المعلمات التشغيلية لنظام التقطير متعدد المراحل، مثل معدلات التدفق ودرجة حرارة المحلول الملحي العلوي وعدد المراحل، على كفاءة الطاقة وإنتاج المياه العذبة. كما تم إجراء دراسة مقارنة لثلاث مناطق ساحلية في الجزائر بناءً على التغيرات المناخية والإمكانات الشمسية.

تمت مقارنة النموذج ببيانات مأخوذة من محطة MSF في الكويت ودراسات قام بها الدسوكي. علاوة على ذلك، تم إجراء تقييمات بيئية واقتصادية لتحليل خفض انبعاثات ثاني أكسيد الكربون وإمكانية الجدوى المالية للنظام. كما تم دراسة تأثير تحسينات انتقال الحرارة على كفاءة الطاقة. وأخيرًا، تم تقديم توصيات لتعزيز موثوقية النظام من خلال الأتمتة، وتحسين الصيانة، ودمج مصادر الطاقة الهجينة.

من خلال تطوير تقنيات تحلية المياه بالطاقة الشمسية، تساهم هذه الدراسة في الإدارة المستدامة لموارد المياه، مما يساعد في مكافحة ندرة المياه وتقليل الاعتماد على الوقود الأحفوري.

الكلمات المفتاحية: تحلية المياه بالطاقة الشمسية الحرارية، الطاقة الشمسية المركزة، تخزين الطاقة الحرارية، عملية التحلية متعددة المراحل(MSF) ، إنتاج المياه المستدامة.

Abstract

Water scarcity is an increasing global challenge, exacerbated by climate change, rapid urbanization, and growing agricultural demands. Desalination constitutes an essential solution; however, conventional technologies, are highly energy-intensive, with electricity consumption accounting for more than half of production costs. Therefore, it is crucial to develop more efficient desalination processes that integrate renewable energy sources.

This research examines the feasibility of integrating solar thermal energy into multi-stage flash distillation (MSF) desalination systems to enhance their sustainability and reduce energy consumption. A hybrid system has been proposed, combining linear Fresnel collectors (LFC),

thermal energy storage, fossil fuel backup, and a single-pass MSF configuration (MSF-OT), ensuring a stable top brine temperature (TBT) of 90°C while optimizing land use.

A numerical model was developed in MATLAB to evaluate the system's performance, considering solar irradiation, geometric configurations, and incidence angles. Additionally, the influence of MSF operational parameters, such as flow rates, top brine temperature, and the number of stages, on energy efficiency and freshwater production was analyzed.

A comparative study was conducted on three coastal regions of Algeria, based on climatic variations and solar potential. The model was validated using data from the MSF plant in Kuwait and studies by El-Dessouky. Furthermore, environmental and economic assessments were carried out to analyze CO₂ emission reductions and the financial viability of the system. The impact of heat transfer improvements on energy efficiency was also studied. Finally, recommendations were formulated to enhance system reliability through automation, maintenance optimization, and the integration of hybrid energy sources.

By advancing solar desalination, this study contributes to sustainable water resource management, helping to combat water scarcity while reducing dependence on fossil fuels.

Keywords: Solar thermal desalination, Concentrated solar power, Thermal energy storage, MSF desalination process, Sustainable water production.

Résumé

La pénurie d'eau représente un défi mondial croissant, aggravé par le changement climatique, l'urbanisation rapide et l'augmentation des besoins agricoles. Le dessalement constitue une solution essentielle ; cependant, les technologies conventionnelles, sont très énergivores, la consommation électrique représentant plus de la moitié des coûts de production. Il est donc crucial de développer des procédés de dessalement plus efficaces et intégrant des sources d'énergie renouvelables.

Cette recherche examine la faisabilité de l'intégration de l'énergie solaire thermique dans les systèmes de dessalement à distillation multi-effet (MSF) afin d'améliorer leur durabilité et de réduire leur consommation énergétique. Un système hybride a été proposé, combinant des collecteurs linéaires de Fresnel (LFC), un stockage d'énergie thermique, un appoint en énergie fossile et une configuration MSF à passage unique (MSF-OT), permettant de maintenir une température stable de la saumure supérieure (TBT) à 90°C tout en optimisant l'occupation du sol.

Un modèle numérique sous MATLAB a été développé pour évaluer les performances du système, en tenant compte de l'irradiation solaire, des configurations géométriques et des angles d'incidence. De plus, l'influence des paramètres opérationnels du MSF, tels que les débits, la température de la saumure supérieure et le nombre d'étages, sur l'efficacité énergétique et la production d'eau douce a été analysée. Une étude comparative a été menée

sur trois régions côtières d'Algérie, en fonction des variations climatiques et du potentiel solaire.

Le modèle a été validé à l'aide de données issues de l'usine MSF du Koweït et des études d'El-Dessouky. En outre, des évaluations environnementales et économiques ont permis d'analyser les réductions d'émissions de CO₂ ainsi que la viabilité financière du système. L'impact des améliorations du transfert thermique sur l'efficacité énergétique a également été étudié. Enfin, des recommandations ont été formulées pour renforcer la fiabilité du système grâce à l'automatisation, à l'optimisation de la maintenance et à l'intégration d'énergies hybrides.

En développant le dessalement solaire, cette étude contribue à une gestion durable des ressources en eau, permettant de lutter contre la pénurie tout en réduisant la dépendance aux combustibles fossiles.

Mots clés: Dessalement solaire thermique, Énergie solaire concentrée, Stockage d'énergie thermique, Procédé de dessalement MSF, Production durable d'eau.

Acknowledgments

First and foremost, I express my deepest gratitude to **God** for granting me the strength, perseverance, and patience to complete this work.

I would like to extend my sincere thanks to **Professor Benamar CHEKNANE** for his invaluable supervision, insightful guidance, and the trust he placed in me throughout this research. His support and expertise have been instrumental in shaping this thesis.

My special appreciation goes to **Professor Noureddine SAID**, whose enriching scientific discussions and valuable expertise have significantly contributed to my research. I am deeply grateful for his technical advice, unwavering availability, and remarkable human qualities, which have greatly supported me in accomplishing this work.

I am also sincerely grateful to **Professor Abdelkader HAMID**, my co-supervisor, for his guidance, constructive feedback, and continuous encouragement throughout this journey.

I extend my warmest thanks to **Professor Marco FOSSA**, PhD, Rector's Delegate to the International Educational Programs at the University of Genoa, Italy, and **Dr. Samuele MEMME**, for their kind hospitality and for providing me with the opportunity to conduct a significant part of this research within their esteemed division. Their support and scientific insights have been invaluable.

My profound gratitude goes to **Professor Faiza ZERMANE**, Director of the laboratory to which I am affiliated, for her continuous support, guidance, and encouragement.

I also wish to express my sincere appreciation to **Dr. Hichem BENDJABESS**, Research Director at UDES, for his invaluable assistance, motivation, and generous support throughout this work. His encouragement and scientific input have been greatly appreciated.

I sincerely appreciate **Dr. Yacine BOUALI** from the University of Science and Technology Houari Boumediene for his invaluable support, insightful guidance, and unwavering availability. His generosity and encouragement have been truly meaningful throughout this journey.

I sincerely thank the jury members, **Professors Djaffar SEMMAR**, **Hacene MAHMOUDI**, and **Rachid BOUKENOUI**, for their time, insights, and valuable feedback, which greatly enhanced this work.

Lastly, I extend my heartfelt gratitude to everyone who, through their knowledge, expertise, and friendship, has contributed in any way to the successful completion of this research.

Dedication

I dedicate this work to:

My father and mother, for their unconditional love and support.

My sisters, brother, and brother-in-law, for always believing in me.

My aunts and uncles, for their kindness and encouragement.

My family and friends, for their unwavering support throughout this journey.

Table of Contents

ملخص	i
Abstract	i
Résumé	ii
Acknowledgments	iv
Dedication	v
Table of Contents	vi
List of Figures	ix
List of Tables	xii
Nomenclature	xiii
GENERAL INTRODUCTION	1
Chapter 1: Overview	3
1.1. Introduction	3
1.2. Background	3
1.2.1. Global Water Scarcity and the Role of Desalination	5
1.2.2. Renewable Energy for Desalination	7
1.3. Linear Fresnel Collectors (LFC)	17
1.3.1. Fundamentals of LFC Technology	17
1.3.2. Advantages over Other Solar Collectors	19
1.3.3. Challenges	19
1.4. Multi-Stage Flash Desalination	20
1.4.1. Process Description	20
1.4.2. Energy Demand	21
1.4.3. Advantages of Once-Through MSF	21
1.5. Coupling of LFC with Once-Through MSF	22
1.5.1. Concept of Direct Coupling	23
1.5.2. Potential Benefits	24
1.5.3. Key Challenges	24
1.6. Need for Parametric Analysis	25
1.7. Research Objectives	26
1.8. Scope and Limitations	26

1.9. Conclusion	26
Chapter 2 : Literature Review	27
2.1. Introduction	27
2.2. Previous Work on Solar-Powered Desalination Systems	27
2.3. Linear Fresnel Collector	35
2.3.1. Compact linear Fresnel	37
2.3.2. Receiver designs	40
2.4. Multi-Stage Flash	42
2.5. Conclusion	43
Chapter 3: Methodology for System Design, Modeling, and Simulation Tools Used	44
3.1. Introduction	44
3.2. System Configuration	44
3.2.1. Solar Energy Generation and Storage	45
3.2.2. The Multistage Flash desalination unit Desalination and Control System	46
3.3. Fresnel Model	49
3.3.1. Optical Model	50
3.3.2. Thermal Model	56
3.3.3. Storage System Model	58
3.3.4. Backup System Model	58
3.4. MSF Model	58
3.4.1. Heat Balance in The Storage Tank (Brine Heater)	59
3.4.2. Mass Flow Rate of Fresh Water Production	61
3.4.3. Temperature Profile Correlations	62
3.4.4. Fundamental Parameters for MSF Evaluation	63
4.5. Conclusion	64
Chapter 4: Parametric Analysis Results	65
4.1. Introduction	65
4.2. Influence of LFC Parameters	65
4.2.1. Impact of Weather Conditions and Solar Irradiation	65
4.2.2. Geometric Effects	72
4.2.3. Incidence Angle Modifier (IAM) Effect	74
4.2.4. Thermal Performance Parameters Effect	74
4.3. Impact of MSF Operational Parameters	76

4.3.1. Performance & Energy Efficiency parameters effects	76
4.3.2. Mass & Heat Transfer parameters effects	78
4.3.3. Flashing & Water Production Characteristics effects	79
4.4. Effects of Changing Site Conditions	80
4.4.1. Climatic Conditions	81
4.4.2. Evaluation of System Efficiency and Energy Output	82
4.5. Conclusion	85
Chapter 5: Feasibility and Performance of an LFC-MSF Desalination System with In Coupling in Algiers	
5.1. Introduction	86
5.2. Description of Study Area	86
5.3. Model Validation	88
5.3.1. Model Validation Using Kuwait plant Data	89
5.3.2. Model Validation Using Data from El-Dessouky et al	90
5.4. Annual System Performance Analysis	92
5.5. Comparative Study of MSF-OT Desalination: With and Without Additional Iso	
5.6. CO2 Emission Rate	
5.7. Trade-Offs Between Energy Consumption and Water Production	
5.8. Economic Analysis of LFC-MSF Desalination	
5.8.1. Economic Analysis	
5.8.2. Comparison with Existing Technologies	
5.9. Techniques for Ensuring System Reliability	
5.10. Conclusion	
GENERAL CONCLUSION	107
Appendix A: Mathematical Formulation	109
Appendix B: Results from the Parametric Study	
Appendix C: Economic Calculation Procedure	
REFERENCES	

List of Figures

Chapter 1	
Fig.1. 1. Histogram of the average daily desalinated water production and the number of	
plants by country in 2023	5
Fig.1. 2. Average water stress by country 2020-2030 [27]	6
Fig.1. 3. Water resources availability and use in MENA countries [27]	7
Fig.1. 4. Classification of desalination processes by type of energy [40].	8
Fig.1. 5. Global map of daily and annual DNI (kWh/m²) based on long-term averaged data	
[53]	10
Fig.1. 6. Solar energy potential and direct normal irradiance in Algeria [60, 61]	11
Fig.1. 7. Market shares of major desalination producers [7].	13
Fig.1. 8. Thermal Desalination Systems Powered by CSP Technology [71]	15
Fig.1. 9. Thermal Desalination Systems Powered by CSP Technology [72]	16
Fig.1. 10. A/ Fresnel lens [10]; B / Fresnel mirrors [10]; C/ Diagram showing the transition	l
from a parabolic trough mirror to a linear Fresnel mirror. [81].	17
Fig.1. 11. Description of a linear fresnel collector [88].	18
Fig.1. 12. Optical losses and performance challenges in LFC systems.	19
Fig.1. 13. Schematic of once through multi stage flash [102].	
Fig.1. 14. Schematic of multi stage flash with brine circulation [102].	
Fig.1. 15. Global market share of desalination technologies by type, 2023 [108]	22
Fig.1. 16. Design of an MSF-OT Desalination System Integrated with LFC and Thermal	
Storage.	24
Chapiter 2	
Fig. 2. 1. A schematic overview of the system as described in [113].	28
Fig.2. 2. Evacuated multi-stage solar water desalination system [114].	28
Fig.2. 3. The experimental set-up of the HDH-SSF system [115].	29
Fig.2. 4. Experimental setup for solar thermal MSF desalination [116].	30
Fig.2. 5. LT-MED unit integrated into a CSP plant [127].	31
Fig.2. 6. LT-MED + TVC unit integrated into a CSP plant [127].	32
Fig.2. 7. TVC-MED unit integrated into a CSP plant [127]	32
Fig.2. 8. RO unit connected to a CSP plant [127]	33
Fig.2. 9. The experimental setup of the solar collecting system [128]	33
Fig.2. 10. The proposed MED-TVC pilot plant driven by solar thermal energy [130]	34
Fig.2. 11. System configuration proposed by Moharram [131]	35
Fig.2. 12. Schematic of the two-stage solar PDC-MSF desalination system [132]	35
Fig.2. 13. The CLFR designs proposed by Rungasamy et al. [141] and Zhu and Chen [142]	. 37
Fig.2. 14. Structure of the proposed two-axis tracking LFC [143].	38
Fig.2. 15. Non-rectangular LFC prototype with southward extension in San Carlos, Argenti	ina
[144]	
Fig 2 16 Illustrations of elevated mirrors designed to minimize end losses [145 146]	39

Fig.2. 17. Depictions of (a) SLFR solar system, and (b) SLFR system with additional support	ort
[147]	40
Fig.2. 18. Photos of experiment SPLFR solar system [148]	40
Fig.2. 19. Receiver configurations for Linear Fresnel Reflectors [159]	41
Chapter 3	
Fig.3. 1. Schematic representation of a solar-driven MSF-OT desalination system with	
thermal energy storage	44
Fig.3. 2. Layout of the Novatec LFC system [139]	45
Fig.3. 3. Layout of a conventional MSF-OT plant.	47
Fig.3. 4. Layout of a novel approach to MSF-OT desalination plant design	48
Fig.3. 5. Block diagram of the proposed control system.	49
Fig.3. 6. Sizing the solar field: calculating collectors and rows.	50
Fig.3. 7. Geometric representation of incidence angles and solar position	52
Fig.3. 8. Representation of the Pillbox sun shape profile.	54
Fig.3. 9. Geometrical representation of the studied collector in SolTrace	54
Fig.3. 10. Ray Tracing Analysis of the LFC System in SolTrace.	55
Fig.3. 11. Comparison of IAM factors: NOVATEC SOLAR system data [32], SolTrace ray	y
tracing results, and polynomial fit [193]	56
Fig.3. 12. Comparative Analysis of Heat Loss: Polynomial Fit and NOVATEC SOLAR	
system [194]	57
Fig.3. 13. Schematic overview of the brine heater and a stage in an MSF-OT plant	59
Fig.3. 14. Flow, Temperature, and Concentration distribution in the MSF-OT plant	61
Chapter 4	
Fig.4. 1. Incident solar flux distribution on the receiver for different seasonal conditions	67
Fig.4. 2. Daily variation of DNI under clear and cloudy conditions in Algiers city	70
Fig.4. 3. Impact of cloud cover on the efficiency of linear fresnel collectors (LFCs)	70
Fig.4. 4. Impact of solar radiation on the performance of the proposed MSF-OT system	
configuration.	71
Fig.4. 5. Impact of ambient temperature on heat loss and LFC efficiency	71
Fig.4. 6. Impact of receiver height on thermal energy generation in an LFC system	72
Fig.4. 7. Impact of collector number on thermal energy generation in an LFC system	73
Fig.4. 8. Impact of geometric losses on efficiency in LFC.	73
Fig.4. 9. Impact of incidence angle on IAM and optical efficiency in LFC	74
Fig.4. 10. Impact of HTF mass flow rate on LFC thermal efficiency.	75
Fig.4. 11. Impact of receiver temperature on heat loss and LFC thermal efficiency	75
Fig.4. 12. Impact of thermal energy input on desalination system performance	76
Fig.4. 13. Impact of feed water flow rate on recovery ratio in MSF desalination system	77
Fig.4. 14. Impact of distillate flow rate on specific thermal energy consumption (STEC)	77
Fig.4. 15. Impact of brine salinity on evaporation rate across stages	78
Fig.4. 16. Impact of top brine temperature and thermodynamic losses on specific heat trans	sfer
area in MSF-OT.	78
Fig.4. 17. Impact of top brine temperature on evaporation rate across stages	79
Fig.4. 18. Impact of MSF-OT stage number on distillate water production	79

Fig.4. 19. Annual daily variability of useful thermal energy in the solar field for selected	
coastal regions of Algeria: (A) Algiers, (B) Oran, and (C) Jijel.	
Fig.4. 20. Variation of DNI in coastal regions of Algeria on clear and cloudy days	
Fig.4. 21. Variation of ambient temperature in coastal regions of Algeria on clear and cloud	ly
days	
Fig.4. 22. LFC optical efficiency in coastal Algeria on favorable and unfavorable days	82
Fig.4. 23. Solar thermal energy and process demand variations on favorable and unfavorable	le
days in Algeria.	
Fig.4. 24. Hourly variation in feedwater intake and distillate production on (A) clear days a	nd
(B) cloudy days.	84
Chapter 5	
Fig.5. 1. Algeria's climate zones [213].	87
Fig.5. 2. Monthly direct insolation and hourly DNI from PVGIS [190]	88
Fig.5. 3. Hourly ambient temperature from PVGIS [190]	88
Fig.5. 4. Comparison of Matlab model predictions with actual plant data	90
Fig.5. 5. Comparison of Matlab model predictions with El-Dessouky et al. data [4]	91
Fig.5. 6. Hourly variations of optical, thermal, and total efficiency in the LFC System	93
Fig.5. 7. Hourly variations in top brine temperature (TBT) throughout the year	93
Fig.5. 8. Impact of thermal energy adjustment on top brine temperature (TBT) stability	94
Fig.5. 9. Seasonal variation in thermal energy utilization and heat recovery in the MSF plan	ıt.
	94
Fig.5. 10. Daily feedwater and distillate production (m ³).	95
Fig.5. 11. Impact of additional isolated tubes on brine flow stability in MSF-OT desalination	
Fig.5. 12. Impact of isolated tubes on MSF-OT performance.	
Fig. 5. 13. CO ₂ Emissions in MSF desalination: Fossil Fuel vs. LFC	
Fig. 5. 14. TBT influence on freshwater production, energy demand, and environmental	
impact in LFC-MSF without additional tubes.	100
Fig. 5. 15. TBT influence on freshwater production, energy demand, and environmental	
impact in LFC-MSF with additional tubes.	101
Appendix B	
Fig.B. 1. Incident solar flux distribution on the receiver at different times on June 21	113
Fig.B. 2. Brine temperature evolution through the condenser tube across stages over 24-hou	
on an optimal day in Algiers.	
Fig.B. 3. Brine temperature evolution in the brine pool across stages over 24-hours on an	
optimal day in Algiers.	113
Fig.B. 4. Influence of steam temperature on top brine temperature	
Fig.B. 5. Influence of steam temperature on its mass flow rate	
Fig.B. 6. Influence of feedwater flow rate on steam flow rate.	
Fig.B. 7. Influence of feed water temperature on steam flow rate	
Fig.B. 8. Influence of feed water temperature on gain output ratio.	
Fig.B. 9. Influence of feed water flow rate on gain output ratio	
Fig.B. 10. Influence of brine pool height on specific heat transfer area	

List of Tables

Chapter 1	
Table 1.1. Overview of the important developments and achievements in thermal and	membra
ne desalination	3
Table 1. 2. Main features of desalination technologies and their appropriate energy	sources
[44]	9
Table 1. 3. Regional and Global CSP Capacity Projections Based on the Hi-Ren	Scenario
[55]	11
Table 1. 4. Water classification by salinity concentration [65, 66]	12
Table 1. 5. Progress of desalination plants in Algeria [70]	14
Table 1. 6. Functionality overview of the four primary CSP technologies [73, 76]	16
Table 1. 7. Energy demand for producing 1 m³ of desalinated water with MSF a	nd MED
Technologies [104]	21
Chapter 2	
Table 2. 1. Solar desalination plants.	
Table 2. 2. Overview of significant advancements in LFC.	35
Chapter 3	
Table 3. 1. Design specifications of the solar plant [139, 186, 187, 188]	46
Table 3. 2. Summary of the desalination unit characteristics.	48
Table 3. 3. Geometrical and optical parameter of the LFC [186, 187, 194]	55
Chapter 4	
Table 4. 1. Seasonal Analysis of Solar Flux and Performance Parameters	68
Table 4. 2. Seasonal Analysis of Solar Flux and Performance Parameters	69
Table 4. 3. Annual energy demand and runtime analysis of LFC, storage, and backup	systems.
	85
Chapter 5	
Table 5. 1. Operational data of Shuaiba South plant [183]	
Table 5. 2. Comparative analysis of model predictions and plant data [183]	90
Table 5. 3. Impact of isolated tubes on MSF-OT system efficiency and productivi	ty across
coastal regions.	
Table 5. 4. Comparative analysis of SEC _{eq} in Fossil Fuel-MSF and LFC-MSF des	
systems	
Table 5. 5. Cost distribution of the LFC-powered MSF-OT desalination system	
Table 5. 6. Impact of additional isolated tubes on performance and cost	
Table 5. 7. Comparison of desalination configurations.	105

Nomenclature

BTE Boiling Temperature Elevation [°C] CAPEX Capital Expenditure [\$] CRF Capital Recovery Factor CSP Concentrating Solar Power DNI Direct Normal Irradiance [W/m²] GOR Gain output ratio HTF Heat Transfer Fluid LCOW Levelized Cost Of Water [\$/m³] LFC Linear Fresnel Collector LMTD Logarithmic Mean Temperature Difference MED Multi-Effect Distillation MSF-OT One-Through Multi-Stage Flash NEA Non-Equilibrium Allowance NS North-South orientation O&M Operating and Maintenance OPEX Operating Expenditure [\$/year] PVGIS Photovoltaic Geographical Information System RO Reverse Osmosis RR Recovery Ratio SECeq Specific Electrical Energy Consumption SEEC Specific Electrical Energy Consumption STEC Specific Thermal Energy Consumption TBT Top Brine Temperature [°C] TMY Typical Meteoroligical Year TVC Thermal Vapor Compression Symbols A Area [m²] Ap Aperture area [m²] Cp Specific heat at constant pressure [kJ/kg-°C] DC Direct capital cost [\$] Ec Electric price [\$/kWh] f Plant's availability factor ftod Time-of-dispatch factor h Specific Entalpy [kJ/kg] H Height of brine pool [m]	Acronyms and Abbreviations		
CRF Capital Recovery Factor CSP Concentrating Solar Power DNI Direct Normal Irradiance [W/m²] GOR Gain output ratio HTF Heat Transfer Fluid LCOW Levelized Cost Of Water [\$/m³] LFC Linear Fresnel Collector LMTD Logarithmic Mean Temperature Difference MED Multi-Effect Distillation MSF-OT One-Through Multi-Stage Flash NEA Non-Equilibrium Allowance NS North-South orientation O&M Operating and Maintenance OPEX Operating Expenditure [\$/year] PVGIS Photovoltaic Geographical Information System RO Reverse Osmosis RR Recovery Ratio SECeq Specific Equivalent Electricity Consumption SEEC Specific Electrical Energy Consumption STEC Specific Thermal Energy Consumption TBT Top Brine Temperature [°C] TMY Typical Meteoroligical Year TVC Thermal Vapor Compression Symbols A Area [m²] Ap Aperture area [m²] Cp Specific heat at constant pressure [kJ/kg·°C] DC Direct capital cost [\$] Ec Electric price [\$/kWh] f Plant's availability factor fload Time-of-dispatch factor h Specific Entalapy [kJ/kg]	BTE	Boiling Temperature Elevation [°C]	
CSP Concentrating Solar Power DNI Direct Normal Irradiance [W/m²] GOR Gain output ratio HTF Heat Transfer Fluid LCOW Levelized Cost Of Water [\$/m³] LFC Linear Fresnel Collector LMTD Logarithmic Mean Temperature Difference MED Multi-Effect Distillation MSF-OT One-Through Multi-Stage Flash NEA Non-Equilibrium Allowance NS North-South orientation O&M Operating and Maintenance OPEX Operating Expenditure [\$/year] PVGIS Photovoltaic Geographical Information System RO Reverse Osmosis RR Recovery Ratio SECcq Specific Equivalent Electricity Consumption SEEC Specific Thermal Energy Consumption STEC Specific Thermal Energy Consumption TBT Top Brine Temperature [°C] TMY Typical Meteoroligical Year TVC Thermal Vapor Compression Symbols A Area [m²] Ap Aperture area [m²] Cp Specific heat a constant pressure [kJ/kg·°C] DC Direct capital cost [\$] Ec Electric price [\$/kWh] f Plant's availability factor ftod Time-of-dispatch factor h Specific Entalapy [kJ/kg]	CAPEX	Capital Expenditure [\$]	
CSP Concentrating Solar Power DNI Direct Normal Irradiance [W/m²] GOR Gain output ratio HTF Heat Transfer Fluid LCOW Levelized Cost Of Water [S/m³] LFC Linear Fresnel Collector LMTD Logarithmic Mean Temperature Difference MED Multi-Effect Distillation MSF-OT One-Through Multi-Stage Flash NEA Non-Equilibrium Allowance NS North-South orientation O&M Operating and Maintenance OPEX Operating Expenditure [S/year] PVGIS Photovoltaic Geographical Information System RO Reverse Osmosis RR Recovery Ratio SECcq Specific Equivalent Electricity Consumption SEEC Specific Thermal Energy Consumption STEC Specific Thermal Energy Consumption TBT Top Brine Temperature [°C] TMY Typical Meteoroligical Year TVC Thermal Vapor Compression Symbols A Area [m²] Ap Aperture area [m²] Cp Specific Leptic [S/kWh] f Plant's availability factor ftod Time-of-dispatch factor h Specific Enthalpy [kJ/kg]	CRF		
DNI Direct Normal Irradiance [W/m²] GOR Gain output ratio HTF Heat Transfer Fluid LCOW Levelized Cost Of Water [\$/m³] LFC Linear Fresnel Collector LMTD Logarithmic Mean Temperature Difference MED Multi-Effect Distillation MSF-OT One-Through Multi-Stage Flash NEA Non-Equilibrium Allowance NS North-South orientation O&M Operating and Maintenance OPEX Operating Expenditure [\$/year] PVGIS Photovoltaic Geographical Information System RO Reverse Osmosis RR Recovery Ratio SECeq Specific Equivalent Electricity Consumption SEEC Specific Electrical Energy Consumption STEC Specific Thermal Energy Consumption TBT Top Brine Temperature [°C] TMY Typical Meteoroligical Year TVC Thermal Vapor Compression Symbols A Area [m²] Cp Specific heat at constant pressure [kJ/kg·°C] DC Direct capital cost [\$] Ec Electric price [\$/kWh] f Plant's availability factor flood Time-of-dispatch factor h Specific Enthalpy [kJ/kg]	CSP		
HTF Heat Transfer Fluid LCOW Levelized Cost Of Water [\$/m³] LFC Linear Fresnel Collector LMTD Logarithmic Mean Temperature Difference MED Multi-Effect Distillation MSF-OT One-Through Multi-Stage Flash NEA Non-Equilibrium Allowance NS North-South orientation O&M Operating and Maintenance OPEX Operating Expenditure [\$/year] PVGIS Photovoltaic Geographical Information System RO Reverse Osmosis RR Recovery Ratio SECeq Specific Equivalent Electricity Consumption SEEC Specific Electrical Energy Consumption STEC Specific Thermal Energy Consumption TBT Top Brine Temperature [°C] TMY Typical Meteoroligical Year TVC Thermal Vapor Compression Symbols A Area [m²] Ap Aperture area [m²] Cp Specific heat at constant pressure [kJ/kg·°C] DC Direct capital cost [\$] Ec Electric price [\$/kWh] f Plant's availability factor ftod Time-of-dispatch factor h Specific Enthalpy [kJ/kg]	DNI		
LCOW Levelized Cost Of Water [\$/m³] LFC Linear Fresnel Collector LMTD Logarithmic Mean Temperature Difference MED Multi-Effect Distillation MSF-OT One-Through Multi-Stage Flash NEA Non-Equilibrium Allowance NS North-South orientation O&M Operating and Maintenance OPEX Operating Expenditure [\$/year] PVGIS Photovoltaic Geographical Information System RO Reverse Osmosis RR Recovery Ratio SECeq Specific Equivalent Electricity Consumption SEEC Specific Electrical Energy Consumption STEC Specific Thermal Energy Consumption TBT Top Brine Temperature [°C] TMY Typical Meteoroligical Year TVC Thermal Vapor Compression Symbols A Area [m²] Ap Aperture area [m²] Cp Specific heat at constant pressure [kJ/kg·°C] DC Direct capital cost [\$] Ec Electric price [\$/kWh] f Plant's availability factor ftod Time-of-dispatch factor h Specific Enthalpy [kJ/kg]	GOR	Gain output ratio	
LFC Linear Fresnel Collector LMTD Logarithmic Mean Temperature Difference MED Multi-Effect Distillation MSF-OT One-Through Multi-Stage Flash NEA Non-Equilibrium Allowance NS North-South orientation O&M Operating and Maintenance OPEX Operating Expenditure [\$/year] PVGIS Photovoltaic Geographical Information System RO Reverse Osmosis RR Recovery Ratio SECeq Specific Equivalent Electricity Consumption SEEC Specific Electrical Energy Consumption STEC Specific Thermal Energy Consumption TBT Top Brine Temperature [°C] TMY Typical Meteoroligical Year TVC Thermal Vapor Compression Symbols A Area [m²] Ap Aperture area [m²] Cp Specific heat at constant pressure [kJ/kg·°C] DC Direct capital cost [\$] Ec Electric price [\$/kWh] f Plant's availability factor ftod Time-of-dispatch factor h Specific Enthalpy [kJ/kg]	HTF	Heat Transfer Fluid	
LMTD Logarithmic Mean Temperature Difference MED Multi-Effect Distillation MSF-OT One-Through Multi-Stage Flash NEA Non-Equilibrium Allowance NS North-South orientation O&M Operating and Maintenance OPEX Operating Expenditure [\$/year] PVGIS Photovoltaic Geographical Information System RO Reverse Osmosis RR Recovery Ratio SECeq Specific Equivalent Electricity Consumption SEEC Specific Electrical Energy Consumption STEC Specific Thermal Energy Consumption TBT Top Brine Temperature [°C] TMY Typical Meteoroligical Year TVC Thermal Vapor Compression Symbols A Area [m²] Ap Aperture area [m²] Cp Specific heat at constant pressure [kJ/kg·°C] DC Direct capital cost [\$] Ec Electric price [\$/kWh] f Plant's availability factor ftod Time-of-dispatch factor h Specific Entalpy [kJ/kg]	LCOW	Levelized Cost Of Water [\$/m³]	
MED Multi-Effect Distillation MSF-OT One-Through Multi-Stage Flash NEA Non-Equilibrium Allowance NS North-South orientation O&M Operating and Maintenance OPEX Operating Expenditure [\$/year] PVGIS Photovoltaic Geographical Information System RO Reverse Osmosis RR Recovery Ratio SEC _{eq} Specific Equivalent Electricity Consumption SEEC Specific Electrical Energy Consumption STEC Specific Thermal Energy Consumption TBT Top Brine Temperature [°C] TMY Typical Meteoroligical Year TVC Thermal Vapor Compression Symbols A Area [m²] Ap Aperture area [m²] Cp Specific heat at constant pressure [kJ/kg·°C] DC Direct capital cost [\$] Ec Electric price [\$/kWh] f Plant's availability factor f _{tod} Time-of-dispatch factor h Specific Enthalpy [kJ/kg]	LFC	Linear Fresnel Collector	
MED Multi-Effect Distillation MSF-OT One-Through Multi-Stage Flash NEA Non-Equilibrium Allowance NS North-South orientation O&M Operating and Maintenance OPEX Operating Expenditure [\$/year] PVGIS Photovoltaic Geographical Information System RO Reverse Osmosis RR Recovery Ratio SEC _{eq} Specific Equivalent Electricity Consumption SEEC Specific Electrical Energy Consumption STEC Specific Thermal Energy Consumption TBT Top Brine Temperature [°C] TMY Typical Meteoroligical Year TVC Thermal Vapor Compression Symbols A Area [m²] Ap Aperture area [m²] Cp Specific heat at constant pressure [kJ/kg·°C] DC Direct capital cost [\$] Ec Electric price [\$/kWh] f Plant's availability factor f _{tod} Time-of-dispatch factor h Specific Enthalpy [kJ/kg]	LMTD	Logarithmic Mean Temperature Difference	
NEA Non-Equilibrium Allowance NS North-South orientation O&M Operating and Maintenance OPEX Operating Expenditure [\$/year] PVGIS Photovoltaic Geographical Information System RO Reverse Osmosis RR Recovery Ratio SECeq Specific Equivalent Electricity Consumption SEEC Specific Electrical Energy Consumption STEC Specific Thermal Energy Consumption TBT Top Brine Temperature [°C] TMY Typical Meteoroligical Year TVC Thermal Vapor Compression Symbols A Area [m²] Ap Aperture area [m²] Cp Specific heat at constant pressure [kJ/kg·°C] DC Direct capital cost [\$] Ec Electric price [\$/kWh] f Plant's availability factor f _{tod} Time-of-dispatch factor h Specific Enthalpy [kJ/kg]	MED		
NEA Non-Equilibrium Allowance NS North-South orientation O&M Operating and Maintenance OPEX Operating Expenditure [\$/year] PVGIS Photovoltaic Geographical Information System RO Reverse Osmosis RR Recovery Ratio SEC _{eq} Specific Equivalent Electricity Consumption SEEC Specific Electrical Energy Consumption STEC Specific Thermal Energy Consumption TBT Top Brine Temperature [°C] TMY Typical Meteoroligical Year TVC Thermal Vapor Compression Symbols A Area [m²] Ap Aperture area [m²] Cp Specific heat at constant pressure [kJ/kg·°C] DC Direct capital cost [\$] Ec Electric price [\$/kWh] f Plant's availability factor f _{tod} Time-of-dispatch factor h Specific Enthalpy [kJ/kg]	MSF-OT	One-Through Multi-Stage Flash	
NS North-South orientation O&M Operating and Maintenance OPEX Operating Expenditure [\$/year] PVGIS Photovoltaic Geographical Information System RO Reverse Osmosis RR Recovery Ratio SEC _{eq} Specific Equivalent Electricity Consumption SEEC Specific Electrical Energy Consumption STEC Specific Thermal Energy Consumption TBT Top Brine Temperature [°C] TMY Typical Meteoroligical Year TVC Thermal Vapor Compression Symbols A Area [m²] Ap Aperture area [m²] Cp Specific heat at constant pressure [kJ/kg·°C] DC Direct capital cost [\$] Ec Electric price [\$/kWh] f Plant's availability factor f _{tod} Time-of-dispatch factor h Specific Enthalpy [kJ/kg]	NEA		
OPEX Operating Expenditure [\$/year] PVGIS Photovoltaic Geographical Information System RO Reverse Osmosis RR Recovery Ratio SEC _{eq} Specific Equivalent Electricity Consumption SEEC Specific Electrical Energy Consumption STEC Specific Thermal Energy Consumption TBT Top Brine Temperature [°C] TMY Typical Meteoroligical Year TVC Thermal Vapor Compression Symbols A Area [m²] Ap Aperture area [m²] Cp Specific heat at constant pressure [kJ/kg·°C] DC Direct capital cost [\$] Ec Electric price [\$/kWh] f Plant's availability factor ftod Time-of-dispatch factor h Specific Enthalpy [kJ/kg]	NS		
OPEX Operating Expenditure [\$/year] PVGIS Photovoltaic Geographical Information System RO Reverse Osmosis RR Recovery Ratio SEC _{eq} Specific Equivalent Electricity Consumption SEEC Specific Electrical Energy Consumption STEC Specific Thermal Energy Consumption TBT Top Brine Temperature [°C] TMY Typical Meteoroligical Year TVC Thermal Vapor Compression Symbols A Area [m²] Ap Aperture area [m²] Cp Specific heat at constant pressure [kJ/kg·°C] DC Direct capital cost [\$] Ec Electric price [\$/kWh] f Plant's availability factor ftod Time-of-dispatch factor h Specific Enthalpy [kJ/kg]	O&M	Operating and Maintenance	
PVGIS Photovoltaic Geographical Information System RO Reverse Osmosis RR Recovery Ratio SEC _{eq} Specific Equivalent Electricity Consumption SEEC Specific Electrical Energy Consumption STEC Specific Thermal Energy Consumption TBT Top Brine Temperature [°C] TMY Typical Meteoroligical Year TVC Thermal Vapor Compression Symbols A Area [m²] Ap Aperture area [m²] Cp Specific heat at constant pressure [kJ/kg·°C] DC Direct capital cost [\$] Ec Electric price [\$/kWh] f Plant's availability factor f _{tod} Time-of-dispatch factor h Specific Enthalpy [kJ/kg]	OPEX		
RO Reverse Osmosis RR Recovery Ratio SEC _{eq} Specific Equivalent Electricity Consumption SEEC Specific Electrical Energy Consumption STEC Specific Thermal Energy Consumption TBT Top Brine Temperature [°C] TMY Typical Meteoroligical Year TVC Thermal Vapor Compression Symbols A Area [m²] Ap Aperture area [m²] Cp Specific heat at constant pressure [kJ/kg·°C] DC Direct capital cost [\$] Ec Electric price [\$/kWh] f Plant's availability factor f _{tod} Time-of-dispatch factor h Specific Enthalpy [kJ/kg]	PVGIS		
$\begin{array}{cccccccccccccccccccccccccccccccccccc$	RO		
$ \begin{array}{cccccccccccccccccccccccccccccccccccc$	RR	Recovery Ratio	
$ \begin{array}{cccccccccccccccccccccccccccccccccccc$	SEC _{eq}	·	
$ \begin{array}{cccccccccccccccccccccccccccccccccccc$	*		
TBT Top Brine Temperature [°C] TMY Typical Meteoroligical Year TVC Thermal Vapor Compression Symbols A Area [m²] Ap Aperture area [m²] Cp Specific heat at constant pressure [kJ/kg·°C] DC Direct capital cost [\$] Ec Electric price [\$/kWh] f Plant's availability factor ftod Time-of-dispatch factor h Specific Enthalpy [kJ/kg]	STEC		
TMY Typical Meteoroligical Year TVC Thermal Vapor Compression Symbols A Area [m²] Ap Aperture area [m²] Cp Specific heat at constant pressure [kJ/kg·°C] DC Direct capital cost [\$] Ec Electric price [\$/kWh] f Plant's availability factor ftod Time-of-dispatch factor h Specific Enthalpy [kJ/kg]	TBT		
	TMY		
$ \begin{array}{c ccccccccccccccccccccccccccccccccccc$	TVC		
Aperture area [m²] Cp Specific heat at constant pressure [kJ/kg·°C] DC Direct capital cost [\$] Ec Electric price [\$/kWh] f Plant's availability factor ftod Time-of-dispatch factor h Specific Enthalpy [kJ/kg]	Symbols		
Aperture area [m²] Cp Specific heat at constant pressure [kJ/kg·°C] DC Direct capital cost [\$] Ec Electric price [\$/kWh] f Plant's availability factor ftod Time-of-dispatch factor h Specific Enthalpy [kJ/kg]	A	Area [m²]	
Cp Specific heat at constant pressure [kJ/kg·°C] DC Direct capital cost [\$] Ec Electric price [\$/kWh] f Plant's availability factor ftod Time-of-dispatch factor h Specific Enthalpy [kJ/kg]	Ap		
DC Direct capital cost [\$] Ec Electric price [\$/kWh] f Plant's availability factor ftod Time-of-dispatch factor h Specific Enthalpy [kJ/kg]			
Ec Electric price [\$/kWh] f Plant's availability factor f _{tod} Time-of-dispatch factor h Specific Enthalpy [kJ/kg]			
f Plant's availability factor f _{tod} Time-of-dispatch factor h Specific Enthalpy [kJ/kg]			
f _{tod} Time-of-dispatch factor h Specific Enthalpy [kJ/kg]			
h Specific Enthalpy [kJ/kg]			
1 17 5		-	
Ho Local solar time			
H _{rc} Receiver height [m]			

i	Single-Stage Desalination Index	
IDC	Indirect capital cost [\$]	
J	Day of the year	
IAM	Incident angle modifier [°]	
L	Length [m]	
M	Mass [kg]	
MC	Operating maintenance cost [\$]	
ṁ	Mass flowrate [kg /h]	
n	Total number of MSF-OT stages	
N	Number	
P	Power [W]	
p	Pressure [Bar]	
Q	Heat energy [kJ]	
U	Overall heat transfer coefficient [W/m².°C]	
V_{ST}	Volume of the storage tank [m ³ /s]	
$V_{\rm v}$	Vapor speed in the demister [m/s]	
V_b	Brine mass flow rate per stage width [kg/(m·s)]	
X	Salinity [ppm]	
у	Specific ratio of sensible heat and latent heat	
Greek letters		
δ	Declination [°]	
δ_{w}	Wire diameter [mm]	
η	Efficiency [%]	
η_0	Maximum optical efficiency [%]	
θ	Solar zenith angle [°]	
θ_{w}	Incident angle of solar radiation on the surface [°]	
ρ	Reflectivity	
ρ_p	Demister density [kg/m ³]	
ρ_{s}	Seawater density [kg/m ³]	
αst	Cost per cubic meter of storage tank [\$/m³]	
α	Absorptivity	
$\alpha_{\rm s}$	Solar altitude angle [°]	
τ	Transmittivity	
φ	Latitude	
$\gamma_{\rm s}$	Solar azimuth angle [°]	
β	Cost per square meter of collector area [\$/m²]	
λ	Latent heat [kJ/kg]	
ω	Solar hour angle [°]	
Subscripts		
ab, ex	Outer surface of the absorber tube	
amb	Ambient	
ave	Average	

aux	Auxiliary fossil buckup
b	Brine
ВН	Brine heater
block	Blocked
С	Condensation
С	Collector
d	Distillate water
D	Total distillate water
Dp	Demister pressure
end	end-loss
ev	Evaporation
f	Feed water
fr	Friction
HTF	Heat Transfer Fluid
HTF-C	Heat Transfer Fluid circulating in the collector
HTF-in	Heat transfer fluid at the intlet of the collector
HTF-out	Heat transfer fluid at the outlet of the collector
inc	Incidence
L	Longitudinal
loss	Heat losses
m	Motor
opt	Optical
p	Pump
R	Rows
S	Steam
shad	Shaded
st	Stage
SF	Solar Field
T	Traversal
th,field	Thermal power provided by the solar field
th,MSF	Thermal power required by the MSF plant
Tot,c	Total number of collectors
u	Useful
v	Vapor

GENERAL INTRODUCTION

Water is a vital resource for all living organisms, playing a fundamental role in human survival, agricultural activities, and industrial development. However, despite its critical importance, ensuring access to clean and safe drinking water remains a major global challenge. Although significant progress has been made in enhancing water accessibility over recent decades, a substantial portion of the global population still lacks reliable access to potable water. The increasing global population, rapid urbanization, and rising living standards have further strained available freshwater resources. Projections indicate that water demand will continue to rise, intensifying pressure on natural reserves. Given that the majority of Earth's water is saline and a significant fraction is locked in ice, desalination has become a viable solution to address growing water scarcity.

Desalination technologies have advanced considerably, leading to the development of various processes aimed at improving efficiency and reducing costs. Among the widely implemented methods, Multi-Stage Flash (MSF) and Reverse Osmosis (RO) constitute a significant share of the global desalination market. While RO has gained preference due to its lower energy consumption, MSF remains a dominant choice in regions with abundant and low-cost fossil fuel resources. However, conventional MSF desalination plants rely extensively on non-renewable energy sources, resulting in high operational costs and considerable environmental implications. To mitigate these challenges, the integration of renewable energy sources into desalination processes has attracted increasing interest as a sustainable approach to water production.

Among renewable energy technologies, Concentrating Solar Power (CSP) systems have demonstrated strong potential in supplying the thermal energy required for desalination. In particular, Linear Fresnel Collectors (LFC) have emerged as a promising CSP technology due to their cost-effectiveness, scalability, and efficient thermal energy conversion. LFC systems concentrate solar radiation onto receiver tubes containing a heat-transfer fluid, which is subsequently used to generate the thermal energy necessary for desalination. The direct integration of LFC with MSF desalination presents an opportunity to enhance energy efficiency, reduce dependency on fossil fuels, and minimize the carbon footprint associated with water production.

The objective of this study is to investigate the feasibility and enhancement of integrating an LFC with a Once-Through Multi-Stage Flash (MSF-OT) desalination system. The proposed approach aims to improve energy efficiency and freshwater production by directly coupling the LFC with the MSF-OT process, thereby minimizing energy losses and enhancing thermal performance. To ensure continuous operation, the system incorporates thermal energy storage and a fossil fuel backup. Additionally, an advanced control mechanism is implemented to regulate fluid flow, temperature, and pressure, increasing overall reliability. A novel design featuring isolated tubes at each stage is introduced to maintain a steady brine flow rate, further improving desalination efficiency and system stability. Through

comprehensive analysis, this research seeks to develop a sustainable and cost-effective desalination solution that leverages solar energy to address water scarcity challenges.

The structure of this thesis is as follows:

- Chapter 1 provides an overview of the issue of water scarcity and the importance of desalination as a sustainable solution. The first part discusses the role of renewable energy, particularly solar thermal energy, in powering desalination systems. The second part focuses on Linear Fresnel Collectors and the Multi-Stage Flash desalination process, as well as their direct coupling. Finally, the need for a parametric analysis is highlighted to emphasize its importance in evaluating system performance, outlining the research objectives, scope, and limitations of this study.
- Chapter 2 presents a comprehensive literature review on solar-powered desalination technologies. It explores existing studies on both LFC and MSF technologies, emphasizing their potential when combined. The chapter also identifies research gaps and the need for further investigation into the direct coupling of LFC with MSF-OT systems.
- Chapter 3 details the methodology employed in this research, covering the system design, modeling techniques, and simulation tools used. It describes the assumptions, governing equations, and computational approaches applied to evaluate system performance.
- **Chapter 4** presents the results of the parametric study, analyzing the impact of various operational and environmental factors on system performance. It also includes sensitivity analyses to evaluate the robustness of the proposed system under different conditions.
- Chapter 5 discusses the detailed findings from the implementation of the novel coupling technique, interpreting the results in the context of existing desalination technologies. It evaluates the implications of the proposed approach, comparing its performance with alternative solar-powered desalination methods in terms of cost-effectiveness, productivity, and environmental sustainability. Furthermore, the section examines the potential challenges and limitations associated with the proposed system.

Finally, a general conclusion summarizes the key findings of the chapters, followed by recommendations to further enhance this work in the future.

Chapter 1: Overview

1.1. Introduction

Solar desalination is often perceived as a solution limited to small-scale technologies aimed at providing water in remote areas. While these approaches are essential for the development of rural regions, they are insufficient to address the growing water deficits in urban centers, where rapid population growth continues to increase demand. Conversely, large-scale conventional desalination is commonly viewed as an expensive and energy-intensive solution, accessible mainly to wealthier nations such as those in the Arabian Gulf. This perception is largely driven by the escalating costs of fossil fuels like oil, natural gas, and coal, which make these technologies less feasible in many regions. This chapter explores the challenges and opportunities of solar water desalination. It begins with background information explaining global water scarcity and the role of desalination, followed by an examination of the increasing energy demand and the need for sustainable solutions, such as renewable energypowered desalination. Next, it introduces the fundamentals of Linear Fresnel Collector (LFC) technology, highlighting its advantages over other solar collectors as well as its challenges. Then, the Multi-Stage Flash (MSF) desalination process is described, including its energy requirements and the advantages it offers. The coupling of LFC with a Once-Through MSF system is then presented, along with a discussion of its potential benefits and the challenges it may face. Finally, the chapter concludes with a summary of the main points.

1.2. Background

Throughout history, the search for safe drinking water has led to important developments. Hippocrates II [1], in 460–370 B.C., observed that boiling water makes it safe to drink and that sun's radiation can be used to purify it. In 1627, Francis Bacon [2] discovered that salt does not evaporate from seawater. By 1750, the first thermal desalination devices [3] were created for ships to provide fresh water during voyages. The development of commercial desalination systems began in 1851 [3], and all systems were thermal at that time. In 1970, reverse osmosis (RO) membranes were introduced for commercial use [4]. Table 1.1 presents an overview of the important developments and achievements in thermal and membrane desalination technologies.

Table 1. 1. Overview of the important developments and achievements in thermal and membrane desalination technologies.

Year	Realisation	
1790	• Thomas Jefferson detailed a practical approach to desalinate	[5]
	seawater for shipboard use.	

Late 1930's	• Numerous small-scale systems for desalinating seawater were built in the Middle East.	[3]
Up to 1950's	• The biggest desalination unit ever built had a production capacity of under 1,892 m ³ /d.	[4]
1957	• Westinghouse established the first industrial-scale flashing chamber in Kuwait, consisting of a four-chamber system with a performance ratio of 3.3.	[4]
	 Silver obtained a patent for declaring that the number of flash stages should be equal to or exceed twice the thermal efficiency of the flash plant. 	[6]
1960	• In Shuwaikh, Kuwait, the first MSF plant was commissioned, boasting 19 stages and a capacity of 440 m³/d, achieving a performance ratio of 5.7. Simultaneously, Guernsey, Channel Islands, launched a second plant with 40 stages, a capacity of 2,775 m³/d, and a performance ratio of 10.	[4]
1970	Enhancements in the field of commercial RO membrane development.	[4]
1980	 Develop and operate low-temperature multiple effect evaporation units integrated with thermal compression technology. Develop and operate low-temperature mechanical vapor compression technologies. 	[4]
1996	• Development of the largest MSF unit in the UAE, designed to operate at 57,735 m ³ /d.	[4]
1999	 Implementation of a large-scale RO plant in Florida, USA. Amplified capacity of the multiple effect evaporation unit. 	[4]
2000	• Design and implementation of a high-efficiency MSF plant with 43 stages and a performance ratio of 13.	[4]
2006	 An MSF unit capacity has been established at 59,000 m³/day. In terms of global desalination distribution, MSF accounts for 57%, MED for 8%, and RO for 35%. 	[6] [7]
2008	• The capacity of the MSF unit has increased to 79,500 m³/day.	[6]
2012	 A total thermal capacity of 23.2 million m³/day has been installed. Installed membrane capacity has been measured at 49.9 million m³/day. 	[7] [8]
	 m³/day. Global desalination technology distribution shows 26% MSF, 8% MED, 61% RO, and 5% categorized as Others. 	
2014	 Global desalination technology distribution indicates 22% for MSF, 8% for MED, 65% for RO, and 5% for Others. 	[9]

	•	Since 2010, global desalination capacity has grown by about 7%							
		per year, with increases of over 1600% in Europe and 1700% in							
2010-2020		Africa, driven by climate change and population growth. RO							
2010-2020		technology leads production, while emerging technologies							
		(EDR, FO, MD) are increasingly used in small and medium-							
		scale plants.							

In the last 10 years, Mediterranean desalination capacity grew by 446.8%, reaching 5.1 million m³/day, while the global total in 2023 is 110 million m³/day.

The southern Mediterranean, while having fewer desalination plants than the north, achieves significantly higher production capacities. Most southern countries produce between 3,014 and 84,850 m³/day, surpassing northern capacities, which range from 120 to 4,700 m³/day. The leading countries in terms of production capacity are all located in the south, including Morocco, Algeria, Tunisia, and Egypt [11].

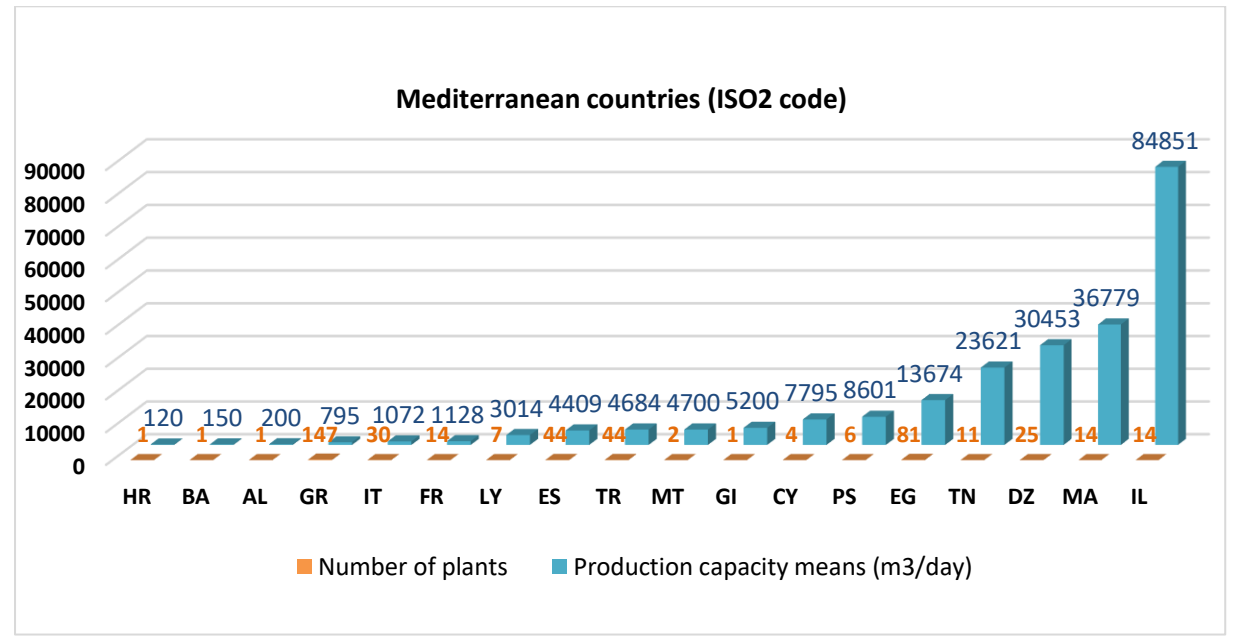


Fig.1. 1. Histogram of the average daily desalinated water production and the number of plants by country in 2023 [12].

1.2.1. Global Water Scarcity and the Role of Desalination

1.2.1.1. Current State

Water is an essential natural resource, as all life on Earth depends on it. It is the most critical of all chemical compounds [3]. Limited access to clean and safe drinking water can severely harm both human living conditions and the environment.

Every year, millions of individuals, including 3,900 children per day [12], die from diseases linked to contaminated drinking water. Currently, over 2.6 billion people lack adequate sanitation facilities, while more than 1.2 billion suffer from insufficient access to safe drinking water [13]. In developing nations, unclean water is responsible for 80-90% of diseases and contributes to over 30% of all deaths [14]. Rapid population growth in these regions intensifies the pressure on already limited water resources [15]. For every 0.5%

increase in global population, there is a corresponding 1.5% rise in freshwater withdrawals [16, 17]. Furthermore, annual demand for fresh water is increasing by 3%, necessitating significant investment in water infrastructure [18]. By 2025, more than 3 billion people in over 48 countries are projected to face conditions of water stress or scarcity [19].

The Earth contains approximately 1,386,000,000 cubic kilometers of water [20], but only about 3% of this is fresh water [21, 22]. Of that fresh water, only 2.5% is suitable for drinking or human consumption [23, 24].

According to the Institute of Medicine, an adult male requires about 3.5 liters of drinking water per day, while an adult female needs around 2.5 liters [25, 26]. Water usage varies significantly between countries, with North Americans averaging about 400 liters per day per person, compared to around 200 liters per day per person in Europe [14]. The hydrological analysis indicates that MENA has among the lowest per capita renewable water resources in the world, and the situation is expected to worsen in the future (Fig. 1.2).

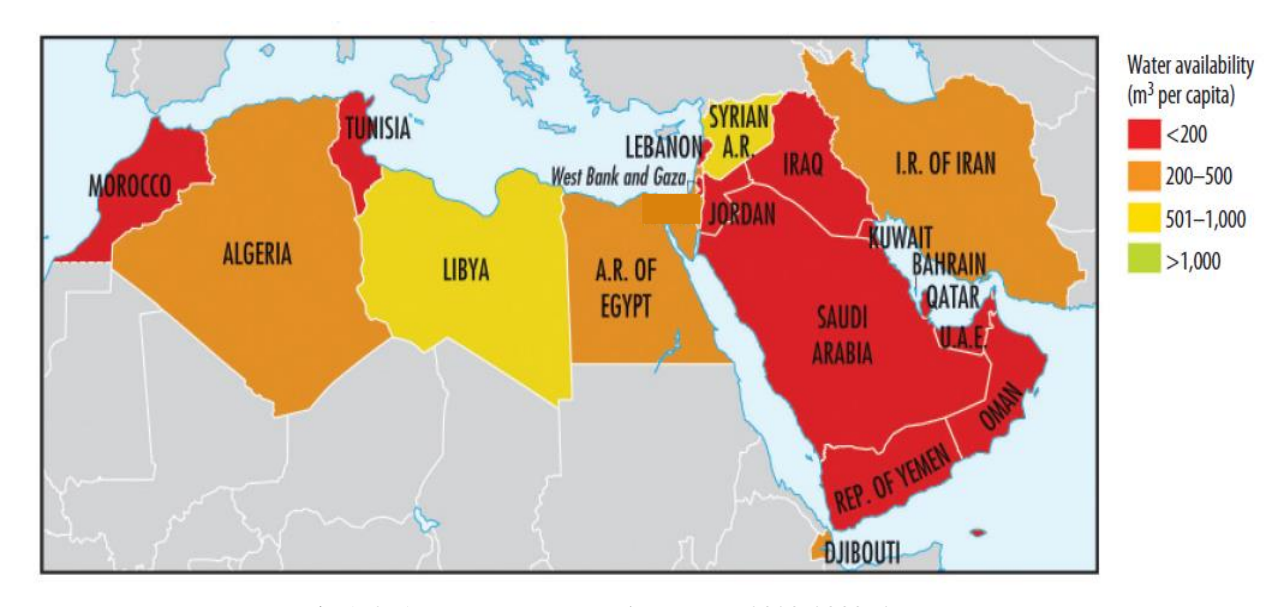


Fig.1. 2. Average water stress by country 2020-2030 [27].

Even minor changes might pose significant issues for populations in areas with limited per capita water supplies. The Food and Agriculture Organization (FAO) considers a total renewable water availability of less than 1,000 m³ per capita as a serious impediment to socioeconomic development and environmental sustainability. Annual water availability below 2,000 m³ per capita is a significant concern, especially during droughts. By 2020-2030, all 21 MENA countries are predicted to have significant water scarcity. This issue is going to get worse as the world's population increases. By 2050, 14 nations are expected to have less than 200 m³ of sustainable water per person [27]. Addressing these challenges is crucial for improving public health and ensuring sustainable access to clean water.

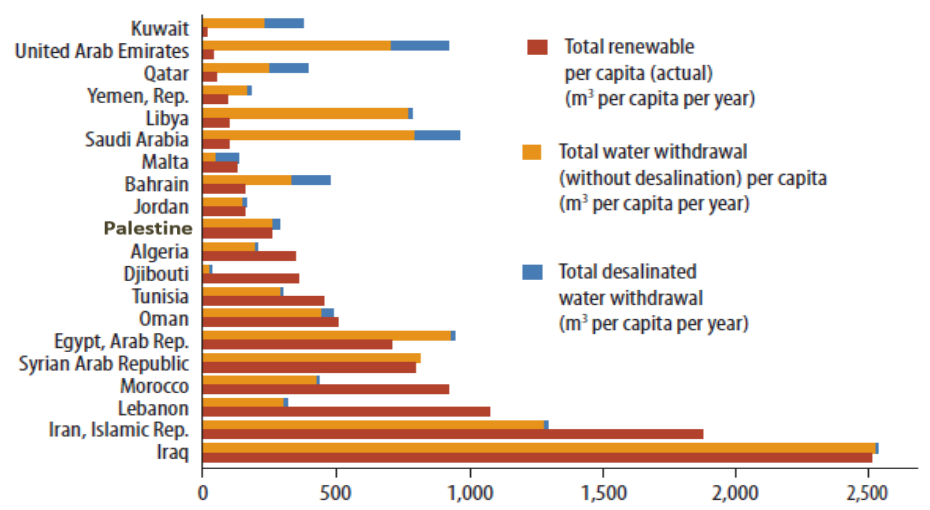


Fig.1. 3. Water resources availability and use in MENA countries [27].

1.2.1.2. Environmental impact

The rising demand for energy is primarily driven by changes in human lifestyles, such as globalization, urbanization, suburban expansion, consumerism, and increased productivity. These factors are leading to a rapid increase in energy consumption. According to a recent report from the World Energy Council (WEC), global energy demand is expected to rise by 50% to 80% compared to 1990 levels by 2020 [28]. Furthermore, BP's statistical evaluation forecasts a 60% increase in energy demand from 2014 levels by 2035 [29]. These trends indicate that significant energy-related challenges may be on the horizon.

Energy in nature is available in various forms and can be divided into two main categories: renewable and non-renewable sources. Renewable energy is sourced from natural processes that are continuously replenished, including solar, wind, hydro, and geothermal energy [30, 31]. These sources are sustainable, meaning they can be harnessed without depleting them, and they generally have a lower environmental impact compared to non-renewable energy sources [32, 33]. Non-renewable energy sources, such as fossil fuels (coal, oil, and natural gas) and nuclear energy, are limited resources that can take millions of years to form. Their extraction and use cause pollution and greenhouse gas emissions, which harm the ecosystem and contribute to climate change. For example, a study in California reported that desalination plants increased water industry emissions from 360 to 800 kg of CO₂ equivalent [34]. Transitioning to renewable energy sources is essential for promoting sustainability, reducing the negative environmental effects of energy use, addressing the global problem of climate change, and preserving the planet's future for future generations.

In summary, the growing global demand for water, combined with decreasing supplies of fresh water and non-renewable energy sources, presents a significant engineering challenge. One promising solution is the use of solar energy for desalinating seawater, which can effectively address both water shortages and energy consumption. As such, solar-powered desalination stands out as a viable approach to these interconnected issues.

1.2.2. Renewable Energy for Desalination

Fossil fuels still dominate global energy use, causing major economic and environmental problems, such as higher costs due to resource scarcity, low energy security, and significant contributions to climate change. For example, traditional MSF desalination systems need over

250 kJ/kg of thermal energy and 3.5 kWh/m³ of electrical energy to produce one cubic meter of fresh water [35], highlighting the need for more sustainable solutions.

Using clean energy for desalination is becoming more popular. This approach is becoming economically competitive as the costs of renewable technologies decline and fossil fuel prices rise [36]. Numerous studies highlight the effectiveness of solar desalination in producing clean water and offering a low-carbon solution to water scarcity. Feng et al. [37] found that using renewable energy like wind and solar could reduce emissions by 79% and water use by 50% in China. However, because renewable energy is not always available, it cannot fully meet the energy needs of water systems. A mix of energy sources and storage systems is needed for reliable supply [38]. Tokui et al. [39], suggest that supplying 40–50% of the energy demand in desalination plants from renewable sources could ensure sustainable operations. However, on a global scale, less than 1% of desalination facilities currently use renewable energy [36], underscoring the untapped potential of this approach.

Renewable energy and desalination are distinct technologies that can be effectively integrated in various ways. Achieving successful combined designs requires collaboration between experts from both fields renewable energy and desalination. Desalination technologies are divided into three types based on the energy used: thermal, mechanical, and electrical. While evaporative processes require all three energy forms to run pumps and auxiliary units, this classification focuses on thermal energy as the primary driver for thermal methods. Classifying by energy input is essential for evaluating compatibility with renewable energy sources, such as solar thermal collectors, photovoltaic panels, and wind turbines (see

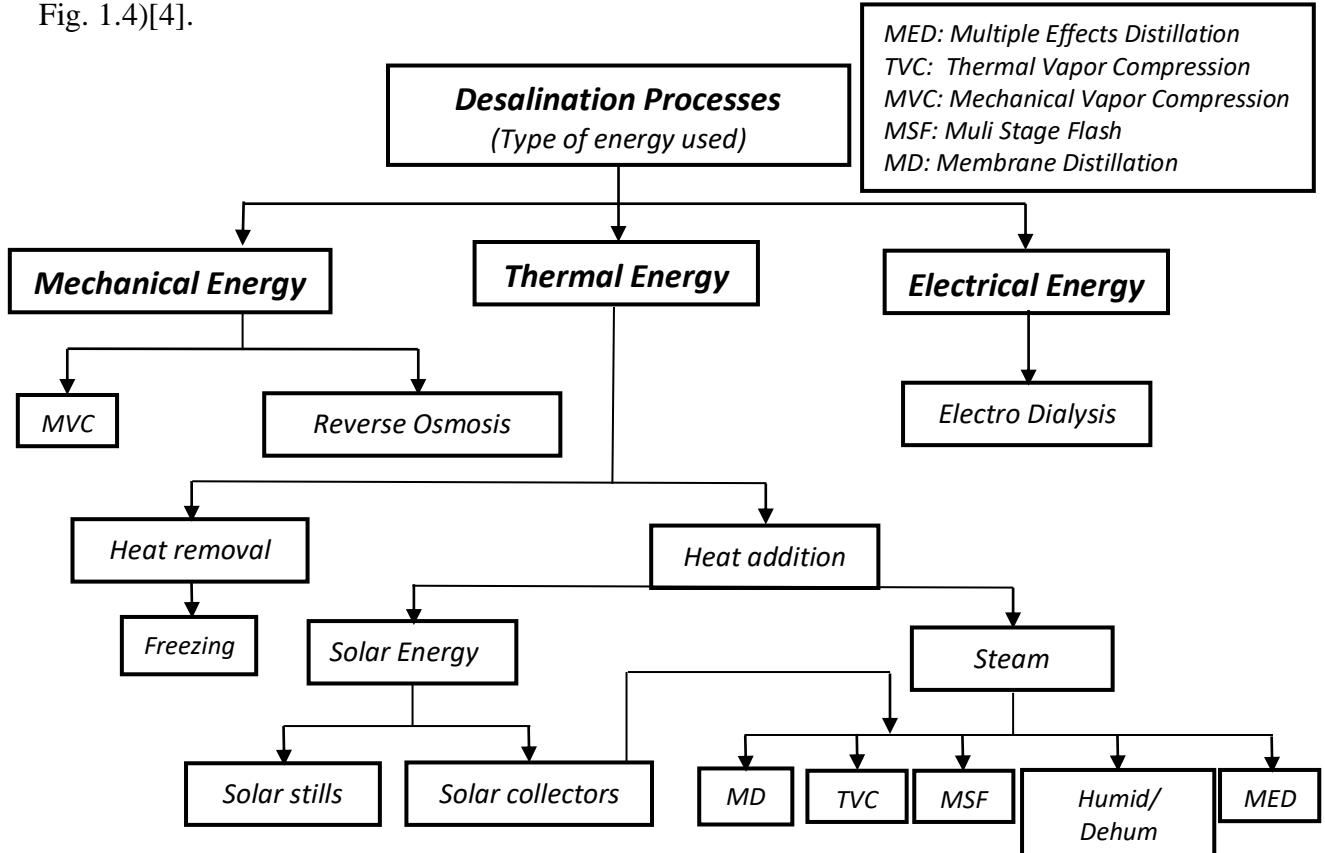


Fig.1. 4. Classification of desalination processes by type of energy [40].

Although solar and wind power may not be continuous, the energy can be balanced by connecting to the power grid. Some desalination systems use solar or wind energy with storage to reduce complexity. Technologies like multi-stage flash, multiple effect distillation, and membrane distillation require significant heat, making energy storage crucial. Choosing the appropriate renewable energy source for desalination depends on factors such as location, water source, demand, infrastructure, and costs [41, 42, 43]. Table 1.2 presents examples of desalination methods along with their corresponding solar energy systems [44]. When selecting a solar-powered desalination system, particularly for remote and arid regions, it must exhibit the following characteristics [45]:

- Simplicity in design and operation
- Ease of handling and maintenance
- Suitability for the specific conditions of the installation site
- Potential for future expansion and optimization of efficiency.

Table 1. 2. Main features of desalination technologies and their appropriate energy sources [44].

Desalination Method	Capacity (m³/day)	Necessary Energy	Temperature Region (°C)	Collector Technology
MD	0.15-10	150-299kWh/m ³	70	Flat plate or vacuum tube
TVC	> 5000	8-10kWh _{th} /m ³	Up to 110	vacuum tube
MSF	>> 10 ⁴	$60-70kWh_e/m^3+1.5-2.0kWh_e/m^3$	90-120	CSP
MED (low temperature)	> 5000	$60-70kWh_e/m^3+1.5-2.0kWh_e/m^3$	70-80	Flat plate
MED	> 5000	60-70kWh _e /m ³ +1.5-2.0kWh _e /m ³	110-160	CSP

1.2.2.1. CSP and Desalination: Site Potential

This section gives an overview of concentrating solar energy potential, as well as suitable sites for CSP and desalination.

• Potential of Concentrating Solar Energy

In recent years, Concentrated Solar Power (CSP) systems have seen significant global growth, reaching a total of 7200 MW of solar thermal electric capacity by the end of 2024 [46]. These systems work by concentrating solar energy from large areas onto smaller surfaces using mirrors or lenses, primarily focusing on the beam component of solar radiation, known as Direct Normal Irradiance (DNI), due to its directional properties. The concentrated solar radiation is then converted into thermal energy, which is used for heating or electricity generation. In CSP yield analysis, the meteorological data used for modeling is crucial, as uncertainties in solar resources, especially long-term DNI data, can impact the feasibility of a project [47]. DNI and solar irradiance at the plant site vary from year to year, and this variability must be accurately understood to estimate long-term solar resources and plant performance [48, 49, 50]. One common method to represent long-term weather data is by creating a Typical Meteorological Year (TMY) for the location. However, TMY doesn't capture year-to-year DNI changes, which can hide extreme solar conditions due to its average nature [51, 52].

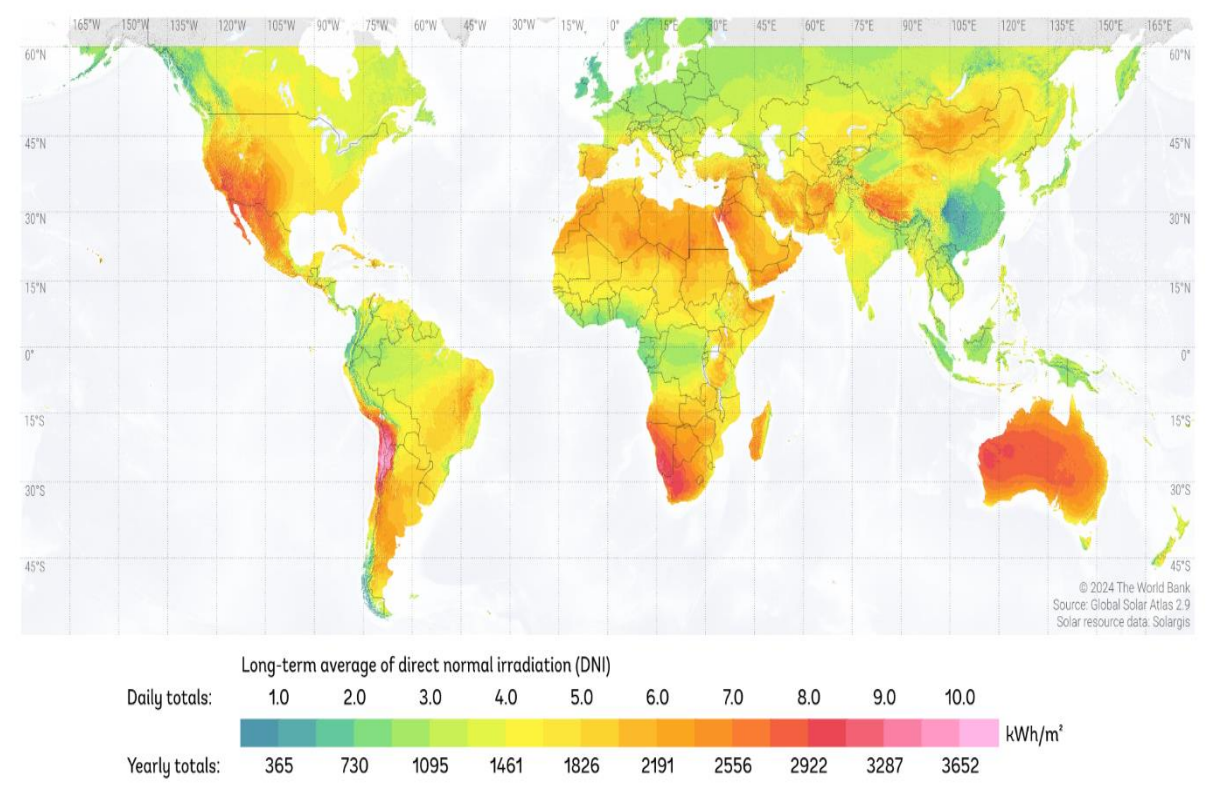


Fig.1. 5. Global map of daily and annual DNI (kWh/m²) based on long-term averaged data [53].

Fig. 1.5 illustrates a global map of daily and annual direct normal irradiation (DNI) (kWh/m²), based on long-term average data [53]. The map shows regions with high DNI potential, ranging from 2000 kWh/m² to over 3000 kWh/m². These regions, largely found in desert and semi-desert areas, are characterized by clear skies, low humidity, and minimal dust or pollution. Notable areas with high DNI include the US Southwest, Middle East, North Africa (MENA), Spain, Chile, Australia, India, and southwestern China.

CSP sector has seen significant growth over the past decade, with global capacity rising from 0.5 GW in 2006 to about 5.0 GW in 2015 [54]. This growth is largely due to the increasing potential of CSP for various applications, especially when combined with thermal energy storage and hybrid systems. While the US and Spain lead in CSP development and capacity, new markets are quickly emerging in countries such as India, Chile, China, South Africa and Morocco [54].

The growth of CSP markets is driven by advancements in technology, lower capital costs, better performance, and increased interest in financing CSP projects. Table 1.3 [55] shows regional and global CSP capacity forecasts for 2030, 2040, and 2050, based on the High-Renewables (Hi-Ren) scenario, which aims for a large share of renewable energy sources like PV, wind, and CSP to meet global electricity needs. According to the table, global CSP capacity is expected to rise significantly, reaching 261 GW by 2030, 664 GW by 2040, and 982 GW by 2050. However, the deployment of CSP is progressing more slowly from 2013 to 2030 compared to later periods, as technological maturity, cost reduction, and investments are projected to progress at a slower pace during this time [55].

Table 1. 3. Regional and Global CSP Capacity Projections Based on the Hi-Ren Scenario [55].

	Capacity (GW)										
	United States	Other OECD Americas	EU	Other OECD	China	India	Africa	Middle East	Other developing Asia	Non- OECD Americas	World
2013	1.3	0.01	2.31	0.01	0.02	0.06	0.06	0.10	0.02	0	4.1
2030	87	6	15	4	29	34	32	52	0.3	2	261
2040	174	18	23	12	88	103	106	131	3	7	664
2050	229	28	28	19	118	186	147	204	9	15	982

• Solar energy potential in Algeria

Algeria is the largest country in North Africa and Africa, covering over two million square kilometers, with nearly two-thirds of its area consisting of desert [56]. In January 2019, the population was 43 million, an increase of 1.9% compared to 2018 [57]. By 2030, the population is projected to reach 51 million [58]. The population is predominantly concentrated in the northern regions and along the Mediterranean coast, while the southern territories, particularly the Sahara, remain sparsely inhabited. Algeria's geographic and climatic conditions endow it with exceptional solar energy resources, making it one of the most favorable locations globally for the deployment of CSP technologies. This substantial potential continues to drive research and development in solar thermal electricity generation. Across the national territory, DNI values consistently exceed 2,000 kWh/m²/year, resulting in an estimated annual solar energy potential of approximately 169,900 TWh equivalent to nearly 3,900 times the country's current electricity consumption [59]. The figure below presents the spatial distribution of solar potential across various regions of Algeria [60, 61].

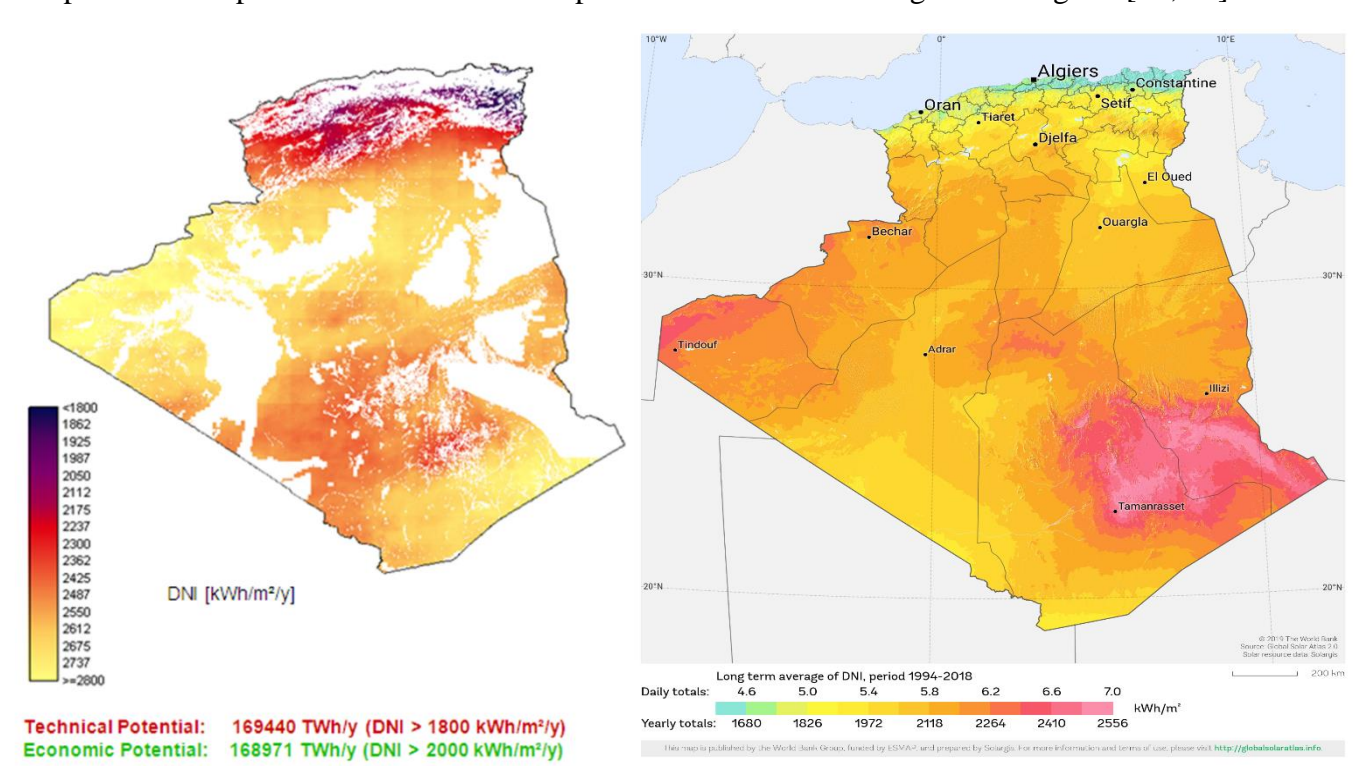


Fig.1. 6. Solar energy potential and direct normal irradiance in Algeria [60, 61].

Potential sites for desalination

The United Nations Environment Program predicts that in this next years, two-thirds of the world's population will face water scarcity [62, 63]. Freshwater resources are unevenly

distributed, with 96.54% of the Earth's water being saline and only 2.53% freshwater [64]. Factors such as rapid population growth, industrial development, and climate change have made regions like MENA, Asia, the United States, and Latin America increasingly reliant on desalination plants to address water scarcity.

Desalination is the process of extracting minerals and salts from saline water to produce freshwater, which can be utilized for human consumption or irrigation. This technique can be applied to seawater and brackish water, each with distinct performance criteria.

Water with a salinity range of 5 to 1000 ppm is commonly found in rivers and lakes, and can also be generated through industrial desalination processes. Generally, water is considered suitable for drinking when its salinity is below 500 ppm. In urban areas, various salinity levels are employed, with water below 150 ppm used for drinking and water with salinity up to 1000 ppm used for other household applications (see Table 1.5).

Table 1. 4. Water classification by salinity concentration [65, 66].

Type	Total Dissolved Solids (TDS)		
Fresh Water	Up to 1000		
Brackish Water	1000-10000		
Salt Water	>10000		
Seawater	10000-50000		
Standard Seawater	35000		

In many arid regions, both coastal and inland, desalination of seawater or brackish water is often the only viable solution for obtaining fresh water. Due to its strategic importance, many countries opt for the relatively costly desalination process, which has proven to be a sustainable source [67]. Since its industrial-scale inception in the 1950s, the desalination industry has made significant progress, especially in Gulf countries, which account for over 50% of global production, as shown in Fig. 1.7. The world desalination capacity now exceeds 26 million cubic meters per day and is expected to double by the end of the first half of this century [7]. The United States is the second-largest producer, holding nearly 20% of the market share, mainly from low-salinity and river water desalination plants. Other countries, such as Algeria, Libya, China, Singapore, Cyprus, and Australia, contribute to the remaining production, with capacities above 100,000 cubic meters per day but below one million cubic meters per day [7].

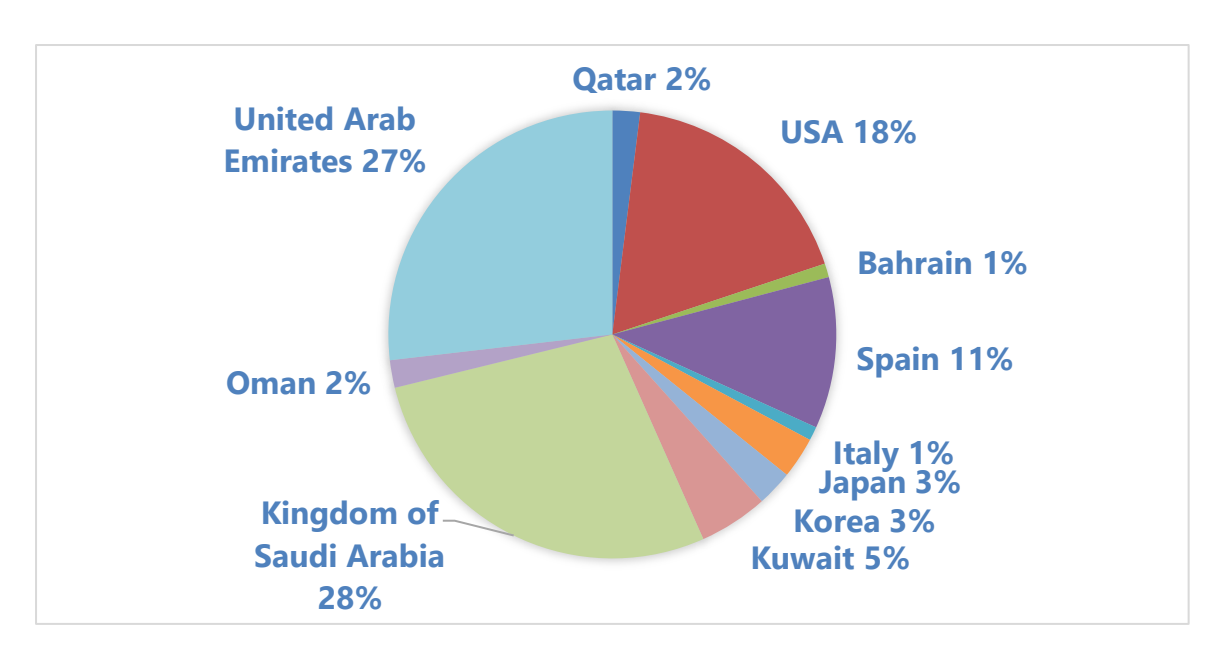


Fig.1. 7. Market shares of major desalination producers [7].

The global desalination market is expanding. By October 2017, approximately 19,372 desalination plants were operating worldwide, producing up to 92.5 million m³ of clean water daily [68]. The Middle East and North Africa (MENA) account for about 45% of the global desalination capacity. MENA is expected to see a 7-9% annual increase in capacity, with future growth anticipated in Asia, the US, and Latin America [69]. As water scarcity remains a concern, MENA countries are expected to rely more on desalination, with renewable energy-driven systems providing a sustainable and cost-effective solution.

• The status of desalination in Algeria

Algeria faces a major challenge in water management due to the scarcity of freshwater resources and increasingly harsh climatic conditions. In response to this growing concern, the country has adopted innovative strategies, with seawater desalination emerging as a key solution. Since the early 2000s, Algeria has made significant investments in the development of desalination infrastructure, aiming to secure a reliable supply of drinking water for regions most severely impacted by drought.

The construction of numerous desalination plants along the Mediterranean coast has steadily increased the national capacity for desalinated water production, reaching substantial volumes in recent years. These efforts have helped alleviate pressure on Algeria's natural water reserves and diversified its water supply sources. To ensure long-term water security, the Algerian government continues to support the expansion of desalination projects and the integration of advanced technologies. The table below outlines the key milestones in Algeria's desalination progress, highlighting the production capacities of various plants commissioned over the years.

Table 1. 5. Progress of desalination plants in Algeria [70].

Year	Location	Capacity (m³/day)	Technology used
1964	Ouled Djellal	Not specified	Demineralization unit
1964	• Arzew	24 m ³ /h (3 units)	Multi-stage flash
1969	• Arzew	4,560	Multi-stage flash
1971	SkikdaSkikdaAnnaba	1,440 720 (2 units) 960 (2 units)	Multi-stage flash Multi-stage flash Echangeurs d'ions
1973	 Annaba 	3,600 (2 units)	Ion Exchangers
1974	Ghazaouat	840	Ion Exchangers
1975	ArzewArzewHassi Messaoud	3,888 (6 units) 960 1,000 (6 units)	Electrodialysis Ion Exchangers Electrodialysis
1976	Hassi Messaoud	110 (2 units)	Electrodialysis
1977	Gassi Touil	55	Electrodialysis
1978	ArzewAnnabaHassi MessaoudBel Abbes	350 14,180 (3 units) 350 (2 units) 1,500	Thermo-compression Multi-stage Flash Electrodialysis Ion Exchangers
1979	 Haoud Berkaoui Hassi Messaoud Rhourd El Baguel Arzew Annaba Annaba Hassi-R'mel 	55 300 (2 units) 25 960 144 (2 units) 576 (2 units) 792 (3 units)	Electrodialysis Electrodialysis Electrodialysis Multi-stage Flash (6 stages) Ion Exchangers Ion Exchangers Reverse Osmosis
1980	AnnabaGhardaiaArzewMostaganem	6,240 (2 units) 960 960 57,600	Ion Exchangers Reverse Osmosis Multi-stage Flash (6 stages) Reverse Osmosis (6 lines)
1981	Rhourd El BaguelBiskraAnnaba	300 (2 units) 864 1,800	Electrodialysis Reverse Osmosis Ion Exchangers
1982	• Reghaia	160	Ion Exchangers
2003-2005	Not mentioned	total capacity of 1,940,000	14 large stations
2009-2011	 Skikda Beni Saf Souk Tlata Honaine Tlemcen Mostaganem 	100,000 200,000 200,000 200,000 200,000 200,000	-

	Fuka	120,000	
	 Tipaza 	100,000	
	 Cape Djinet 	100,000	
	Skikda, Jijel, Tizi	300,000 per Station	New Desalination Stations
2026	Ouzou, Chlef,	(6 stations)	
	Mostaganem, Tlemcen	(O Stations)	(Planned).

1.2.2.2. Solar Thermal Energy Advantages

CSP systems are reliable and widely used technologies that capture thermal energy from solar radiation using reflector mirrors to focus sunlight onto a receiver. The receiver absorbs heat, which can range from medium temperatures (450°C – 550°C) to high temperatures (600°C – 1000°C). This thermal energy is transferred to a working fluid, such as thermal oil, molten salt, water, air, hydrogen, or helium, to drive the generators in the power block. To ensure electricity generation even when solar energy is unavailable, CSP plants can be integrated with thermal storage systems [71]. These systems are commonly combined with thermal desalination technologies such as MED or MSF to generate fresh water on a large scale, eliminating the reliance on fossil fuels and boosting sustainability, as shown in Fig. 1.

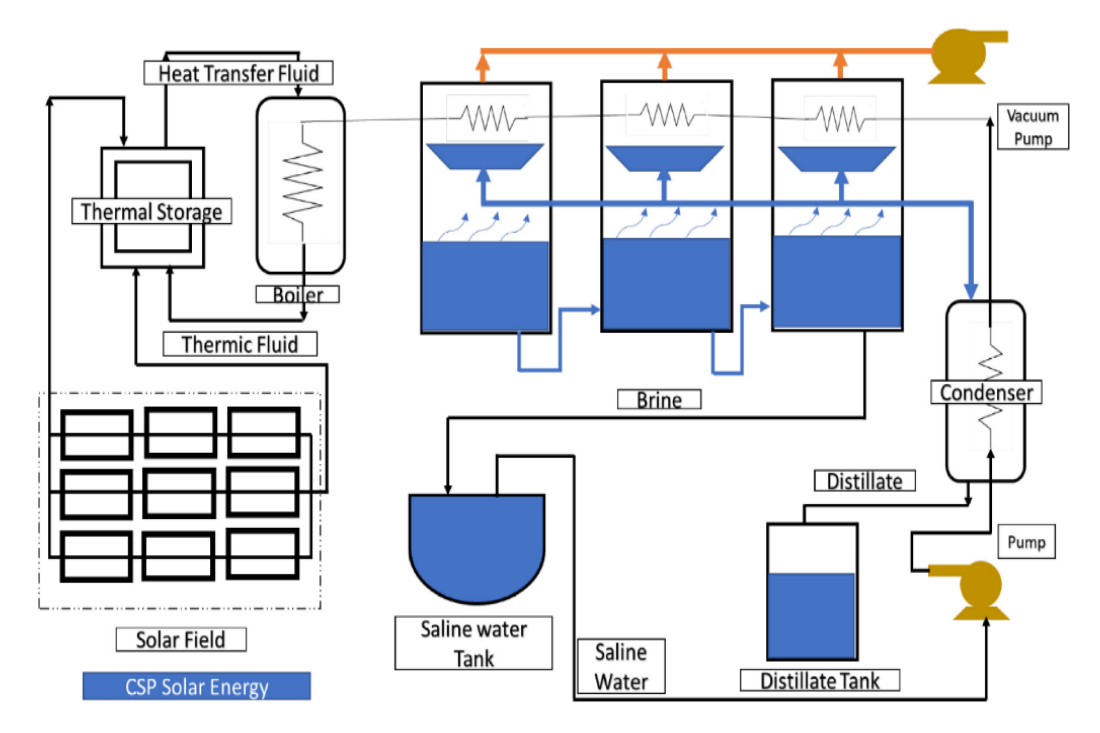


Fig.1. 8. Thermal Desalination Systems Powered by CSP Technology [71].

CSP technologies are divided into four main types: Parabolic Trough Collectors (PTC), Solar Parabolic Dishes (SPD), Linear Fresnel Collectors (LFC), and Solar Power Towers (SPT) [72]. Fig. 1.9 illustrates each technology, and Table 1.6 summarizes their functionality [73, 74]. Each technology efficiently generates high temperatures but differs in sun tracking and light concentration methods.

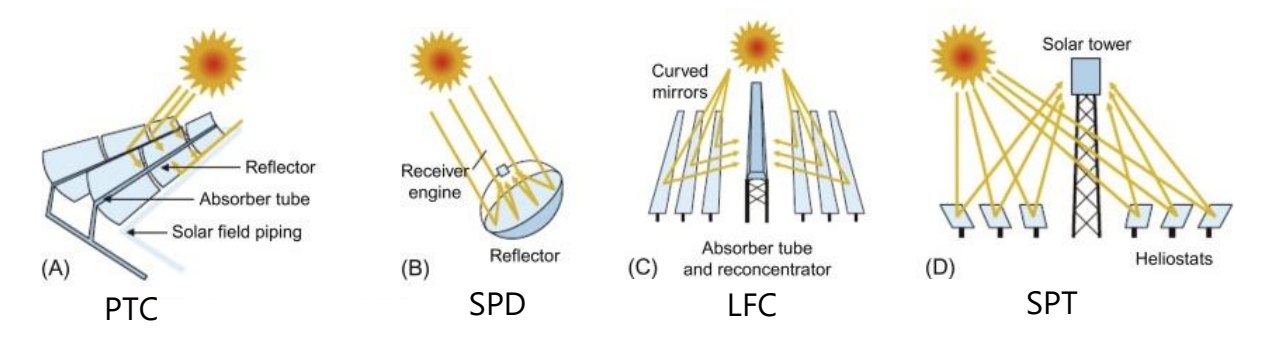


Fig.1. 9. Thermal Desalination Systems Powered by CSP Technology [72].

LFCs and PTCs are line-focusing technologies that use a linear receiver to collect solar radiation, while SPTs and SPDs are point-focusing technologies that concentrate sunlight at a single point [75]. Line-focusing systems, like PTCs and LFCs, work at moderate temperatures as they spread solar energy along a line. Point-focusing systems, like SPDs and SPTs, reach higher temperatures by concentrating energy onto a small point, creating more intense heat.

Among the four technologies, PTC has the highest power generation potential, ranging from a few megawatts to several hundred megawatts, due to its large solar collection area and efficient heat transfer. LFC and SPD have power capacities from a few megawatts to over 100 megawatts, but SPD systems usually generate only 10 to 25 kW. This is because the dish-shaped mirrors focus sunlight onto a small receiver, limiting the solar collection area and heat transfer.

However, SPD systems are very efficient at peak performance because their small receiver area focuses sunlight more, resulting in higher temperatures and better energy conversion. The concentration factor, which is the ratio of the collector area to the receiver area, is usually less than 100 for PTC and LFC, but can exceed 1000 for SPT and SPD [74].

The annual efficiency of CSP is influenced by factors such as solar power availability, receiver performance, heat transfer fluid quality, tracking accuracy, and efforts to reduce system losses. Among the four CSP technologies, SPD has the highest efficiency.

CSP Technology	Operating Temperature [°C]	Typical Capacity [MW]	Peak Efficiency [%]	Annual Efficiency [%]	Concentration Ratio
PTC	250-550	100-300	20-25	14-22	30-80
LFC	150-550	10-200	18-20	13-18	30-80
SPD	600-1500	0.01- 0.025	28-32	18-25	1000-3000
SPT	500-1200	10-200	22-24	15-23	200-1000

Table 1. 6. Functionality overview of the four primary CSP technologies [73, 76].

Thermal energy storage (TES) is used in many CSP plants to enable continuous operation during periods without sunlight by storing heat in a tank. However, not all CSP plants use TES due to the extra cost. Around 40% of CSP plants in Spain have included TES in their design [77].

Several factors must be considered when selecting the right solar collector system, including the type of application, required capacity, and available storage options. The available land area often limits the number of collectors that can be used. Additionally, geographical location is crucial, as it affects key factors such as peak solar efficiency and concentration ratio. For example, using a sun tracking system instead of a fixed system in solar still desalination can increase productivity by 22% and improve overall efficiency by 2% [78, 79].

1.3. Linear Fresnel Collectors (LFC)

Linear Fresnel concentrator is essentially a parabolic trough concentrator with a segmented mirror, designed based on the Fresnel lens segmentation principle, as depicted in Fig. 1.10. A and 1.10. B. These segments, referred to as reflectors, are aligned along a common axis, as illustrated in Fig. 1.10. C. Each reflector is slightly curved, with its radius of curvature varying according to its position [80].

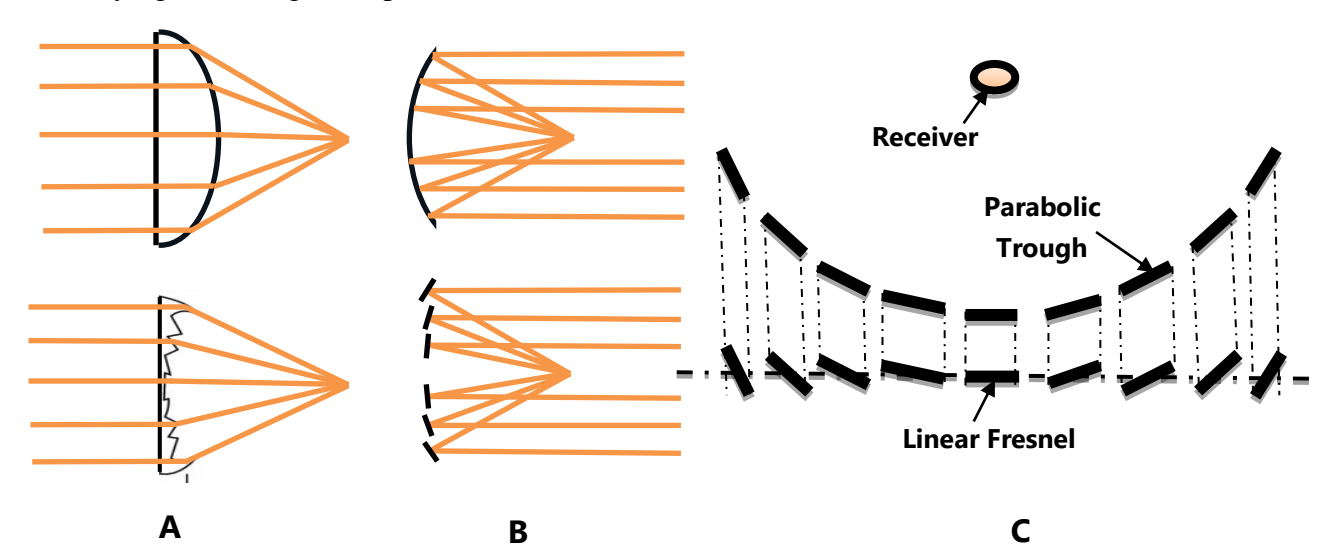


Fig.1. 10. A/ Fresnel lens [10]; B / Fresnel mirrors [10]; C/ Diagram showing the transition from a parabolic trough mirror to a linear Fresnel mirror. [81].

1.3.1. Fundamentals of LFC Technology

A linear Fresnel collector, shown in Fig. 1.11, has three main parts: the reflectors, the receiver, and sun-tracking system. These parts work together to convert solar energy into heat.

The reflectors are positioned to direct all incident solar rays on their surface toward the receiver located at the top of the concentrator [82]. Although curved reflectors offer better efficiency [83], flat ones are more commonly used due to their simpler design. These flat reflectors are arranged to form a parabola, with each being mobile to track the sun's movement. They are spaced apart to prevent optical losses, and the distance between the concentrator and the receiver is also carefully determined for optimal performance.

The receiver, positioned at the focal point of the concentrator, is a crucial component in solar energy systems. It consists of three main parts: the absorber, the secondary reflector, and thermal insulation (Fig. 1.11) [82, 84, 85]. The receiver is shielded by a metal casing to protect it from external environmental factors. Its function is to capture concentrated solar

radiation, convert it into heat, and transfer this heat to the fluid circulating through the absorber. The absorber, located at the heart of the receiver, can reach temperatures over 250°C in the case of Fresnel linear collectors. The temperature difference between the absorber and the surrounding environment leads to heat losses through radiation, convection, and conduction, which are minimized by the secondary reflector and thermal insulation.

The absorber is the key element for transferring thermal energy from the concentrated solar flux to the heat transfer fluid. It can be designed in various shapes such as tubular, multitubular, or parallele-pipedal [82, 80, 86, 87], and can be positioned either horizontally or vertically based on the system's needs [88, 89].

The secondary reflector plays a vital role in optimizing the system's efficiency. Made from a reflective material, it ensures an even distribution of solar rays across the absorber, reduces optical losses, and protects the absorber from external convection by enclosing it. There are several types of secondary reflectors, including wing-shaped, trapezoidal, and compound (CPC) models, which are selected to match both the absorber and the concentrator [90].

Thermal insulation is critical for minimizing heat losses. It can be made from various materials, with glass being particularly effective in reducing radiative losses due to its transparency to short wavelengths and its opacity to infrared wavelengths. Moreover, glass helps reduce convective losses by creating an enclosed space around the absorber. Additional insulation materials, such as glass wool or rock wool, are used to limit conductive losses. Finally, a solar tracking system ensures that the reflectors maintain the correct orientation throughout the receiver's operation, guaranteeing continuous reception of solar radiation [91, 92].

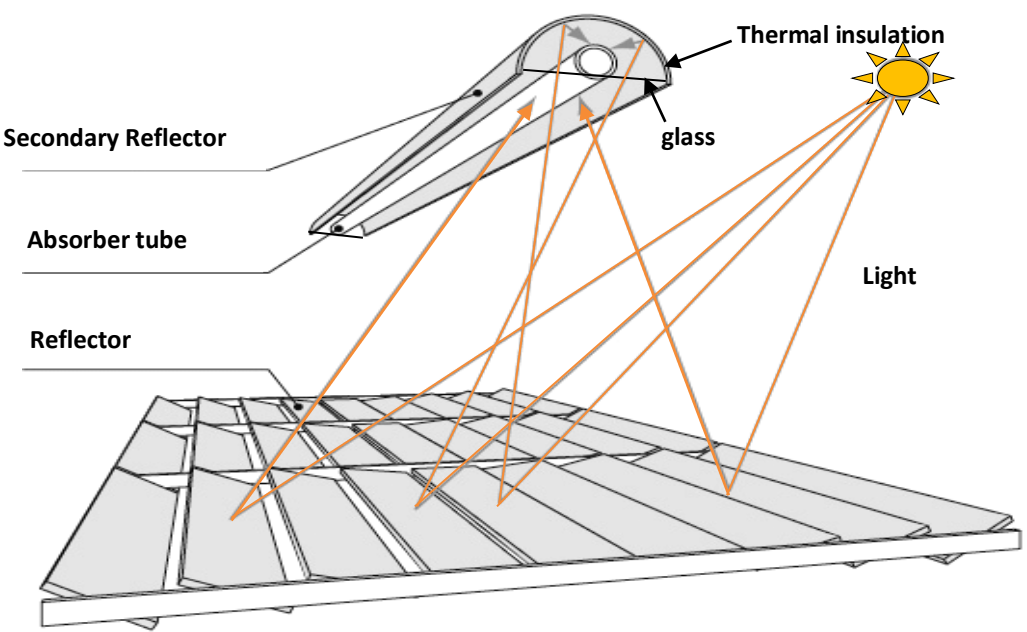


Fig.1. 11. Description of a linear fresnel collector [88].

However, this type of collector is significantly affected by shading and blocking losses between adjacent mirrors. While increasing the receiver height can minimize these losses, but it adds extra costs. To learn more about the design and latest research on linear [93].

In summary, this type of concentrated solar collector uses flat RLC mirrors (compact linear reflectors) that rotate to follow the sun and direct its rays onto one or two absorber tubes (Fig. 1.11). The concentrated solar energy heats a fluid in a horizontal tube, with temperatures reaching up to 500°C, making it ideal for thermal desalination. It can also be used for electricity generation, steam production, or cooling through a standard thermodynamic cycle. However, its optical performance is 30 to 40% lower than that of parabolic trough solar collectors [94].

1.3.2. Advantages over Other Solar Collectors

The LFC was chosen for its many advantages over other technologies, including:

- Design Simplicity: LFCs have a fixed receiver, reducing complexity and maintenance. Unlike parabolic troughs, the absorber does not move with the reflectors, allowing for larger absorbers. Mirrors are placed close to the ground, minimizing wind loads and structural requirements. Their flat design simplifies maintenance and optimizes land use [95].
- Cost-Effectiveness: LFC systems offer lower capital and maintenance costs compared to parabolic troughs or central tower systems. They provide an economical and efficient solution by utilizing flat or slightly curved mirrors, which are more affordable and simpler to construct than parabolic reflectors. This design choice significantly reduces both construction and operational expenses. Additionally, the use of fixed receivers eliminates the need for complex moving parts, enhancing system reliability and further lowering costs [95, 96].
- Suitability for Desalination: LFC systems provide the medium-temperature heat (90–120°C) required for the flashing process in MSF-OT plants [97].

1.3.3. Challenges

LFC systems face several challenges, primarily due to higher optical losses. These include lower concentration factors, reduced efficiency under diffuse solar radiation, and sensitivity to optical and tracking errors. Shading and blocking losses, especially at high solar zenith angles, are also significant issues, as illustrated in Fig. 1.12.

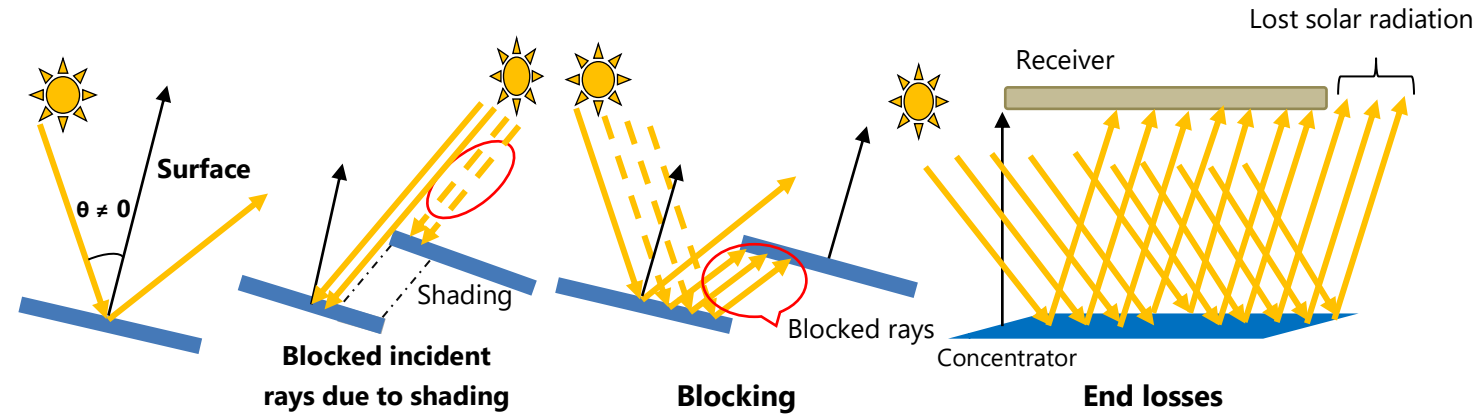


Fig.1. 12. Optical losses and performance challenges in LFC systems.

Improving efficiency requires addressing these challenges through better optical design and alternative configurations. Mitigating shading and blocking losses often involves increasing mirror spacing or raising receiver height, which can increase costs. Additionally, precise alignment and advanced tracking systems are critical for achieving optimal performance.

1.4. Multi-Stage Flash Desalination

1.4.1. Process Description

The Multi-Stage Flash (MSF) desalination method, despite being more expensive than reverse osmosis, is the most reliable for large-scale desalination due to 50 years of field experience. It accounts for over 93% of thermal desalination production and 26% of global desalination output [98]. MSF is widely used for its high productivity, flexibility, and simple control, representing over 60% of global seawater desalination capacity [99, 100]. It produces high-quality freshwater for various industries and is effective in removing boron from drinking water to near-zero levels [101].

The MSF process produces distilled water by boiling feedwater and then condensing the vapor. To achieve this, the system reduces pressure across a series of vessels, or stages, which allows the feedwater to boil at temperatures below its usual boiling point. There are two main types of MSF processes: once-through MSF and brine-circulation MSF, with the latter commonly used in industrial applications.

1.4.1.1. Once-through MSF (MSF-OT)

In the Once Through MSF (MSF–OT) configuration, seawater flows through the process a single time, as shown in Fig.1.13. Similar to a single-stage flashing process but involves a larger number of flashing stages where the same flashing mechanism is repeated.

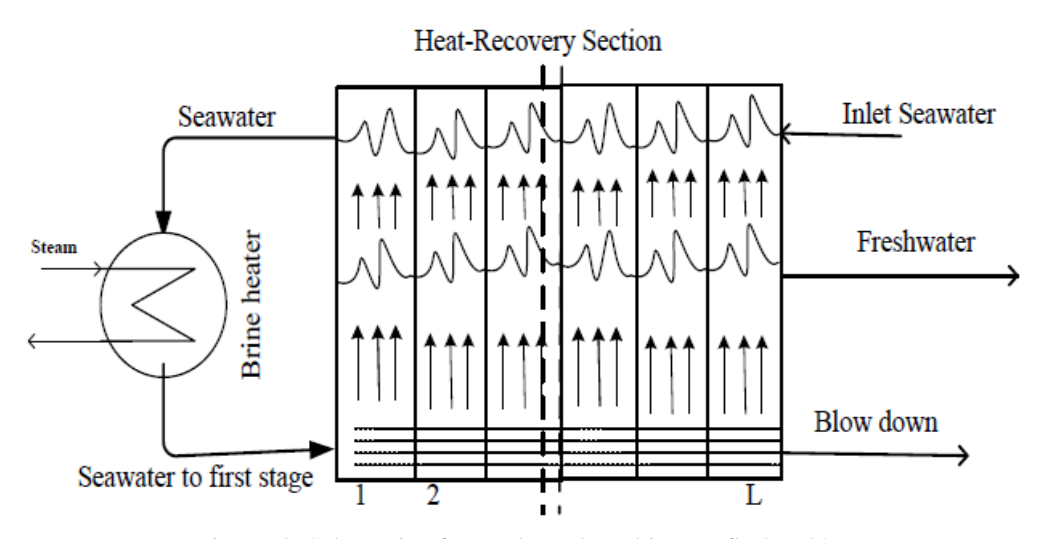


Fig.1. 13. Schematic of once through multi stage flash [102].

The process begins by heating the water under pressure until it reaches the top brine temperature (TBT), usually between 90 and 120°C. It is then introduced into a chamber with reduced pressure, where it rapidly vaporizes (Flash). Some of the vapor condenses on the tubes at the top, while the liquid collects below. The cooling seawater supplies the necessary heat for vaporization. This Flash process occurs in multiple stages, each with lower pressure, and can involve up to 40 stages in total.

Seawater is heated to the top brine temperature by passing through condenser tubes in various stages, starting from the last stage where the temperature is the lowest. It is preheated by absorbing heat from the steam condensation. The seawater is then brought to 120°C using

steam from a boiler or power plant. During the flash process, saltwater droplets may be carried along with the steam. These droplets are separated using a demister, a type of mesh that limits the passage of the droplets, which then fall to the bottom of the chamber.

1.4.1.2. Brine circulation MSF (MSF-BR)

Fig.1.14 shows the MSF process with brine circulation. In this configuration, the brine exiting the final stage is divided into two streams: one is recycled and combined with the incoming seawater feed, while the other, the blowdown, is discharged into the sea [103].

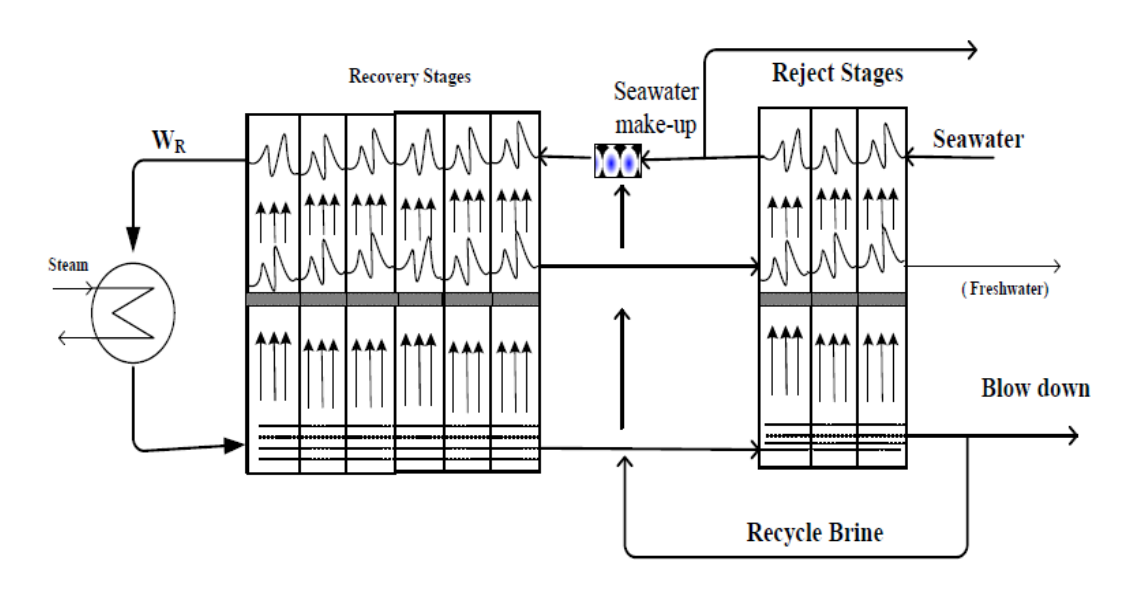


Fig.1. 14. Schematic of multi stage flash with brine circulation [102].

1.4.2. Energy Demand

Energy demand is a critical factor influencing the size and cost of a solar system. For a MSF plant, the typical energy consumption is approximately $10-16~\rm kWh_T/m^3$, which includes $7-12~\rm kW_{th}/m^3$ of thermal energy and $2.5-4~\rm kWh_e/m^3$ of electrical energy, used for pumping and auxiliary systems. These values, along with those for other thermal desalination methods, are detailed in Table 1.7 [104]. Optimizing energy use is essential for reducing costs and improving system efficiency. This underscores the importance of integrating sustainable energy sources into desalination processes.

Table 1. 7. Energy demand for producing 1 m³ of desalinated water with MSF and MED Technologies [104].

Thermal Method	Thermal Energy (kW _{th} /m³)	Electrical Energy (kWh _e /m³)	Total Energy (kWh _T /m³)
MSF	7-12	2.5-4	9.5-16
MED	4-7	1.5-2	5.5-9

1.4.3. Advantages of Once-Through MSF

The MSF process offers several advantages, including the production of high-quality fresh water with less than 30 ppm TDS [105], a long history of successful commercial use, and the ability to handle large capacities of water. It benefits from strict plant control, which enhances operation and maintenance, and can be combined with other processes, such as RO, to

optimize energy efficiency and reduce costs [106]. The process is also associated with low risk of scaling due to the evaporation not occurring directly around the heating tubes, and it primarily uses thermal energy, which can be cost-effective when low-pressure steam from power plant turbines is utilized. Additionally, MSF is simple to operate with minimal pretreatment requirements and allows for semi-operational functionality during cleaning periods [107].

The main disadvantages of the MSF process are its high energy consumption, particularly for boiling seawater, as well as its high capital and operating costs, especially in comparison to reverse osmosis [107]. Currently, RO is a highly efficient desalination technology, known for its low environmental impact, producing significantly fewer greenhouse gas emissions than other methods. It offers benefits such as a high desalination rate and low energy consumption [108]. Before RO became prevalent (see Fig. 1.15), MSF Distillation was the leading technology for seawater desalination. It offers low operational costs when excess heat is harnessed for the distillation process and boasts a high Gain Output Ratio (GOR). In some low-income regions, MSF remains the most common desalination method due to the high expenses associated with pre-treating seawater for reverse osmosis [108].

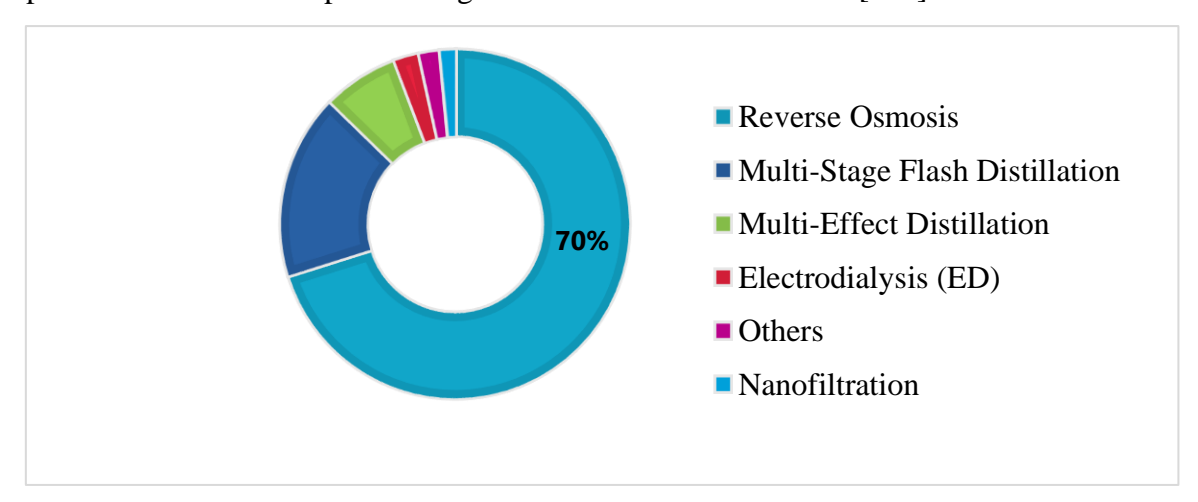


Fig.1. 15. Global market share of desalination technologies by type, 2023 [108].

MSF plants have consistently operated reliably, with certain units reaching the highest production capacities [109]. This success has driven significant growth in production capacity [110], allowing for substantial reductions in both capital and operating costs [111]. Additionally, the direct heat input required for MSF systems aligns effectively with the output of solar collectors, offering significant potential for integrating solar energy into the desalination process.

1.5. Coupling of LFC with Once-Through MSF

The information on desalination and renewable energy presented in the previous sections, particularly focusing on concentrating solar power systems, demonstrates that LFC offers significant advantages due to its vast resource potential and strong development prospects. As a renewable energy technology capable of storing and delivering power on demand, LFC is well-suited to power MSF-OT plants, which require continuous operation.

1.5.1. Concept of Direct Coupling

This study proposes a sustainable design that integrates LFC with thermal storage, a fossil backup, and an MSF-OT system to enhance the continuous operation of desalination plants, as shown in Fig. 1.16. This coupling eliminates intermediate energy conversions, reducing efficiency losses and ensuring continuous operation. It also optimizes energy use and enhances the reliability and cost-effectiveness of the system. The coupling system includes:

1. Solar Collection System (LFC):

The LFC focuses solar radiation onto receiver tubes containing a heat-transfer fluid. The selected LFC configuration is optimized to deliver thermal energy within the range of 90–120°C, suitable for the MSF-OT plant's flashing process.

2. Heat-Transfer Fluid (HTF):

A specialized heat-transfer oil with a low freezing point is used to ensure safe operation under varying conditions. This oil is heated in the LFC system and acts as the medium to transfer energy to the thermal storage tank.

3. Thermal Storage Tank:

The storage tank serves a dual purpose: it acts as a heat exchanger and a reservoir for thermal energy. It maintains a consistent supply of thermal energy to the desalination plant, especially during periods of low solar irradiance or at night. An agitator is incorporated to prevent thermal stratification, ensuring uniform temperature distribution.

4. Desalination Unit (MSF-OT Plant):

The heated brine is introduced into the flash chambers of the MSF-OT plant, where a series of pressure reductions induce flash evaporation. The vapor is condensed into freshwater, while the remaining brine is discharged. The system is designed to maintain the TBT at a consistent 90°C, optimizing performance and minimizing scaling issues.

5. Oil Drain System:

During nighttime or adverse conditions, oil from the absorber tubes is directed to an oil drain tank, minimizing heat losses. When required, the stored oil is returned to the LFC to be reheated and continue operation.

6. Control System:

Advanced sensors and controllers regulate fluid flow, temperature, and pressure to maintain system efficiency. The control system ensures smooth operation by responding to fluctuations in solar energy availability and plant demand.

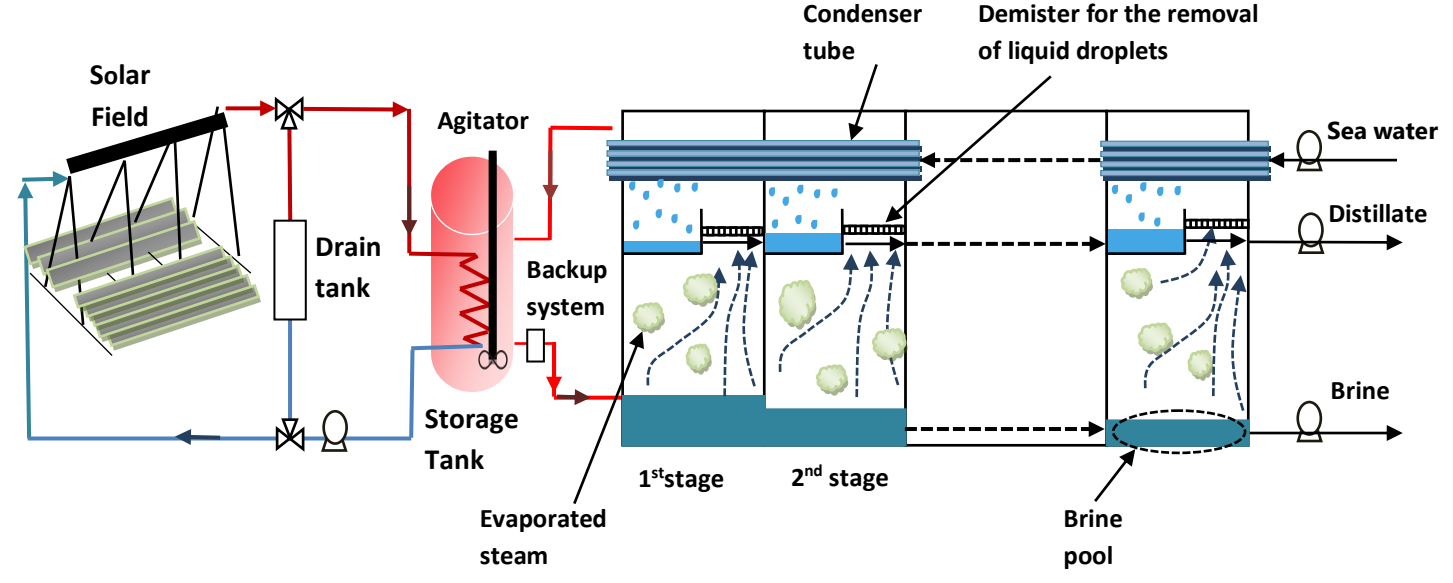


Fig.1. 16. Design of an MSF-OT Desalination System Integrated with LFC and Thermal Storage.

1.5.2. Potential Benefits

Efficiency Gains:

• Directly connecting the LFC system to the MSF-OT plant increases overall efficiency by minimizing energy losses and making better use of solar energy. The system can work consistently, even when sunlight is low, providing a reliable supply of freshwater.

Cost Reduction:

• A simpler design reduces both the capital and operational costs, making the system more affordable.

Scalability:

• The system can be easily expanded by adding more LFC units or storage tanks to meet growing water demand.

Environmental Sustainability:

- Relying on solar energy reduces the need for external energy sources, providing more energy security.
- Using only solar energy for operation significantly reduces the carbon footprint, supporting a more eco-friendly approach to desalination.

1.5.3. Key Challenges

- Solar energy varies throughout the day and seasons, so thermal storage or backup systems are needed to ensure a steady heat supply, especially when there's little sunlight.
- Effective thermal storage is required to keep the desalination plant running smoothly during times when solar energy is unavailable, like at night or on cloudy days.
- In case of insufficient solar energy, a backup system powered by fossil fuels may be needed to maintain operations, which can increase costs and reduce environmental benefits.

• The heat from the LFC needs to meet the specific temperature and flow requirements of the desalination process. If not properly controlled, this could affect the efficiency of desalination.

1.6. Need for Parametric Analysis

Parametric analysis is the process of studying how changes in important factors affect the performance of the LFC and MSF-OT system. It helps understand how modifying these factors can improve the efficiency and operation of the solar-powered desalination plant. The main factors to consider include:

Solar irradiance intensity and variation: The amount and fluctuation of solar energy received by the LFC system, which directly affects its thermal output and the desalination process.

Feed water salinity and temperature: The level of salt content and the temperature of the incoming water, which influence the energy required for desalination and the overall efficiency of the MSF-OT process.

Flow rates and thermal energy inputs: The rate at which fluid moves through both the LFC and MSF-OT systems, as well as the amount of thermal energy provided by the LFC, which impacts desalination performance.

Number of MSF stages and pressure drops: The number of stages in the MSF-OT process and the pressure differences between stages, which affect the efficiency and energy consumption of the desalination process.

Understanding these parameters ensures that the thermal output from the LFC is appropriate for the MSF-OT system's needs.

In direct coupling systems, such as integrating LFC with MSF desalination, parametric analysis is essential for optimizing performance. It helps identify the best operating conditions to maximize water production while minimizing energy use, ensuring the system runs efficiently. Additionally, it plays a key role in assessing the system's feasibility by evaluating whether it can consistently perform under real-world conditions, confirming its reliability and effectiveness.

Despite its importance, detailed parametric analysis of LFC-MSF coupling remains limited in existing research. Most studies focus on:

- ✓ Examining solar collectors or desalination systems separately, rather than their combined integration.
- ✓ Investigating other configurations, such as coupling LFC with MED or using parabolic trough collectors for powering MSF.

This research gap highlights the need for comprehensive parametric studies to assess how direct LFC-MSF integration can enhance the performance and efficiency of solar-powered desalination systems.

1.7. Research Objectives

This research aims to:

- Develop a high-fidelity numerical model of the LFC-MSF system and conduct a comprehensive parametric analysis to identify optimal design configurations and operating conditions.
- Assess the economic feasibility and environmental impact, considering key thermodynamic and fluid flow phenomena.
- Investigate the feasibility of a novel dual-function thermal storage tank that serves as both a heat exchanger and a storage medium, reducing system complexity while ensuring thermal stability.
- Examine the potential for integrating isolated tubes within the MSF-OT unit to regulate brine flow dynamics and implement an automated control system for real-time monitoring and optimization of critical parameters, including fluid flow, temperature, and pressure, to enhance efficiency and operational stability.
- Provide scientifically validated insights to support the design, optimization, and large-scale implementation of LFC-MSF desalination technologies.

1.8. Scope and Limitations

- Scope: This research will focus on a specific range of LFC and MSF-OT configurations, considering typical operating conditions in [specific geographical region or climate]. The analysis will include a comprehensive evaluation of key performance metrics, including desalination capacity, thermal efficiency, specific energy consumption, and levelized cost of water.
- Limitations: The model will incorporate simplifying assumptions, such as steady-state operation, neglecting certain minor heat losses, and assuming constant ambient conditions. The economic analysis will be based on current market prices and may not fully account for future technological advancements or potential cost reductions.

1.9. Conclusion

In conclusion, addressing water shortages requires sustainable solutions, particularly as urban growth and energy demands increase. Solar desalination offers a promising approach by using clean energy to produce fresh water. Understanding the causes of water scarcity, the challenges of energy consumption, and the potential of solar desalination systems is crucial for developing effective strategies to meet the growing demand for water while reducing environmental impacts. Continued research and investment in renewable technologies are vital for improving the efficiency and accessibility of solar desalination. The next chapter will present a comprehensive literature review on various developed models for the solar desalination process, focusing on their strengths and weaknesses.

Chapter 2 : Literature Review

2.1. Introduction

This chapter offers a concise review of existing research on solar-powered desalination systems, focusing on two key technologies: Linear Fresnel Concentrators and Multi-Stage Flash desalination. It examines efforts to enhance the performance of LFC systems by minimizing optical losses through modifications to the design of concentrators and receivers.

Additionally, the chapter reviews mathematical models used for MSF desalination, which are critical for evaluating system performance. These models support the analysis and prediction of essential parameters, leading to more efficient operation of solar desalination systems.

2.2. Previous Work on Solar-Powered Desalination Systems

The use of renewable energy sources to power desalination technologies is a clean, inexhaustible, and viable means of producing fresh water in many locations today. Numerous researchers have focused on developing and analyzing various solar desalination systems. These investigations comprise a range of experimental and theoretical studies that explore the integration of solar power plants with desalination units. Hanafi [112] performed a transient analysis of a solar multi-stage flash desalination unit. The study verified that employing water as a heat transfer fluid in solar collectors, along with increasing the number of storage tanks and their volume, could enhance water production efficiency.

Nafey et al. [113] conducted a study on a compact flash desalination unit integrated with a 2.39 m² flat plate solar collector (see Fig. 2.1), which operated at the Faculty of Petroleum and Mining Engineering in Suez, Egypt. Their investigation encompassed both theoretical and experimental analyses conducted over the course of one year (2005), evaluating the system's performance under varying environmental conditions. They developed a mathematical model to predict the productivity of the entire system, including its collector, flash unit, and condenser, across a broad range of operational parameters. Their findings revealed a strong correlation between the results obtained from the proposed mathematical model and those observed experimentally.

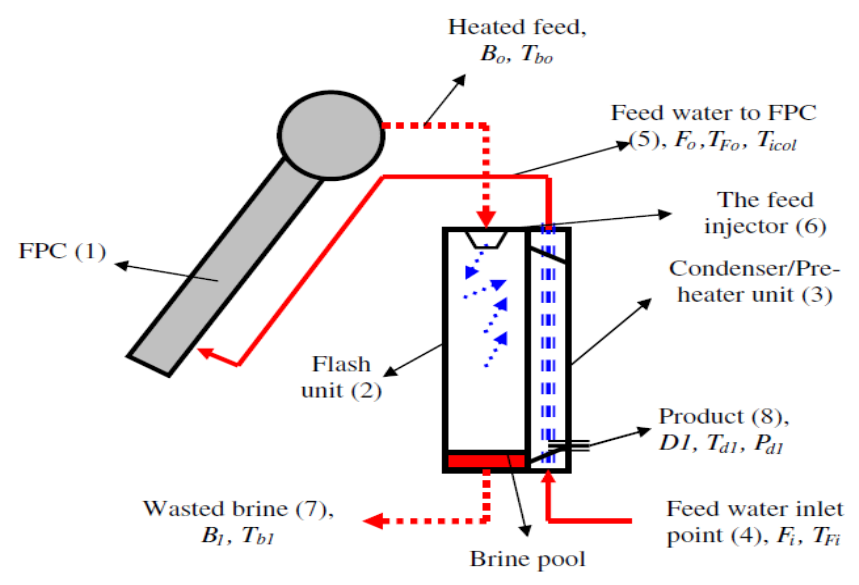


Fig.2. 1. A schematic overview of the system as described in [113].

The study determined an optimal feeding water rate of approximately 0.0183 kg/s. During summer, the system exhibited a daily productivity range of 4.2 to 7 kg/day/m², while during winter, this range reduced to about 1.04 to 1.45 kg/day/m². The unit's performance ratio varied between 0.7–0.8 in winter and 0.8–0.9 in summer, consistent with typical values for a single-stage MSF system. Furthermore, the collector efficiency factor was estimated at approximately 0.93, with a heat removal factor of about 0.88. The researchers noted a direct correlation between increased solar radiation and heightened system productivity. In summary, the study concluded that the simplicity of the solar desalination system rendered it an effective solution for providing fresh water to small communities lacking technical infrastructure.

Reddy et al. [114] carried out both theoretical and experimental investigations on an evacuated multistage solar desalination system, which includes inclined trays acting as evaporator-condenser units. These trays are maintained at reduced pressure using a vacuum pump and are outfitted with silk cloth to enhance evaporation. Feed water heated by solar collectors flows over the silk cloth as a thin film (see Fig. 2.2).

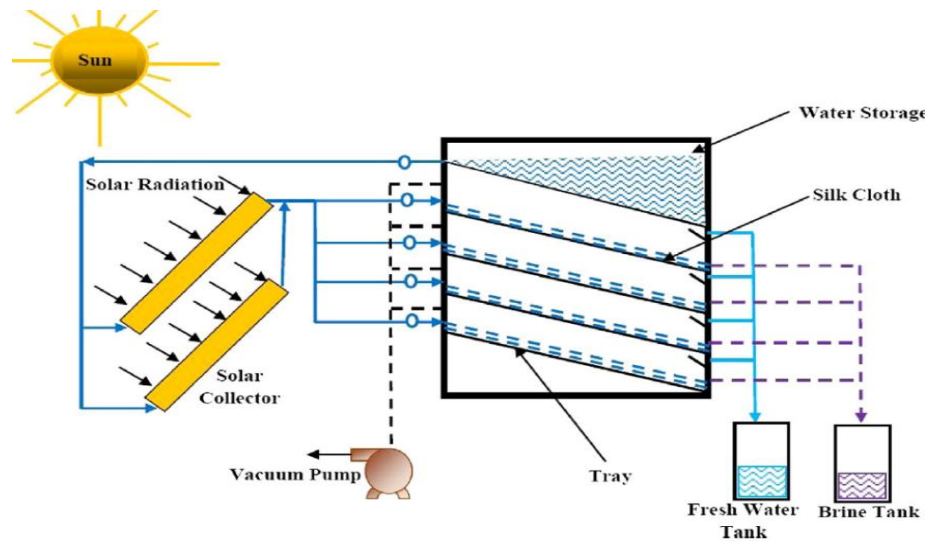


Fig.2. 2. Evacuated multi-stage solar water desalination system [114].

Their study identified the optimal system configuration as comprising 4 stages with a mass flow rate of 55 kg/m²/day, regardless of climatic conditions. Their results show that distillate yield increases as the mass flow rate decreases from 150 kg/m²/day to 55 kg/m²/day due to enhanced evaporation, but decreases further to 30 kg/m²/day due to lower stage temperatures. Additionally, distillate yield rises with a decreasing gap between stages but declines with increasing salinity. The fourth stage consistently yields the highest distillate, while the first stage yields the least. Moreover, collector outlet temperature and distillate yield increase with decreasing wind velocity. Adjusting heat input affects distillate yield, with pressure significantly impacting yield, achieving a maximum of 28.04 kg/m²/day and a minimum of 13.33 kg/m²/day, demonstrating the system's potential to fulfill freshwater needs.

Kabeel and El-Said [115] conducted an experimental study in August 2013 in Tanta City, Egypt, involving a laboratory investigation of a pilot small-scale hybrid air humidification and dehumidification—water flashing evaporation (HDH–SSF) desalination system powered by solar thermal energy (as shown in Fig. 2.3). Their research aimed to evaluate the system's performance under actual climatological conditions and compare experimental results with theoretical predictions from previous studies, investigate the impact of using nano-fluid as a working fluid for the solar water loop on system productivity enhancement and identify factors and parameters influencing system productivity. The study revealed a close correspondence between simulated and measured variations in water production and performance ratio values across different parameters.

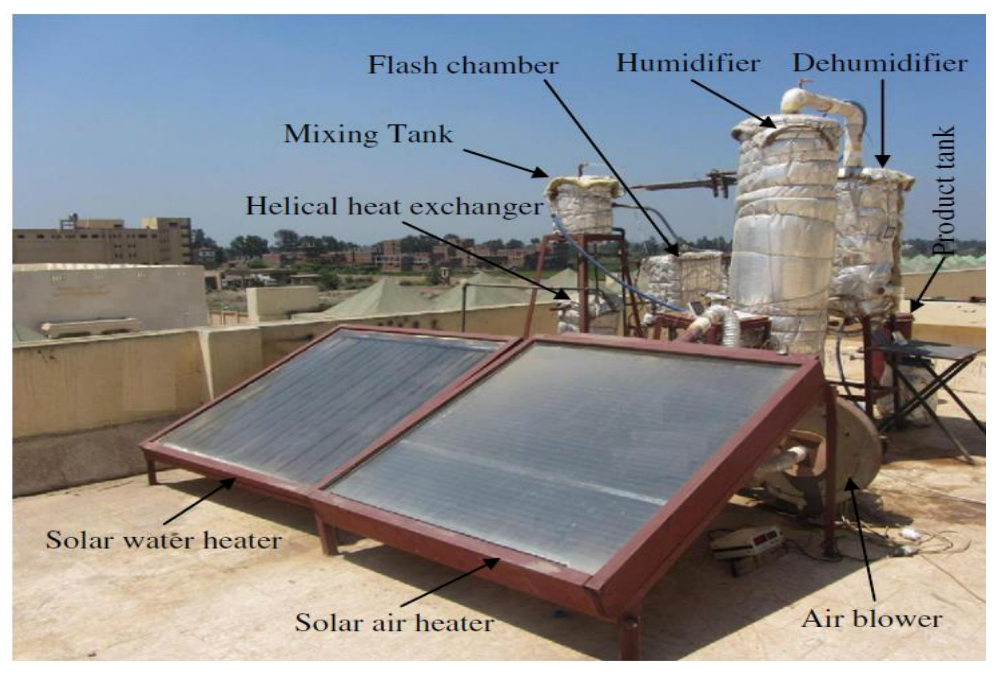


Fig.2. 3. The experimental set-up of the HDH-SSF system [115].

Results indicated that freshwater production increased with solar radiation. while the performance ratio of the SSF unit ranged between 0.32 and 1.4, with flashing temperatures varying between 3 and 9°C. Under specific test and operational conditions, the system achieved a maximum productivity of 41.8 kg/day. Additionally, the efficiency of the solar water heater was found to be influenced by the nano-particle volume fraction, while the humidifier efficiency was primarily affected by increasing water mass flow rate rather than

the air mass flow rate, reaching approximately 98%. Collector efficiencies were measured at about 55% and 56% for the solar water heater and solar air heater, respectively.

Darawsheh et al. [116] developed and tested a solar MSF desalination system using flat plate solar collectors and multistage vacuum chambers (as shown in Fig. 2.4). The goal was to improve the system's performance and reduce costs. The study found that applying a 20 kPa vacuum pressure increased the distillation rate by 53% and reduced energy use. Thermal storage helped control temperatures and extended operating time. Brine temperature increased by 25–41°C with solar insolation of 650–900 W/m², while changes in brine flow rate had little effect. Higher brine flow rates reduced performance. Although the system's efficiency was limited by the number of stages and collector size, vacuum pressure significantly improved performance and lowered costs.

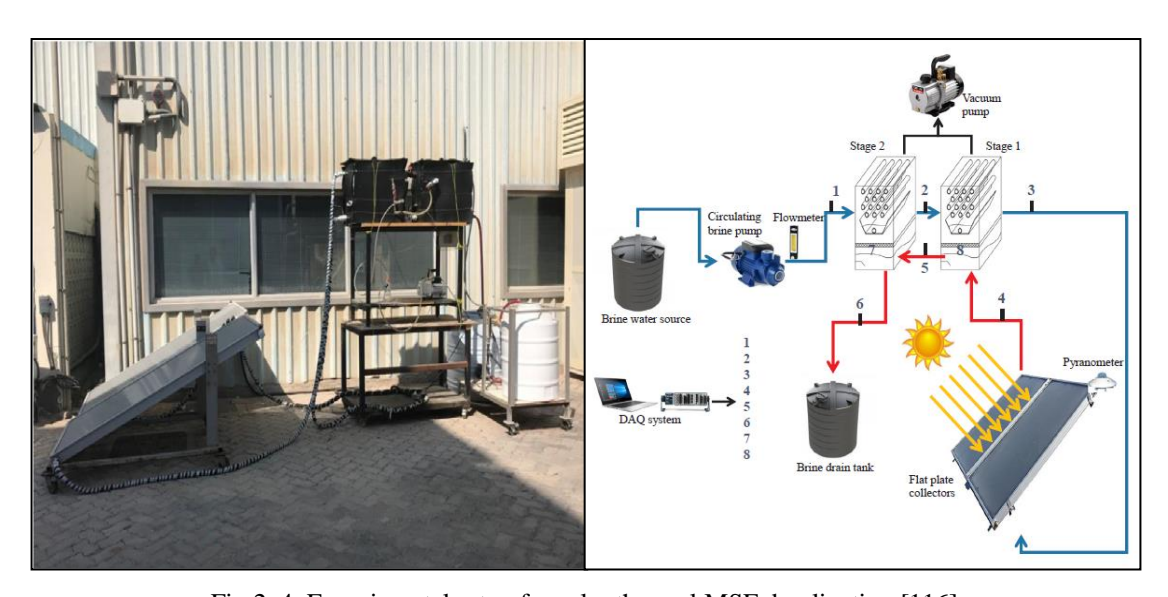


Fig.2. 4. Experimental setup for solar thermal MSF desalination [116].

On a different aspect, various pilot plants have been established to integrate a solar concentration collector with a reverse osmosis (RO), a multi-stage flash (MSF), or a multi-effect distillation (MED) plant [117, 118]. Table 2.1 provides a depiction of pilot projects for indirect solar desalination.

	Table 2. 1. Solar desamlation plants.		
Plant Location	Solar collectors	Desalination process	m ³ /d
La Paz, Mexico [119,120]	Flat plate + parabolic trough	MSF, 10 stages	10
Takami Island, Japan [119]	Flat plate	ME, 16 effects	16
La Desired Island, French Caribbean [121]	Evacuated tube	ME, 14 effects	40
Abu Dhabi, UAE [122]	Evacuated tube	ME, 18 effects	120
Area of Hzag, Tunisia [120]	Solar collector	Distillation	0.1-0.35
Safat, Kuwait [120]	Solar collector	MSF	10
Kuwait [119]	Solar electricity generation	MSF	25
	system	RO	20
Margarita de Savoya, Italy [119]	Solar pond	MSF	50-60
El Paso, Texas [120]	Solar pond	MSF	19
Islands of Cape Verde [117]	Solar pond	Atlantis "Autoflash"	300

Table 2. 1. Solar desalination plants.

Solar pond	ME, TC	30
Solar pond	MED	3000
Low concentration	MSF	0.3
Low concentration	MSF	10
Parabolic trough	MSF auto-regulated	100
Parabolic trough	ME	6000
Parabolic trough	ME, 55 stages; MSF, 75	500
	stages	
Parabolic trough	ME, heat pump	72
	Solar pond Low concentration Low concentration Parabolic trough Parabolic trough Parabolic trough	Solar pond MED Low concentration MSF Low concentration MSF Parabolic trough MSF auto-regulated Parabolic trough ME Parabolic trough ME, 55 stages; MSF, 75 stages

Trieb et al. [126] were among the early contributors to research on the fusion of CSP with desalination. They discussed the various CSP options for seawater desalination, including both electricity and steam-based methods. Their findings highlighted the economic feasibility of this technology in the MENA region, indicating its ability to address both present and future demands for electricity and water.

Palenzuela et al. [127] conducted a techno-economic analysis examining various configurations for integrating large-scale solar desalination with CSP in two representative locations: the Mediterranean Sea and the Arabian Gulf. The study explored various configurations beyond direct coupling with CSP (CSP+LT-MED), considering CSP + MED setups and comparing them with CSP combined with Reverse Osmosis (RO). Additionally, the analysis incorporated three conventional refrigeration processes into the power cycle to provide a thorough evaluation of the options available. The four different CSP + Desalination configurations considered are:

Configuration #1 integrates the Low-Temperature Multiple Effect Distillation (LT-MED) unit, condensing steam from the Low-Pressure Turbine (LPT) for fresh water production with four extractions due to a higher steam temperature (Fig. 2.5) .

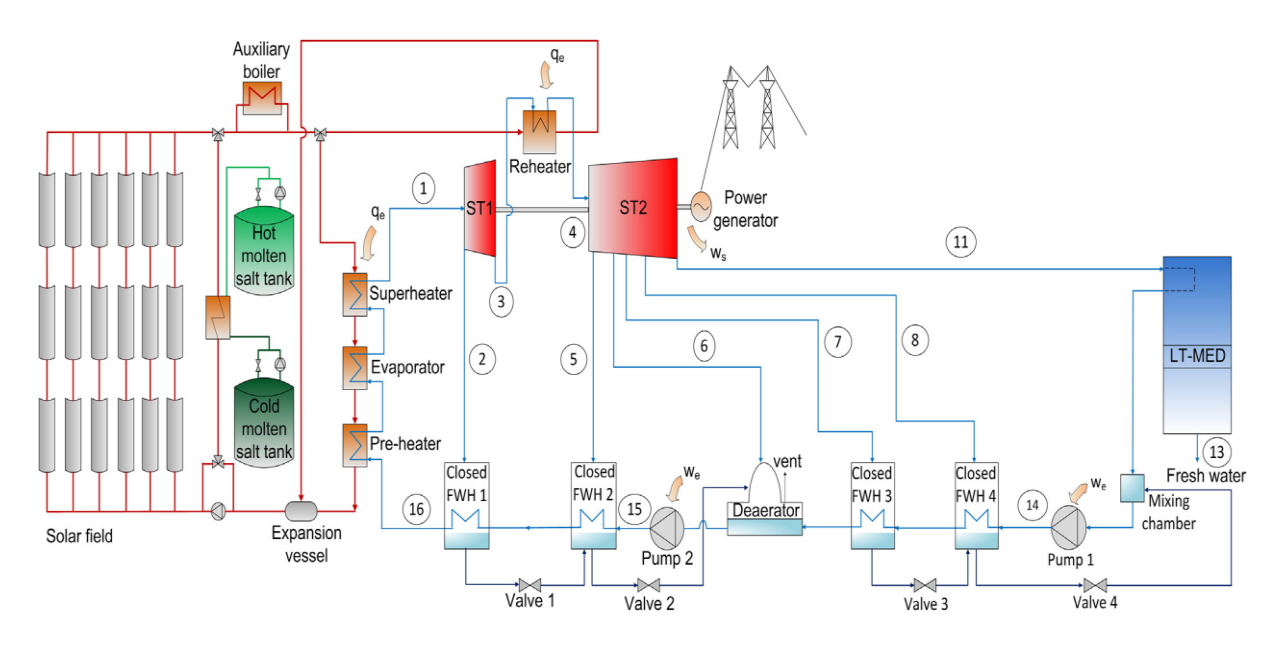


Fig.2. 5. LT-MED unit integrated into a CSP plant [127].

Configuration #2 diverts part of the exhaust steam for steam ejectors, using higher-pressure motive steam from the LPT to drive the LT-MED process, while the rest is condensed through the power cycle condenser.

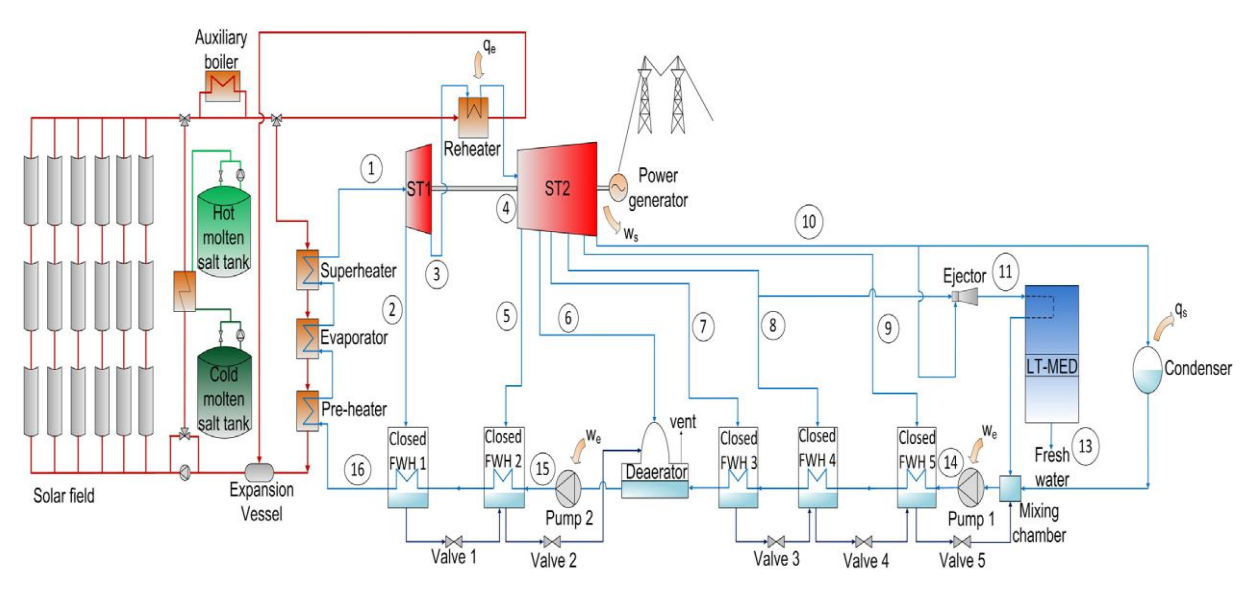


Fig. 2. 6. LT-MED + TVC unit integrated into a CSP plant [127].

Configuration #3 employs a Thermo-Vapor Compressor (TVC)-MED system powered by high-pressure steam from the LPT, with all turbine exhaust steam condensed in the power cycle's cooling system, while Configuration #4 combines Reverse Osmosis (RO) with CSP, operating independently from power generation.

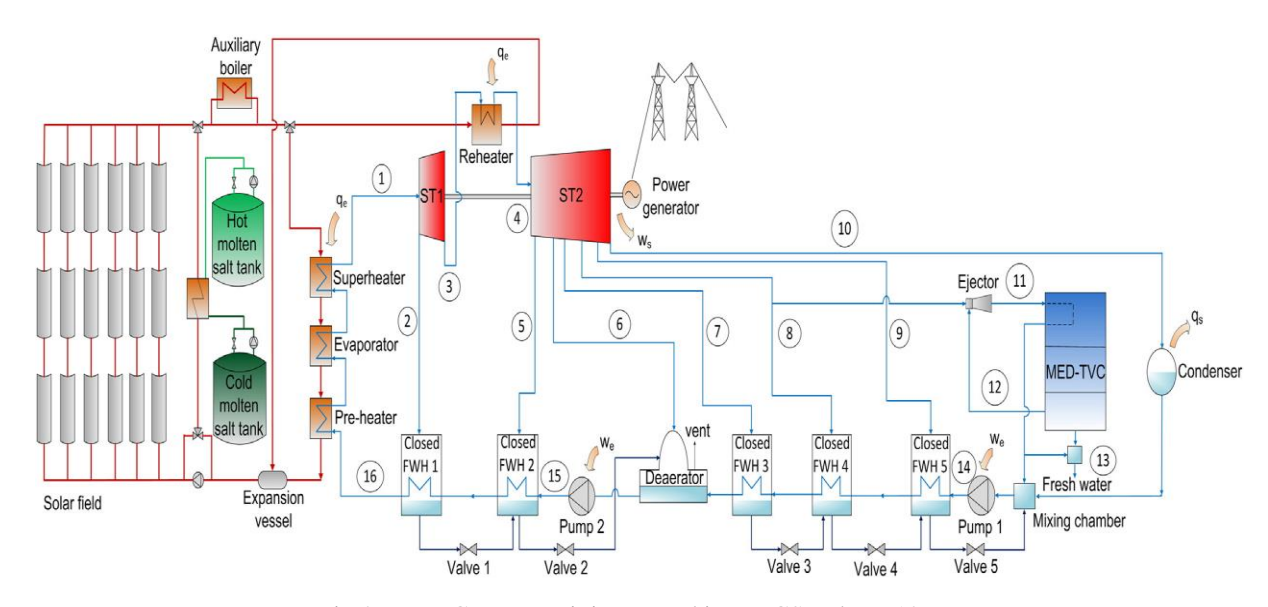


Fig.2. 7. TVC-MED unit integrated into a CSP plant [127].

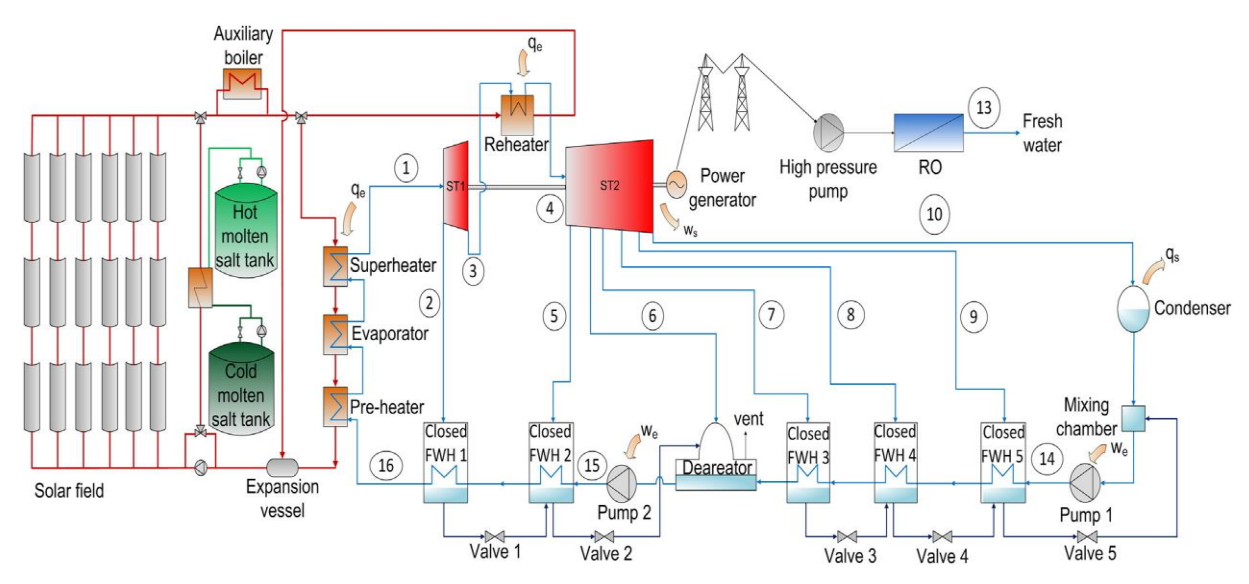


Fig.2. 8. RO unit connected to a CSP plant [127].

The analysis indicates that in the Arabian Gulf, the most favorable combination for CSP and desalination involves integrating a LT-MED through thermocompression (LT-MED+TVC) into the power cycle (Fig. 2.6.), offering enhanced reliability and adaptability to demand curves compared to other configurations. In the Mediterranean basin, directly using electricity from a CSP plant in a RO unit (Fig. 2.8) is challenging to surpass, although integrating a LT-MED by fully replacing the condenser shows promise. However, differences between LT-MED with thermocompression and CSP with RO integration are often marginal, especially when employing dry cooling to minimize water consumption. This suggests that integrating a LT-MED with thermocompression into a CSP plant presents a viable option for solar desalination along Mediterranean shores, despite slight variations in effectiveness compared to other configurations.

Hamed et al. [128] performed an experimental study to characterize the thermal and optical performance of a new Linear Fresnel Collector capable of supplying heat to a MED-TVC installation (see Fig. 2.9). A 55,737 m² solar field area was discovered to be required to produce 13.6 MW_{th} of thermal energy to power the MED-TVC unit. The authors proposed lowering the exit temperature of the Heat Transfer Fluid to increase the thermal efficiency of the solar field.

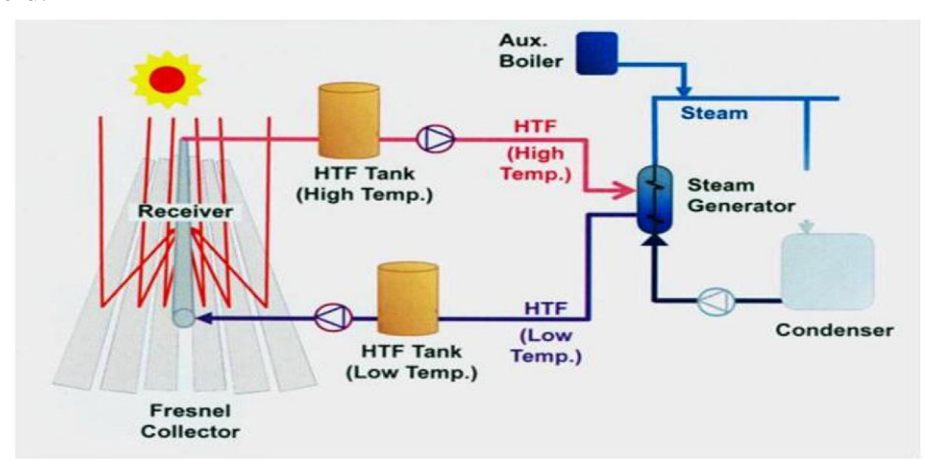


Fig.2. 9. The experimental setup of the solar collecting system [128].

Extensive research was undertaken to explore the integration of a solar concentrating system with a thermal desalination plant, as detailed in the preceding paragraphs. Notably, no prior research was identified concerning the coupling of a multistage flash plant with a linear Fresnel collector, despite its potential benefits. Consequently, this study chooses to merge these two systems for feasibility analysis, a decision informed by the literature reviews of each system presented in the following subsections.

Al-Othman et al. [129] performed a simulation study aimed at exploring the application of parabolic troughs (PTCs) in connection with a solar pond to fulfill the entire energy demands of MSF desalination. Their findings indicate that employing two PTCs with a combined aperture area of 3160 m² could satisfy roughly 76% of the energy needs. The residual 24% can be addressed by using a solar basin covering an area of 0.53 km².

Alhaj et al. [130] proposed a plant design based on a solar field with a linear Fresnel collector that supplies heat to a multi-effect distillation plant with thermal vapor compression (MED-TVC) (Fig. 2.10). The system performance is investigated and a control strategy for reducing electric pumping is proposed. According to the findings, 1 m² of solar field produces 8.5 m³ of distillate per year under Qatar's climate. Electric pumping energy was reduced by 40% as a result of the proposed control strategy.

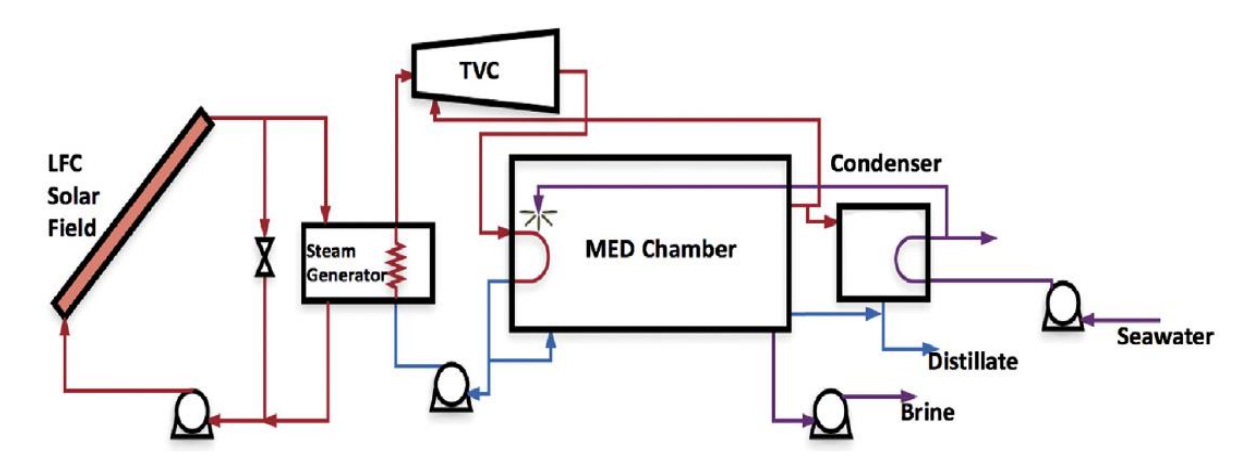


Fig.2. 10. The proposed MED-TVC pilot plant driven by solar thermal energy [130].

Moharram et al. [131] investigated a solar power plant integrated with desalination techniques in Ras Gharib, Egypt. The system utilizes parabolic trough collectors (PTCs) to generate heat for a steam Rankine cycle, with thermal storage ensuring continuous operation. An MSF unit is used as a condenser, and an RO unit helps increase freshwater output. In July, the system produces 16,000 m³/day of water and 12.65 MW of electricity, while in January, it produces 12,250 m³/day of water and 9.0 MW. Annually, it averages 14,054 m³/day of water and 10.8 MW of electricity, with costs of \$0.487/m³ for water and \$0.0458/kWh for electricity.

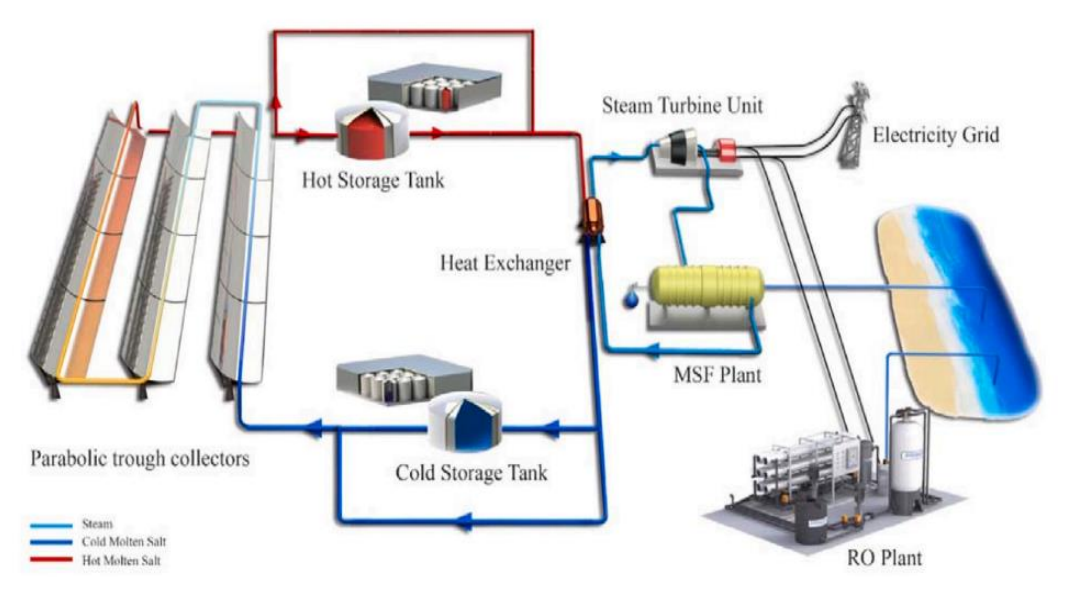


Fig.2. 11. System configuration proposed by Moharram [131].

Babaeebazaz et al. [132] developed a two-stage solar PDC-MSF desalination unit and tested its performance under different feedwater flow rates and pressure. They found that solar radiation and flow rates were key factors affecting productivity, and recommended using a TES for better control. The system produced 3.22 L of water in 5 hours at a flow rate of 0.7 L/min and 10 kPa vacuum pressure. Increasing the flow rate from 0.7 to 1.3 L/min reduced productivity by 76.4%. The system's scalability and significant reduction in water production costs demonstrate its efficiency, scalability, and cost-effectiveness.

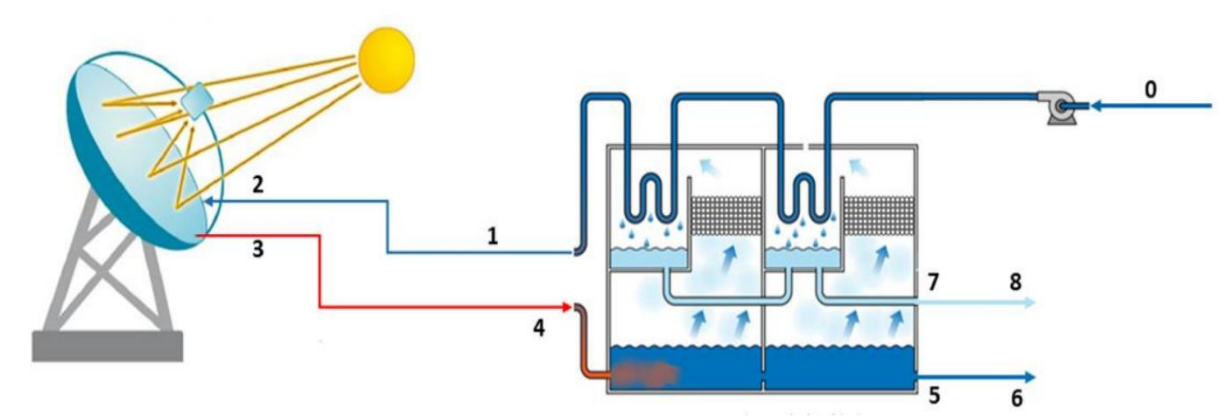


Fig.2. 12. Schematic of the two-stage solar PDC-MSF desalination system [132].

2.3. Linear Fresnel Collector

The concentration of sunlight has been used since ancient China for practical purposes. A legend says that Archimedes used a "burning mirror" to focus the sun's rays on the invading Roman fleet and drive them away from Syracuse. Table 2.2 provides an overview of the significant advancements in LFC technologies.

Table 2. 2. Overview of significant advancements in LFC.

Year	Realization	Ref(s)
19th	• Italian inventor Alessandro Battaglia made significant early	[133]
Century	contributions to solar concentrators. His recently rediscovered	

	patents laid the foundation for linear Fresnel reflector	
	technology, though no evidence of their practical application has been found.	
1960s	Giovanni Francia (1911–1980), an Italian engineer, played a key LFC system, building prototypes in Genoa (1963) and Marseille (1964). He stressed the importance of economic viability and simple technology, recognizing flat mirrors as essential for large-scale solar applications. 1968: Professor Giovanni Francia designed and built the first modern solar concentration plant in Sant'Ilario, near Genoa, Italy, capable of producing 1 MW.	[82]
1973	Dr. Ioannis Sakkas tested the legend of Archimedes by using 60 sailors and mirrors to concentrate sunlight onto a plywood silhouette, setting a ship on fire within minutes.	[133]
• 1990s	Australian researcher David Mills contributed to the advancement of LFR technology by developing the compact linear Fresnel reflector (CLFR). This innovation uses parallel focal lines to improve mirror efficiency, directing light to the appropriate focal line.	[134]
2001	SolarMundo, a Belgian company, initiated a large-scale LFC project in Liège with 2400 m² of mirrors. However, the project faced challenges due to poor performance and high costs, especially for large power outputs. Key components like the absorber tube, secondary mirror, and tracking system required further development.	[135]
2004	The first solar installation utilizing Linear Fresnel Reflectors, with a capacity of 1 MWe, was incorporated into the Liddell coal power plant (2000 MWe) in Australia.	[136]
2008	The FresDemo prototype, with an area of 1433 m² and a capacity of 800 kWth, was constructed by SPG at the Plataforma Solar de Almería (PSA) and became operational.	[137]
2008	The Kimberlina demonstration solar plant, with a 26,000 m ² area and a capacity of 5 MWe, was launched by Ausra (now part of Areva Solar) in California.	[138]
April 2009	The Puerto Errado I (PE1) plant, the first commercial LFC installation with a capacity of 1.4 MWe, was connected to the grid in Spain.	[139]
2010	The construction of the second LFC plant, Puerto Errado II (PE2), which spans 302,000 m ² and has a capacity of 30 MWe.	[134]
2010	The French company CNIM developed its own LFC prototype, marking a key step in the progression of the technology.	[134]
2011	ALSOLEN, a member of the ALCEN group, emerged as a new French actor in the LFC sector, contributing to the industry's growth.	[140]

• A number of companies are now offering LFC systems, with prominent names like Novatec Solar, Solar Power Group (SPG),

Areva Solar (formerly Ausra), and Industrial Solar (previously PSE, then Mirroxx). Emerging players, especially in France, include SolarEuromed, which is working on its LFC prototype.

Classic LFCs are primarily designed to generate heat at a moderate temperature suitable for large-scale industrial processes or commercial-scale electricity production. Numerous LFC designs can be found in the literature, and these designs encompass a range of configurations, including variations in the primary reflector design, receiver design, and other innovative design features. The upcoming section will elaborate on these aspects. Various collector designs are available. Some of them have advanced through the stages of design and engineering, while others were primarily intended for theoretical exploration or are still undergoing conceptual evaluation.

2.3.1. Compact linear Fresnel

A. Rungasamy et al. [141] improved compact linear Fresnel receivers by adding an etendue-conserving mirror field. However, this advancement demands a precise and intelligent tracking system for the mirrors, which increases the system's cost. The design of the etendue-matched mirror field is shown in Fig.2.13.a.

Zhu and Chen [142] conducted a study on compact LFC designs. They compared a standard CLFR field with a fully alternating field and three hybrid fields containing 72%, 52%, and 36% alternating mirrors. The design ensured no blocking or shading, as shown in Fig. 2.13.b. Their findings showed that hybrid CLFR fields had higher focus ratios than the standard design and included a larger percentage of efficient alternating mirrors. Experimental tests on a small-scale CLFR collector built in Nottingham, England, with a 1500 mm mirror focal length and a horizontal receiver, revealed a low land cover ratio of 0.95 and a geometric concentration ratio of 15.14.

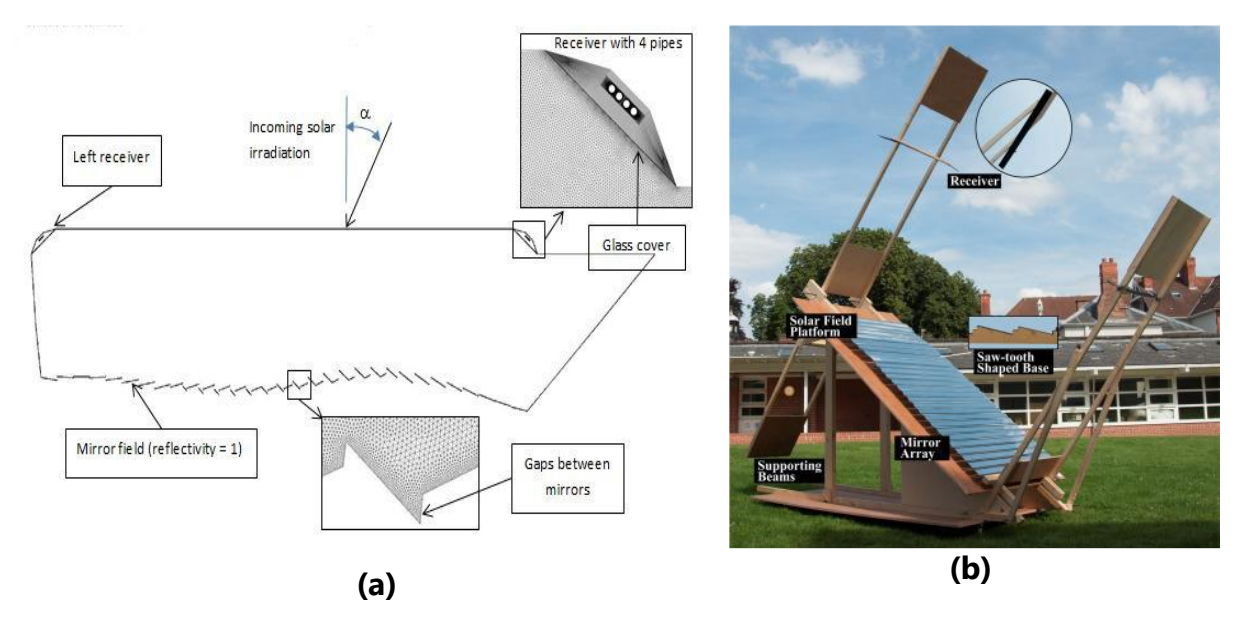


Fig.2. 13. The CLFR designs proposed by Rungasamy et al. [141] and Zhu and Chen [142].

LFC system, especially those with a relatively short length, faces considerable end losses, which result in shading at the front of the receiver. This issue has driven many researchers to explore solutions to mitigate it. One of the simplest approaches involves moving or extending the receiver a few meters back to reduce these end losses.

Yang et al. [143] developed a two-axis tracking system to reduce end losses in north-south-oriented LFCs, as shown in Fig. 2.14.a. The system features V-shaped slide rails and a linear actuator to adjust the reflector's position. Through modeling, ray tracing, and experimental testing, the system improved optical efficiency by 8% to 50%. This design is particularly cost-effective for systems larger than 5 m² and is well-suited for constrained spaces, such as rooftops (see Fig. 2.14.c), making it a strong candidate for industrial heat applications.

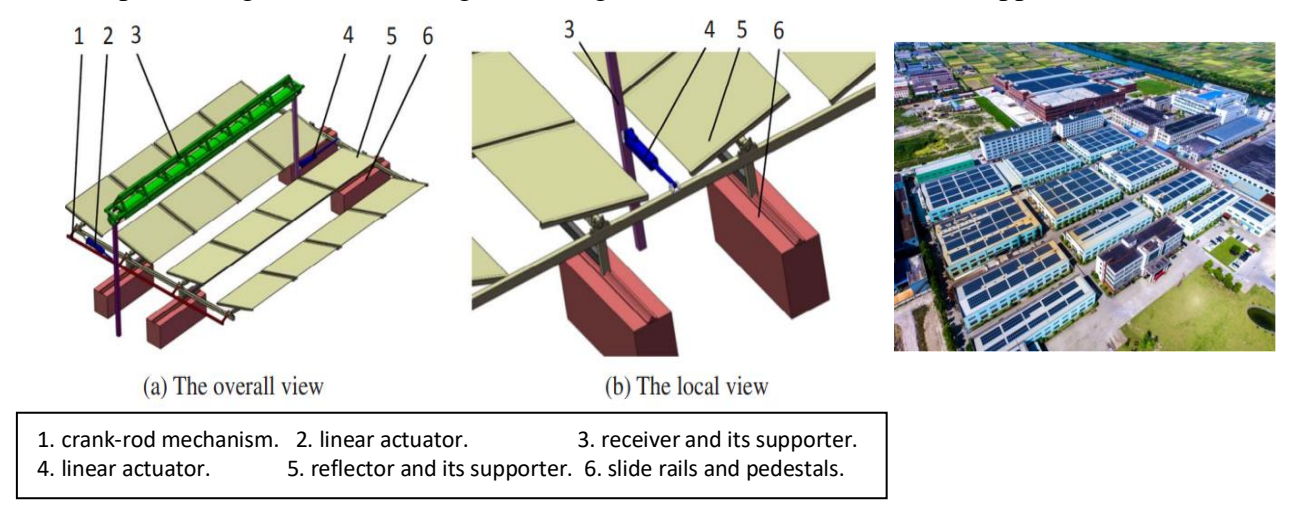


Fig.2. 14. Structure of the proposed two-axis tracking LFC [143].

A non-rectangular LFC was designed and tested in San Carlos, Argentina by Hongh and Larsen [144], with the receiver extending a few meters beyond the solar field, as shown in Fig. 2.15. This design enhances thermal efficiency during winter compared to traditional rectangular configurations. Wind tunnel experiments revealed that heat loss increased with wind speed, particularly when the wind was perpendicular to the absorber axis, and was generally higher when the wind was parallel to the absorber axis.



Fig. 2. 15. Non-rectangular LFC prototype with southward extension in San Carlos, Argentina [144].

Another method explored in the literature to reduce optical losses involves the use of an elevated mirror field. As shown in Fig. 2.16.a, an advanced linear Fresnel collector was optimized for the Plataforma Solar de Almería (Spain) by Pulido-Iparraguirre et al. [145] using optical ray-trace techniques. Modifications such as tilting the concentrator and receiver, receiver displacement, and concentrator rotation were implemented. These changes resulted in improvements of 2% to 61% in monthly power compared to a standard collector. This provides a more consistent thermal power profile throughout the year, highlighting the technology's potential. Ma and Chang [146] also investigated this concept with a two-meterlong linear Fresnel collector experimental system oriented along a horizontal north-south axis (see Fig.2.16.b). Their findings indicated that addressing the end loss in the linear Fresnel reflector system substantially enhanced thermal performance. They reported an approximately 50% increase in instantaneous thermal efficiency, with nearly a 20% improvement observed in the afternoon, compared to the initial reflector field.

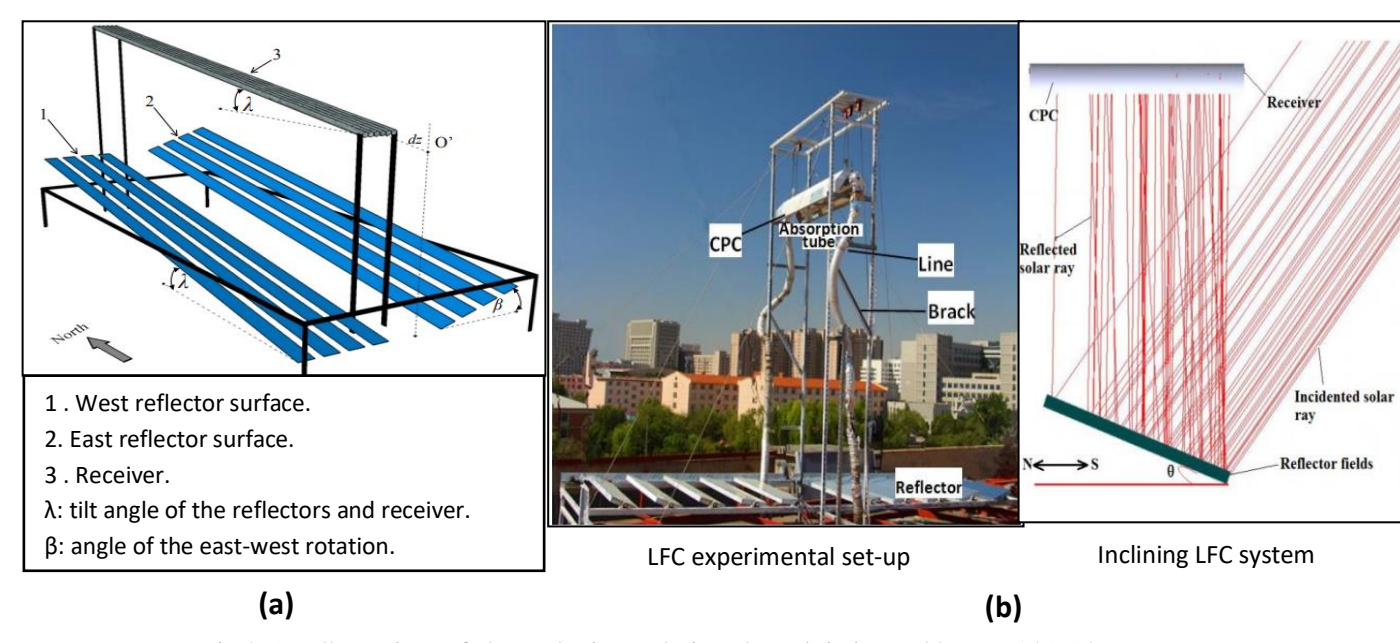


Fig.2. 16. Illustrations of elevated mirrors designed to minimize end losses [145, 146].

Zhu et al. [147] developed a scalable linear Fresnel reflector (SLFR) system that uses an evacuated tube with a selective absorbing coating and closely arranged flat mirrors to minimize shading and blocking. Installed in Guangzhou, China, the system is oriented eastwest and rotates along the north-south axis to reduce optical losses. This design led to a significant increase in thermal efficiency, achieving a maximum of 64%, which was higher than the efficiency before the adjustments.

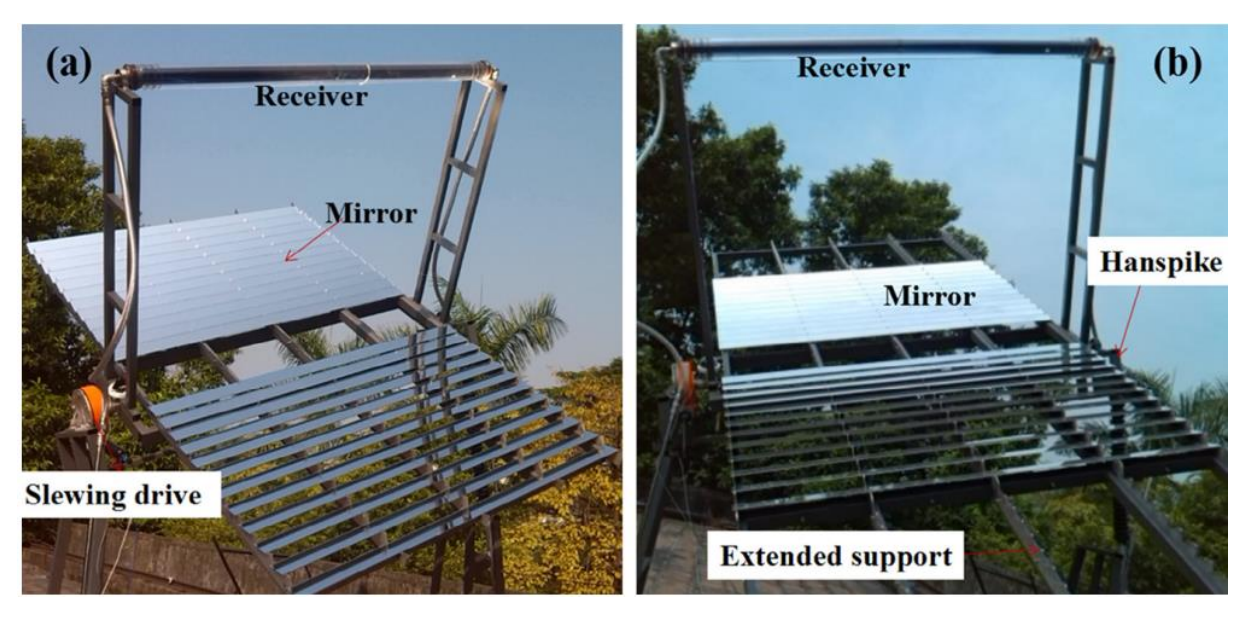


Fig. 2. 17. Depictions of (a) SLFR solar system, and (b) SLFR system with additional support [147].

In a separate study, Zhu et al. [148] proposed a movable receiver incorporating an evacuated tube with a compound parabolic collector (CPC) to minimize end losses. The system attained a maximum thermal efficiency of 66% and a thermal loss coefficient of 1.32 W/m²·°C. This design achieved a peak thermal efficiency of 66% and a thermal loss coefficient of 1.32 W/m²·°C. Compared to conventional LFC configurations, the SPLFR system demonstrated superior performance with lower thermal losses.



Fig.2. 18. Photos of experiment SPLFR solar system [148].

2.3.2. Receiver designs

Considerable effort has been devoted to optimizing receiver design to enhance optical efficiency. Tsekouras et al. [149] investigated a single-tube trapezoidal cavity (Fig.2.19.d) and reported a maximum optical efficiency of 69.3%, with a thermal efficiency of 55.7% at 300°C. Alternative geometries have also been explored for single-tube cavity designs. Montes et al. [150] examined a CPC-based cavity receiver (Fig.2.19.c) with a glass-covered aperture, achieving 66.19% thermal efficiency and 36.13% exergy efficiency at an inlet temperature of 293°C and an outlet temperature of 393°C. Beltagy et al. [151] reported a daily thermal

efficiency of approximately 40%, while Ajdad et al. [152] estimated an annual efficiency of around 45% for a similar configuration.

Numerous researchers have examined multi-tube cavity receivers, typically featuring a trapezoidal design with tubes positioned in the upper section. Depending on the configuration, solar radiation is either directly absorbed by the tubes or first captured by an absorber plate.

Mokhtar et al. [153] investigated a trapezoidal cavity receiver with four internal tubes and no cover glass, reporting a maximum efficiency of 29%. Qiu et al. [154, 155] and Sahoo et al. [156] studied an eight-tube configuration in a similar cavity. Qiu et al. [154] found that the instantaneous thermal efficiency ranged from 48.3% to 72.0%, with an annual optical efficiency between 44.7% and 60.1%. Sahoo et al. [156] reported a collector thermal efficiency between 68% and 72.8%.

Bellos et al. [157] investigated an LFC with a flat absorber, consisting of a flat cover, an absorber plate, and three tubes at the back, with insulation to minimize thermal losses. Experimental tests conducted in winter showed an optical efficiency of 25.5% and a thermal efficiency of 24.5% for inlet temperatures up to 100°C. Pauletta [158] proposed a flat evacuated receiver, achieving a maximum efficiency of 65% at a fluid temperature 200°C above ambient, with an optical efficiency of 70%.

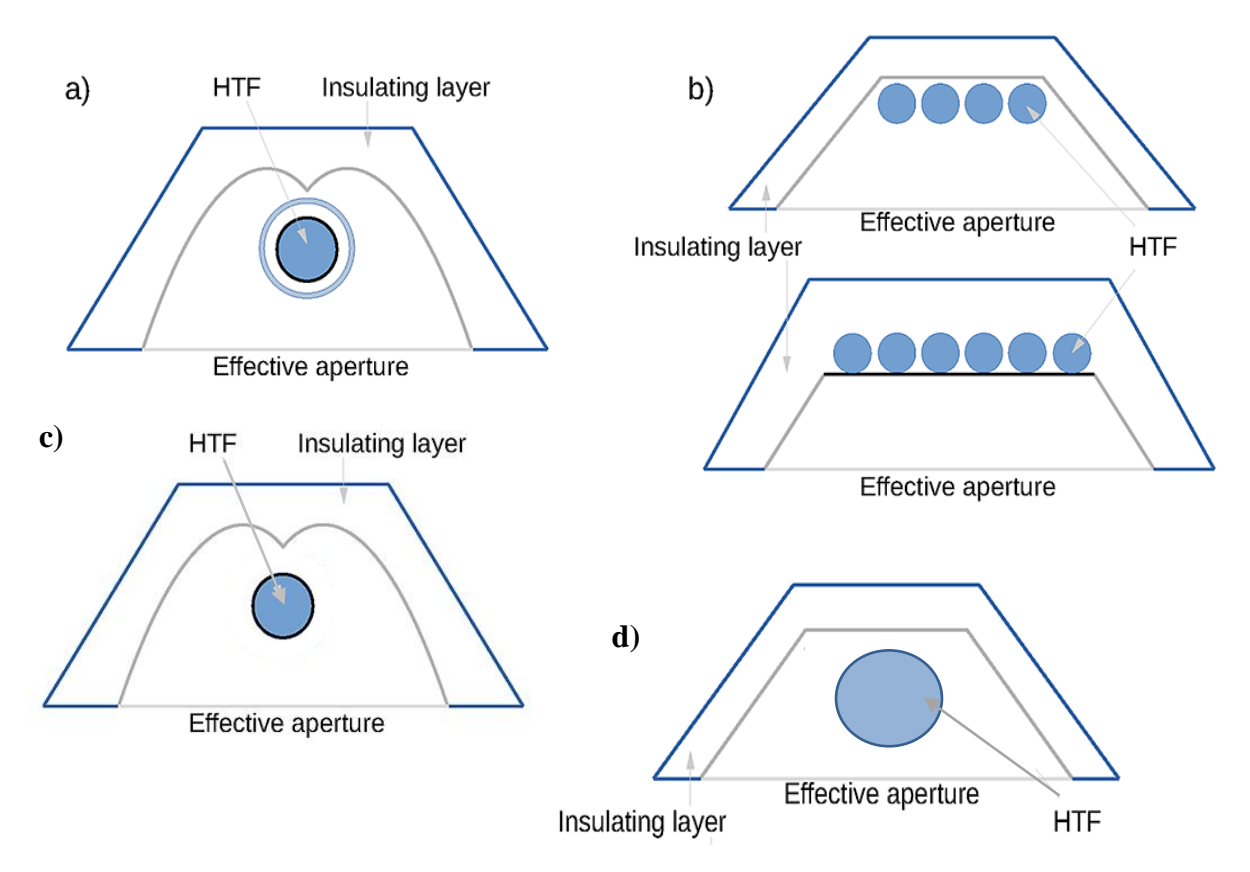


Fig.2. 19. Receiver configurations for Linear Fresnel Reflectors [159].

To achieve operating temperatures of 400–500°C, evacuated tubes were introduced; however, their low intercept factor necessitated the use of secondary concentrators to improve efficiency. Qiu et al. [160] analyzed a similar configuration (Fig. 2.19.a) and reported a maximum optical efficiency of 65%, with annual mean values ranging from 34.8% to 55.2%,

depending on latitude. The system's average annual thermal efficiency is estimated at 46%. Additionally, Ma et al. [161] investigated the impact of LFC design on optical performance and identified a peak efficiency of 68%. Further studies on thermal losses in these receivers are provided in Refs. [162, 163].

2.4. Multi-Stage Flash

Mathematical models and thermodynamic analysis are fundamental in determining the design parameters of flashing chambers in MSF systems. By applying mass and energy balance equations along with heat transfer principles, these models facilitate performance evaluation, optimize design aspects, and provide insight into brine behavior within the flashing chamber. Over the years, numerous models have been developed to support these studies [66, 164, 165-166].

Omar [167] and Ettouney et al. [168] developed steady-state models to analyze variations in flashed vapor, thermodynamic losses, and heat transfer coefficients in MSF systems. Building upon these studies, Helal et al. [169] and Rosso et al. [170] utilized simulations to assess key operational parameters, including brine flow rate, freshwater yield, and temperature profiles. Their work also examined the influence of top brine temperature (TBT) on overall system efficiency.

El-Dessouky et al. [171] introduced simplified methods for estimating MSF performance ratios, streamlining the evaluation process. Similarly, Tanvir and Mujtaba [172] integrated mass and energy balances with physical property correlations to examine the effects of seawater and steam temperature variations on plant performance, freshwater production, TBT, and bottom brine temperature (BBT).

Abdel-Jabber et al. [173] developed a comprehensive steady-state model to predict MSF plant design and operational characteristics. Their approach incorporated critical parameters such as stage dimensions, tube bundle length, and demister size while analyzing temperature distributions and flow rates to enhance overall system performance.

Qi et al. [174] proposed a three-dimensional model for the flash tank, employing Fluent software to simulate the flashing process. Their analysis of flow, heat transfer, and mass transfer revealed key insights into gas-liquid phase interactions, leading to a theoretical strategy for increasing the flash rate while reducing investment costs.

Said et al. [175] introduced a dynamic model aimed at optimizing MSF system design and operation. This model accounted for seawater temperature fluctuations, daily variations in freshwater demand, and the presence of non-condensable gases. It was also used to determine the optimal number of stages required to minimize freshwater production costs.

Fulaij et al. [176, 177] developed a computational fluid dynamics (CFD) model to simulate vapor and brine droplet flow in the MSF demister under steady-state conditions. Their findings demonstrated that vapor velocity significantly influences demister performance, while vapor temperature has a negligible effect on pressure drop.

Maniar and Deshpande [178], Gambler and Badreddin [179], Sowgath [180], and Alsadaie [181] highlighted the significance of model-based approaches in analyzing the dynamic behavior of MSF systems. Their research emphasized the role of modeling in improving processes such as system start-up, shutdown, fault detection, troubleshooting, and the development of control mechanisms to restore steady-state operation efficiently.

Nigim and Eaton [182] developed a computational field model to predict the flashing process within a flashing chamber. Similarly, Hasan et al. [183] proposed a dynamic model for industrial-scale MSF processes, validated using operational data from a seawater desalination plant. Their findings indicated that while winter conditions enhance productivity, they also result in higher steam consumption and a lower performance ratio.

2.5. Conclusion

In conclusion, this chapter emphasizes that solar-powered desalination technologies offer a promising and sustainable solution to address the growing challenge of global water scarcity. Significant advancements in systems such as Linear Fresnel Concentrators have greatly enhanced their efficiency, making solar desalination more viable for real-world applications. As research progresses, these technologies are anticipated to become more cost-effective, playing a critical role in providing clean water to regions facing water shortages. The integration of LFC with MSF desalination systems represents an exciting and dynamic area of research.

The next chapter will explore the methodology for system design, modeling, and the simulation tools used in this coupling. It will introduce a novel design to enhance the system's performance.

Chapter 3: Methodology for System Design, Modeling, and Simulation Tools Used

3.1. Introduction

In this chapter, the solar desalination system is modeled and analyzed in detail. It begins by introducing a novel approach that integrates LFC with MSF-OT desalination. The chapter details the key parameters governing each system, specifying their types, operational conditions, and characteristic values. Additionally, it introduces a newly proposed configuration that modifies the conventional MSF-OT design to enhance its performance.

Each system "LFC and MSF-OT" is modeled independently to better understand their individual behaviors. The chapter then identifies the critical parameters required for evaluating the performance of the integrated system. By combining these technologies, the study aims to improve desalination efficiency while reducing energy consumption.

3.2. System Configuration

This study develops a MATLAB model to simulate the steady-state operation of a solar desalination system, which comprises five primary components: a linear Fresnel collector field, a thermal energy storage tank, a fossil fuel backup, an MSF-OT unit, and a control system. A schematic representation of the system is provided in Fig. 3.1. This section details the system components, referencing existing installations as sources for the key geometric and operational parameters.

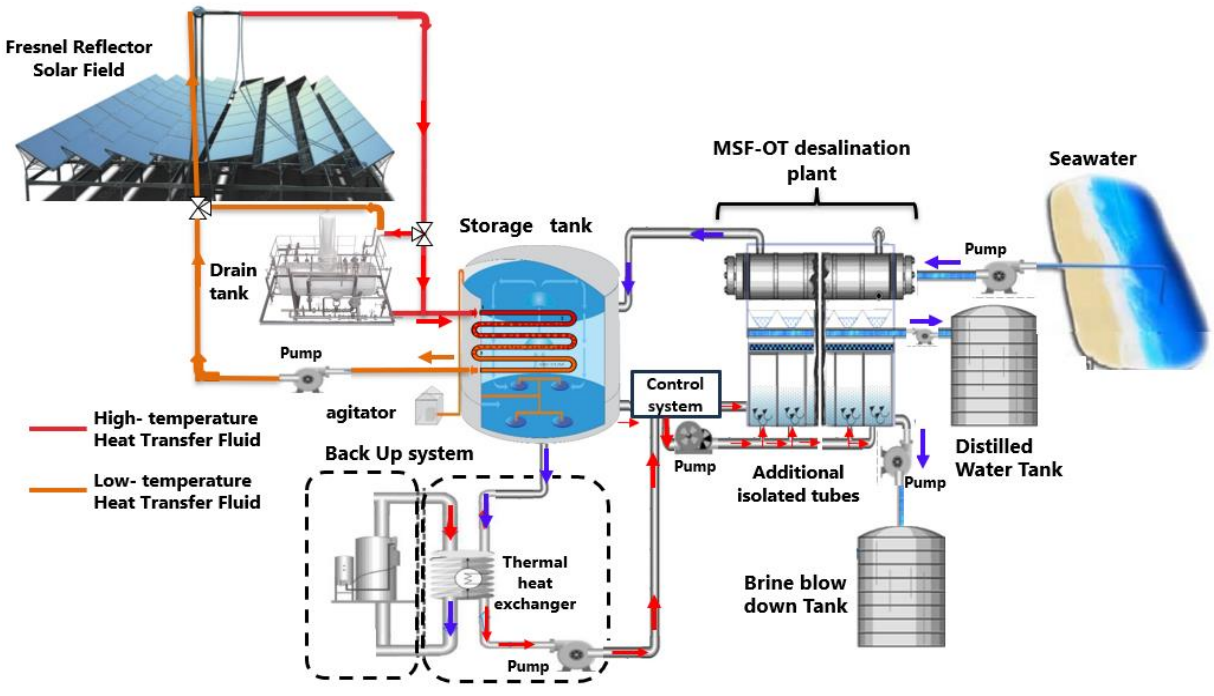


Fig. 3. 1. Schematic representation of a solar-driven MSF-OT desalination system with thermal energy storage.

3.2.1. Solar Energy Generation and Storage

This part includes the LFC field, the thermal energy storage tank, and the fossil fuel backup system, which together ensure the capture, storage, and delivery of thermal energy to the desalination unit. To assess the feasibility of the LFC-MSF-OT system, the solar field model is based on data from an existing operational facility. The selected LFC was chosen to meet the MSF-OT process temperature requirements, typically ranging from 90°C to 110°C [184, 185]. For temperatures below 200°C, a heat-transfer fluid with a low freezing point was necessary, and Therminol-66 was identified as the most suitable option.

The LFC design follows the geometrical and optical parameters of the Novatec LFC system [139]. The collector field consists of 14 units, each with an aperture area of 513.6 m², resulting in a total aperture area of 7,190 m². Each unit is composed of 16 parallel rows of flat glass mirrors, with eight mirrors per row, aligned to form a collector row. Multiple collector rows are arranged in parallel, creating the complete solar field (Fig.3.2).

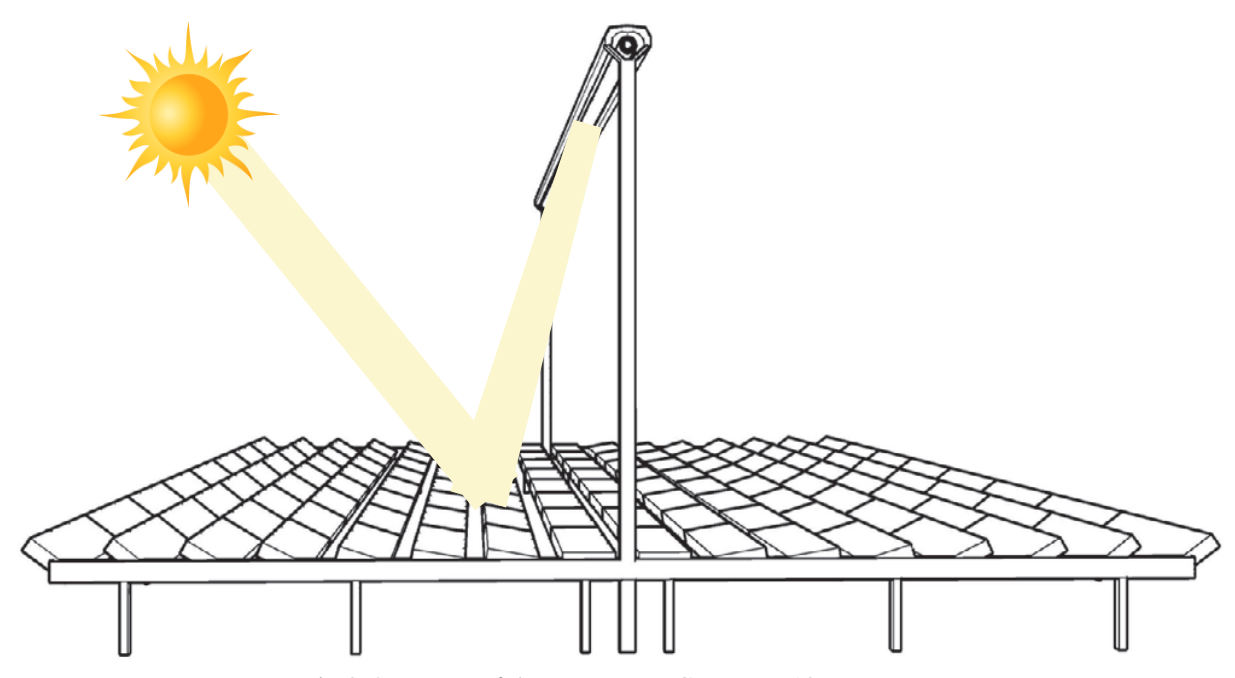


Fig.3. 2. Layout of the Novatec LFC system [139].

The proposed solar desalination system, illustrated in Fig. 3.1, incorporates a single thermal energy storage (TES) tank that performs two critical functions: it serves simultaneously as a heat exchanger and a thermal buffer, enabling efficient regulation of the thermal energy supplied to the brine. This dual functionality ensures stable thermal conditions, which are essential for the reliable operation of the MSF desalination process.

To prevent thermal stratification and ensure uniform temperature distribution within the storage medium, a mechanical agitator is integrated into the TES tank. This internal mixing mechanism maintains homogeneity of the heat transfer fluid, thereby supporting a consistent TBT of approximately 90 °C under varying operating conditions. Such thermal stability is crucial for maintaining high desalination efficiency and operational continuity.

During periods of reduced solar irradiance, such as nighttime or overcast conditions, an oil drain tank (also depicted in Fig. 3.1) collects the heat transfer fluid from the absorber tubes to

minimize standby thermal losses. When the temperature at the outlet header of the absorber field drops below that of the inlet header, indicating insufficient solar heating, the stored oil is recirculated through the absorber tubes. This process re-establishes adequate thermal conditions within the system and ensures a continuous heat supply to the desalination unit. To further guarantee uninterrupted operation, particularly during extended periods of low solar availability, the system integrates an auxiliary boiler powered by fossil fuels. This backup thermal source compensates for energy deficits when the combined contribution from the solar field and TES tank is insufficient to meet the thermal demands of the MSF plant.

This hybrid configuration, which couples solar thermal energy with conventional auxiliary heating, enhances the system's overall reliability, flexibility, and efficiency. It allows for consistent desalination performance irrespective of diurnal or seasonal variations in solar radiation, thereby contributing to the sustainability and resilience of the freshwater production process. The specifications of the solar plant components, including the LFC, thermal energy storage system, and fossil fuel backup, are detailed in Table 3.1. These components are designed based on a reference solar irradiance of 950 W/m² and are used to evaluate the annual efficiency of the solar field.

Table 3. 1. Design specifications of the solar plant [139, 186, 187, 188].

		· · · · · · · · · · · · · · · · · · ·
LFC Solar Field		
	Field aperture area	$7,190 \text{ m}^2$
	Field thermal power	6.7 MW _t
	Field HTF	Therminol-66
	Receiver type	Schott PTR 70
	Loop inlet HTF temperature	100°C
	Loop outlet HTF temperature	180°C
	Loop optical efficiency	0.546
	Loop thermal efficiency	0.953
	Total tracking power	0.002 MW _e
	Heat loss at design	166.2 W/m
Storage System		
	Hours of storage at design	4 hr
	Total tank volume	400 m ³
	Loss coefficient from tank	$0.4 \text{ W/m}^2\text{K}$
	Storage media	Seawater
Backup heater		
	Auxiliary natural gas boiler power	0.084 MWh

3.2.2. The Multistage Flash desalination unit and Control System

This part comprises the MSF-OT unit and an integrated control system. The MSF-OT unit utilizes thermal energy to drive the desalination process, converting seawater into fresh water through multi-stage flashing. Meanwhile, the control system continuously monitors and

regulates key operational parameters, ensuring efficient energy utilization, stable performance, and optimal freshwater production.

3.2.2.1. Conventional Plant

Fig. 3.3 illustrates the fundamental layout of a conventional MSF-OT plant. The process begins as brine enters the first chamber, where it is heated in the brine heater to reach the required TBT. Once heated, the brine undergoes rapid evaporation in vacuum-controlled stages, a process known as "flashing." To maintain the required pressure conditions in each stage and remove non-condensable gases, a vacuum pump is employed. The resulting vapor then condenses, transferring heat to the incoming feedwater and generating freshwater, as schematically depicted in Fig. 3.3.

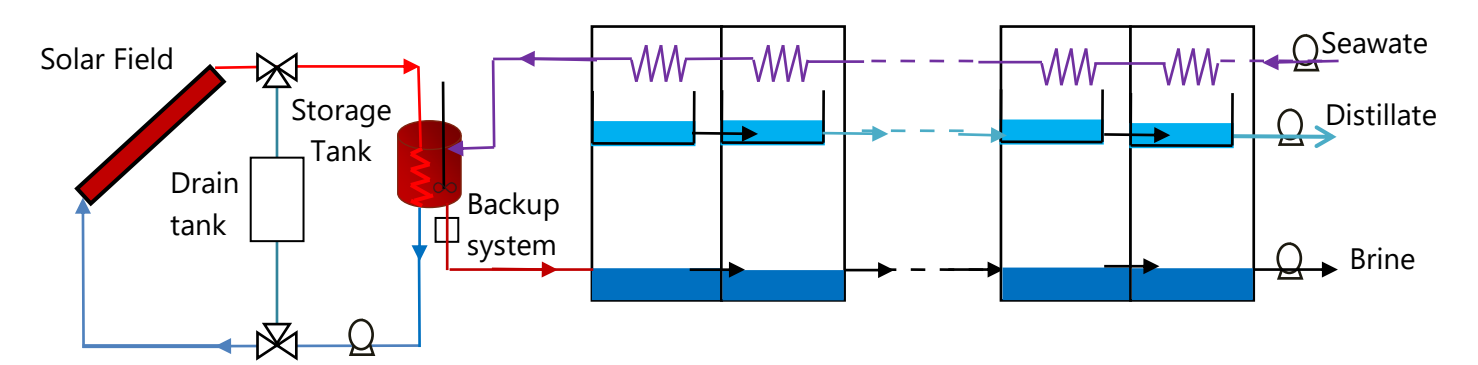


Fig.3. 3. Layout of a conventional MSF-OT plant.

To prevent brine droplets from reaching the condenser tubes, a demister is installed above the brine pool in each stage. This component plays a crucial role in minimizing scaling and corrosion by effectively separating vapor from liquid. Engineered for optimal performance, demisters typically consist of wire mesh structures arranged in cylindrical or multi-layered pad formations. Their efficiency is primarily influenced by mesh density and wire diameter, both of which impact droplet capture and pressure drop [189].

Operational data indicate that commercial MSF plants generally comprise 20 to 30 stages, with TBT values ranging from 90°C to 110°C. The temperature difference between consecutive stages typically falls within 2.5°C to 3.0°C, ensuring efficient heat recovery and overall desalination performance [184, 185].

3.2.2.2. Novel Approach to Plant Design

An advanced methodology has been introduced to enhance freshwater production in the MSF-OT plant. This approach divides the seawater intake into two streams: the primary stream enters the first stage, where its flow rate gradually decreases due to evaporation across successive stages, while the secondary stream is distributed through isolated tubes to each stage. This controlled distribution allows precise flow adjustments, ensuring a stable brine flow throughout the system. However, the efficiency of this strategy is dependent on the available temperature and pressure differentials between the stages, as illustrated in Fig. 3.4.

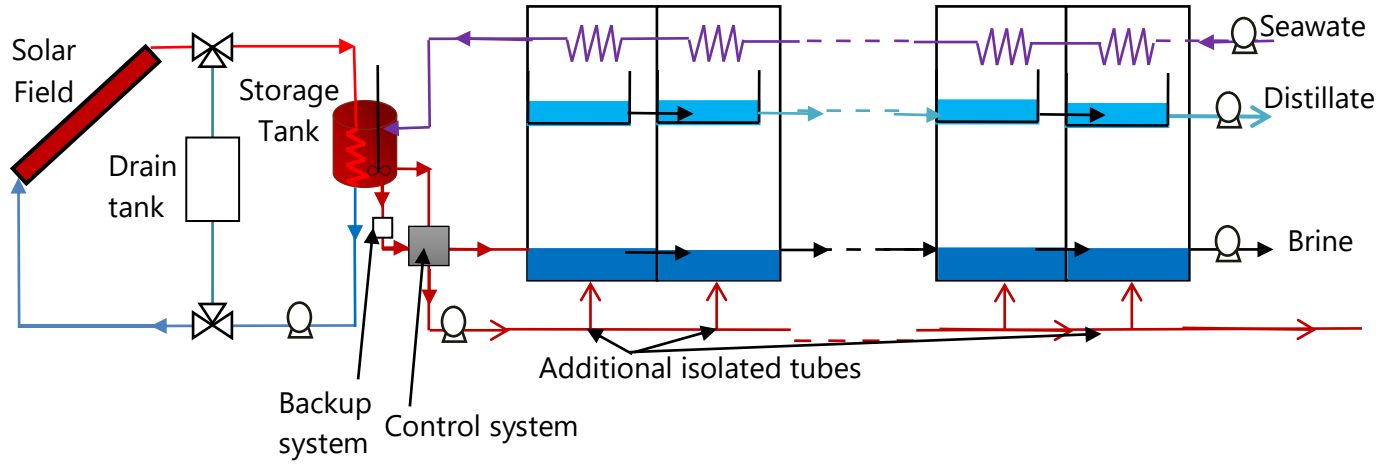


Fig.3. 4. Layout of a novel approach to MSF-OT desalination plant design.

Table 3.2 summarizes the key characteristics of the MSF-OT desalination unit analyzed in this study. These parameters define its design and operational performance. The data serve as a reference for assessing system efficiency and effectiveness.

Parameter	Value	Unit
Seawater loading	100	m ³ /hr
Seawater inlet temperature	25	°C
Seawater salinity	35,000	Ppm
Number of stages	20	-
Brine blowdown temperature	40	°C
Top brine temperature (TBT)	90	°C
Stage Width	1.543	M
Stage Length	2.532	M
Stage Height	2.742	M
Steam temperature	120	°C

Table 3. 2. Summary of the desalination unit characteristics.

3.2.2.3. Control System

An advanced control system has been designed to regulate brine flow within the brine pool by continuously monitoring and adjusting key operational parameters. This intelligent system ensures stability, enhances efficiency, and prevents fluctuations that could disrupt performance. By integrating real-time data acquisition and automated adjustments, it optimizes energy utilization and maintains ideal operating conditions, ultimately improving desalination efficiency and reliability.

Fig. 3.5 illustrates the control block diagram of the proposed system, highlighting essential features such as solar radiation input, thermal energy storage, and temperature and pressure sensors. These elements work together to optimize heat transfer, regulate fluid dynamics, and ensure the continuous and reliable operation of the MSF-OT plant, maintaining a stable freshwater production rate.

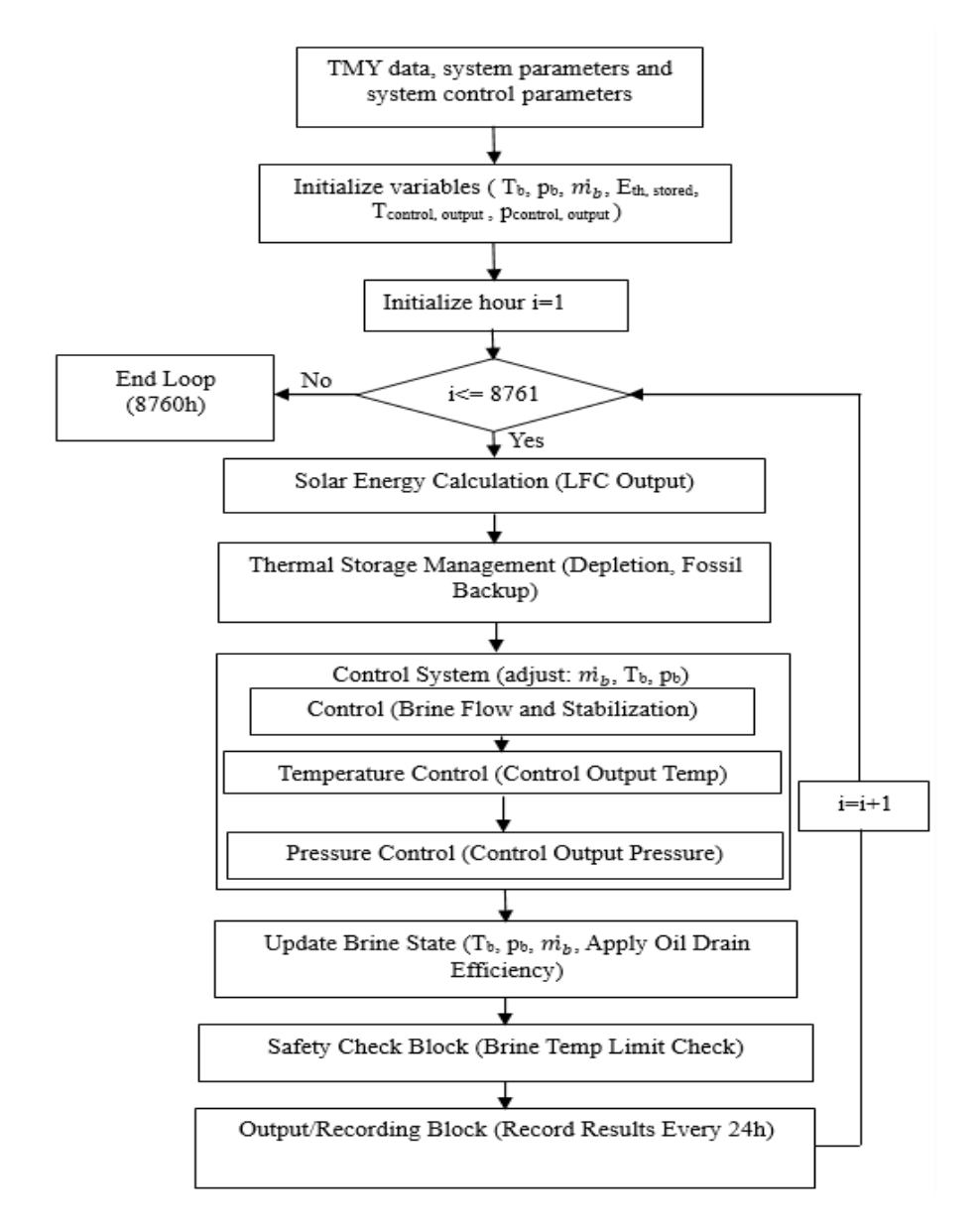


Fig.3. 5. Block diagram of the proposed control system.

3.3. Fresnel Model

This section outlines a mathematical model developed to analyze the performance of the proposed system under real operating conditions. Using TMY weather data for Algeria, the model incorporates essential parameters such as the optical efficiency of the linear Fresnel collector, the thermos-physical properties of Therminol-66 (HTF) [188], and meteorological variables including DNI, ambient temperature, and wind speed [190]. The analysis focuses on three key performance indicators: collector field power, thermal energy consumption, and the HTF outlet temperature at the hot header. These parameters are assessed on an hourly basis over an average year to provide a detailed evaluation of system efficiency.

The section is divided into three main parts: the optical model, the thermal model, and the storage system model, each addressing a critical aspect of the system's operation.

3.3.1. Optical Model

A detailed analysis of input parameters was conducted to assess system performance, energy efficiency, and heat transfer effectiveness, ensuring optimal design and operation for solar energy applications in various climatic conditions.

Based on the defined solar field parameters, the sizing process involved calculating the required number of collectors per row (N_C) and the total number of rows (N_R). Using these values, the total number of collectors ($N_{Tot,c}$) was calculated as:

$$N_{Tot,c} = N_C \times N_R \tag{1}$$

The total aperture area (A_{SF}) of the solar field was then obtained by multiplying $N_{Tot,c}$ by the aperture area (A_p) of a single LFC, expressed as:

$$A_{SF} = N_{Tot,c} \times A_p = N_R \times N_C \times A_p \tag{2}$$

Number of rows (N_R)

Number of collectors per row (N_c)

Fig.3. 6. Sizing the solar field: calculating collectors and rows.

Solar field efficiency is compromised by losses such as shading, inter-row blocking, and end-loss, where a portion of reflected radiation fails to reach the receiver. These losses become critical under off-design conditions, directly impacting thermal energy generation, which is determined using Eq. (3).

$$P_{inc} = \eta_{opt}(\theta_L, \theta_T) \times A_p \times DNI \tag{3}$$

In this formulation, the direct normal irradiance (DNI) is expressed in W/m², while the optical efficiency η_{opt} is defined as:

$$\eta_{opt}(\theta_L, \theta_T) = \eta_{end} \times \eta_{shad} \times \eta_{block} \times \eta_0 \times IAM(\theta_L, \theta_T)$$
(4)

Here, η_0 represents the peak optical efficiency of the LFC under normal incidence (θ_w =0°). The factors η_{end} , η_{shad} , and η_{block} quantify the impact of end losses, shadowing, and blocking, respectively, as given by Eqs. (5), (6), and (7).

The calculation of end loss efficiency depends on the longitudinal incidence angle (θ_L) , receiver height (H_{rc}) , and collector length (L_R) .

$$\eta_{end} = 1 - \frac{H_{rc}}{L_R} \times \tan(\theta_L) = 1 - \frac{H_{rc}}{L_C \times N_C} \times \tan(\theta_L)$$
(5)

A two-dimensional model was developed to optimize mirror inclinations in each row, accounting for the shading effects of secondary reflectors on primary reflectors. Pino et al. [191] applied this approach to evaluate the impact of inter-row shading. This analysis enabled the calculation of the total shaded area between rows. The shadowing efficiency, defined in Eq. (6), is determined as the ratio of the shaded area (A_{shad}) to the aperture area (A_p).

$$\eta_{shad} = 1 - \frac{A_{shad}}{A_p} \tag{6}$$

In a similar manner, the blocking effect is quantified by the blocking factor, which is the ratio of the blocked area (A_{block}) to the aperture area (A_p). Accordingly, the blocking efficiency is expressed as:

$$\eta_{block} = 1 - \frac{A_{block}}{A_p} \tag{7}$$

The Incidence Angle Modifier (*IAM*) defines how the optical efficiency (η_{opt}) of a solar collector varies with the incidence angle (θ_w), which is the angle between the sun's rays and the normal to the collector's aperture plane. This dependency is mathematically formulated based on a reference solar angle, specific to the collector's design and intended use (Eq. (8)).

$$IAM = \frac{\eta_{opt}(\theta_w)}{\eta_{opt}(\theta_{w,ref})} \tag{8}$$

In LFC systems, the IAM is defined as the ratio of the optical efficiency at a given solar position to its value when the sun is at zenith ($\alpha_s = 90^\circ$, $\gamma_s = 0^\circ$). This parameter provides a practical alternative to time-consuming ray-tracing simulations, as its analytical formulation ensures reliable results while significantly reducing computational effort. Several IAM estimation models exist in the literature, with the factored approach being one of the most commonly used [192]. This method decomposes IAM into two independent components: longitudinal (IAM_L) and transversal (IAM_T), as defined in Eq. (9). These components are determined by varying the longitudinal and transversal contributions of the solar zenith angle (θ_T and θ_L , respectively).

$$IAM = IAM_L \times IAM_T \tag{9}$$

This study utilizes the correlations from [193] to determine the IAM using a cubic polynomial functions based on θ_T and θ_L . Their accuracy was evaluated by comparing the results with raytracing simulations performed in SolTrace software and experimental data from the NOVATEC SOLAR system [194, 91] (see ray tracing section). The corresponding expressions are given in Eqs. (10) and (11).

$$IAM_T = 0.9896 + 0.044 \times \theta_T - 0.0721 \times \theta_T^2 - 0.2327 \times \theta_T^3$$
(10)

$$IAM_{L} = 1.0031 - 0.2259 \times \theta_{L} + 0.5368 \times \theta_{L}^{2} - 1.6434 \times \theta_{L}^{3} + 0.722 \times \theta_{L}^{4}$$
(11)

The transversal (θ_T) and longitudinal (θ_L) incidence angles are determined by the solar azimuth angle (γ_s) and solar altitude angle (α_s), which define the sun's position relative to the collector (see Fig. 3.7). Their mathematical expressions are provided in Eqs. (12) and (13) [96].

$$\theta_T = tan^{-1} \left(\frac{|\sin(\gamma_s)|}{\tan(\alpha_s)} \right) \tag{12}$$

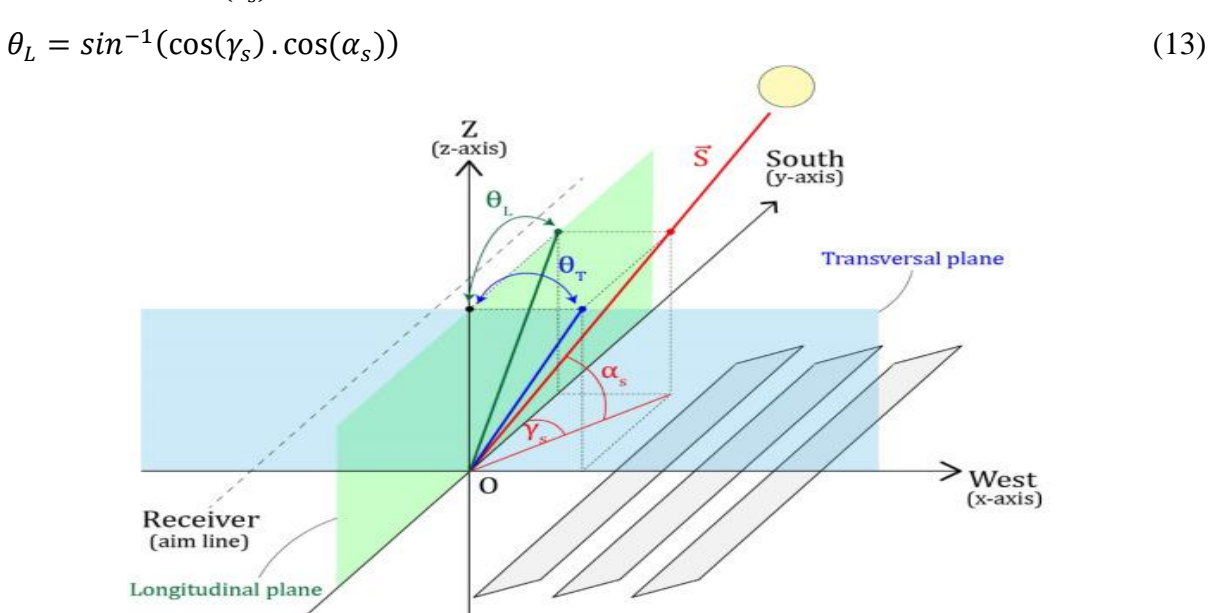


Fig.3. 7. Geometric representation of incidence angles and solar position.

3.3.1.1. Ray Tracing

Ray tracing is a widely used technique for analyzing the optical properties of concentrating solar collectors. This method simulates the trajectories of a large number of randomly generated photons emitted from a defined light source, tracing their paths from emission to absorption. The distribution and intensity of these rays are determined by calculating the intersection points between the reflected rays and the receiver surface using vector-based approaches.

To evaluate the optical performance of solar collectors, many ray tracing programs incorporate the Monte Carlo (MC) method, which relies on statistical sampling to solve complex mathematical problems. This approach is particularly advantageous for modeling intricate optical interactions that are difficult to address using conventional numerical techniques. In this study, the SolTrace software [195] is employed to investigate the influence of linear Fresnel (LF) field parameters on optical efficiency.

A. Overview of SolTrace

SolTrace is a ray-tracing software developed by the National Renewable Energy Laboratory (NREL) to simulate and analyze the optical behavior of solar energy systems. While primarily designed for solar applications, it is also suitable for general optical system modeling. The software was introduced to address the limitations of earlier tools such as

OPTDSH [196] and CIRCE [197], enabling the study of more complex optical configurations with greater accuracy.

The ray-tracing methodology implemented in SolTrace follows the approach outlined by Spencer and Murty (1962) [198]. This process involves a series of coordinate transformations and optical calculations for each traced ray. Initially, the ray's origin and direction are transformed from global coordinates to the local coordinate system of the optical component. The point of intersection between the ray and the first optical surface is then determined. Depending on the interaction type (reflection, refraction, or diffraction) the ray's new trajectory is computed. The updated ray is subsequently transformed back to the global coordinate system, and the process is repeated as the ray propagates through successive optical elements. This iterative procedure continues until the ray is either absorbed, reflected out of the system, or exits its defined path [198].

B. Simulation of the Studied LFC Using SolTrace

The simulation process in SolTrace follows a structured approach, beginning with the definition of solar parameters, followed by the characterization of optical properties and the configuration of the collector's geometry. Once these elements are set, ray tracing is performed to track light interactions, and the results are then analyzed to evaluate the system's optical performance.

B.1. Sun Definition: At the beginning of the simulation, the sun's shape and position are specified. Its position can be defined in two ways:

- ✓ By entering the latitude (φ) , day of the year (J), and local solar hour (Ho).
- ✓ By selecting a point in the global coordinate system and using a vector to define its direction or by directly assigning directional parameters. This method involves calculating the x, y, and z coordinates of the sun, where the z-axis points north, the y-axis points toward the zenith, and the x-axis points west.

The x, y, and z coordinates of the sun, along with its azimuth (γ_s) and elevation (α_s) angles, are computed using Eqs. (16)–(20). These calculations require key parameters, including latitude (φ) (positive for the Northern Hemisphere, negative for the Southern Hemisphere), the day of the year (J), and the local solar time (Ho) [12].

$$\delta = \arcsin(0.39795\cos(0.98563(J-173))) \tag{14}$$

$$\omega = 15(Ho - 12) \tag{15}$$

$$\alpha_{s} = \arcsin\left(\sin\left(\delta\right) \cdot \sin\left(\varphi\right) + \cos\left(\delta\right) \cdot \cos\left(\varphi\right) \cdot \cos\left(\omega\right)\right) \tag{16}$$

$$\gamma_s = \arccos((\sin(\delta).\cos(\varphi) - \cos(\delta).\sin(\varphi).\cos(\omega)) / \cos(\alpha_s))$$
 (17)

$$x = -\sin(\gamma_s) \times \cos(\alpha_s) \tag{18}$$

$$y = \sin(\alpha_s) \tag{19}$$

$$z = \cos(\gamma_s) \times \cos(\alpha_s) \tag{20}$$

Where ω and δ (°) represent the solar hour angle and the declination, respectively.

Sun shape profiles can be categorized into three types: Gaussian, Pillbox, and user-defined. For this study, the Pillbox profile with a uniform distribution is utilized. This model is well-suited for various applications and is characterized by a half-angle of 4.6 mrad, as shown in Fig. 3.8.

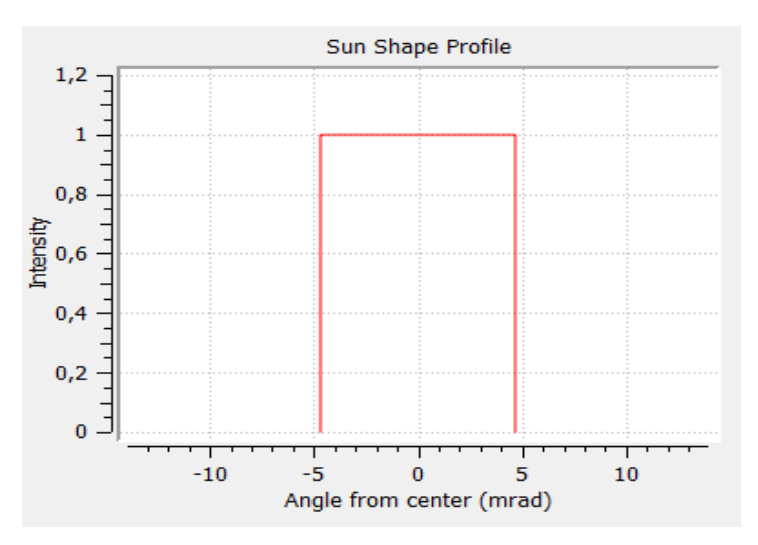


Fig.3. 8. Representation of the Pillbox sun shape profile.

B.2. Optical Properties and Collector Geometry Definition

In SolTrace, the geometric configuration is organized into stages, with each stage representing a specific system component. In this study, the collector is divided into two main sections: the concentrator and the receiver. The concentrator consists of 16 elements, as illustrated in Fig. 3.9. Each element corresponds to a row of flat mirrors, with each row containing eight primary mirrors. Each mirror measures 0.75 m in width and 5.35 m in length, with a spacing of 0.2857 m between adjacent mirrors. For simulation purposes, only the front surface of each mirror is considered. The Schott PTR 70 receiver consists of a stainless steel absorber tube enclosed within a glass envelope. It incorporates a selective coating for high solar absorption, vacuum insulation to minimize heat loss, and an anti-reflective layer to enhance optical efficiency. The selected interaction mode for the concentrator and receiver is reflection, except for the glass, which interacts through refraction.

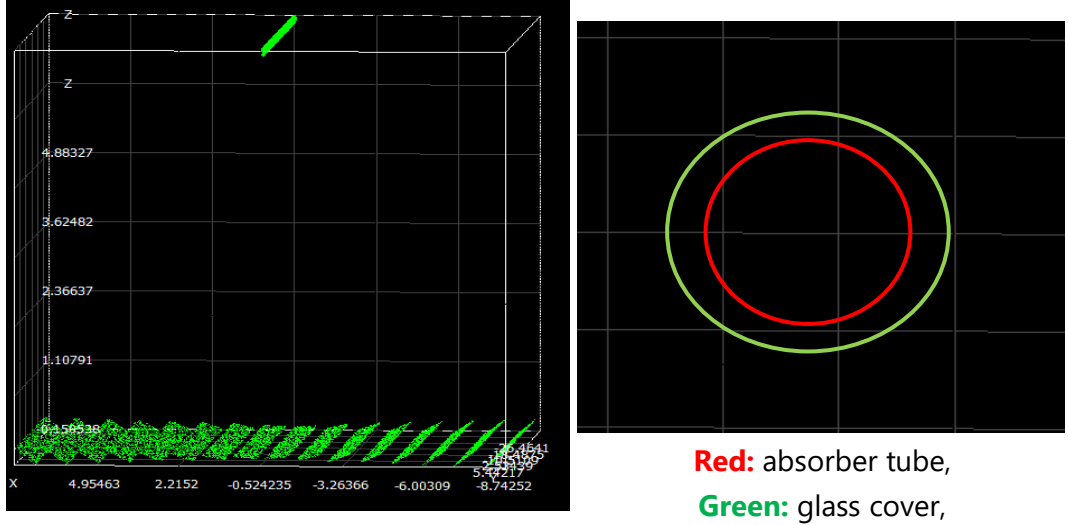


Fig.3. 9. Geometrical representation of the studied collector in SolTrace.

All essential optical and geometrical parameters required for the collector's simulation are summarized in Table 3.3.

Table 3. 3. 0	Geometrical and	l optical	parameter o	of the LFC	[186, 187, 194].

Concentrator		Receiver		
Parameter	value	Absorber tube	glass	Unit
Reflectivity, ρ	0.70	0.10	0.10	-
Transmissivity, τ	1.00	0.00	1.00	-
Slope error	3.00	1.00	0.95	mrad
Specularity error	0.50	0.20	0.22	mrad
Error type	Gaussien	Gaussien	Gaussien	-
Refraction indicies	1.00	1.10	1.46	-
Primary mirror length	5.35	Receiver height above the	7.4	m
Primary mirror witdh	0.75	primary reflectors	7.4	m
Distance between mirrors in a row	0.2857	Absorber outer diameter	0.07	m
Distance between rows in a control unit	0.304	Glass envelope outer diameter	0.115	m

B.3. Ray tracing

Fig. 3.10 presents a sample ray tracing simulation performed in SolTrace, incorporating the specific conditions of the Algiers region with a direct normal irradiation of 1000 W/m². Each initialized ray is represented as a line on the corresponding mirror, with its position randomly assigned. Rays that are successfully reflected onto the receiver's aperture are depicted in yellow and are similarly displayed on the target. Conversely, rays that are lost due to reflection outside the receiver are represented as red lines on the corresponding mirrors.

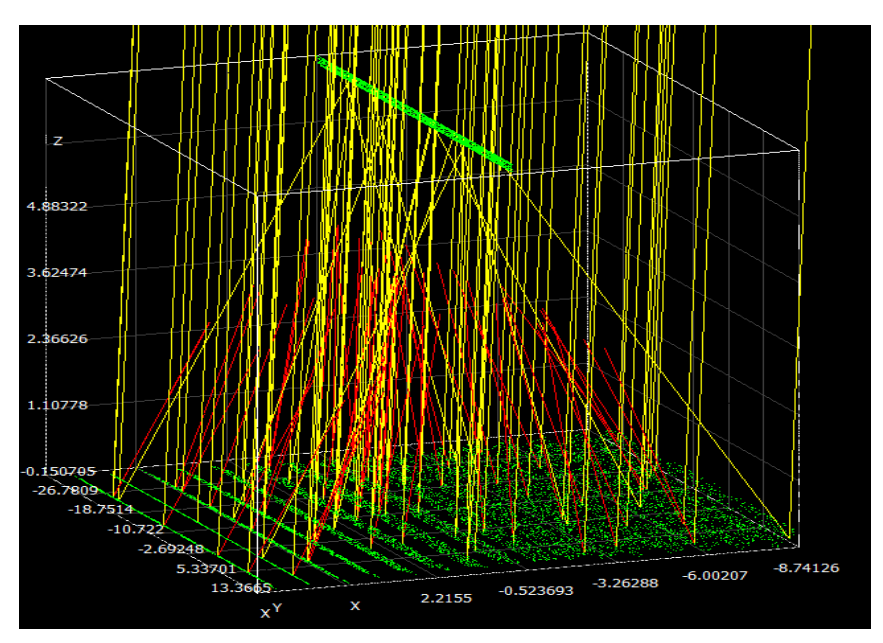


Fig.3. 10. Ray Tracing Analysis of the LFC System in SolTrace.

B.4. Validation of IAM Equations Using Ray Tracing Simulations and Experimental Data

IAM values play a fundamental role in solar field design, as they significantly influence both optical efficiency and thermal performance. To assess the accuracy of Eqs. (10) and (11), their predictions were compared with experimental data from the NOVATEC SOLAR system [91, 194] and ray tracing simulations performed using SolTrace.

The simulations were conducted using input parameters aligned with the experimental setup to ensure consistency in evaluation. The results demonstrated strong agreement between the polynomial fit and the SolTrace simulations, with a root mean square error (RMSE) of 2.12% for the longitudinal IAM and 4.35% for the transverse IAM. Similarly, when compared to the NOVATEC SOLAR experimental data, the RMSE values were found to be 1.25% and 3.02%, respectively, as illustrated in Fig. 3.11. These results indicate that the proposed equations accurately capture IAM variations with high precision. The low RMSE values further validate their effectiveness in modeling optical behavior, making them a valuable tool for optimizing the performance of solar collector systems.

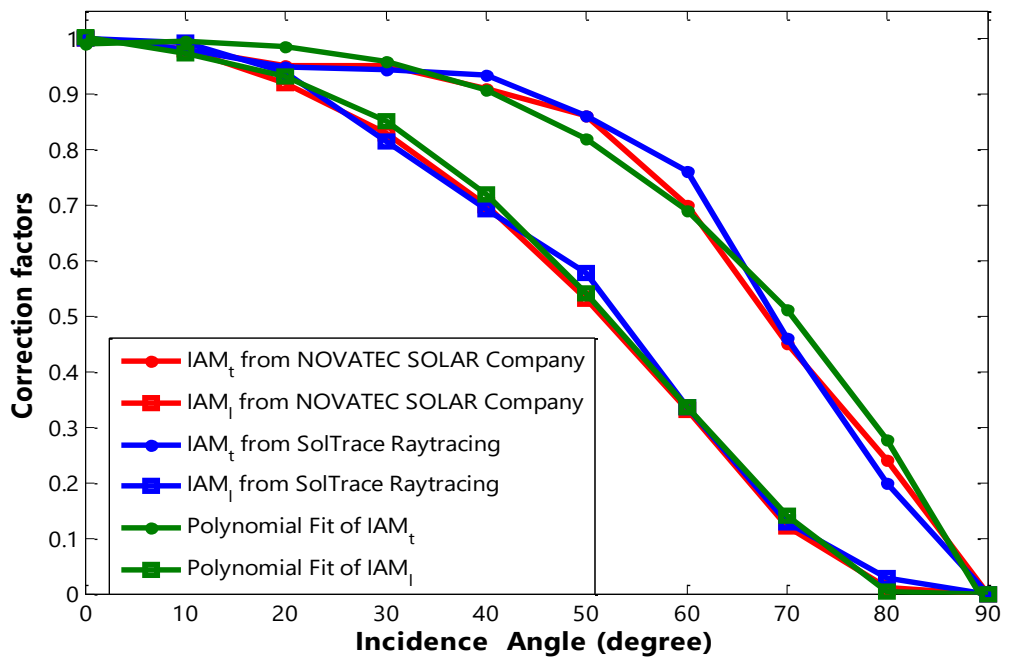


Fig.3. 11. Comparison of IAM factors: NOVATEC SOLAR system data [32], SolTrace ray tracing results, and polynomial fit [193].

3.3.2. Thermal Model

The performance of an LFC depends on its ability to efficiently convert incident solar energy into useful thermal power (P_u). However, not all the collected energy can be utilized, as some is lost due to heat dissipation in the solar field and through the piping system. To accurately determine the net useful thermal power, these losses must be taken into account. The following equation explains how the useful thermal power is calculated.

$$P_u = P_{inc} - P_{pipes} - P_{loss} \tag{21}$$

The overall thermal losses in the system arise from both the piping network and the solar receivers. In this study, a constant value of 0.86 W/m² is used to represent piping losses [199]. Meanwhile, the thermal losses of the LFC receivers were assessed using the model described in [200] and validated against experimental data from the NOVATEC SOLAR system [194]. The following equation quantifies these losses.

$$P_{loss} = A_{ab.ex} \times (3.88699 \times (T_{ave} - T_{amb}) + 0.00808 \times (T_{ave} - T_{amb})^2)$$
 (22)

Where T_{ave} is the average temperature of the fluid within the solar field, T_{amb} is the ambient temperature, and $A_{ab,ex}(m^2)$ is the external surface area of the absorber tube.

The results depicted in Fig. 3.12 confirm a strong correlation between the polynomial fit and the measured data, supporting the model's reliability. Any slight variations can be attributed to external factors such as fluctuations in solar irradiance and ambient temperature, as well as potential measurement uncertainties.

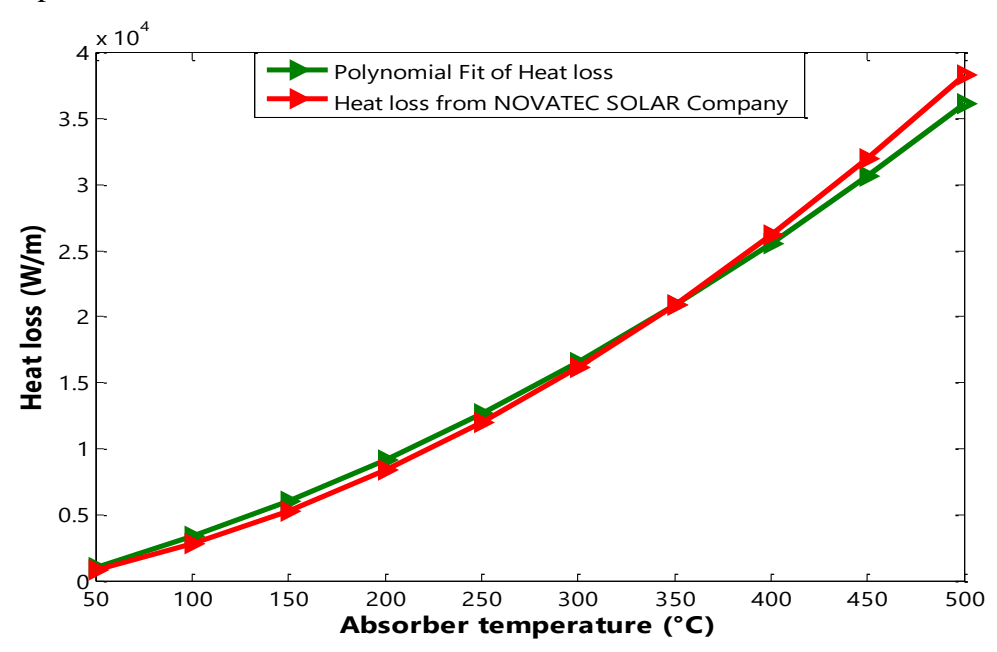


Fig. 3. 12. Comparative Analysis of Heat Loss: Polynomial Fit and NOVATEC SOLAR system [194].

The useful thermal power can also be evaluated using an alternative mathematical expression that incorporates key thermodynamic parameters. This approach provides a comprehensive analysis of the energy effectively utilized within the system and is expressed by the following equation:

$$P_{u} = \dot{m}_{HTF-C} \cdot Cp_{HTF} \cdot \Delta T_{SE} \tag{23}$$

Where the mass flow rate of the heat transfer fluid (HTF) supplied to the heat exchanger is defined as:

$$\dot{m}_{HTF-C} = \frac{\dot{m}_f \cdot Cp_f \cdot (T_{BT} - T_{f1})}{Cp_{HTF} \cdot \Delta T_{SE}} \tag{24}$$

In Eqs. (17) and (18), $\Delta T_{SE}(^{\circ}\text{C})$ represents the temperature difference across the exchanger (tank). Cp_{HTF} (kJ/kg· $^{\circ}$ C) denotes the specific heat capacity of Therminol-66 [188]. \dot{m}_f (kg/h) corresponds to the feed seawater flow rate, while Cp_f (kJ/kg· $^{\circ}$ C) is the specific heat capacity

of the feed water at constant pressure. T_{BT} (°C) refers to the top brine temperature, and T_{fI} (°C) is the temperature at the exit of the first stage of the MSF system.

3.3.3. Storage System Model

Efficient energy management is essential for maintaining the stability and performance of solar thermal systems.

A thermal storage system plays a crucial role by storing excess energy generated during peak solar radiation periods and releasing it when solar input is insufficient. The amount of stored thermal energy is determined by the surplus accumulated over a specific time interval, from t₁ and t₂, and is quantified using the following expression:

$$E_{th,stored} = \sum_{i=t_1}^{t_2} (P_{th,field}(i) - P_{th,MSF})$$
(25)

 $P_{th,MSF}$ denotes the thermal power required to operate the MSF plant, while $P_{th,field}$ represents the thermal power produced by the solar field. The latter is determined using Eq. (26):

$$P_{th.field} = P_u.N_{Tot.c} = P_u.N_C.N_R \tag{26}$$

3.3.4. Backup System Model

This section examines the challenge of maintaining a consistent TBT at the inlet of the MSF desalination system, particularly under reduced solar radiation conditions. A decline in solar energy availability, especially during winter, can lead to insufficient thermal input, affecting system performance. To mitigate this issue, a fossil-fuel backup system can be integrated to compensate for the energy deficit and ensure the required TBT is maintained. This approach, known as the "Topping Mode" [201], involves placing the auxiliary heating system between the thermal storage tank and the first stage of the MSF process. The operation of this backup system follows specific control criteria, which are outlined as:

$$P_{aux} = \begin{cases} P_{th,MSF}.f_{tod} - P_{th,field} & if & P_{th,field} < P_{th,MSF}.f_{tod} \\ 0 & if & P_{th,field} \ge P_{th,MSF}.f_{tod} \end{cases}$$

$$(27)$$

Here, f_{tod} denotes the time-of-dispatch factor, which is implemented for the current time step to adjust the operation accordingly.

3.4. MSF Model

This section presents a dynamic model for the MSF desalination process, developed in MATLAB to simulate system behavior by computing mass and energy balances at each stage. The model evaluates fluid flow dynamics and thermal variations to assess system performance. It provides insights into heat transfer efficiency, phase change processes, and operational stability. To ensure accuracy and applicability, the model is formulated based on well-defined assumptions, outlined as follows:

- The distillate product is assumed to be completely salt-free at each stage.
- Brine within each stage is considered well-mixed, ensuring a uniform temperature distribution.

- Salt deposition in condenser tubes is neglected.
- Non-condensable gases are entirely removed by a vacuum pump, preventing any impact on system performance.
- Heat losses to the surroundings are considered negligible.
- Thermodynamic equilibrium between vapor and liquid phases is maintained, with quasi-steady state conditions across all stages.
- The thermophysical properties of seawater, brine, and distillate, including specific heat capacity and enthalpy, are temperature-dependent.
- The inlet seawater temperature is fixed at 25°C.
- The system operates with a continuous seawater supply of 100 m³/h.
- The TBT is assumed to be 90°C.

3.4.1. Heat Balance in The Storage Tank (Brine Heater)

The brine heater is a crucial component of the MSF desalination process, supplying the necessary thermal energy for evaporation. This subsection analyzes its heat balance, accounting for thermal input, heat losses, and temperature variations to evaluate system efficiency. As shown in the plant scheme in Fig. 3.13, the steady-state equations apply to each stage i, where i ranges from 1 to n, representing the total number of stages.

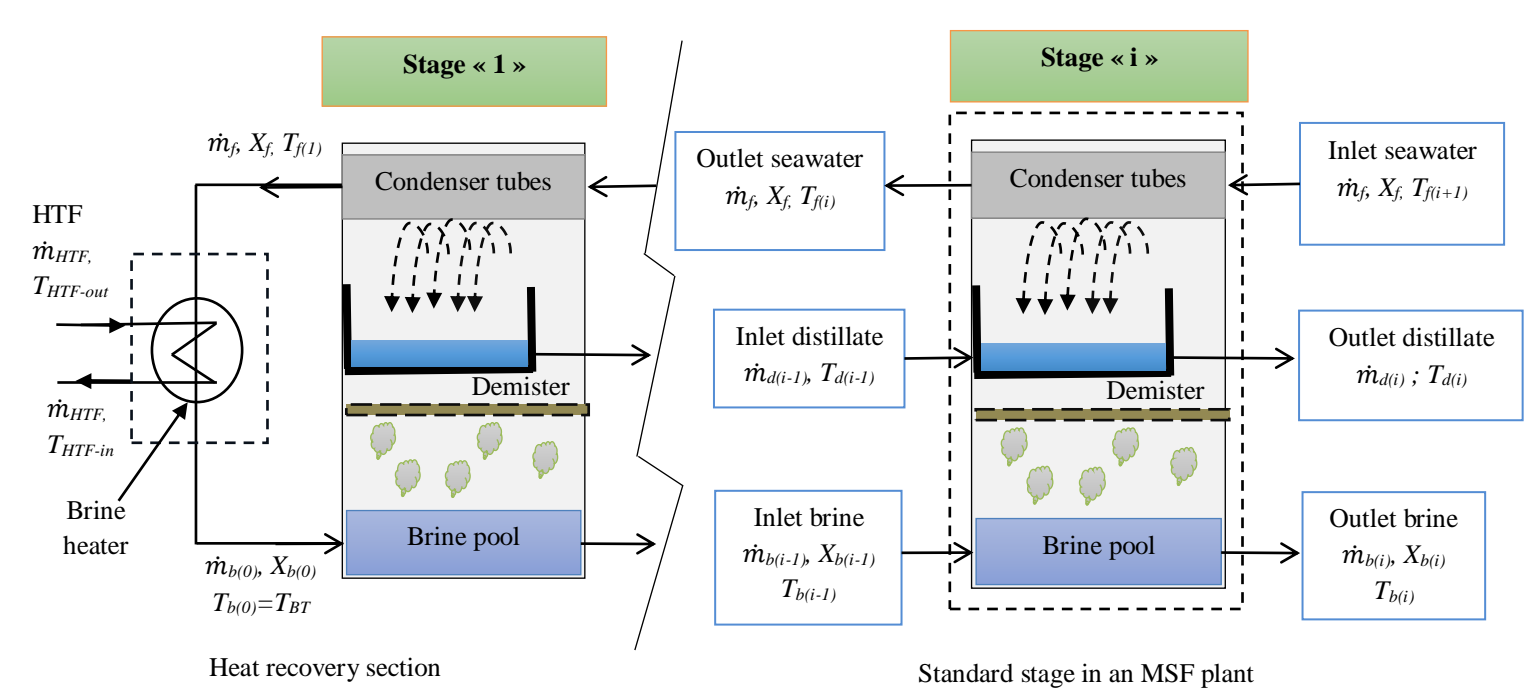


Fig.3. 13. Schematic overview of the brine heater and a stage in an MSF-OT plant.

As depicted in the heat recovery section of Fig. 3.13, the useful sensible heat energy (\dot{Q}_f) transferred from the solar field to raise the brine temperature is determined using Eq. (28). In this equation, \dot{m}_f represents the mass flow rate of the feed seawater, while $Cp(T_f)$ denotes its specific heat capacity at constant pressure, which varies with temperature. The term $T_{b(0)}$ corresponds to the brine temperature entering the first chamber of the MSF-OT, also known

as the top brine temperature (T_{BT}), whereas $T_{f(I)}$ represents the temperature of the feed water after exiting the condenser in the first chamber.

$$\dot{Q}_f = \dot{m}_f \cdot Cp(T_f) \cdot \left(T_{b(0)} - T_{f(1)}\right) \tag{28}$$

Since the feedwater mass flow rate and salt concentration remain constant throughout the brine heater (i.e., $\dot{m}_f = \dot{m}_{b(0)}$ and $X_f = X_{b(0)}$), the heat transfer balance is defined in Eq. (29). The equation's right-hand side represents the thermal energy absorbed by the heat transfer fluid (HTF), with *HTF-out* and *HTF-in* indicating its exit and entry temperatures, respectively. The subscript *BT* designates the top brine temperature.

$$\dot{m}_f \cdot (Cp(T_{BT}).T_{BT} - Cp(T_{f(1)}).T_{f(1)}) = \dot{m}_{HTF} \cdot (Cp(T_{HTF-out}).T_{HTF-out} - Cp(T_{HTF-in}).T_{HTF-in})$$
(29)

To evaluate the heat transfer in the brine heater, Eq. (30) is applied, incorporating the overall heat transfer coefficient (U_{BH}), the heat transfer area (A_{BH}), and the logarithmic mean temperature difference ((LMTD)_{BH}) as defined in Eq. (31). These parameters specifically correspond to the brine heater unit, denoted by the subscript BH.

$$\dot{m}_{HTF} \cdot (\mathcal{C}p(T_{HTF-out}).T_{HTF-out} - \mathcal{C}p(T_{HTF-in}).T_{HTF-in}) = U_{BH} \cdot A_{BH} \cdot (LMTD)_{BH}$$
 (30)

$$(LMTD)_{BH} = \frac{\left[(T_{HTF-out} - T_{BT}) - (T_{HTF-out} - T_{f(1)}) \right]}{\ln \left(\frac{T_{HTF-out} - T_{BT}}{T_{HTF-out} - T_{f(1)}} \right)}$$
(31)

Flash evaporation in MSF desalination begins when a supercooled liquid is heated to its saturation temperature at a given pressure. Once this temperature is reached, further heating induces vaporization, while the remaining brine flows into successive lower-pressure stages. The pressure gradient enables the movement of both brine and freshwater without requiring a pump. The brine mass flow rate in each stage is determined by Eq. (32), where $\dot{m}_{b(i)}$ represents the brine flow rate at the i^{th} stage. The stages are sequentially numbered from 1 to n, representing the total number of stages in the MSF system.

$$\dot{m}_{b(i)} = \dot{m}_{b(i-1)} - \dot{m}_{b(i-1)} \cdot y_{(i)} \tag{32}$$

At each stage *i*, the parameter $y_{(i)}$ quantifies the ratio of sensible heat to latent heat and is determined using Eq. (33). This calculation incorporates λ_{ν} , the latent heat of vaporization, which depends on temperature, and $\Delta T_{st(i)}$, the corresponding temperature drop.

$$y_{(i)} = \frac{c_{p(T_f)} \cdot \Delta T_{st(i)}}{\lambda_{\nu}(T_{\nu})} \tag{33}$$

3.4.1.1. Brine Flow Rate

The brine flow rate within each stage's brine pool is a key parameter that is adjusted in the process. In conventional MSF-OT, the model defines the mass flow rate balance within the flash chamber based on Eq. (34), as depicted in Fig. 3.14, while excluding the red isolated tubes. The term $\dot{m}_{d(i)}$ represents the distillate mass flow rate at the i^{th} stage.

$$\dot{m}_{b(i)} = \dot{m}_{b(i-1)} - \dot{m}_{d(i)} \tag{34}$$

The proposed system includes additional insulated piping at each stage to maintain a stable brine flow rate by compensating for evaporative losses and minimizing sensible heat dissipation. It is assumed that heat losses through the insulated tubes are negligible. This configuration maintains a consistent brine flow across all stages, as depicted in Fig. 3.14, where the added red tubes highlight the modifications.

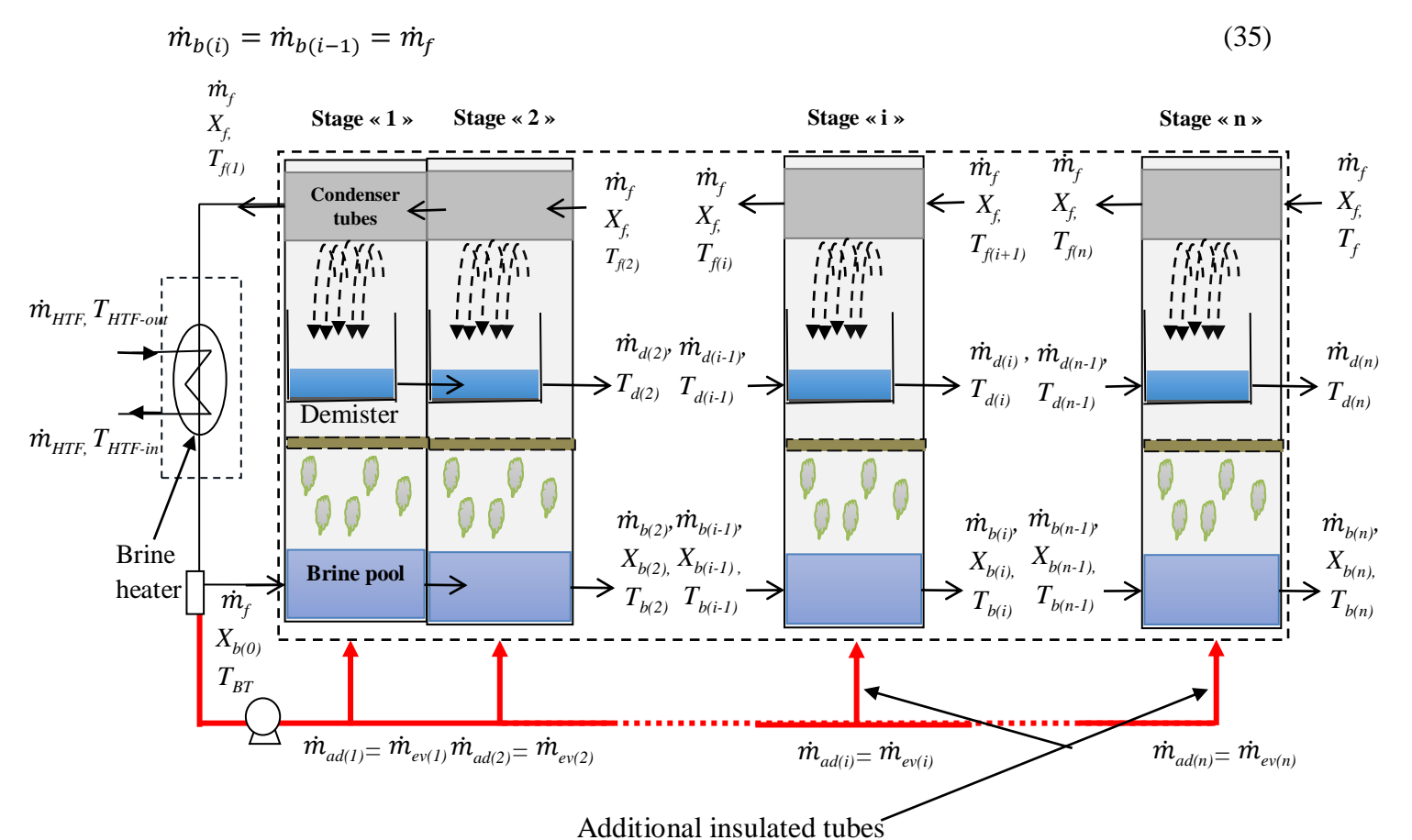


Fig.3. 14. Flow, Temperature, and Concentration distribution in the MSF-OT plant.

In conventional MSF-OT, the temperature difference ΔT_{st} is defined as:

$$\Delta T_{st(i)} = T_{b(i-1)} - T_{b(i)} \tag{36}$$

In contrast, the proposed design assumes a constant ΔT_{st} across all stages, calculated using the formula:

$$\Delta T_{st} = \frac{(T_{BT} - T_n)}{n} \tag{37}$$

Eq. (38) defines the salinity balance at each stage, taking into account the mass flow rates of both the inlet and outlet brine, as well as their respective salt concentrations.

$$X_{b(i)} \times \dot{m}_{b(i)} = X_{b(i-1)} \times \dot{m}_{b(i-1)} \tag{38}$$

3.4.2. Mass Flow Rate of Fresh Water Production

Freshwater is produced at each stage of the MSF desalination process through the conversion of the brine's sensible heat into latent heat during evaporation, assuming it equals

the latent heat released during condensation. The volume of distillate generated at each stage is then calculated using Eq. (39).

$$\dot{m}_{d(i)} = \dot{m}_{b(i-1)} \cdot y_{(i)} \tag{39}$$

The total distillate mass flow rate of the plant, represented as \dot{m}_D , is calculated by summing the distillate mass flow rates from all stages. This cumulative value represents the overall distillate output, reflecting the combined contributions from each stage in the desalination process, as outlined in Eq. (40).

$$\dot{m}_D = \sum_{i=1}^n \dot{m}_{d(i)} \tag{40}$$

Eq. (41) describes the energy balance at each i^{th} stage, where the subscripts "in" and "out" denote the respective quantities at the inlet and outlet. This equation accounts for the energy entering and leaving the system at each stage, ensuring the conservation of energy throughout the desalination process.

$$\dot{m}_{f,in} \cdot Cp(T_{f,in}) \cdot T_{f,in} + \dot{m}_{b,in} \cdot Cp(T_{b,in}) \cdot T_{b,in} - \dot{m}_{f,out} \cdot Cp(T_{f,out}) \cdot T_{f,out} - \dot{m}_{b,out} \cdot Cp(T_{b,out}) \cdot T_{b,out} - \dot{m}_{d} \cdot Cp(T_{d}) \cdot T_{d} = 0$$

$$(41)$$

3.4.3. Temperature Profile Correlations

This subsection presents the temperature correlations used to model heat transfer across the stages of the MSF-OT process. These correlations are essential for predicting temperature variations at each stage.

Eq. (42) is used to determine the feed water temperature $(T_{f(i)})$. This calculation relies on the temperature increase $(\Delta T_{f(i)})$ in the condenser tube, which is influenced by the heat exchange from the preceding stages of the process, as explained in Eq. (43).

$$T_{f(i)} = T_f + \sum_{i=1}^n \Delta T_{f(i)}$$
 (42)

$$\Delta T_{f(i)} = T_{f(i)} - T_{f(i+1)} \tag{43}$$

The brine temperature in stage i, as defined by Eq. (44), is influenced by $\Delta T_{st(i)}$, which represents the temperature drop within the stage.

$$T_{b(i)} = T_{BT} - \sum_{i=1}^{n} \Delta T_{st(i)}$$
 (44)

The vapor release temperature, $T_{v(i)}$, is determined by Eq. (45) and is influenced by the brine temperature ($T_{b(i)}$), along with the boiling temperature elevation (BTE) and the non-equilibrium allowance (NEA). BTE represents the increase in the boiling temperature of a pure liquid due to dissolved substances, such as salts in seawater, under a given pressure [202]. NEA, on the other hand, accounts for deviations from thermodynamic equilibrium during the flashing process. It is defined as the temperature difference between the brine pool and the flashed-off vapor, specifically the difference between the average outlet temperature of the evaporator and the vapor temperature [203, 204]. The corresponding equations for BTE and NEA are provided in Appendix A.

$$T_{v(i)} = T_{b(i)} - BTE_{(i)} - NEA_{(i)}$$
(45)

The distillate temperature, $T_{d(i)}$, drops below the vapor temperature at the demister outlet due to friction and condensation losses. This behavior is modeled by Eq. (46), where $\Delta T_{fr(i)}$ and $\Delta T_{c(i)}$ represent frictional and condensation losses around the condenser tube bundle, respectively. However, in this study, both effects are assumed to be negligible and are therefore not considered. The term $\Delta T_{Dp(i)}$ represents the temperature drop resulting from the pressure loss across the demister. This pressure loss and the associated temperature reduction, calculated using the well-established Antoine equation, are determined through the relations presented in Appendix A.

$$T_{d(i)} = T_{v(i)} - \Delta T_{Dp(i)} - \Delta T_{fr(i)} - \Delta T_{c(i)}$$
(46)

3.4.4. Fundamental Parameters for MSF Evaluation

In MSF desalination, several parameters are essential for evaluating system efficiency and operational performance. These metrics provide a detailed understanding of the system's thermal behavior and energy consumption, helping assess its overall functionality. The key parameters include:

• Gain Output Ratio (GOR)

The GOR is a key performance metric for evaluating thermal desalination efficiency, particularly in multi-stage and multi-effect systems. Defined as the ratio of distillate mass flow (\dot{m}_D) to heating fluid mass flow (\dot{m}_s), as given in Eq. (47), a higher GOR indicates improved water production per unit of heat input. However, it is constrained by the number of effects and influenced by factors such as heat transfer efficiency, energy losses, and system design [204].

$$GOR = \frac{\dot{m}_D}{\dot{m}_S} \tag{47}$$

• Recovery Ratio (RR)

The Water Recovery Ratio quantifies the efficiency of a desalination system by measuring the fraction of feed seawater converted into fresh water. An increased RR signifies improved system effectiveness, maximizing freshwater yield from the available intake. It is expressed as [205]:

$$RR = \frac{\dot{m}_D}{\dot{m}_f} \tag{48}$$

• Specific Thermal Energy Consumption (STEC)

The STEC is another critical parameter for assessing the thermal efficiency of an MSF system. It is determined, as shown in Eq. (49), by the ratio of thermal energy supplied to the mass flow rate of the produced distillate (kJ/kg). A lower STEC reflects better energy efficiency, resulting in cost savings [206].

$$STEC = \frac{P_{th,field}}{\dot{m}_D} \tag{49}$$

4.5. Conclusion

This chapter outlined the modeling of a solar desalination system that integrates Linear Fresnel Collectors with Multi-Stage Flash desalination. It covered the key system parameters, operational conditions, and introduced a modified MSF design aimed at improving performance. By varying these parameters, a deeper understanding of how to further develop and optimize the system is gained. Therefore, the next chapter will present the results of the parametric analysis and explore their implications for system performance.

Chapter 4: Parametric Analysis Results

4.1. Introduction

This chapter aims to analyze the performance of the LFC-MSF desalination system by examining key influencing factors. It is structured into three main sections:

The first section investigates the impact of LFC parameters on system efficiency. This includes an assessment of weather conditions, solar irradiation, geometric configurations, and the angle of incidence on energy capture and thermal performance.

The second section focuses on the MSF operational parameters, exploring how variations in flow rates, top brine temperature, and the number of stages affect energy consumption, mass and heat transfer, flashing dynamics, and overall water production.

The third section evaluates the influence of site-specific conditions by analyzing the implementation of the LFC-MSF system in three coastal regions of Algeria. This comparative study examines the effects of climatic variations, including solar radiation availability, cloud cover, and ambient temperature, on system efficiency and feasibility.

4.2. Influence of LFC Parameters

The performance of an LFC-based desalination system relies on key parameters such as mirror arrangement, receiver design, optical efficiency, operating temperature, weather conditions, and solar irradiation. These factors play a crucial role in solar energy capture, flux distribution, heat transfer efficiency, and freshwater production, directly impacting the system's reliability and output.

4.2.1. Impact of Weather Conditions and Solar Irradiation

4.2.1.1. Impact of Solar Irradiation on Flux Distribution

To evaluate the impact of solar irradiation on flux distribution and thermal energy absorption, the configuration was simulated at key time points:

- Winter (December 17th)
- Equinox (March 21st / September 22nd)
- Summer (June 2nd)

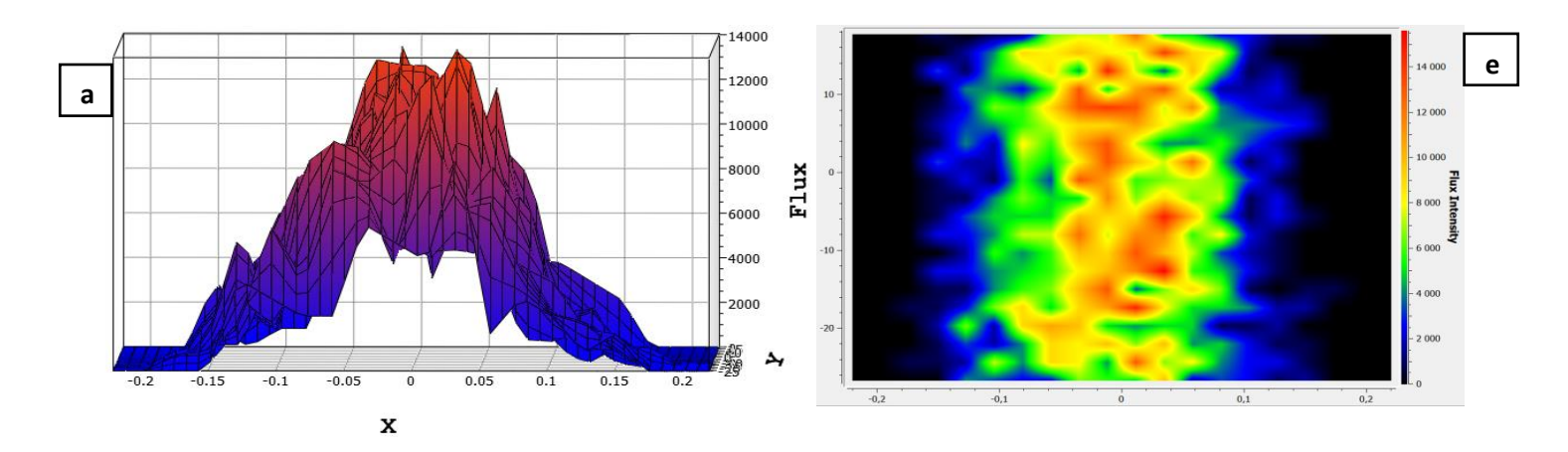
These simulation dates were chosen to analyze the LFC prototype's performance variations both over a single day and throughout an entire year, using solar noon as a reference point for comparison. For each simulation, a solar flux distribution map within the absorber tube was generated using SolTrace software, providing critical insights into the intensity and uniformity of incident radiation on the receiver. This directly influences heat transfer efficiency, thermal energy absorption, and overall system performance. The following

analysis, based on these flux distribution results, provides a comprehensive assessment of the LFC's optical and thermal behavior under varying solar conditions.

The DNI values that were used to simulate the solar flux distribution on the receiver were taken from PVGIS-SARAH-2 Solar Radiation Database [190]. The obtained DNI values follow a clear seasonal trend, reaching a maximum of 944.1 W/m² during the summer and a minimum of 644 W/m² during the winter. March 21 and September 22 show intermediate values of 833.2 W/m² and 806.5 W/m², respectively. This variation is directly influenced by the solar altitude angle, which determines the intensity of incident radiation. A higher solar elevation in summer results in increased DNI, whereas a lower altitude in winter reduces DNI due to an extended atmospheric path length.

Figs. 4.1 (a–d) illustrate the solar flux distribution on the receiver for four key seasonal dates. These figures demonstrate how variations in DNI affect the intensity and uniformity of energy concentration on the receiver. The summer period (Fig. 4.1d) exhibits the most intense and concentrated flux due to the high solar altitude and reduced optical losses. Conversely, the winter period (Fig. 4.1a) presents a more diffused energy profile with lower peak flux values, attributed to increased atmospheric attenuation and a wider dispersion of incident rays. The mid-season days, such as March 21 and September 22 (Figs. 4.1b and 4.1c), display an intermediate flux pattern, representing a transition between the two seasonal extremes. Although their DNI values are lower than in summer, the flux distribution remains relatively stable, ensuring moderate yet consistent solar energy availability.

The four contour plots (Figs. 4.1e–4.1h) illustrate a rapid increase in flux intensity in the intermediate region of the absorber tube, gradually decreasing toward both sides. This distribution enhances heat absorption in the central region, while the lower flux at the edges may contribute to thermal losses. The non-uniform flux distribution is primarily influenced by the optical configuration of the linear Fresnel reflector and the incidence angle of incoming radiation. This pattern leads to a localized concentration of energy, which can improve overall thermal performance but may also necessitate careful thermal management to mitigate excessive temperature gradients within the absorber tube.



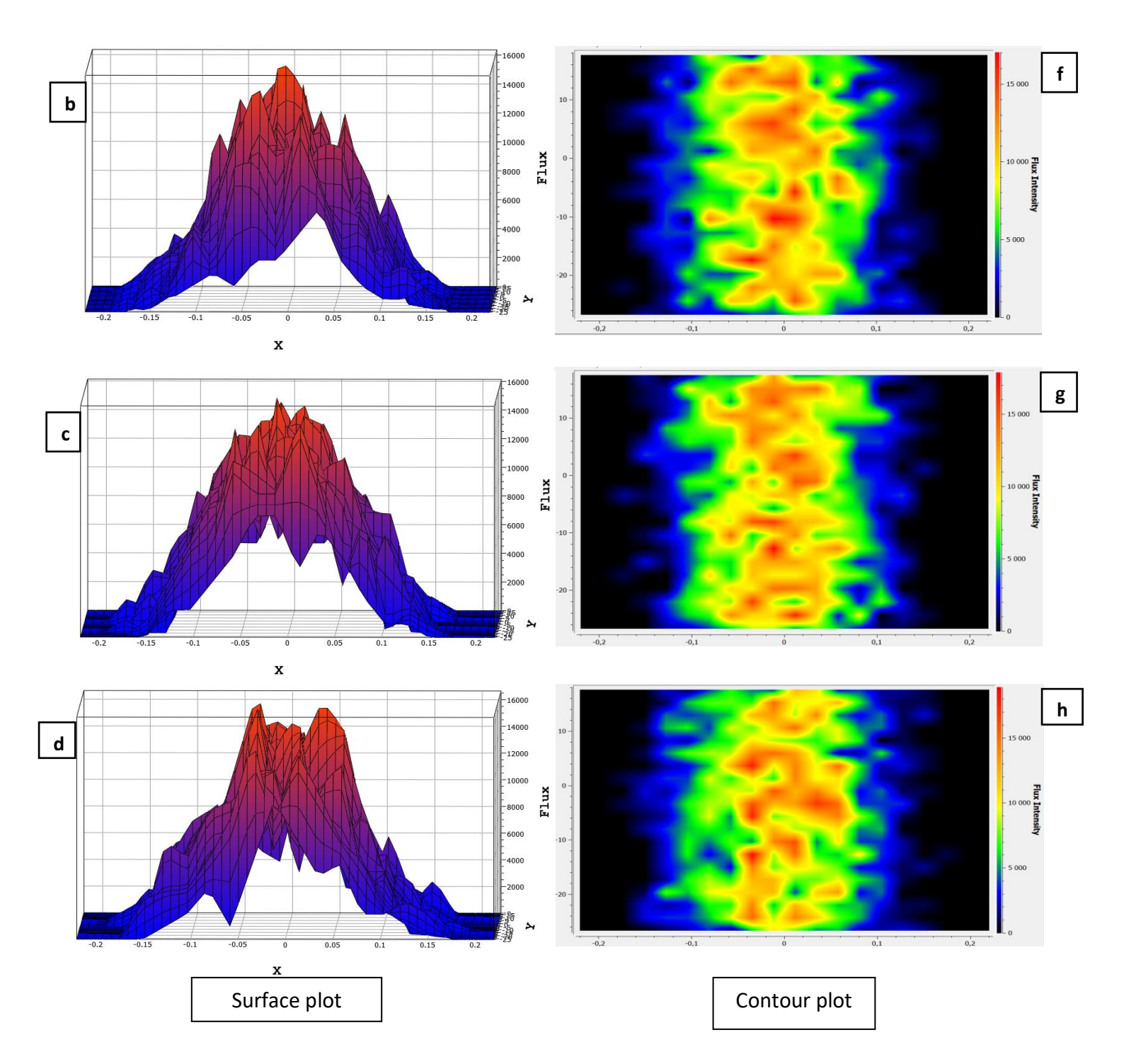


Fig.4. 1. Incident solar flux distribution on the receiver for different seasonal conditions. (a,e) Winter period (December 21), (b,f) Spring equinox (March 21), (c,g) Autumn equinox (September 21), and (d,h) Summer period (June 21).

Table 4.1 provides a comprehensive overview of key solar energy parameters across different seasons. It highlights seasonal variations in DNI, solar flux distribution, and performance metrics critical for solar thermal applications. The analysis includes DNI variability, the number of sun rays, power per ray, peak flux, uncertainty factors, and flux uniformity.

The number of sun rays captured by the system varies slightly across seasons, reaching 57,611 in summer and decreasing to 56,944 in winter, while the power per ray increases significantly from 39.66 W in winter to 45.82 W in summer due to higher solar radiation

intensity. Peak solar flux follows a similar trend, with the highest value of $16,034.6 \text{ W/m}^2$ in summer and the lowest at $13,250.3 \text{ W/m}^2$ in winter, with the equinoxes falling within an intermediate range. Although a higher peak flux enhances thermal energy absorption, it also introduces challenges such as thermal stress and material degradation, highlighting the need for effective thermal management strategies. The uncertainty in peak flux estimates ranges from $\pm 22.36\%$ to $\pm 23.57\%$, with the highest variation in autumn, likely due to atmospheric fluctuations and measurement uncertainties, while the average flux uncertainty remains low ($\pm 0.69\%$), ensuring reliable estimations. Flux uniformity values (1.09-1.11) indicate efficient energy distribution, with improved concentration in summer and the equinoxes, whereas winter exhibits minor deviations.

Table 4. 1. Seasonal Analysis of Solar Flux and Performance Parameters.

	Winter period (December 17)	Spring Equinox (March 21)	Autumn Equinox (September 22)	Summer period (June 2)
Day N°	351	80	265	153
DNI (W/m ²)	644	833.2	806.5	944.1
Sun ray count	56944	57548	57232	57611
Power per ray (W)	39.66	43.73	43.97	45.82
Peak flux (W/m ²)	13250.3	15030.6	14377.0	16034.6
Peak flux uncertainty (%)	+/- 22.36	+/- 22.94	+/- 23.57	+/- 22.36
Avg. Flux (W/m ²)	3597.41	3865.50	3941.84	4170.97
Avg. flux uncertainty (%)	+/- 0.69	+/- 0.69	+/- 0.69	+/- 0.69
Uniformity	1.09	1.11	1.10	1.11

This analysis highlights the significant impact of seasonal variations on DNI, solar flux distribution, and power per ray, with summer providing the highest energy potential for solar thermal applications. The consistent flux uniformity across seasons ensures stable optical performance. However, the increased thermal stress during peak summer flux and the reduced DNI in winter must be carefully considered in the design of solar desalination systems.

The DNI value can also vary throughout the day due to changes in the sun's position, which influence atmospheric interference and the angle at which solar rays reach the Earth's surface. The following results analyze the DNI on a chosen day (June 2) at different times (6 AM, 12 PM, and 6 PM) to evaluate its daily impact on solar energy capture and utilization (the incident solar flux maps are presented in Appendix B).

The results in Table 4.2 show that DNI fluctuates significantly throughout the day, reaching its highest value at noon (944.1 W/m²) and decreasing during the morning (6 AM) (628W/m²) and evening (6 PM) (650 W/m²). This variation directly impacts the sun ray count, which

follows a similar trend, peaking at midday (57,611 rays). Since the power per ray also reaches its maximum at 12 PM (45.82 W), this confirms that solar intensity is at its highest around noon.

For LFCs, the peak flux follows the DNI trend, rising from 12,058.1 W/m² in the morning to a maximum of 16,034.6 W/m² at noon before slightly decreasing to 14,628.7 W/m² in the evening. Similarly, the average flux reaches its highest value at midday (4,170.97 W/m²), highlighting the strong influence of solar position on energy concentration. Despite these variations, the flux uniformity (1.08–1.11) remains stable, ensuring a consistent distribution of solar energy throughout the day

Day		2 nd June	
Day time	6 AM	12 PM	6 PM
DNI (W/m ²)	628	944.1	650
Sun ray count	56248	57611	56890
Power per ray (W)	32.66	45.82	32.30
Peak flux (W/m ²)	12058.1	16034.6	14628.7
Peak flux uncertainty (%)	+/- 23.57	+/- 22.36	+/- 21.32
Avg. Flux (W/m ²)	2927.45	4170.97	2983.93
Avg. flux uncertainty (%)	+/- 0.69	+/- 0.69	+/- 0.69
Uniformity	1.08	1.11	1.10

Table 4. 2. Seasonal analysis of solar flux and performance parameters.

Daily variations in DNI, solar flux, and power per ray strongly influence LFC performance, peaking at noon when energy capture is maximized. Throughout the day, peak flux uncertainty decreases ($\pm 23.57\%$ to $\pm 21.32\%$), indicating greater stability, while the constant average flux uncertainty ($\pm 0.69\%$) ensures reliable and consistent measurements.

4.2.1.2. Impact of Cloud Cover and Atmospheric Conditions

Direct Normal Irradiance varies with atmospheric conditions, significantly influencing the performance of LFCs, which rely on direct sunlight to concentrate energy efficiently. Solar radiation data from TMY weather files, provided by the PVGIS-SARAH-2 Solar Radiation Database [190], are used to identify clear and cloudy days in Algiers city. Fig.4.2 variation of under conditions. illustrates the daily DNI these On a clear day, DNI follows a smooth curve, peaking around solar noon. However, on a cloudy day, DNI remains zero for most of the day, with only three recorded values: 200 W/m² at 8:00, 50 W/m² at 12:00, and 100 W/m² at 14:00, indicating heavy cloud cover with brief sunlight penetration.

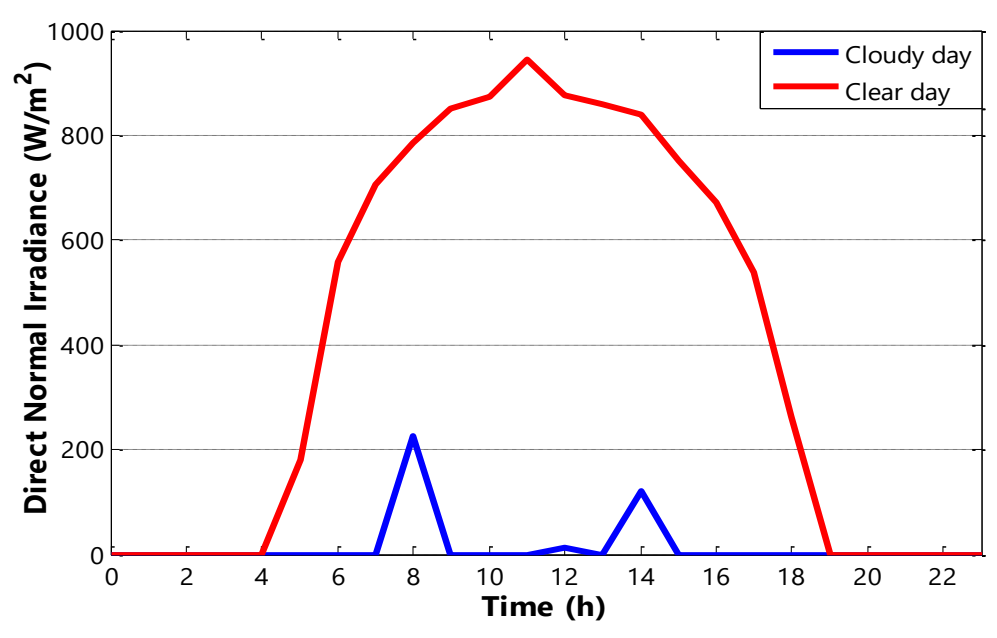


Fig.4. 2. Daily variation of DNI under clear and cloudy conditions in Algiers city.

The following graph illustrates the impact of cloud cover on the efficiency of LFCs, which, in turn, affects the overall performance of the desalination system. Fig. 4.3 clearly demonstrates that as cloud cover increases, the efficiency of the LFC system decreases. Under clear skies (0% cloud cover), the system operates at maximum efficiency, corresponding to the clear day selected above. However, as cloud cover increases, the amount of DNI reaching the system declines, leading to a reduction in efficiency. This decrease in DNI becomes more pronounced with increasing cloud cover, and at 100% cloud cover, the system's efficiency is significantly diminished. This behavior underscores the LFC's dependence on direct sunlight and its reduced capability to capture energy under cloudy conditions.

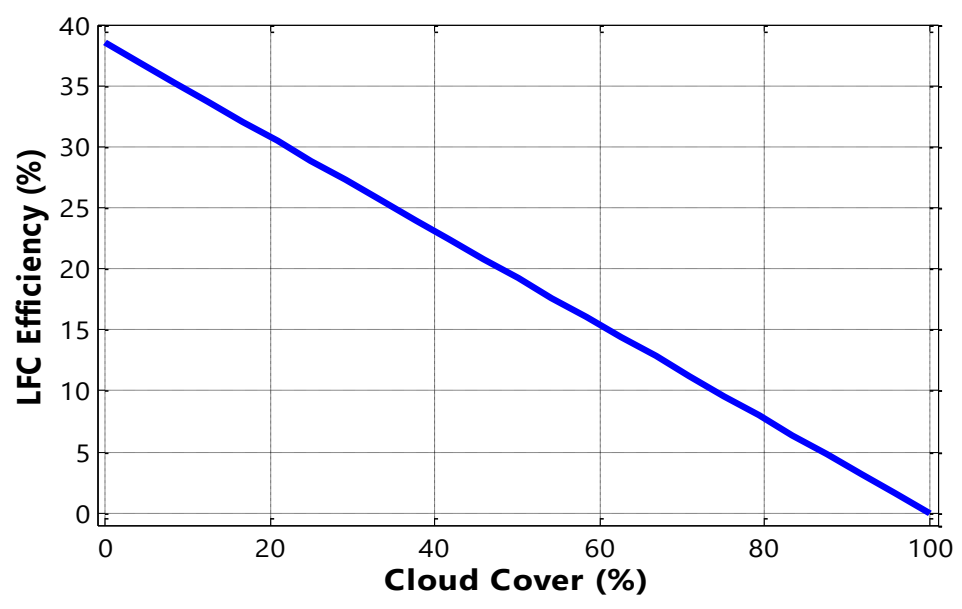


Fig.4. 3. Impact of cloud cover on the efficiency of linear Fresnel collectors (LFCs).

Fig. 4.4 illustrates the influence of DNI on system performance. At low radiation levels (200 W/m²), thermal energy generation and freshwater production decline considerably, reducing efficiency and highlighting the need for backup energy sources or thermal storage. As DNI increases to moderate levels (500 W/m²), the system operates more efficiently,

maintaining stable performance under typical solar conditions. At high radiation levels (900 W/m^2), both thermal and freshwater outputs reach their highest levels, showcasing the system's maximum efficiency and performance under ideal conditions.

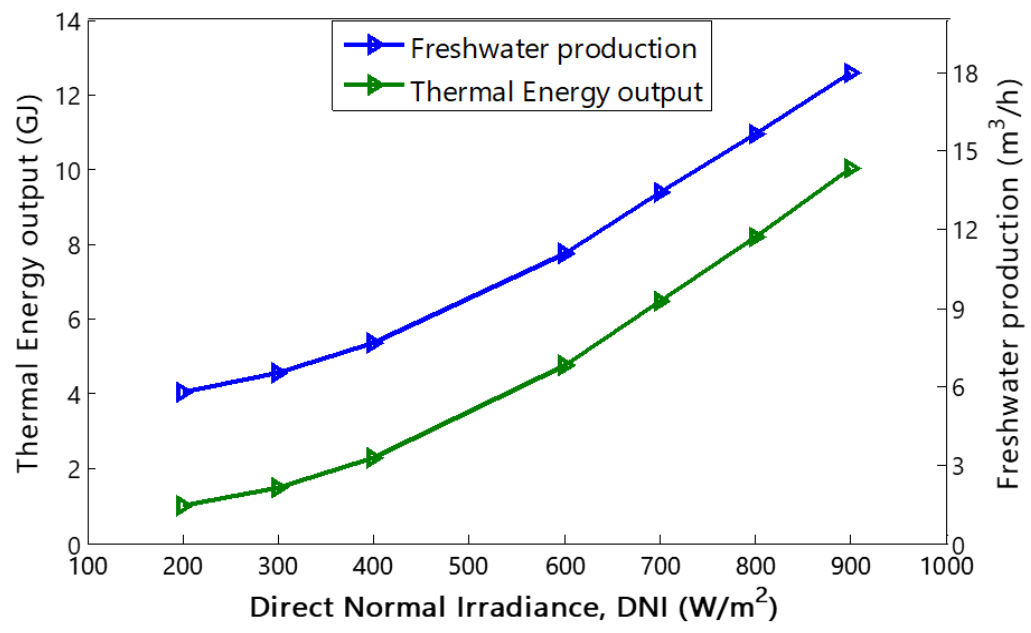


Fig.4. 4. Impact of solar radiation on the performance of the proposed MSF-OT system configuration.

4.2.1.3. Impact of Ambient Temperature on Thermal Losses

The thermal performance of the studied receiver (Schott PTR) is strongly influenced by ambient temperature. Fig. 4.5 illustrates how heat losses and efficiency evolve as the ambient temperature increases from 10°C to 50°C, while maintaining a fixed absorber temperature of 140°C. An increase in ambient temperature reduces the temperature gradient between the absorber and its surroundings, thereby lowering convective and radiative heat losses. This reduction in thermal dissipation allows the receiver to retain more absorbed energy, achieving an efficiency of around 34.39% at 50°C.

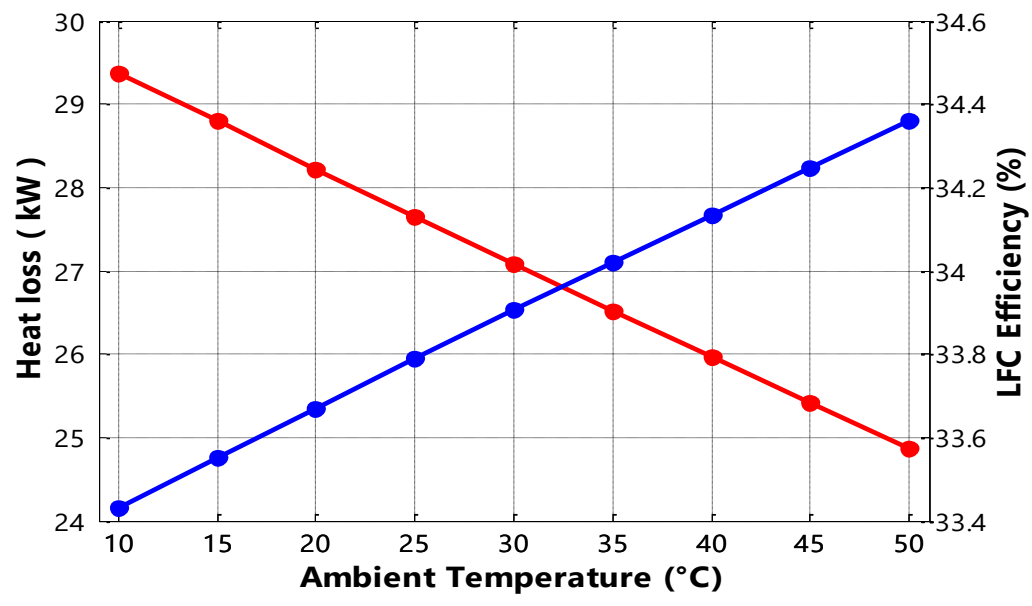


Fig.4. 5. Impact of ambient temperature on heat loss and LFC efficiency.

4.2.2. Geometric Effects

The receiver height and number of collectors play a crucial role in the thermal performance of an LFC system. The receiver height influences optical efficiency, while the number of collectors determines solar energy absorption. However, too many collectors can lead to shading effects and end losses, reducing overall efficiency. A balanced design is essential for effective energy conversion and improved desalination performance.

As shown in Fig. 4.6, increasing the receiver height results in a decline in thermal energy output due to higher optical and convective losses. Greater heights lead to beam divergence and increased wind exposure, reducing the amount of absorbed solar energy. While radiative losses remain relatively constant, the decrease in thermal energy affects desalination efficiency, limiting evaporation rates and freshwater production.

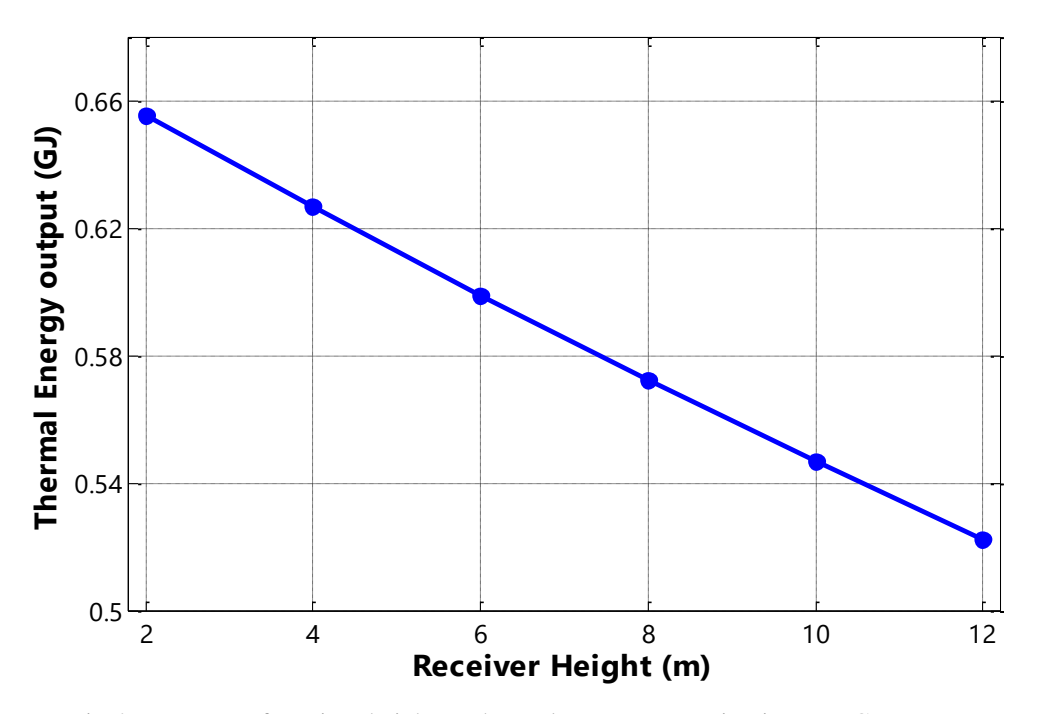


Fig.4. 6. Impact of receiver height on thermal energy generation in an LFC system.

Fig. 4.7 shows that increasing the number of collectors in an LFC system leads to a proportional rise in thermal energy output, indicating a linear relationship between these parameters. Each additional collector contributes to improved energy absorption and conversion, enhancing overall system performance. This rise in thermal energy directly benefits desalination efficiency by increasing energy availability, which enhances the evaporation rate and boosts freshwater production in MSF desalination systems.

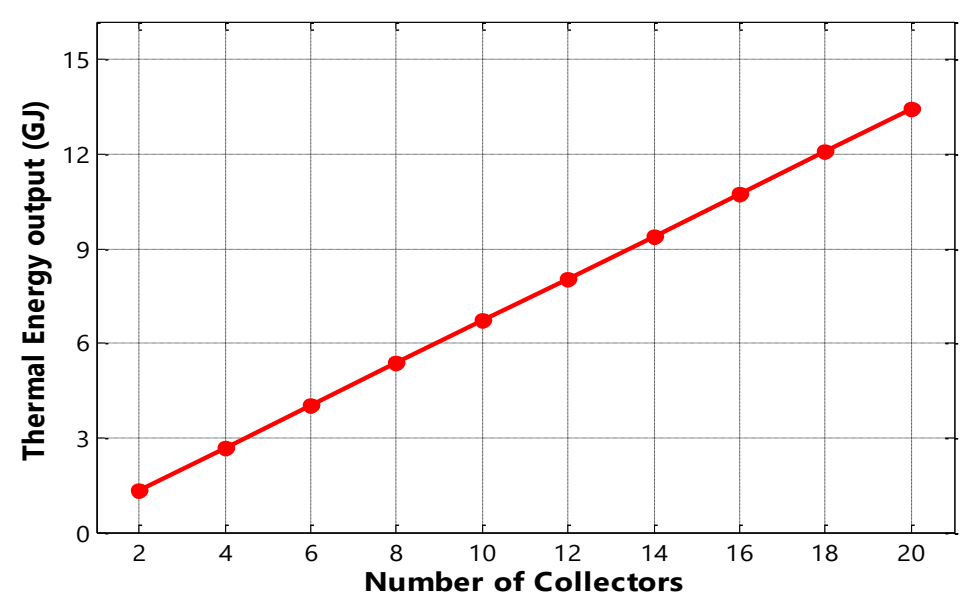


Fig.4. 7. Impact of collector number on thermal energy generation in an LFC system.

However, beyond a certain number of collectors, factors such as geometric losses, and thermal dissipation may introduce non-linearity, affecting overall efficiency. Fig. 4.8 illustrates the impact of geometric losses (shading and blocking) on LFC efficiency, represented by two distinct trends. The red line indicates shading losses, which reduce the amount of solar radiation reaching the receiver, while the black line represents blocking losses, which obstruct optimal light reflection onto the absorber. As these losses increase from 0% to 100%, the system's efficiency declines linearly from 50% to 0%. This decline highlights the importance of minimizing shading and blocking through improved mirror configurations and receiver positioning. Proper mirror spacing and receiver positioning help minimize these losses, ensuring a higher fraction of incident radiation reaches the absorber.

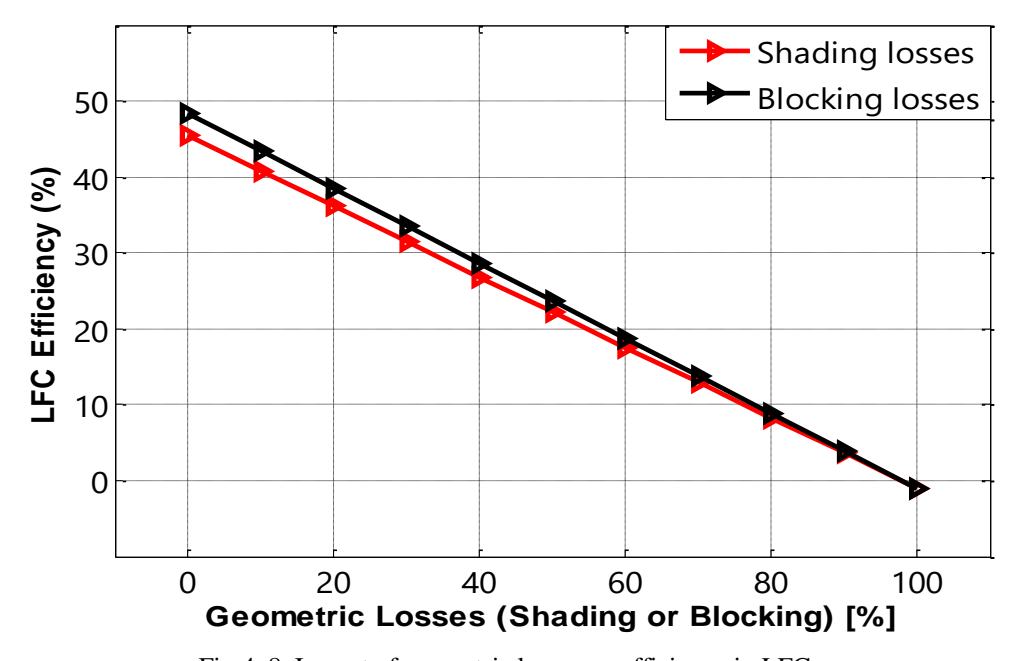


Fig.4. 8. Impact of geometric losses on efficiency in LFC.

4.2.3. Incidence Angle Modifier (IAM) Effect

Fig. 4.9 illustrates the effect of the incidence angle on the IAM and optical efficiency in LFC system. As the incidence angle increases from 0° to 90° , IAM declines due to higher reflection losses and reduced solar radiation absorption by the receiver.

The transversal IAM (black line) decreases gradually, as larger angles reduce the mirrors' ability to effectively direct sunlight onto the receiver, leading to uneven light concentration and lower energy capture. In contrast, the longitudinal IAM (red line) drops more significantly, primarily affecting the uniformity of sunlight distribution along the receiver's length. These differences highlight the sensitivity of LFC systems to angular variations, reinforcing the importance of advanced tracking mechanisms and precise optical alignment to minimize losses.

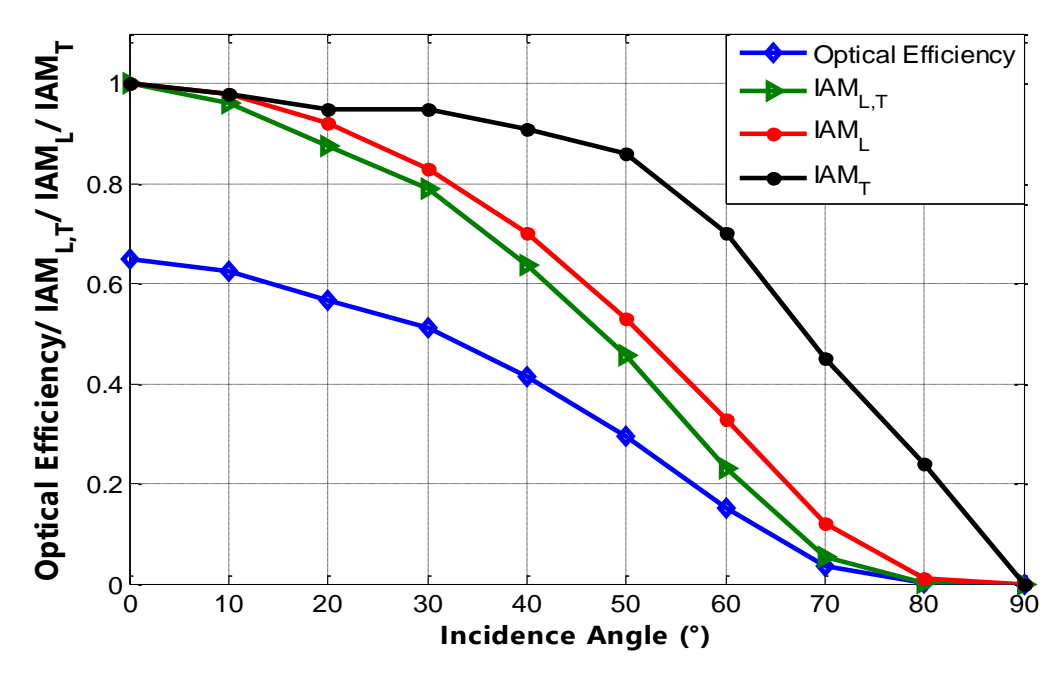


Fig.4. 9. Impact of incidence angle on IAM and optical efficiency in LFC.

4.2.4. Thermal Performance Parameters Effect

LFC thermal efficiency is influenced by several key parameters, including mass flow rate, receiver temperature, and other factors. Some of these parameters, such as solar radiation and ambient temperature, are introduced in the subsection above. These factors dictate how efficiently the system absorbs and transfers heat to the working fluid.

The effect of HTF mass flow rate on LFC thermal efficiency (Fig. 4.10) shows that efficiency increases as the flow rate rises. At low flow rates, the fluid remains in the absorber longer, causing higher heat losses and reducing efficiency. As the flow rate increases, heat transfer improves, enhancing performance. However, excessive increases in the HTF mass flow rate may lead to diminishing returns, as the fluid may not have sufficient time to absorb heat effectively. Additionally, pumping power requirements rise with higher flow rates, which can impact the overall system efficiency. Therefore, an optimal flow rate must be determined to balance thermal performance and energy consumption.

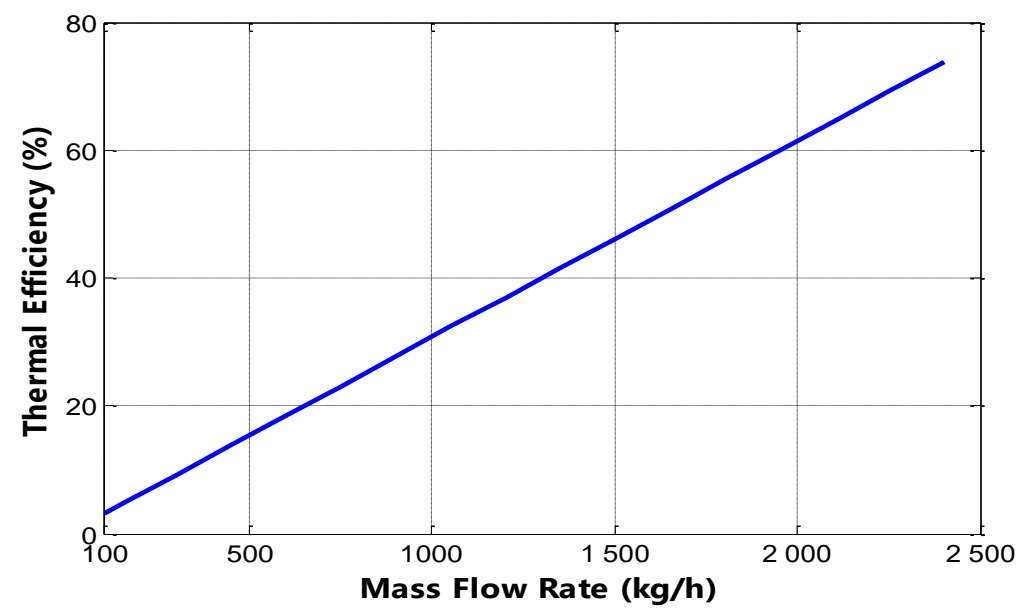


Fig.4. 10. Impact of HTF mass flow rate on LFC thermal efficiency.

The impact of receiver temperature on heat loss and efficiency is a key aspect of the system's thermal performance. As the temperature increases, radiative and convective losses intensify, leading to greater energy dissipation. Heat loss rises from 0.54 kW at 40°C to 8.57 kW at 200°C, while thermal efficiency declines from 64.56% to 61.84% (see Fig. 4.11). This decrease occurs because excessive heat loss reduces the net energy transferred to the working fluid. While higher temperatures enhance heat transfer, they also amplify energy losses, limiting efficiency gains. Therefore, maintaining an optimal receiver temperature is essential to balancing heat absorption and losses.

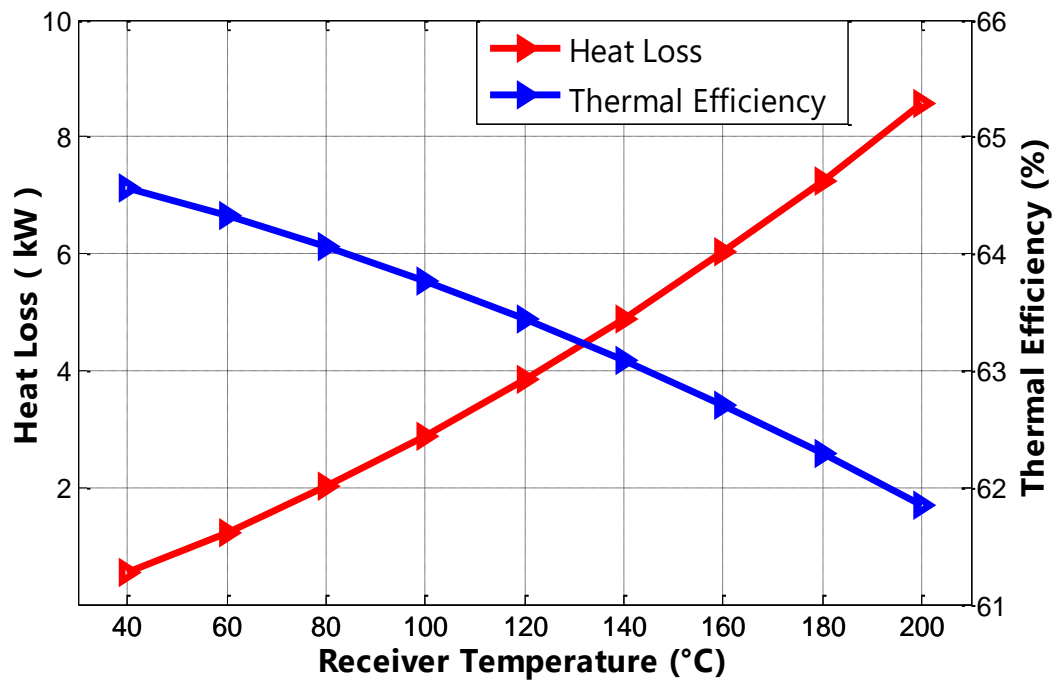


Fig.4. 11. Impact of receiver temperature on heat loss and LFC thermal efficiency.

4.3. Impact of MSF Operational Parameters

MSF desalination plant relies on critical operational parameters that impact freshwater yield and energy use. Assessing their influence helps enhance performance and develop strategies for higher output with lower energy demand. This section examines the impact of top brine temperature, number of flashing stages, and thermodynamic losses on system efficiency. It evaluates key performance indicators, including energy efficiency, heat transfer area, brine salinity. The analysis covers a temperature range of 85–110°C, stage variations from 10 to 30, and thermodynamic losses between 0.5 and 2°C to identify optimal operating conditions.

4.3.1. Performance & Energy Efficiency parameters effects

Fig. 4.12 illustrates the impact of thermal energy input on the desalination system's performance, particularly its effects on the Gain Output Ratio (GOR) and the Top Brine Temperature (TBT). As thermal energy input increases, GOR decreases, indicating a decline in energy efficiency. At 1.2 GJ, the GOR is approximately 4.4, but it drops to 1.3 at 4 GJ due to rising thermal losses. Meanwhile, TBT increases from 85.3°C at 1.2 GJ to 109.4°C at 4 GJ, which can lead to scaling, salt precipitation, and material degradation. These issues negatively impact system performance, increase maintenance costs, and reduce overall efficiency, highlighting the necessity of effective thermal energy management to ensure operational reliability and longevity.

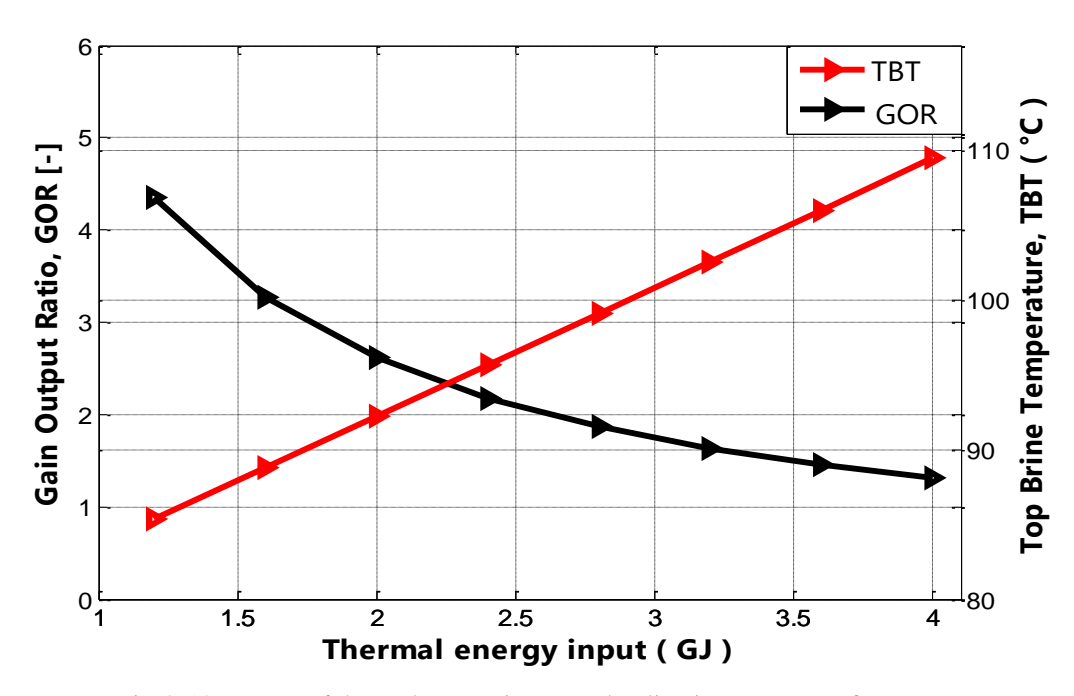


Fig.4. 12. Impact of thermal energy input on desalination system performance.

Recovery Ratio (RR) in desalination systems represents the fraction of feed water (M_f) converted into distilled water (M_d) [205]. As shown in Fig. 4.13, it decreases as feed water increases while distilled water remains constant. Conversely, for a fixed M_f , a higher M_d results in a greater RR, indicating improved water recovery. However, an excessive increase in RR can lead to a higher brine concentration, increasing the risks of scaling, corrosion, and

boiling temperature elevation (BTE), which negatively impact thermal efficiency and energy consumption.

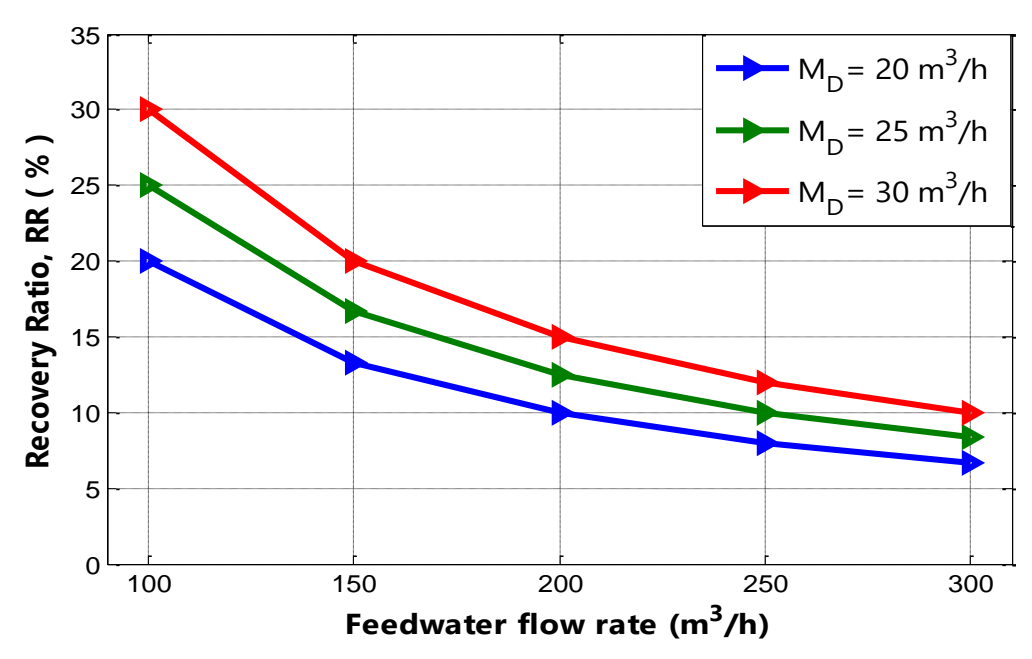


Fig.4. 13. Impact of feed water flow rate on recovery ratio in MSF desalination system.

Fig. 4.14 illustrates the relationship between Specific Thermal Energy Consumption (STEC) and distillate flow rate in a thermal desalination system. As the distillate flow rate increases from 15 m 3 /h to 40 m 3 /h, STEC decreases from 418 kWh/ m 3 to 157 kWh/m 3 , indicating improved energy efficiency. A lower STEC means less thermal energy is required per unit of freshwater, which enhances overall system performance. However, beyond 30 m 3 /h, the decline slows due to heat losses and operational limitations.

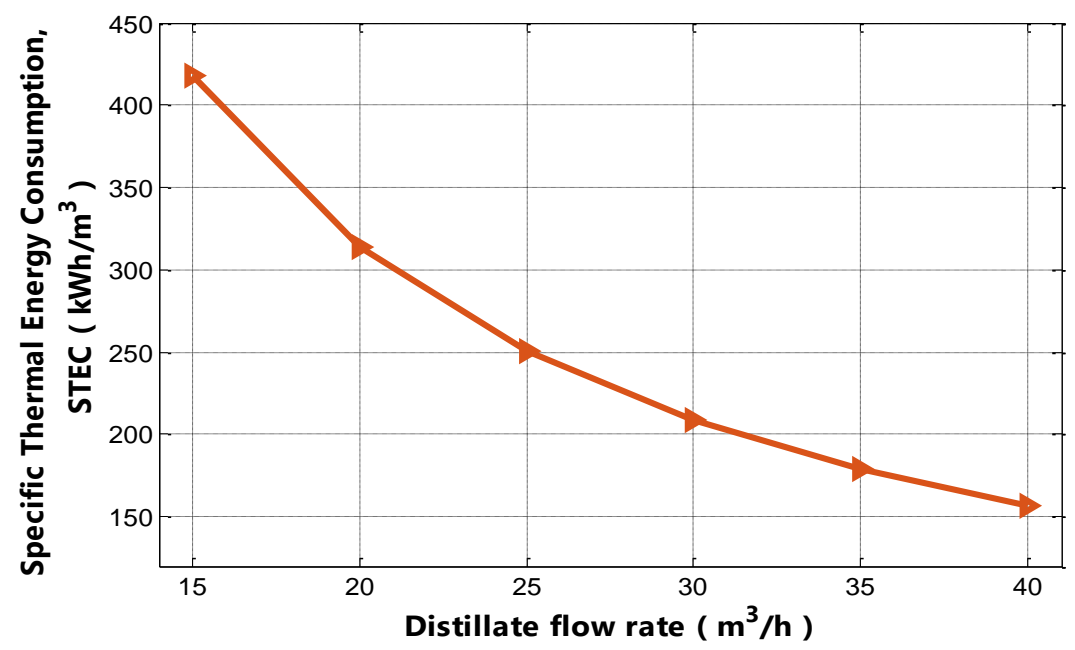


Fig.4. 14. Impact of distillate flow rate on specific thermal energy consumption (STEC).

4.3.2. Mass & Heat Transfer parameters effects

The graphs in Fig. 4.15 illustrate how increasing brine salinity negatively affects the evaporation rate. As salinity increases across the stages, boiling point elevation (BTE) reduces the available temperature gradient, leading to a decline in evaporation efficiency and freshwater production. Moreover, elevated salinity increases the risk of scaling and fouling, further compromising heat transfer and overall system performance.

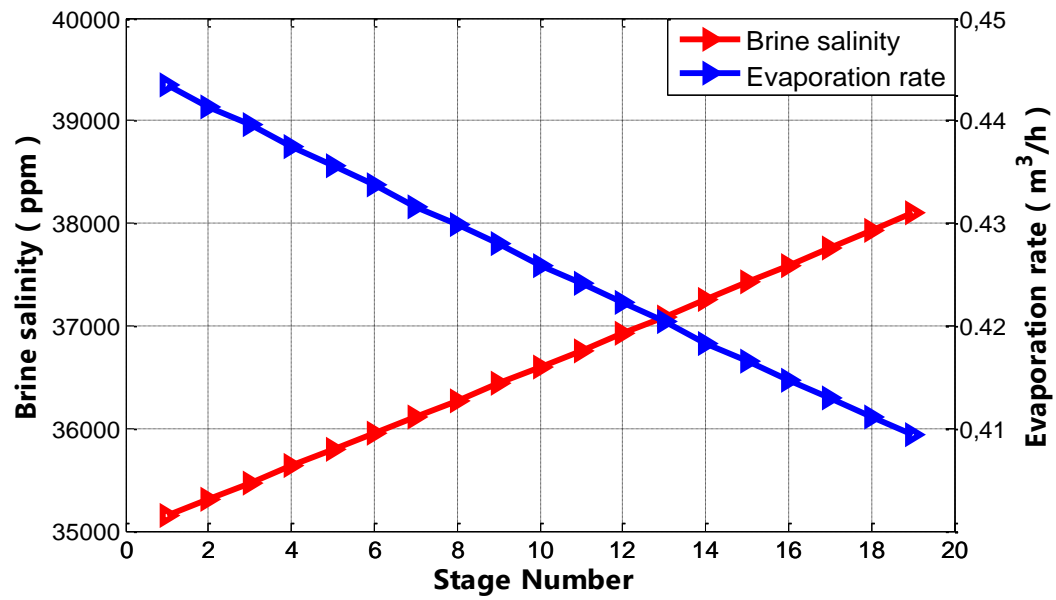


Fig.4. 15. Impact of brine salinity on evaporation rate across stages.

The relationship between specific heat transfer area, top brine temperature, and thermodynamic losses is illustrated in Fig. 4.16, showing that as the top brine temperature increases and thermodynamic losses decrease, the required heat transfer area reduces. This occurs because a higher temperature gradient enhances heat transfer efficiency, decreasing the surface area needed for effective thermal exchange. As further depicted, a reduction in thermodynamic losses leads to an increase in condensing vapor temperature, which amplifies the temperature driving force and further minimizes the heat transfer area.

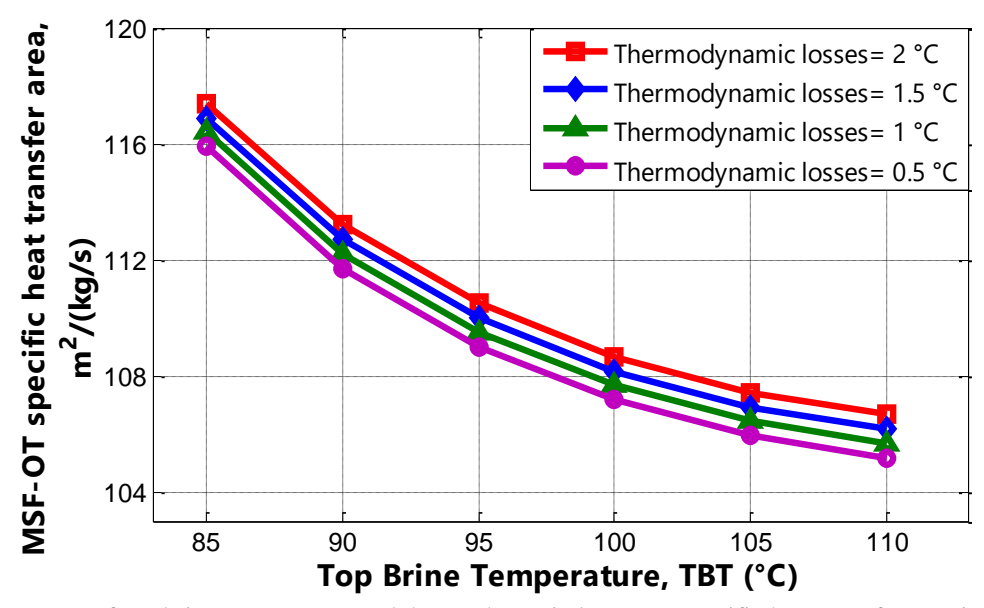


Fig. 4. 16. Impact of top brine temperature and thermodynamic losses on specific heat transfer area in MSF-OT.

4.3.3. Flashing & Water Production Characteristics effects

The figure below illustrates the evaporation rate across multiple stages as the top brine temperature (TBT) increases. A rise from 90°C to 110°C amplifies the thermal gradient, accelerating phase change and enhancing freshwater production. Higher temperatures improve efficiency by promoting greater vapor generation. However, excessively high TBT can accelerate scaling and fouling, reducing heat transfer performance.

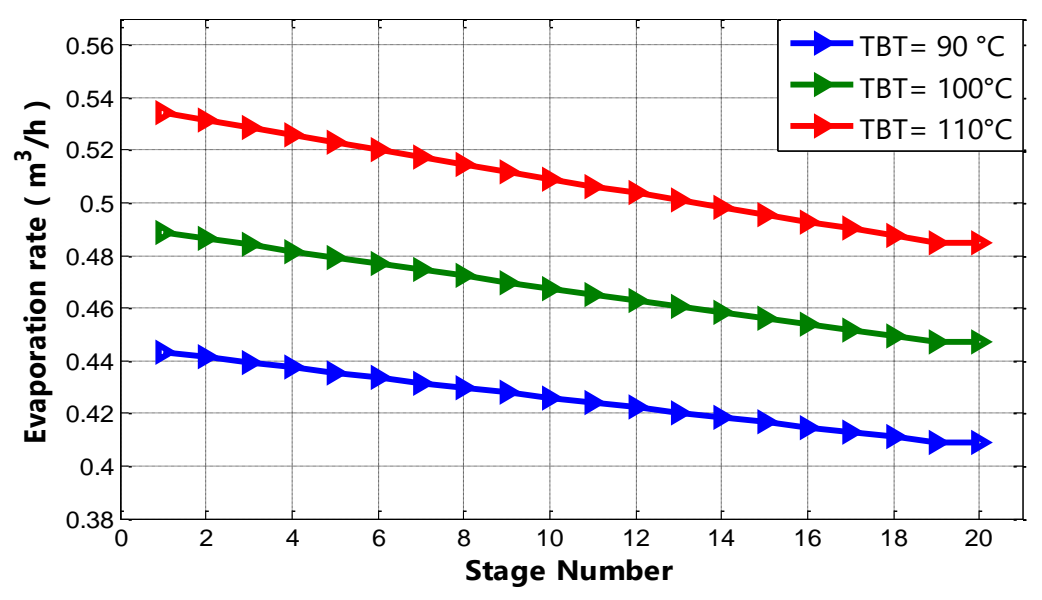


Fig.4. 17. Impact of top brine temperature on evaporation rate across stages.

MSF stage count directly impacts distillate production. As shown in Fig. 4.18, Increasing the number of stages from 10 to 30 enhances heat recovery, leading to higher evaporation rates and improved freshwater yield. More stages enable efficient thermal energy utilization, boosting overall system performance. Nevertheless, beyond a certain limit, further increases may result in diminishing efficiency due to greater heat losses, pressure drops, and operational challenges.

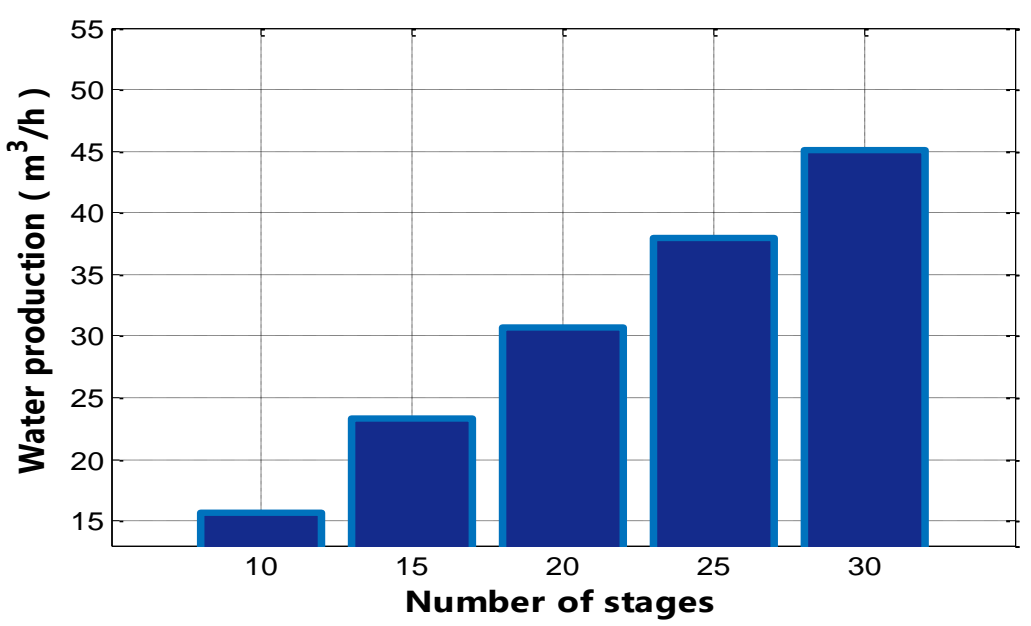


Fig.4. 18. Impact of MSF-OT stage number on distillate water production.

4.4. Effects of Changing Site Conditions

The following analysis investigates the implementation of the LFC-MSF desalination system at three coastal regions in Algeria: Jijel (36°49'12''N, 05°44'21''E) in the east, Algiers (36°45'07''N, 03°04'46''E) in the center, and Oran (35°47'10''N, 0°08'57''W) in the west. It evaluates how variations in site conditions influence the system's performance and efficiency. Key environmental factors, such as ambient temperature, solar radiation, and feedwater quality, play a critical role in determining the system's operational efficiency. These factors directly affect essential processes like heat transfer, evaporation rates, and freshwater production, as outlined in the sensitivity analysis in earlier sections.

To determine favorable and unfavorable days for thermal energy production in these regions, a MATLAB-based numerical model was developed using TMY weather data from the PVGIS-SARAH-2 database [190]. The analysis identifies optimal and suboptimal periods: May 16 and January 3 in Algiers, May 22 and January 17 in Oran, and June 30 and January 5 in Jijel, as illustrated in Figs. 4.19.A–4.19.C.

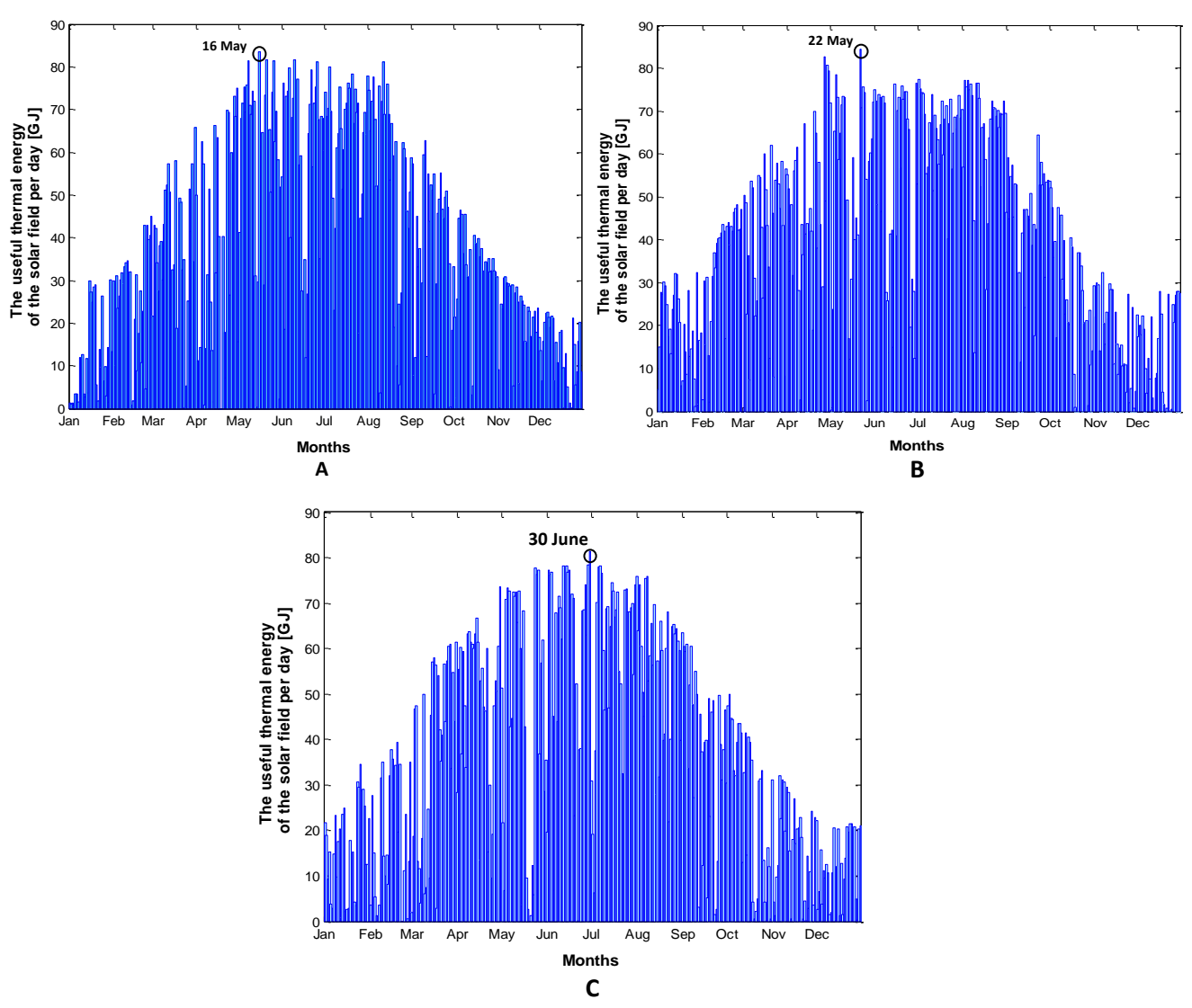


Fig.4. 19. Annual daily variability of useful thermal energy in the solar field for selected coastal regions of Algeria: (A) Algiers, (B) Oran, and (C) Jijel.

4.4.1. Climatic Conditions

Fig. 4.20 shows the daily variation of DNI for three coastal regions, each displaying unique trends. On clear days, the DNI profile follows a bell-shaped curve, rising gradually in the morning, peaking between 898 and 984 W/m², and then decreasing in the afternoon. During cloudy conditions, the peak value drops below 400 W/m², indicating a significant reduction in solar radiation.

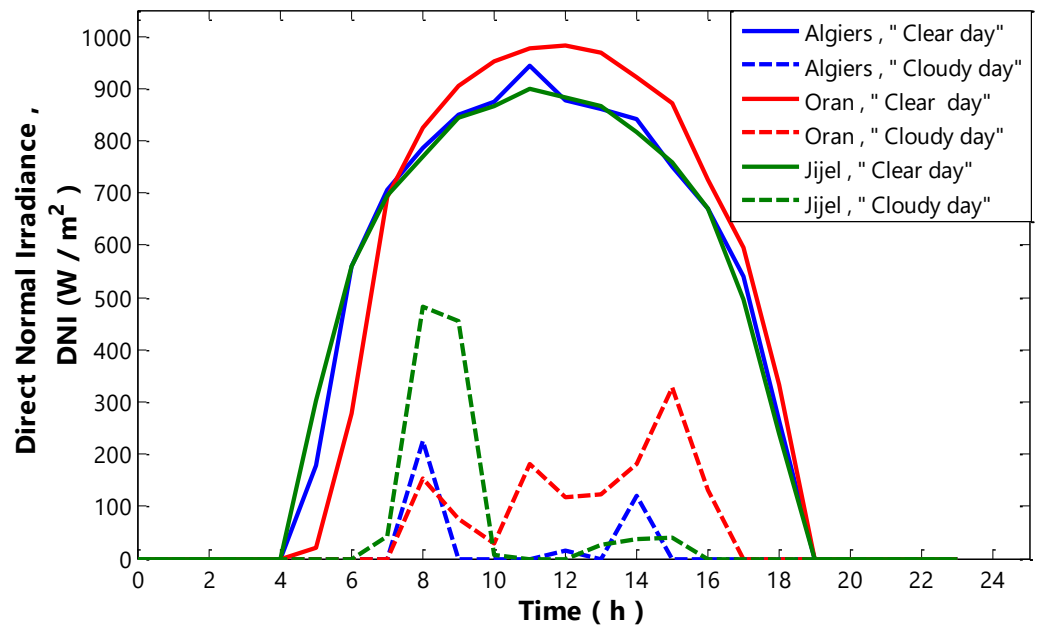


Fig.4. 20. Variation of DNI in coastal regions of Algeria on clear and cloudy days.

The temperature across Algeria rises from east to west, with the eastern regions showing greater seasonal variation [208]. As shown in Fig. 4.21, daily temperatures begin around 13°C in the morning, peaking between 20°C and 25°C by midday, and then remain relatively stable throughout the day. The eastern regions experience a longer cooling period during winter compared to the west [208], which is particularly noticeable in the daily temperature fluctuations.

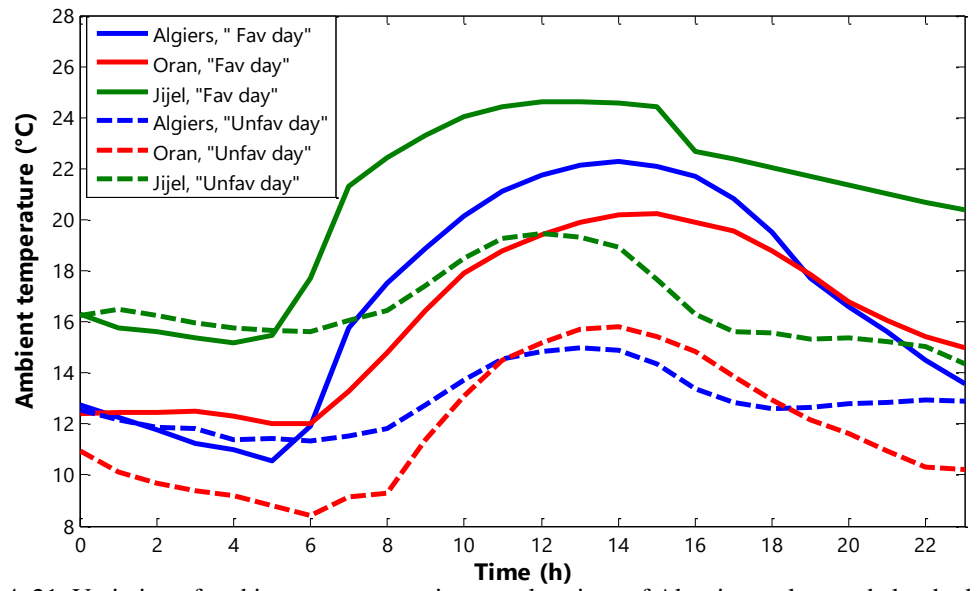


Fig.4. 21. Variation of ambient temperature in coastal regions of Algeria on clear and cloudy days.

The weather conditions presented above, including DNI and ambient temperature (Fig. 4.20 and Fig. 4.21, respectively), show minimal variation across the three coastal regions, indicating a stable and abundant solar energy potential. This consistency in weather patterns highlights the significant potential for implementing solar-driven desalination systems in these areas.

4.4.2. Evaluation of System Efficiency and Energy Output

LFC optical efficiency exhibits a distinct daily pattern, as depicted in Fig. 4.22, with variations between favorable and unfavorable conditions. Under optimal circumstances, efficiency starts at 36–40% in the morning, peaks at 60–62% around midday, and gradually declines in the afternoon. In contrast, adverse weather conditions, including cloud cover, dust, and humidity, lead to reduced efficiency, with midday values dropping to 22–30% and further decreasing to 13–21% during the morning and evening. These variations emphasize the strong influence of environmental conditions on the optical efficiency of LFCs, which typically ranges from 30% to 70% [209].

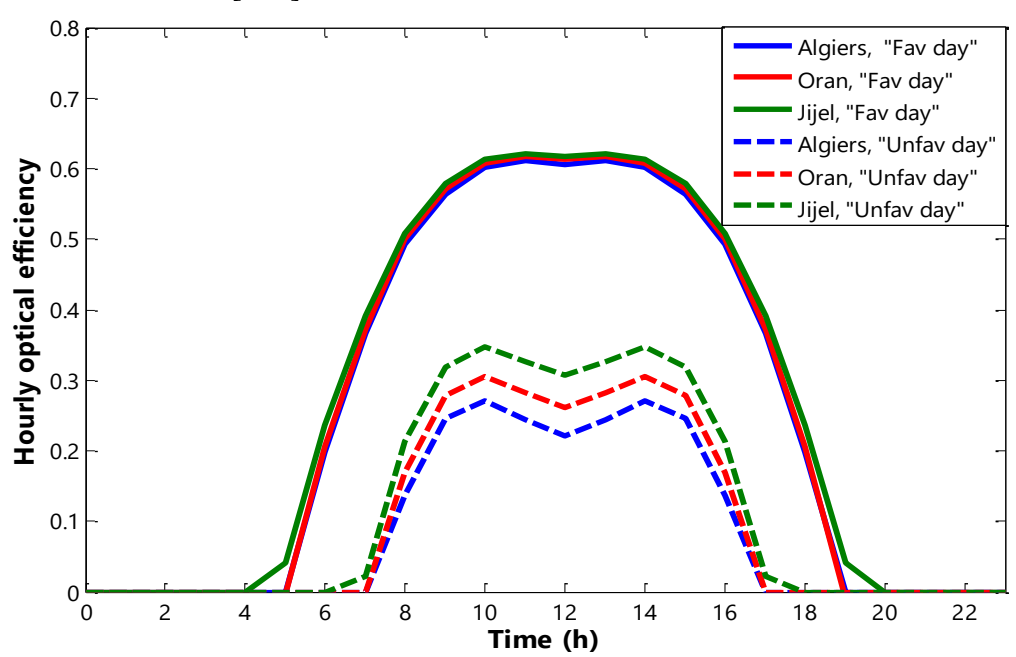


Fig.4. 22. LFC optical efficiency in coastal Algeria on favorable and unfavorable days.

Thermal energy production variability significantly impacts the efficiency and stability of solar-driven desalination systems [210]. Fig. 4.23 illustrates the solar field's energy supply compared to the MSF-OT plant's requirements under different climatic conditions. On favorable days, energy production can exceed demand by 148%, allowing for stable operation and surplus storage. However, under adverse conditions, such as cloud cover and rainfall, output may drop to 26% of the required energy, highlighting the importance of storage and backup solutions. These results emphasize the potential of LFC technology for effective implementation in Algeria's coastal regions.

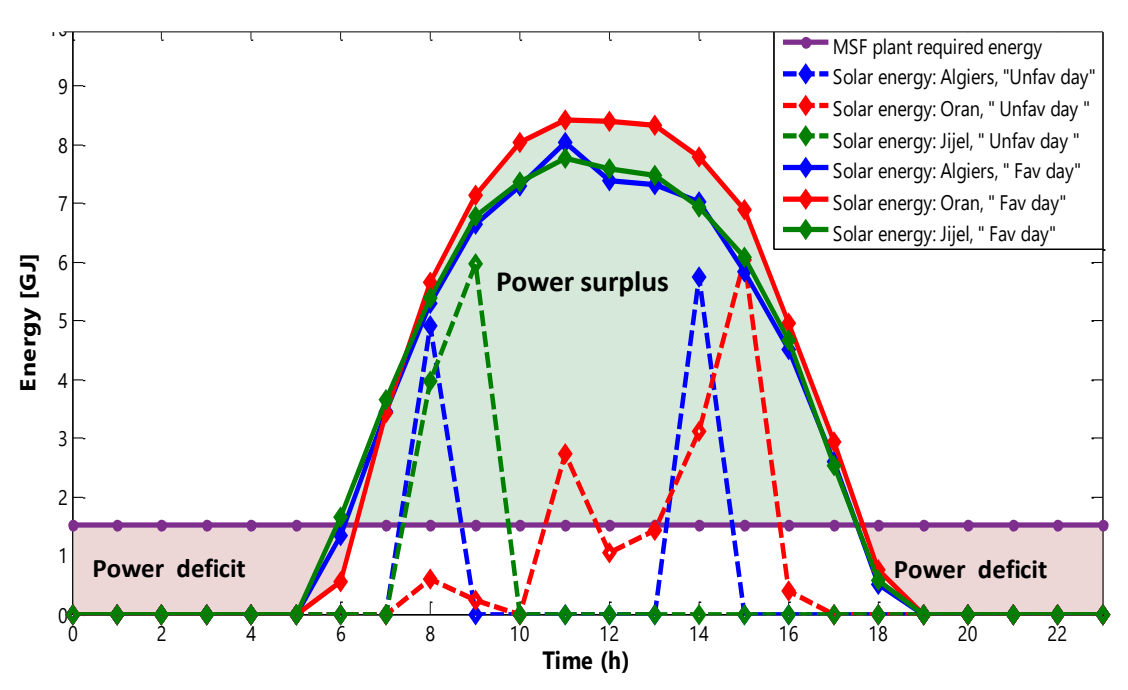
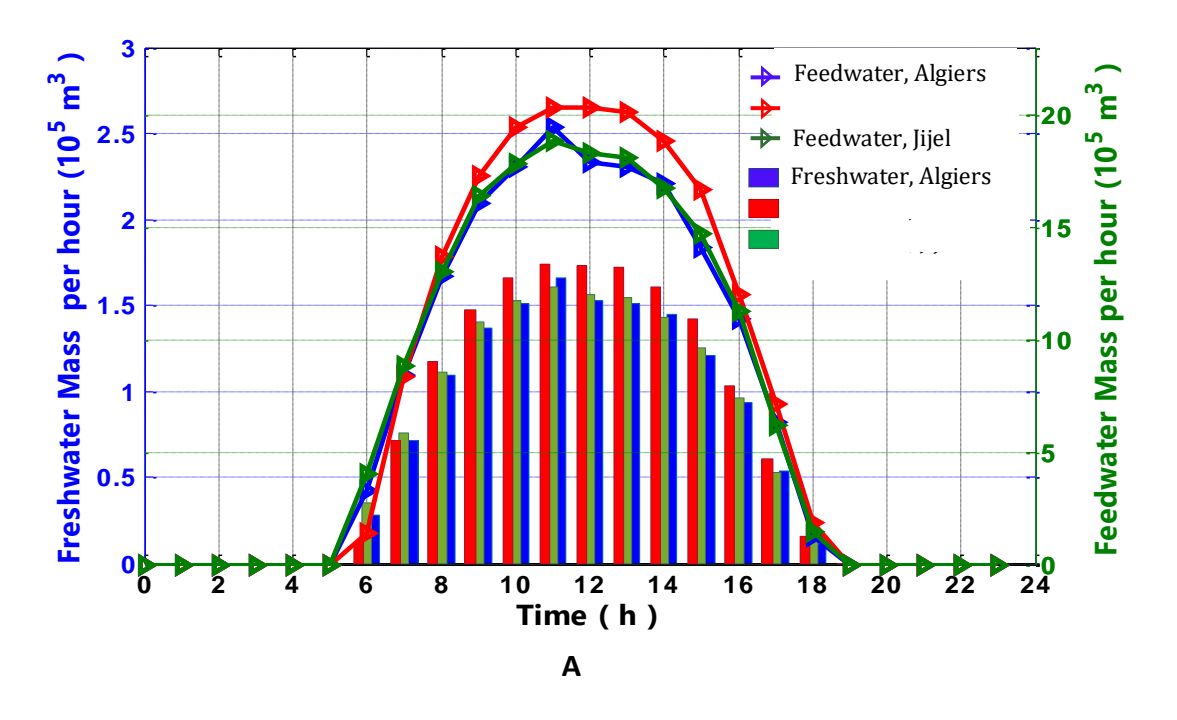


Fig.4. 23. Solar thermal energy and process demand variations on favorable and unfavorable days in Algeria.

Fig. 4.24 depicts the hourly variation in feedwater input and distillate production on both favorable and unfavorable days across the three studied regions. The trends closely follow the energy generation pattern, exhibiting similar fluctuations in all locations. On the most favorable day (see Fig. 4.24.A), distillate production peaks at 1.7×10^5 m³ per hour at noon, sourced from 2.0×10^6 m³ of feedwater. Under unfavorable conditions (Fig. 4.24.B), reduced solar availability lowers both feedwater intake and freshwater output, while system efficiency remains stable.



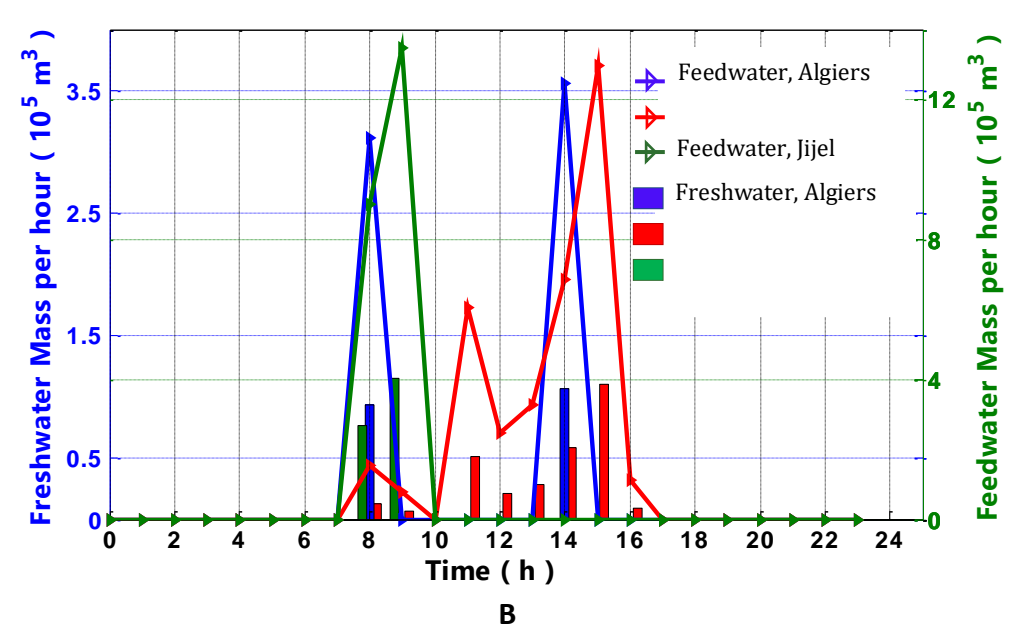


Fig. 4. 24. Hourly variation in feedwater intake and distillate production on (A) clear days and (B) cloudy days.

To ensure uninterrupted operation during periods of low or no solar radiation, this study explores the integration of direct solar energy, storage, and backup support. Excess energy collected during peak sunlight hours is stored for later use, ensuring continued operation when solar input is insufficient. If stored energy falls short of demand, backup systems compensate for the deficit.

Table 4.3 presents the annual energy consumption and operational distribution among the LFC, storage, and backup systems across the three studied coastal cities. The results reveal minimal variation between locations, highlighting the system's reliability under diverse conditions. On average, 30% of operational hours are covered by the LFC, demonstrating its strong performance under favorable sunlight conditions. The storage system plays a crucial role, sustaining 63% of total working hours, ensuring extended operation beyond daylight availability. The backup system, used only as a last resort, accounts for 7% of operational hours, minimizing reliance on conventional energy sources. These insights are essential for the economic assessment of the system, as they provide a basis for evaluating storage capacity, backup energy costs, and overall system feasibility.

Table 4. 3. Annual energy demand and runtime analysis of LFC, storage, and backup systems.

Metrics	Zone	LFC	Storage	Fossil Fuel backup
	Algiers	2,636	5,431.2	692.8
Annual working hours (h/year)	Oran	2,735	5,867.9	157.1
	Jijel	2,498	5,270.9	991.1
Average values (h/year)		2,623	5,523.3	613.7
	Algiers	4,589.27	9,455.72	1,206.16
Energy consumed by the system (GJ)	Oran	4,761.63	10,210.14	273.35
•	Jijel	4,349.02	9,176.64	1,725.5
Average values (GJ)		4,566.64	9,614.17	1,068.34
	Algiers	30.09	62	7.91
Percentage of work hours (%)	Oran	31.2	67	1.8
. ,	Jijel	28.5	60.17	11.31
Average values (%)		30	63	7

4.5. Conclusion

This chapter examined the key factors influencing the performance of the LFC-MSF desalination system, including LFC parameters, MSF operational parameters, and site-specific variations. The results demonstrate the system's potential for efficient solar-driven desalination while emphasizing the need for further improvements to enhance performance, scalability, and adaptability to varying environmental conditions.

The next chapter will explore the feasibility of implementing a conventional MSF desalination system powered by LFC, incorporating the novel coupling approach introduced in Chapter 3, under Algiers' climatic conditions. Additionally, it will investigate the integration of isolated tubes within the MSF plant as a performance enhancement strategy. A comparative analysis will be conducted to evaluate these configurations (with and without isolated tubes) against a conventional MSF system operating on fossil fuels under identical conditions.

Chapter 5: Feasibility and Performance of an LFC-MSF Desalination System with Innovative Coupling in Algiers

5.1. Introduction

The feasibility of integrating an LFC-powered MSF desalination system with an innovative coupling strategy under the climatic conditions of Algiers is a critical aspect that requires thorough investigation.

This chapter provides a comprehensive analysis of the LFC-MSF desalination system, focusing on performance assessment, energy efficiency, and economic viability. First, the solar potential in Algiers is evaluated to determine its suitability for integration with the desalination process. Model validation is then conducted using reference data from the Kuwait MSF plant and El-Dessouky's studies, ensuring the accuracy and reliability of performance predictions. Subsequently, the annual performance of the system is analyzed, followed by an assessment of CO₂ emissions to quantify its environmental benefits.

A comparative study of the MSF-OT system is also presented, examining the impact of additional heat transfer tubes on thermal performance and freshwater production. The trade-offs between energy consumption and water yield are explored to optimize system efficiency. Furthermore, an economic analysis assesses the financial viability of the proposed system, comparing it with alternative desalination technologies. Finally, strategies to enhance system reliability are discussed, with a focus on maintenance optimization, automation, and hybrid energy integration to improve long-term performance and sustainability.

5.2. Description of Study Area

Algeria, the largest country in Africa, is located in North Africa between latitudes 35°–38°N and longitudes 8°–12°E. It covers an area of 2,381,741 km² and has a population of approximately 43.9 million, with a density of 18 inhabitants/km² [211]. The country exhibits a transitional climate, ranging from a Mediterranean influence in the north to semi-arid and arid conditions in the central and southern regions (Fig. 5.1). Annual precipitation varies significantly, from 500 mm in the northern coastal areas to 150 mm in the arid south, with an average temperature of 12°C [212]. Algeria's coastal region, extending over 1,200 km along the Mediterranean Sea [211], serves as the economic and demographic hub of the country. However, these regions are increasingly facing water scarcity due to growing demand, limited freshwater resources, and the impacts of climate change. Given their direct access to seawater, desalination has become a strategic solution to ensure a sustainable water supply.

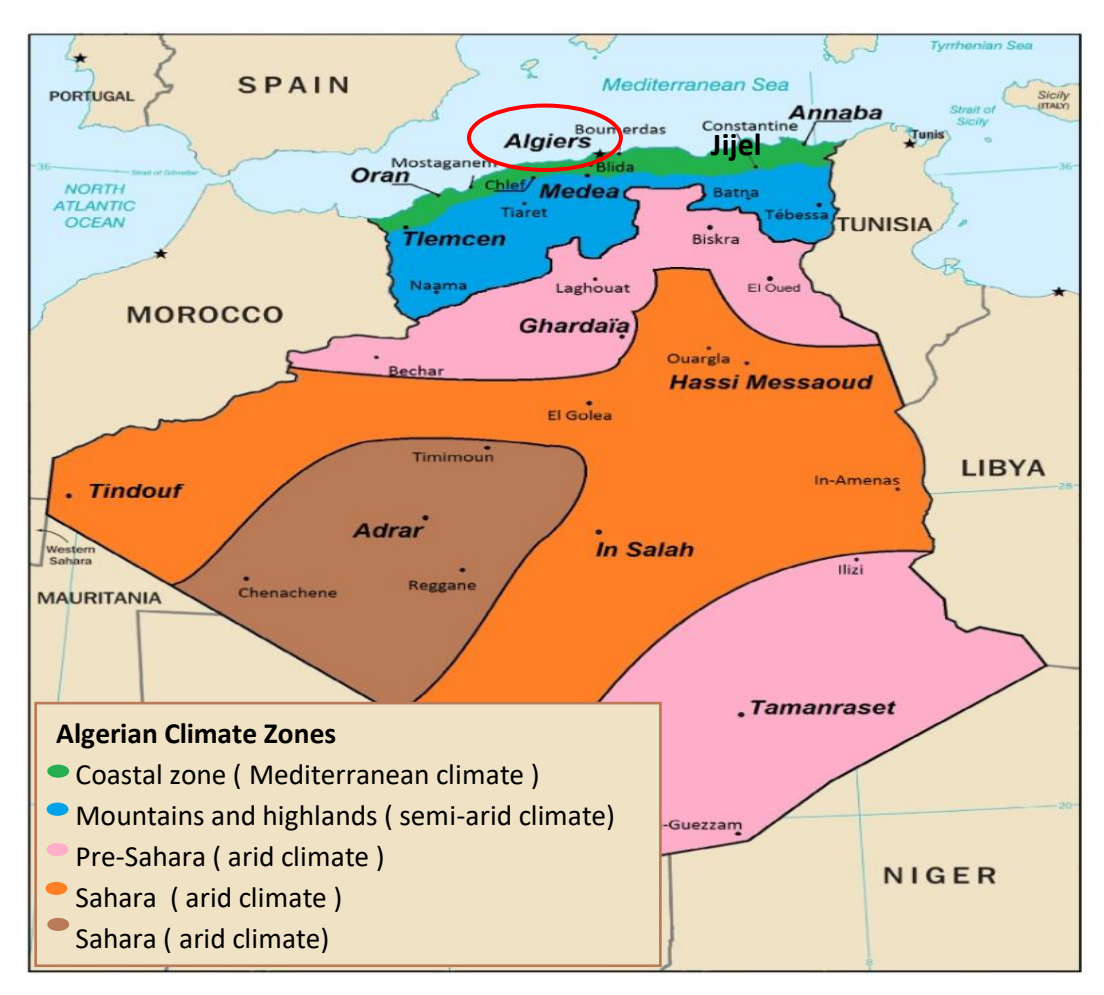


Fig.5. 1. Algeria's climate zones [213].

As confirmed by the sensitivity analysis discussed in Chapter 4, which examined variations in coastal conditions from east to west, the results indicate a high degree of similarity in environmental conditions across the entire coastal region. Therefore, Algiers has been selected as a representative site to assess the feasibility of implementing the LFC-MSF system in Algeria's coastal areas. Moreover, the findings from this study could potentially be extended to similar coastal regions across Africa.

Algiers, strategically located on Algeria's central coast, benefits from high solar potential, abundant water resources, and favorable climatic conditions for renewable energy applications. Its geographical position ensures substantial solar irradiation year-round, making it an ideal site for solar-powered desalination. To evaluate the proposed desalination system, a MATLAB-based simulation was performed using meteorological data specific to Algiers. The simulation relied on a TMY dataset from the PVGIS-SARAH-2 Solar Radiation Database [190], providing accurate solar radiation and environmental parameters (see Fig. 5.2 and Fig. 5.3).

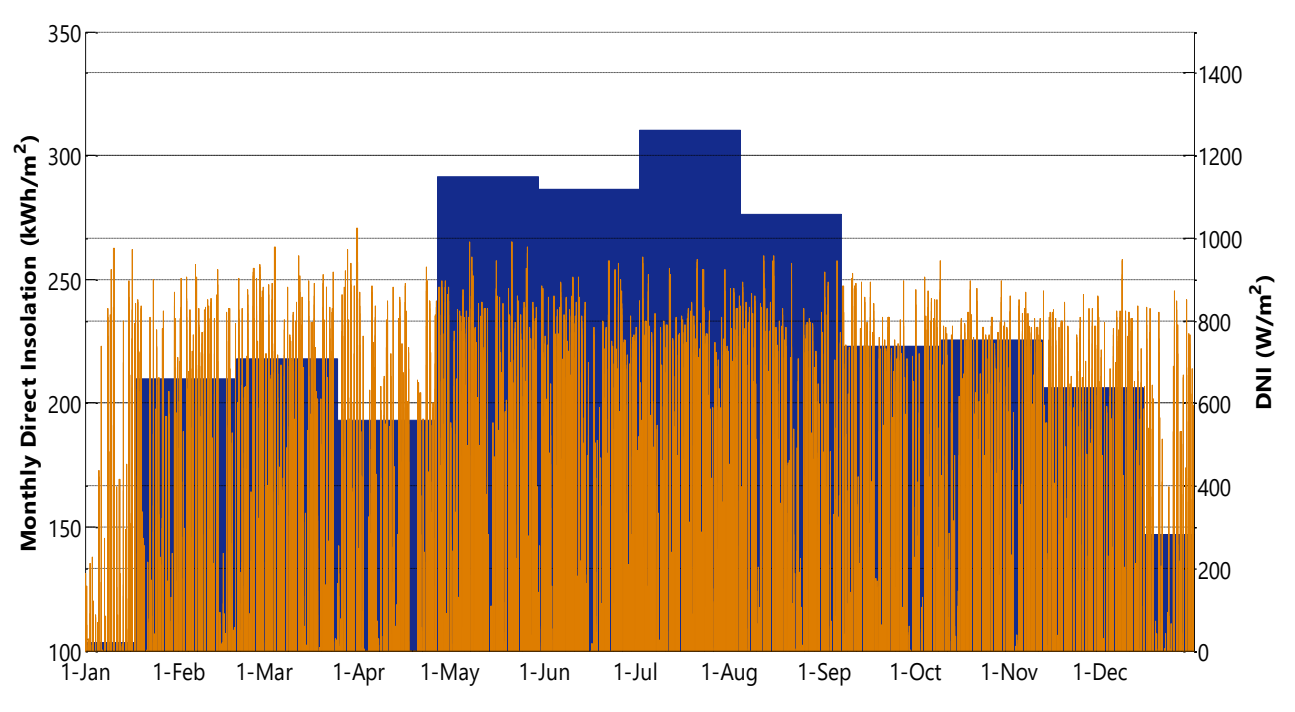
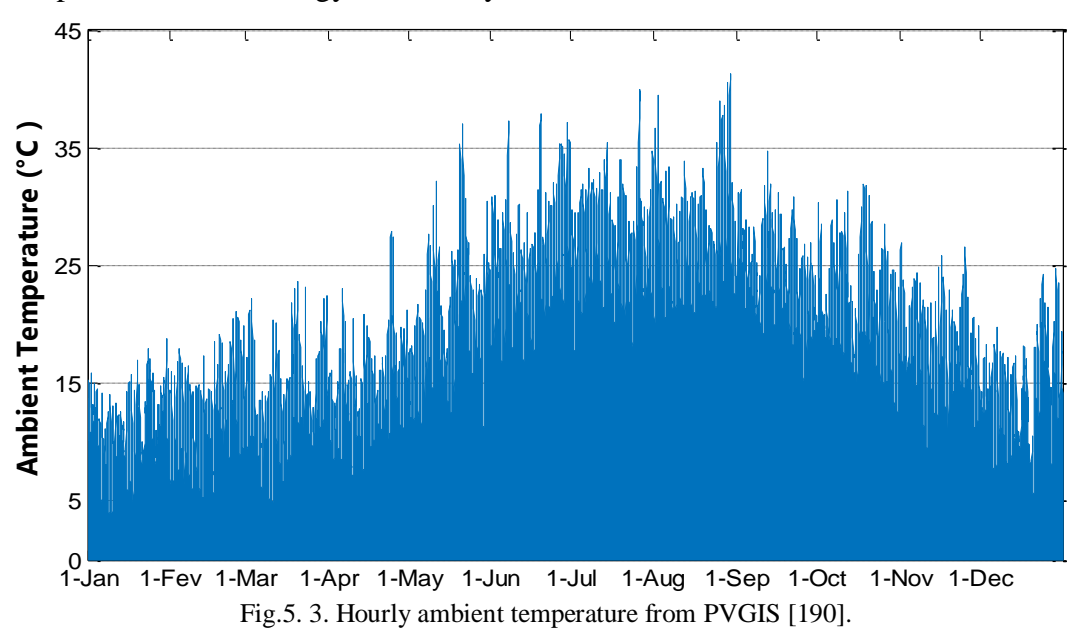


Fig.5. 2. Monthly direct insolation and hourly DNI from PVGIS [190].

Fig. 5.2 illustrates the variation in direct insolation on a monthly average and the annual DNI trend, which stays above 850 W/m² for prolonged periods. Fig. 5.3 shows representative ambient temperatures, peaking at 41°C. According to TMY data, insolation reaches its maximum in July at 310 kWh/m², with daily averages exceeding 10 kWh/m², making summer the peak period for solar energy availability.



5.3. Model Validation

This section presents the validation of the MATLAB model by comparing its results with real operational data collected from a plant in Kuwait [183] and reference data from El-Dessouky et al. [4]. The comparison aims to assess the model's accuracy in replicating real-world conditions and predicting system performance. Any deviations between the simulated

and actual data are analyzed to refine the model and improve its reliability for practical applications.

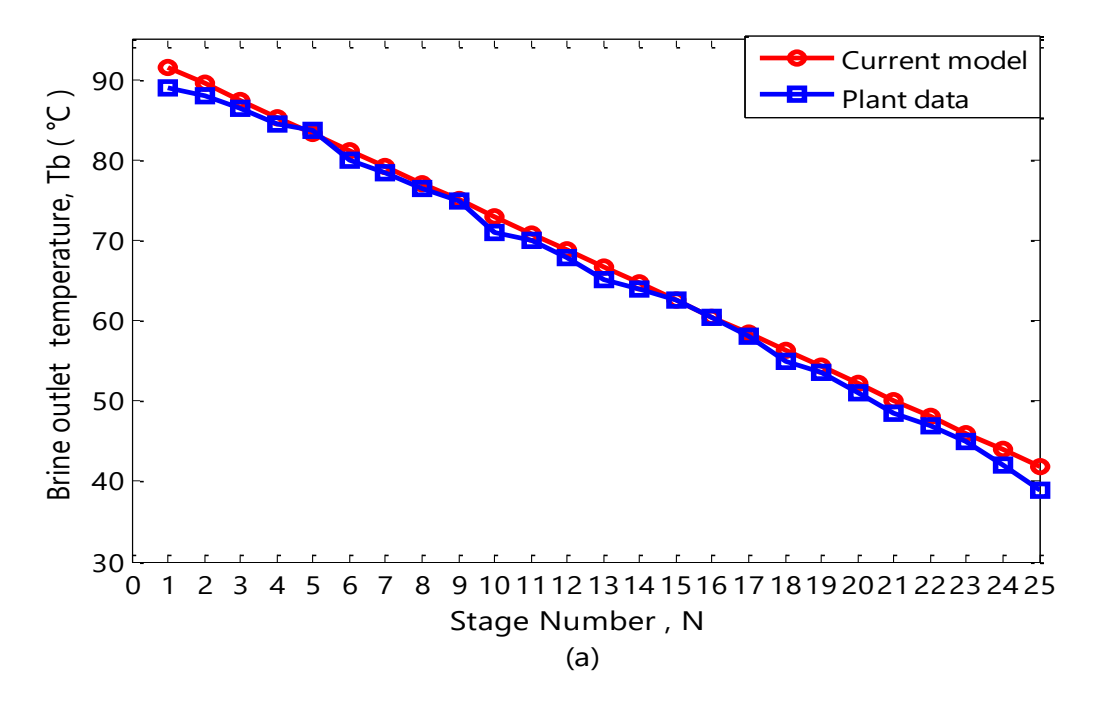
5.3.1. Model Validation Using Kuwait plant Data

The accuracy of the results was evaluated by analyzing the brine and distillate outlet temperatures at each stage. The steady-state findings were then compared with those provided by Hasan et al. [183]. This comparison was conducted under the same plant and operating conditions, as detailed in Table 5.1.

Table 5. 1. Operational	l data of Shuaiba	South plant [183].
-------------------------	-------------------	---------------	-------

Parameter	Value
Stage Number Intake seawater flowrate Steam flowrate Distillate flowrate Seawater temperature Steam temperature Top Brine Temperature (TBT)	25 2425.64 kg/s 30.00 kg/s 247.13 kg/s 23.57 °C 105.20 °C 91.62 °C

The comparison of brine outlet temperatures over 25 stages is illustrated in Fig. 5.4.a, demonstrating strong consistency between model predictions and actual plant data. Similarly, Fig. 5.4.b presents the distillate outlet temperature comparison, further confirming the model's accuracy. The close agreement between these results highlights the model's reliability in simulating system behavior. Minor deviations likely attributed to measurement uncertainties, operational fluctuations, or external condition variations.



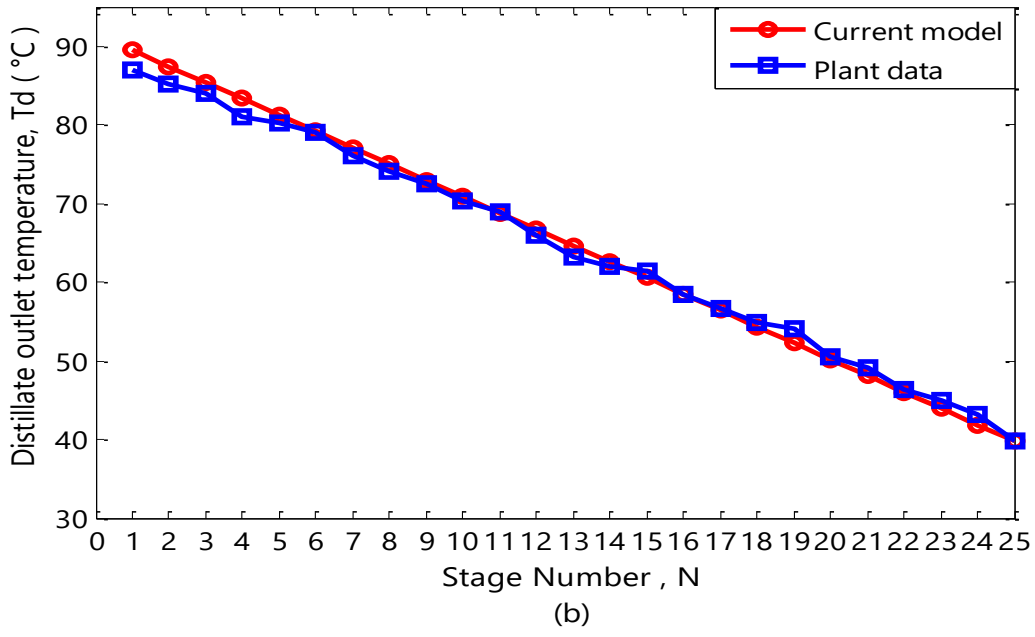


Fig. 5. 4. Comparison of Matlab model predictions with actual plant data.

Table 5.2 presents additional results comparing both datasets, focusing on key parameters such as distillate flow rate, TBT, brine blowdown temperature, and the gain output ratio. The analysis reveals a strong agreement between the model and real plant data, with only minor discrepancies observed. These variations remain within acceptable accuracy thresholds, further validating the model's effectiveness in simulating the thermal and operational behavior of the desalination system.

Parameter	Actual plant [183] Current mod		Relative error
Gain Output ratio (-)	8.00	8.02	0.250
TBT (°C)	91.62	91.61	0.011
Distillate flowrate (kg/s)	247.13	247.322	0.078
Brine blowdown Temperature (°C)	39.80	41.87	5.201

Table 5. 2. Comparative analysis of model predictions and plant data [183].

5.3.2. Model Validation Using Data from El-Dessouky et al.

To further validate the system's reliability, the proposed model was compared with the El Dessouky model. Fig. 5.5 presents a comparison between the model's predictions and data from [4] for key parameters, including leaving brine flow rate (Fig. 5.5.A), stage temperature (Fig. 5.5.B), and leaving brine salinity (Fig. 5.5.C) over 20 stages. Fig. 5.5.A illustrates the reduction in brine flow rate due to the mass loss resulting from the flashing process. Fig. 5.5.B shows how the brine outlet temperature decreases across stages, driven by the flashing mechanism. In Fig. 5.5.C, the growing salt concentration is highlighted, as the distillate, with much lower salt content, causes the salinity of the brine to increase. This phenomenon naturally occurs as water evaporates, leading to higher brine concentration.

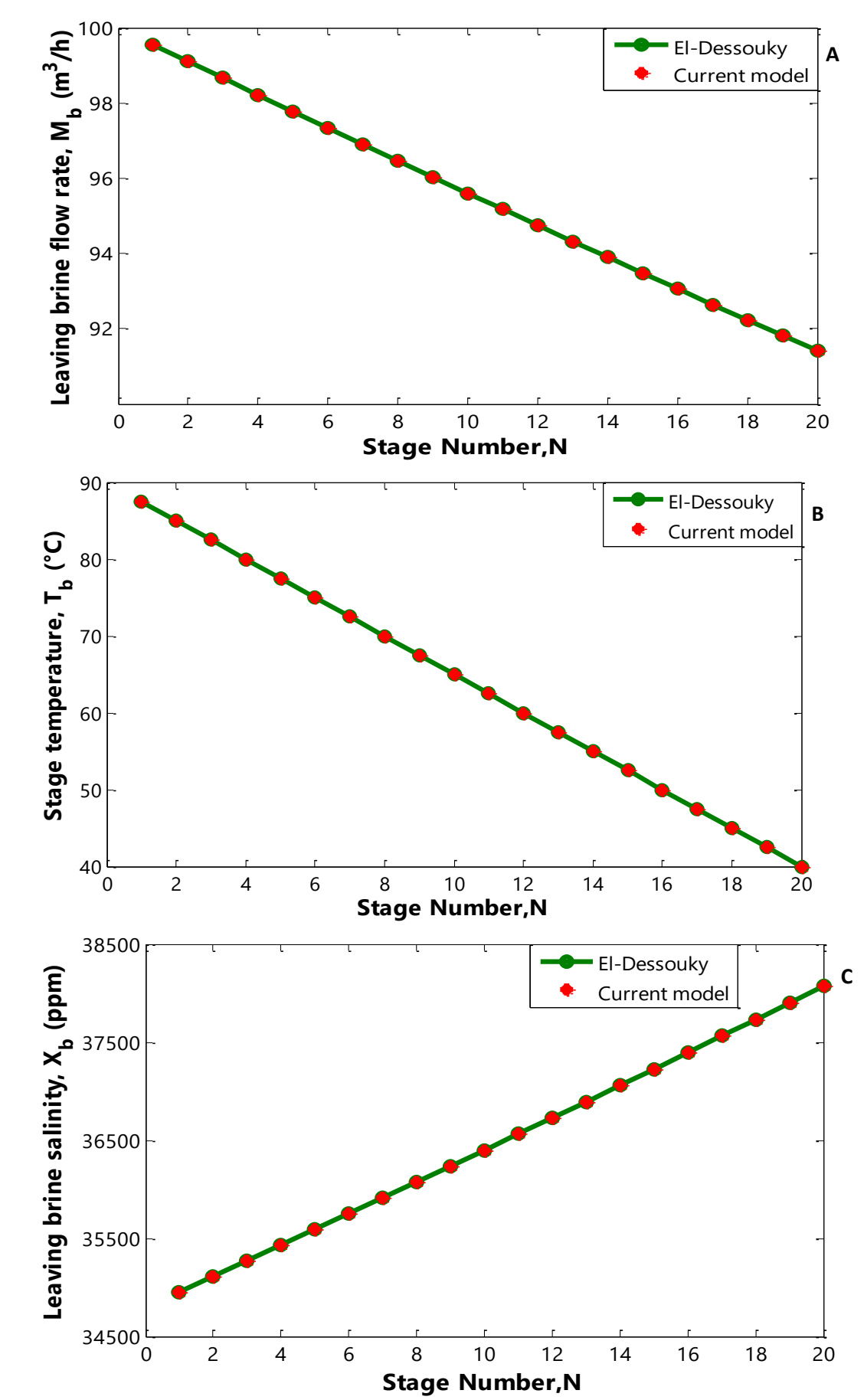


Fig.5. 5. Comparison of Matlab model predictions with El-Dessouky et al. data [4].

The results reveal strong agreement between the two models. Specifically, the deviations in brine flow rate and salinity are under 0.07%, and the relative error in stage temperature is extremely low at 0.005%.

5.4. Annual System Performance Analysis

This section provides an evaluation of the system's overall performance through the analysis of three critical efficiency indicators: optical efficiency, thermal efficiency, and total efficiency. These metrics are essential for understanding how the system operates over time, as they are influenced by factors such as seasonal variations, environmental conditions, and system design. Analyzing the hourly variations in these efficiencies provides valuable insights into the system's operational behavior and helps identify potential areas for improvement across different periods.

Fig. 5.6 presents the hourly evolution of these efficiencies, where the optical efficiency curve (grey) follows a bell-shaped pattern, dropping to approximately 31% in winter and peaking at nearly 62% in summer. This variation is closely related to the sun's position, which affects the system's optical performance. During periods of higher solar elevation, such as in summer, the plant benefits from reduced end-losses and an increase in cosine efficiency, defined by the angle between the incident sunlight and the reflected beam on each mirror surface. On average, the daily cosine efficiency varies from about 0.5 in winter to approximately 0.8 in summer. A comparison between the two solstices under clear-sky conditions indicates that shading-related losses are 33% higher in winter than in summer. Meanwhile, blocking effects are more significant in summer but have a relatively minor impact on the overall field efficiency.

The blue curve illustrates the evolution of thermal efficiency, demonstrating consistently high values throughout the year, with an average of 74.7% and only minor fluctuations. This stability highlights the system's ability to maintain efficient heat transfer under normal operating conditions. However, noticeable deviations occur on certain days, likely caused by fluctuations in DNI and ambient temperature. These variations impact the system's capacity to absorb and convert solar energy, occasionally leading to drops or peaks in efficiency.

While optical efficiency dictates how effectively sunlight is captured and redirected onto the receiver, thermal efficiency determines the extent to which the absorbed energy is converted and transferred to the working fluid. The total efficiency, represented by the red curve, is a result of the combined influence of these two factors. It follows a trend similar to optical efficiency, fluctuating between 22.8% and 46.3% over the year.

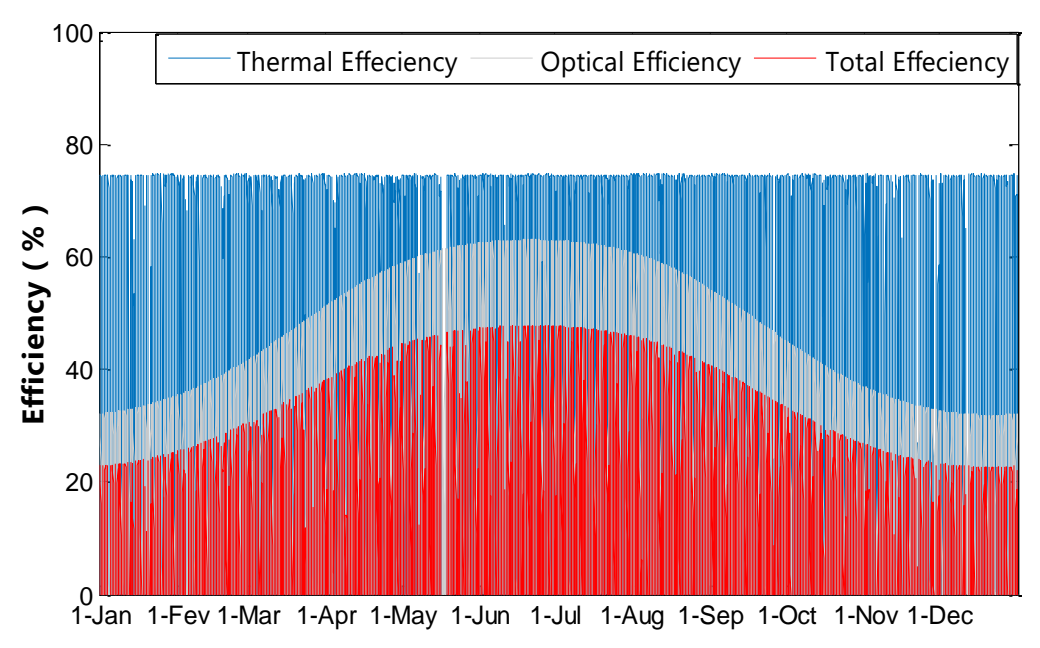


Fig.5. 6. Hourly variations of optical, thermal, and total efficiency in the LFC System.

Ensuring a stable TBT is essential for the efficient and uninterrupted operation of MSF desalination plants. Since solar irradiance varies throughout the year, effective thermal management is required to maintain system performance. Fig. 5.7 illustrates the daily TBT variations over the course of a year. During periods of strong solar radiation, TBT remains within the range of 87°C to 148°C, allowing for efficient desalination. However, in winter and on cloudy days, it drops to 30°C, causing thermal energy shortages that can disrupt plant operation. To address these fluctuations, a novel coupling strategy is introduced to stabilize TBT at 90°C (Fig. 5.8). This solution combines an LFC plant, thermal storage tank, a fossil fuel backup system, and an advanced control mechanism to dynamically regulate heat distribution based on real-time MSF plant energy requirements.

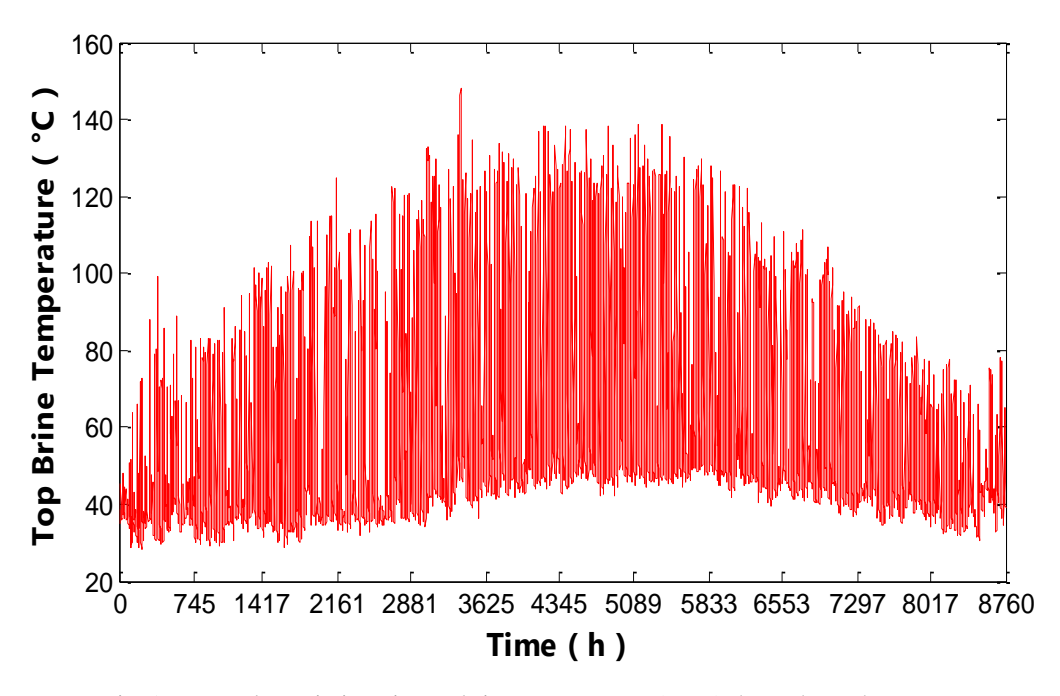


Fig.5. 7. Hourly variations in top brine temperature (TBT) throughout the year.

Fig. 5.8 illustrates the variation in TBT before and after adjusting the thermal energy supplied to the feedwater in the brine heater. Before the adjustment, significant fluctuations in TBT were observed on certain days in winter and summer, leading to instability in the flashing process and negatively affecting the overall performance of the MSF plant. After the adjustment, the control system effectively regulates the thermal energy input, maintaining a stable TBT of 90°C across all climatic conditions.

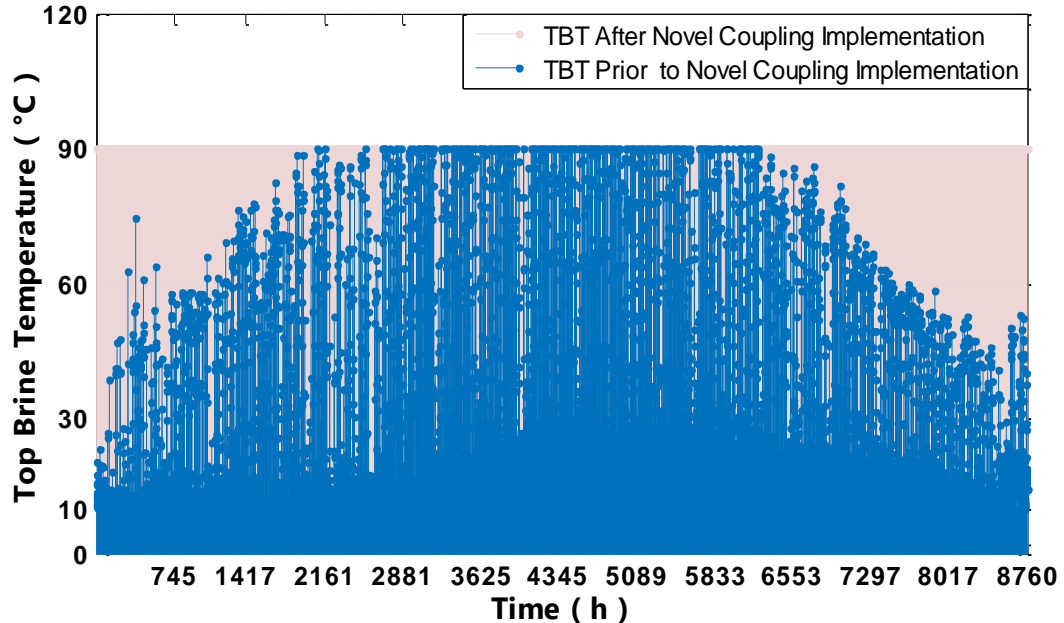


Fig. 5. 8. Impact of thermal energy adjustment on top brine temperature (TBT) stability.

Prior to implementing the proposed novel coupling strategy, the evolution of thermal energy required to heat the incoming feedwater from seawater temperature to the TBT is presented in Fig. 5.9. The results highlight the contributions of both preheat recovery energy from the MSF plant and the useful energy supplied by the solar array. In winter, fluctuations in solar intensity result in a lower energy supply for brine heating, with the solar field delivering around 10 GJ/day compared to 271.8 GJ/day in summer. Such energy deficits can affect plant performance.

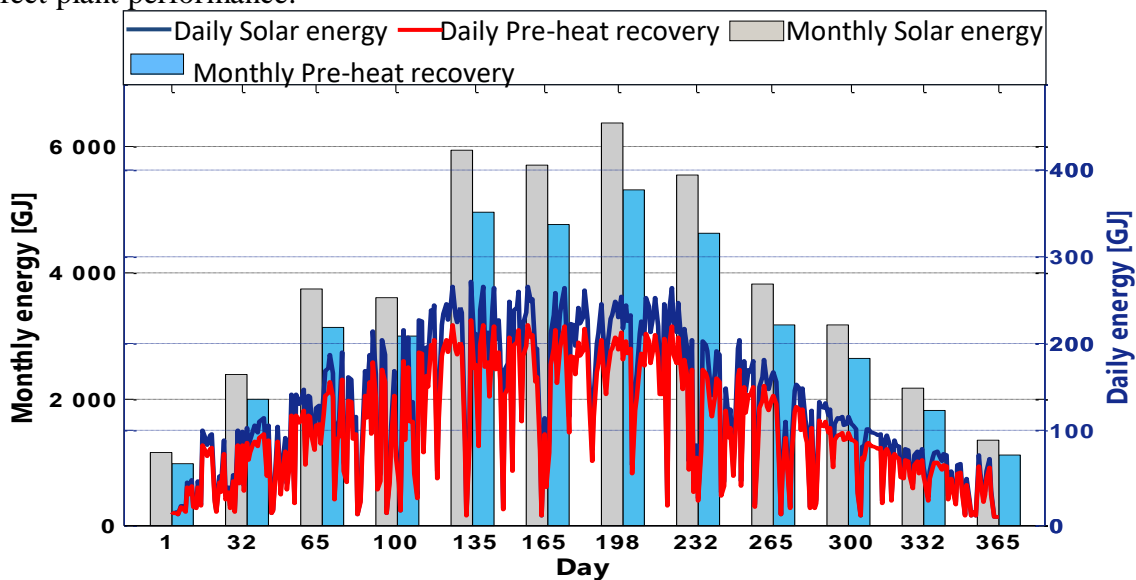


Fig. 5. 9. Seasonal variation in thermal energy utilization and heat recovery in the MSF plant.

With the integration of the proposed coupling strategy, the storage tank, acting as a brine heater, provides the necessary heat to sustain the flashing process, maintaining the TBT at 90°C. The system adjusts energy consumption based on solar availability, drawing more thermal energy during periods of low radiation and less when solar input is strong. This approach ensures a more stable and efficient energy supply, with the system achieving an average of 2,333.2 GJ per month in winter and 5,169.2 GJ in summer.

The performance of the MSF desalination system exhibits significant seasonal variations, as illustrated in Fig. 5.10. The highest distillate production was recorded on June 3, reaching 1,154.6 m³ from 7,220.5 m³ of feedwater, corresponding to a gain output ratio (GOR) of 3. This was achieved without active energy regulation, instead depending exclusively on variations in the feedwater mass flow rate to sustain system operation and achieve the target TBT. In contrast, on December 30, the system produced only 51.2 m³ of distillate from 320.23 m³ of feedwater under the same conditions.

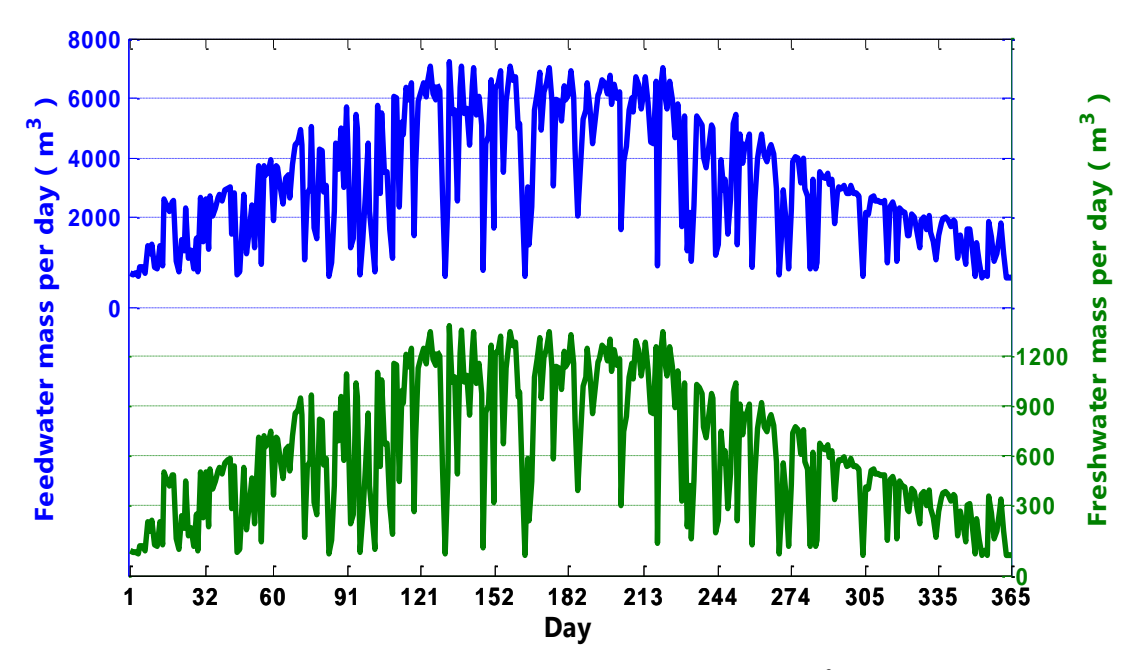


Fig.5. 10. Daily feedwater and distillate production (m³).

Following the integration of the proposed coupling strategy, which employs a 7,190 m² solar collector and delivers a feedwater flow rate of 100 m³/h to the MSF plant, the system achieved an average distilled water production rate of 28.5 kg/m²/day (equivalent to 204.92 m³/day).

5.5. Comparative Study of MSF-OT Desalination: With and Without Additional Isolated Tubes

This section explores the influence of isolated tubes in MSF-OT desalination systems. These tubes play a crucial role in replenishing the brine lost due to flashing across all stages, maintaining system balance, and enhancing freshwater production efficiency.

The variation in brine flow rate within MSF-OT desalination plants is illustrated in Fig. 5.11, comparing cases with and without isolated tubes using Mediterranean seawater (35,000

ppm salinity) [214]. In the absence of these tubes, the brine flow rate progressively declines as evaporation occurs at each stage, diminishing the available brine supply, as noted in [4]. However, the integration of isolated tubes (red line) mitigates these losses by continuously restoring the evaporated brine, ensuring a more stable flow.

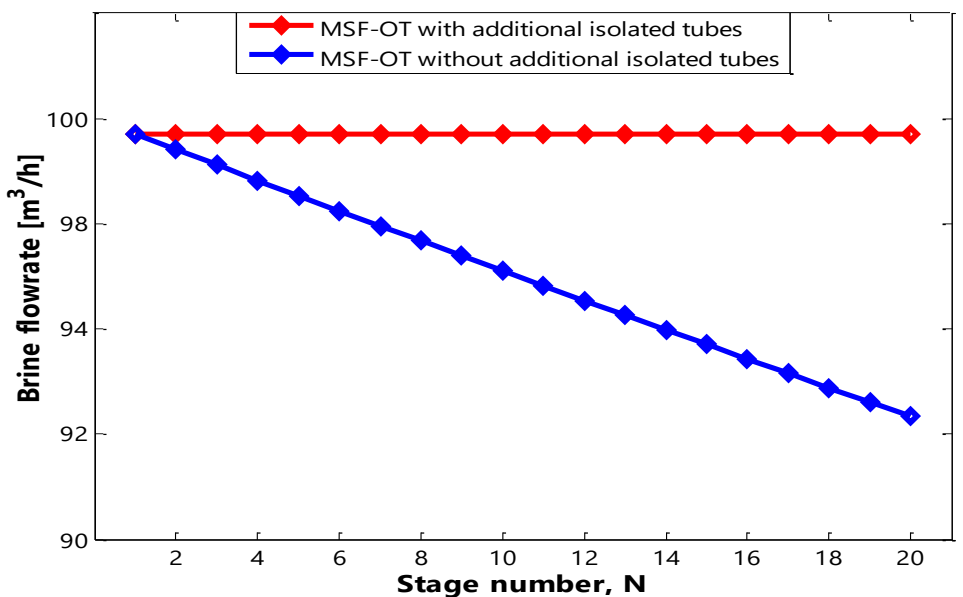


Fig.5. 11. Impact of additional isolated tubes on brine flow stability in MSF-OT desalination.

Fig. 5.12 compares the performance of MSF-OT systems with and without isolated tubes, focusing on Specific Thermal Energy Consumption (STEC), feed mass flow rate, and freshwater production for a 100 m³/h feedwater input. The integration of isolated tubes reduces STEC to 194.9 kWh/m³, compared to 203.9 kWh/m³ in the conventional system. This reduction primarily results from increased freshwater production, enhanced heat recovery, and reduced thermal losses, achieved through the implementation of the novel solar thermal coupling approach. In this case, freshwater production improves by 4.6%, reaching 32.1 m³/h compared to 30.7 m³/h in the conventional setup. This gain is attributed to a stabilized brine flow, which maintains consistent evaporation and minimizes efficiency losses caused by brine depletion.

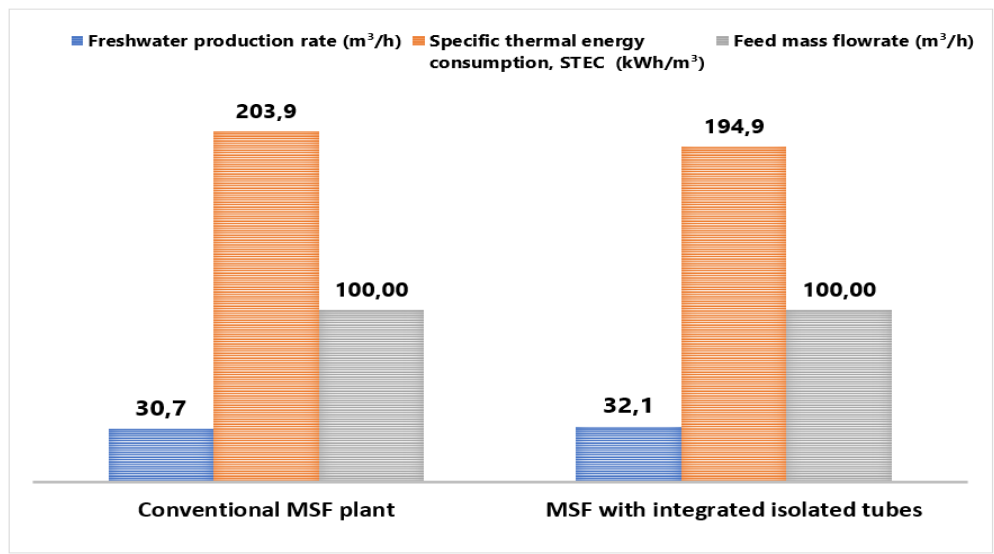


Fig.5. 12. Impact of isolated tubes on MSF-OT performance.

Desalination efficiency depends on key indicators such as STEC and GOR [4, 206]. Adjusting these parameters enhances productivity and reduces energy costs. The results presented in Table 5.3 highlight the impact of isolated tubes on MSF-OT system performance and reveal how productivity (kg/m²/day) varies across different regions.

The findings indicate that incorporating isolated tubes positively influences system efficiency. With these modifications, STEC decreases from 203 kWh/m³ to 194.9 kWh/m³, signifying lower energy consumption. Simultaneously, GOR increases from 3 to 3.14, reflecting greater freshwater generation. These changes suggest better thermal performance and more efficient heat utilization.

Furthermore, the results compare the productivity of the two approaches across the coastal climates of Oran, Algiers, and Jijel, while keeping STEC and GOR values constant. As shown in Table 5.3, the proposed approach achieves the highest productivity in Oran (38.5 kg/m²/day), followed by Algiers (29.7 kg/m²/day) and Jijel (25.3 kg/m²/day), all exceeding the outputs of the conventional system. These variations are primarily driven by regional climatic conditions: Oran's warmer and sunnier environment promotes higher evaporation rates, whereas Jijel's cooler and more humid climate results in lower productivity [215, 216].

Table 5. 3. Impact of isolated tubes on MSF-OT system efficiency and productivity across coastal regions.

Parameter	Value			
	MSF with additional isolated tubes	Conventional model of MSF		
GOR	3.14	3		
Specific thermal power consumption (kWh/m³)	194.9	203.9	Algiers	
Productivity (kg/m²/day)	29.74	28.5		
GOR	3.14	3		
Specific thermal power consumption (kWh/m³)	194.9	203.9	Oran	
Productivity (kg/m²/day)	38.54	37.75		
GOR	3.14	3		
Specific thermal power consumption (kWh/m³)	194.9	203.9	$\it Jijel$	
Productivity (kg/m²/day)	25.34	24.57		

5.6. CO2 Emission Rate

Carbon dioxide (CO₂) emissions play a critical role in accelerating climate change, contributing to global temperature rise, ocean acidification, and more frequent extreme weather events. The desalination sector, which is highly dependent on fossil fuel-based energy, is a significant emitter of CO₂ due to its intensive energy requirements. Minimizing these emissions is essential for reducing environmental impact and promoting sustainable freshwater production. The integration of LFCs into desalination systems presents a sustainable approach to reducing CO₂ emissions, potentially lowering them by up to 50% [217]. This section evaluates the impact of incorporating LFCs into an MSF desalination system and compares its performance with a conventional fossil fuel-powered system.

Desalination's environmental impact is influenced by its specific equivalent electricity consumption (SEC_{eq}) and the carbon footprint of the energy source (EF). In Algeria, the energy sector's emission factor is 0.528 kg CO₂/kWh [218]. Greater SEC_{eq} values indicate higher energy demand, resulting in increased CO₂ emissions in fossil fuel-based systems. To quantify these emissions, the following formula is applied [219]:

$$CO_2 \ emissions = SEC_{eq} \times EF$$
 (50)

SEC_{eq}, or total equivalent specific energy consumption, quantifies the total energy demand of a system by combining electrical and thermal energy contributions. It is calculated as the sum of the specific electrical energy consumption (*SEEC*) and the effective specific thermal energy consumption (*STEC*), with the latter adjusted by the efficiency factor (η_{cdt}) to represent the actual useful energy contribution. This relationship is expressed as:

$$SEC_{eq} = SEEC + STEC \times \eta_{cdt}$$
 (51)

The SEC $_{eq}$ values of two desalination technologies, Fossil Fuel-MSF and LFC-MSF, are compared in Table 5.4. Notably, the Fossil Fuel-MSF system exhibits a high SEC $_{eq}$ of 209.9 kWh/m³, highlighting its complete dependence on fossil fuels, which results in substantial energy consumption and significant environmental concerns. In contrast, the LFC-MSF system operates with a hybrid energy approach, utilizing only 10% fossil fuel while the remaining 90% of the required energy is supplied by solar power through an LFC. This integration of solar energy dramatically reduces the SEC $_{eq}$ to 32.39 kWh/m³, demonstrating the efficiency of renewable energy incorporation in desalination processes.

 $Table \ 5. \ 4. \ Comparative \ analysis \ of \ SEC_{eq} \ in \ Fossil \ Fuel-MSF \ and \ LFC-MSF \ desalination \ systems.$

Energy Integration in MSF Desalination	Production (m³/Day)	Fossil Fuel Fraction	Emission Factor	SEC _{eq} (kWh/m ³)
Fossil Fuel	223	100%	0.582	209.9
LFC	223	10%	0.582	32.39

The transition from fossil fuel-powered desalination to solar-integrated technologies represents a significant step toward reducing environmental impact. Fig. 5.13 clearly illustrates this reduction in CO₂ emissions. As shown, the conventional Fossil Fuel-MSF system is highly energy-intensive, emitting 110.8 kg of CO₂ per cubic meter of desalinated water. This substantial carbon footprint results from its complete reliance on fossil fuels, contributing to greenhouse gas emissions and environmental degradation.

On the other hand, the LFC-MSF system, which utilizes LFCs as a renewable heat source, achieves a substantial reduction in emissions, lowering them to just 17.1 kg of CO₂ per cubic meter (a notable decrease of 93.73 kg/m³). With a daily output of 223 m³, the LFC-MSF system achieves substantial carbon savings of 20,902.79 kg per day, exceeding 7.63 million kg annually. Although it still depends on grid electricity for auxiliary functions and retains a fossil fuel backup, the system greatly minimizes environmental impact.

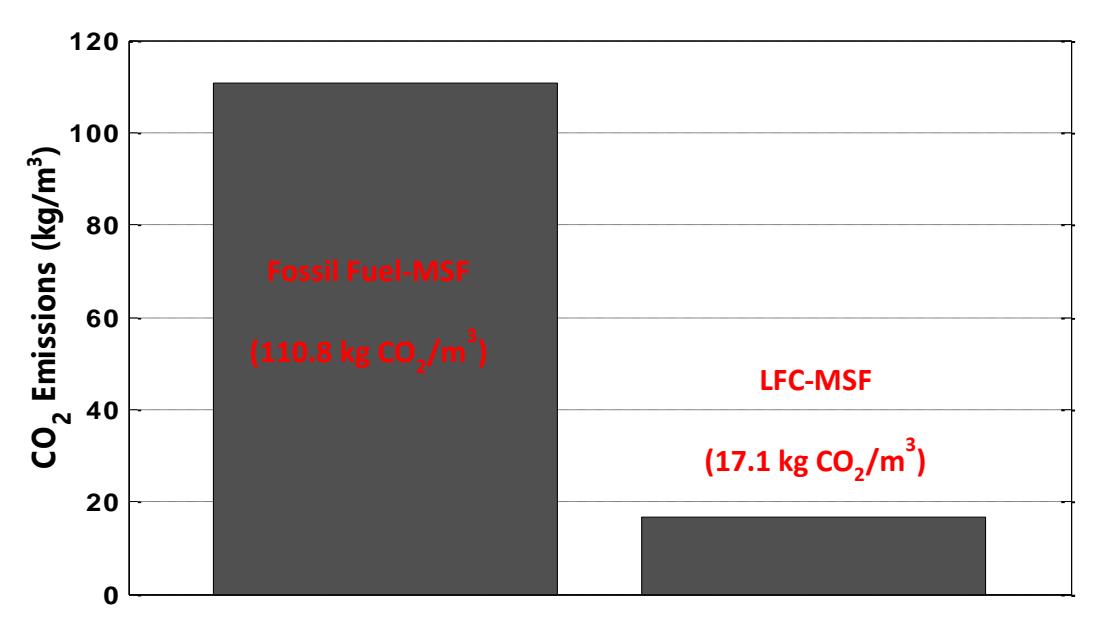


Fig.5. 13. CO₂ Emissions in MSF desalination: Fossil Fuel vs. LFC.

5.7. Trade-Offs Between Energy Consumption and Water Production

In the novel coupling of the LFC-MSF desalination system, continuous and stable water production is achieved by integrating thermal energy storage (TES) with a backup fossil fuel system. The system's efficiency is primarily influenced by the top brine temperature (TBT), which affects energy consumption, freshwater yield, and environmental impact [220]. To analyze these effects, a parametric study is conducted, varying TBT from 85°C to 110°C to assess its impact on system performance. Fig. 5.14.A illustrates how TBT influences freshwater production and energy use, while Fig. 5.14.B highlights its impact on GOR and CO₂ emissions in a solar-powered MSF-OT system without additional tubes.

As shown in Fig. 5.14.A, increasing TBT to 110°C enhances GOR, resulting in higher freshwater output and improved thermal efficiency. However, Fig. 5.14.B reveals a trade-off: a higher TBT also leads to a significant increase in CO₂ emissions due to greater energy consumption, particularly when fossil fuels supplement solar energy during low-radiation periods. According to [55], prolonged exposure to high TBT levels accelerates scaling and component degradation, affecting system longevity. Lowering the TBT to 85°C reduces both energy consumption and CO₂ emissions; however, it also compromises freshwater production, diminishing overall system performance.

To achieve an optimal balance between efficiency and sustainability, a TBT range of 90°C–100°C is recommended, as it enhances water output while mitigating environmental impact and dependence on fossil fuels.

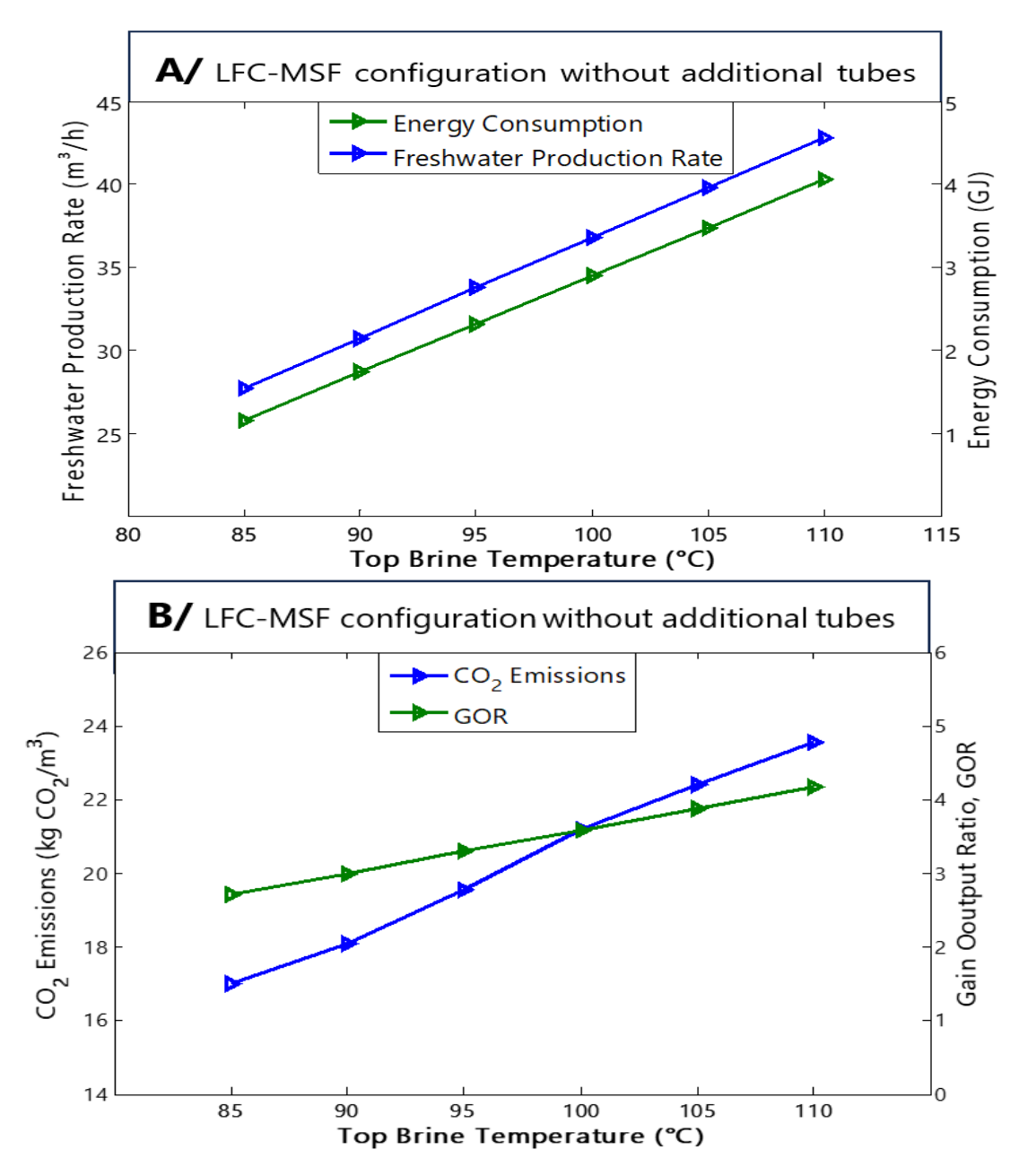


Fig.5. 14. TBT influence on freshwater production, energy demand, and environmental impact in LFC-MSF without additional tubes.

Fig. 5.15 illustrates the impact of incorporating isolated tubes in an LFC-MSF system, building on the analysis presented in Fig. 5.14. The results follow a similar trend, reinforcing the key findings.

A detailed comparison of MSF-OT configurations with and without isolated tubes (Figs. 5.14 and 5.15) highlights both the advantages and trade-offs of this design modification. The integration of isolated tubes enhances energy efficiency, directly contributing to increased freshwater production. However, this improvement also introduces operational challenges, particularly higher electrical energy consumption. The additional pumping power required to circulate seawater through the extended piping network increases overall energy demand, which, in turn, results in higher CO₂ emissions, especially when fossil fuels supplement solar energy during periods of low irradiation.

To address these challenges, several mitigation strategies can be implemented. The use of high-efficiency pumps, optimized tube geometry, and the integration of photovoltaic energy sources can significantly reduce power consumption and emissions. However, these improvements require substantial initial investment, necessitating a thorough evaluation of their long-term economic feasibility and overall impact on system performance.

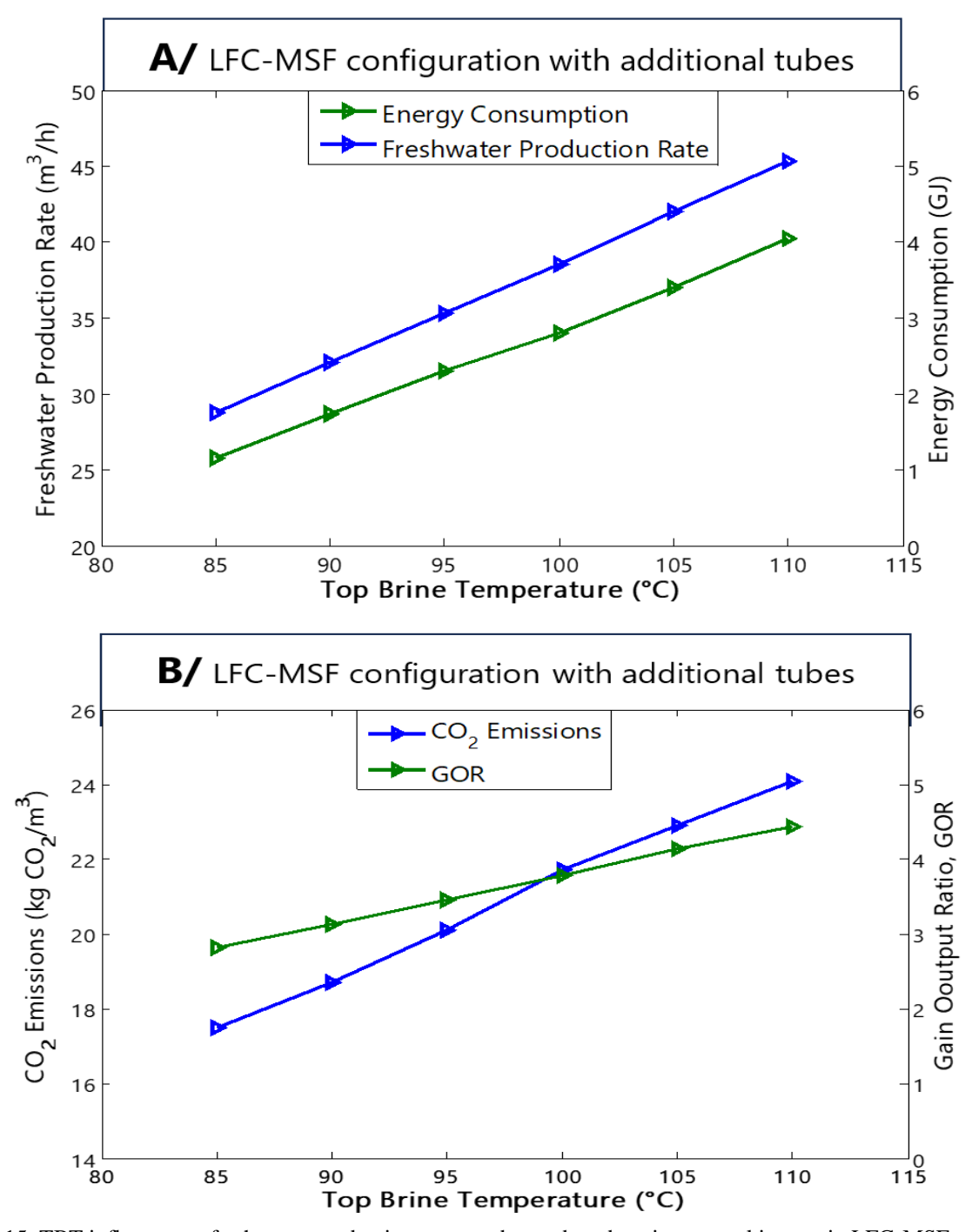


Fig.5. 15. TBT influence on freshwater production, energy demand, and environmental impact in LFC-MSF with additional tubes.

5.8. Economic Analysis of LFC-MSF Desalination

The integration of LFCs into desalination systems represents a promising solution for sustainable water production, leveraging solar energy to reduce reliance on fossil fuels. LFC technology offers lower installation and maintenance costs compared to other CSP systems, making it a viable option for large-scale desalination. However, despite its potential to decrease long-term energy expenses, the high initial capital investment remains a major challenge.

5.8.1. Economic Analysis

The economic viability of LFC-driven MSF desalination is primarily assessed through the Levelized Cost of Water (LCOW), a key metric that accounts for both capital expenditures (CAPEX) and operational expenditures (OPEX) over the system's lifespan. CAPEX encompasses the upfront investment in solar collectors, heat exchangers, and supporting infrastructure, while OPEX includes recurring costs such as maintenance, energy consumption, and labor. To provide a comprehensive financial evaluation, capital costs are annualized using the capital recovery factor (CRF), which distributes initial investments over the system's operational lifetime. This approach enables a direct comparison with conventional desalination technologies. The LCOW is determined based on capital investment, O&M expenses, plant lifespan, water output capacity, and the discount rate. Its calculation follows the equation:

$$LCOW = \frac{CAPEX \times CRF + OPEX}{Annual\ Water\ Production}$$
 (52)

Where:

$$CRF = \frac{i \times (1+i)^n}{(1+i)^n - 1} \tag{53}$$

In this equation, i is the discount rate, and n is the plant's operational lifespan in years.

The CAPEX of an LFC-powered MSF-OT desalination system is categorized into direct and indirect costs. Direct costs include the procurement and installation of core components such as the solar collector, desalination unit, storage tank, and backup systems, in addition to construction and land acquisition expenses. Indirect costs, typically estimated at 25% of direct costs, cover insurance, transportation, engineering services, and administrative fees. A detailed cost distribution is provided in Table 5.5, with additional details available in Appendix C.

Table 5. 5. Cost distribution of the LFC-powered MSF-OT desalination system.

Capital cost components	Value
Capital Cost (CAPEX)	\$
Solar array	207542
Storage Tank	91200
Natural Gas Backup	52 000
MSF	598608
Building	134602

Land		80615	
Total Direct Capital (DC)		1512566	
Indirect (IDC)		378142	
Total CAPEX		1890708	
Interest rate	5%		
Plant availability (f)	95%		
Plant life time ($P_{lifetime}$)	30 year		
Chemical cost (<i>chem_c</i>)	0.03/m^3		
Electrical cost (E_c)	0.05 \$/kWh		
Specific power consumption (SPC)	5 kWh/m ³		
Annual Operating and Maintenance (O&M)	ф	
	,	\$	
Electrical		19331	
Labor		7733	
Chemicals		1933	
Maintenance (<i>MC</i>)		14258	
Total O&M		43255	

To estimate the annual water production, the average daily production rate $(\dot{m}_{d,av})$ is multiplied by 365 and adjusted by the plant's availability factor (f), which represents the percentage of time the plant is operational throughout the year.

Table 5.6 shows the performance improvements of the LFC-MSF system before and after integrating insulated tubes, focusing on LCOW and recovery ratio (RR). Additional parameters were addressed earlier. The recovery ratio for MSF systems typically ranges from 25% to 50% [221]. Before the modification, the system operated with an efficiency of 30.7%, which falls within this range. Following the integration of insulated tubes, efficiency increased to 32.1%. Although this modification resulted in higher initial costs, the long-term energy savings justify the investment, thereby enhancing the system's economic viability.

The LCOW for the system powered by the novel coupling approach, incorporating insulated tubes, was calculated at \$2.15/m³, demonstrating its feasibility. In comparison, the LCOW for conventional MSF is \$1.9/m³ (see Table 5.6). The difference in costs is primarily attributed to the additional pumps required to supply feedwater to the extra tubes and the added material costs for the tubes themselves. Despite these additional expenses, the integration of insulated tubes contributes to significant reductions in energy consumption, making the overall system more economically sustainable in the long run.

Table 5. 6. Impact of additional isolated tubes on performance and cost.

Configurations	Without additional isolated tubes	With additional isolated tubes	
Brine flowrate quantity	Decreases progressively across stages	Quantity is constant in all stages.	
Top Brine Temperature, TBT	The system operates steadily at 90°C	The system operates steadily at 90°C	
Desalination Efficiency, RR	30.7 %	32.1 %	
Specific thermal energy consumption, STEC	203.9 kWh/m ³	194.9 kWh/m ³	

Specific equivalent electricity consumption, SEC _{eq}	29.46 kWh/m ³	29.38 kWh/m ³
Cost (\$/m ³)	1.9	2.15

5.8.2. Comparison with Existing Technologies

To evaluate the effectiveness of the proposed desalination system, a comparative analysis is conducted against existing technologies. The assessment focuses on key performance parameters, including efficiency, TBT, production capacity, cost, and environmental impact in terms of CO₂ emissions. By comparing these metrics, the study aims to highlight the improvements, advantages, and potential trade-offs of the new system compared to both conventional and solar-powered desalination methods, as presented in Table 5.7.

- Conventional MSF desalination, powered by fossil fuels, remains one of the most widely adopted desalination methods due to its relatively low cost, ranging from \$0.52 to \$1.75 per cubic meter. However, this approach is highly energy-intensive, requiring between 90 and 110 kWh/m³, and has a substantial environmental impact, emitting approximately 24 kg of CO₂ per cubic meter of desalinated water. Although cost-effective, its high energy demand and carbon footprint present significant sustainability challenges.
- Solar-powered MSF systems provide a sustainable alternative to conventional fossil-fuel-driven desalination by utilizing renewable energy sources. MSF systems with solar collectors achieve a cost of \$0.97/m³ but require extensive surface areas and are highly dependent on solar irradiance. In contrast, parabolic trough collector (PTC)-based MSF systems offer higher energy efficiency but at a higher cost of \$2.72/m³, with significant capital and operational expenses. Additionally, energy storage or backup heating is often required to ensure continuous operation.
- Multi-effect distillation with thermal vapor compression (MED-TVC) integrated with an LFC operates at a TBT of 62°C, achieving a desalination cost of \$3.09/m³. While highly efficient, the complexity and cost of multi-effect heat transfer and vapor compression limit its large-scale adoption. The system's performance also depends on solar variability and the effectiveness of heat recovery mechanisms.
- This innovative LFC-MSF system, featuring a novel coupling mechanism, offers a cost-effective and environmentally sustainable solution for seawater desalination. It achieves a desalination cost of \$1.9 per cubic meter while significantly reducing CO₂ emissions to 17.1 kg per cubic meter when applied to an MSF-OT plant without additional tubes. Its ability to scale efficiently and adapt to diverse climatic conditions makes it a compelling alternative to both conventional and solar-powered desalination technologies. In the case of adding tubes, the system achieves a desalination cost of \$2.15 per cubic meter, with CO₂ emissions of 18.7 kg per cubic meter. While this cost is slightly higher due to additional material and pumping expenses, the integration of insulated tubes enhances energy efficiency, making the system more sustainable in the long run. Compared to conventional MSF, which has high thermal energy demands, and RO, which relies heavily on electricity, the LFC-MSF system offers a balanced trade-off between cost, energy consumption, and environmental impact.

Table 5. 7. Comparison of desalination configurations.

Location	Desalination technology	Solar integration	Efficiency %	TBT (°C)	Capacity (m³/d)	Cost (\$/m³)	CO ₂ (kgCO ₂ /m ³)	Ref
-	MSF	Fossil Fuel	-	90- 110	50,000-70,000	0.52- 1.75	24	[222]
Italy	RO	PV	-	-	-	1.71	-	[223]
-	MSF-RO	PV	-	<100	0.017-0.021	1.35	0.0023	[224]
American coastal cities	MSF	solar collector	40	-	1,000	0.97	-	[225]
North Africa	MSF	Solar pond	10.5	<95	15	5.48	-	[117]
North America	MSF	PTC	-	90	2,230	2.72	-	[226]
-	MED-TVC	LFC	-	62	9,000	3.09	0.22	[227]
Algeria	MSF without insulated tubes	LFC	30.7	90	223	1.9	17.1	_ This study
	MSF with insulated tubes	LFC	32.1	90	223	2.15	18.7	

5.9. Techniques for Ensuring System Reliability

The proposed LFC-MSF system offers several advantages, particularly the potential for sustainable water desalination powered by solar energy. However, its implementation presents significant challenges. The intermittency of solar energy induces fluctuations in thermal input, necessitating the integration of efficient thermal energy storage systems or supplementary fossil fuel-based backup solutions. These requirements not only add complexity to system design but also contribute to increased capital and operational expenditures.

Additionally, the high initial investment associated with infrastructure (including solar collectors, heat exchangers, and desalination units) remains a major obstacle to large-scale deployment. The long-term durability of the system is challenged by factors such as scaling, corrosion, and maintenance requirements, all of which can degrade efficiency and elevate operational costs over time. Moreover, the environmental impact of brine disposal raises sustainability concerns. Without proper management, the discharge of concentrated brine into aquatic ecosystems can have detrimental effects on marine biodiversity. Several targeted strategies can be employed to mitigate these challenges:

✓ Enhancing thermal storage efficiency: The integration of advanced phase-change materials (PCMs) improves heat retention, allowing the system to maintain stable operation during periods of low solar radiation. This reduces energy fluctuations and ensures a more consistent desalination process.

- ✓ Optimizing energy management: Expanding thermal storage capacity and implementing predictive control strategies help regulate energy use, minimizing reliance on fossil fuels. Smart energy management systems can anticipate fluctuations and adjust operations accordingly, improving overall efficiency.
- ✓ <u>Increasing system reliability:</u> Hybridization with photovoltaics (PV) and wind power provides additional energy sources, reducing the impact of solar intermittency and ensuring continuous system operation. A diversified energy mix enhances reliability and lowers dependency on conventional backup sources.
- ✓ <u>Maximizing operational efficiency:</u> Regular maintenance, optimized heat recovery techniques, and automation help streamline system performance while reducing energy losses. Automated monitoring and control systems can detect inefficiencies, optimize resource use, and minimize downtime.
- ✓ <u>Extending system lifespan:</u> The integration of anti-corrosion and anti-scaling technologies minimizes material degradation, reduces maintenance requirements, and enhances the long-term durability of system components.
- ✓ <u>Enhancing economic feasibility:</u> Strategic site selection based on solar resource availability, land accessibility, and proximity to seawater enhances system performance and cost-effectiveness.
- ✓ The integration of smart control systems further improves efficiency by dynamically adjusting operations based on real-time environmental conditions and energy availability.

By addressing these challenges through targeted strategies, the LFC-MSF system can become a more viable and sustainable solution for large-scale desalination, improving both environmental and economic outcomes.

5.10. Conclusion

This chapter first examined the feasibility of an LFC-powered MSF desalination system under Algiers' climatic conditions. Afterward, a description of Algiers highlighted its solar potential for sustainable desalination. The model validation, using data from the Kuwait MSF plant and El-Dessouky, confirmed its reliability and accuracy. Next, the annual system performance was analyzed, assessing freshwater yield and energy efficiency. The CO₂ emission rate was quantified, demonstrating the environmental benefits of solar integration. A comparative study of the MSF-OT system, with and without additional tubes, revealed improvements in heat transfer and water production. Subsequently, the trade-offs between energy consumption and water production were examined to optimize system performance.

Following this, the economic analysis evaluated cost-effectiveness, while a comparison across different desalination technologies provided insight into the system's competitiveness. Afterward, strategies for enhancing system reliability were explored, focusing on maintenance optimization, improved thermal management, and hybrid energy integration.

Finally, key recommendations were proposed to ensure long-term operational stability and sustainable desalination performance.

GENERAL CONCLUSION

The escalating global demand for freshwater, compounded by the intensification of energy consumption and the urgency of environmental preservation, underscores the critical need for sustainable desalination technologies. In this context, solar energy represents a compelling solution, offering an environmentally benign and renewable alternative to conventional energy sources in freshwater production.

This study proposed and assessed the integration of a Linear Fresnel Collector (LFC) with a Multi-Stage Flash Once-Through (MSF-OT) desalination system. The integrated configuration was designed to improve thermal efficiency, reduce operational losses, and ensure system continuity through the incorporation of thermal energy storage and backup energy sources. A detailed parametric analysis was conducted to investigate the impact of key variables (including solar irradiance, ambient temperature, and both optical and thermal properties of the LFC) on the overall system performance. Additionally, the influence of MSF-specific parameters, such as feedwater flow rates and temperature gradients, on the plant's gain output ratio and thermal efficiency was thoroughly examined. The study also evaluated climatic variability along Algeria's Mediterranean coastline, revealing favorable conditions for the deployment of regionally adapted solar desalination units, particularly in areas where access to centralized infrastructure is limited. This geographic assessment supports the strategic potential of localized, solar-driven freshwater production in semi-arid and coastal environments.

The feasibility of the proposed solar-driven MSF-OT desalination system was rigorously assessed using a dynamic simulation model developed in MATLAB. The model's reliability was confirmed by comparing its results with experimental data from the Kuwait MSF plant and reference results from El-Dessouky, ensuring its accuracy and robustness. Annual performance simulations, utilizing Typical Meteorological Year (TMY) data, facilitated a thorough evaluation of hourly thermal balances, brine temperature fluctuations, and freshwater production. A case study involving a 20-stage once-through MSF system integrated with an LFC demonstrated favorable outcomes. The system consistently maintained a Top Brine Temperature (TBT) of 90°C, produced 223 m³ of freshwater daily, achieved a Gain Output Ratio (GOR) of 3, and exhibited a Specific Thermal Energy Consumption (STEC) of 203.9 kWh/m³. The Levelized Cost of Water (LCOW) was estimated at \$1.90/m³, with CO₂ emissions reduced to 17.1 kg/m³ for the system without additional isolated tubes.

Incorporating additional insulated tubes led to a slight increase in LCOW to \$2.15/m³ and CO₂ emissions to 18.7 kg/m³, due to the increased material and pumping costs. However, the integration of these tubes significantly enhanced thermal efficiency, contributing to the system's long-term sustainability and overall performance. When compared to conventional MSF systems, which are characterized by high thermal energy demands and considerable environmental impacts, the LFC-integrated MSF-OT system offers a more sustainable alternative, balancing cost, energy consumption, and environmental considerations

effectively. This study emphasizes the potential of solar-powered MSF desalination systems as a viable solution for mitigating freshwater shortages in coastal regions. It establishes a strong foundation for the large-scale deployment of these systems, demonstrating clear economic and environmental advantages in sustainable water production.

Building on the findings of this study, future research should address several critical aspects to further enhance the performance and feasibility of LFC-MSF-OT desalination systems:

- Investigating the integration of phase-change materials and nanocomposite coatings to improve energy retention, enhance heat transfer efficiency, and extend component lifespan, thereby increasing overall system reliability and performance.
- Evaluating the potential for expanding LFC-integrated desalination to large-scale applications by analyzing system modularity, optimizing plant layouts, and assessing land and resource requirements to efficiently meet growing freshwater demands.
- Exploring the integration of LFCs with complementary renewable energy sources, such as photovoltaics and wind power, to enhance system resilience, improve energy security, and ensure continuous operation under varying climatic conditions.
- Conducting large-scale pilot studies to validate system performance in real-world conditions, refine design parameters, and optimize operational strategies, thereby facilitating the transition from research to commercial deployment.
- Implementing advanced automation technologies, including artificial intelligence (AI) and the Internet of Things (IoT), to enhance real-time monitoring, improve process optimization, and increase overall operational efficiency.

Appendix A: Mathematical Formulation

This appendix presents key equations used in the MATLAB model in detail [4].

A.1. Saturation Pressure of Seawater, p_s (kPa)

Seawater saturation pressure varies with temperature, as described in Eq. (A.1).

$$p_s = 1.39225 - 0.16566 \cdot T_s + 0.01094 \cdot T_s^2 - 1.29965 \cdot 10^{-4} \cdot T_s^3 + 1.36705 \cdot 10^{-6} \cdot T_s^4$$
 (A.1)

A.2. Specific Heat Capacity of Seawater, *Cp* (kJ/(kg·°C))

The specific heat capacity varies with temperature as defined by Eq. (A.2), for W=X/10000 (2%–16%) and T between 10°C and 180°C.

$$Cp = 0.001 \cdot (B_1 + B_2 \cdot T + B_3 \cdot T^2 + B_4 \cdot T^3)$$
(A.2)

Where:

$$\begin{split} B_1 &= 4206.8 - 6.6197 \cdot W + 1.2288 \cdot 10^{-2} \cdot W^2 \\ B_2 &= -1.1262 + 5.4178 \cdot 10^{-2} \cdot W - 2.2719 \cdot 10^{-4} \cdot W^2 \\ B_3 &= 1.2026 \cdot 10^{-2} - 5.3566 \cdot 10^{-4} \cdot W + 1.8906 \cdot 10^{-6} \cdot W^2 \\ B_4 &= 6.8777 \cdot 10^{-7} + 1.517 \cdot 10^{-6} \cdot W - 4.4268 \cdot 10^{-9} \cdot W^2 \end{split}$$

A.3. Latent Heat of Seawater, λ (kJ/kg)

Seawater latent heat is determined by Eq. A3 for temperatures ranging from 5°C to 200°C.

$$\lambda = 2501.897 - 2.407 \cdot T + 1.19222 \cdot 10^{-3} \cdot T^2 - 1.5863 \cdot 10^{-5} \cdot T^3 \tag{A.3}$$

A.4. Density of Seawater, ρ_s (kg/m³)

Seawater density is defined by Eq. (A.4) and is valid for $0 < X < 160 \times 10^3$ ppm and temperatures between 10° C and 180° C.

$$\rho_s = (A_1 F_1 + A_2 F_2 + A_3 F_3 + A_4 F_4) \cdot 1000 \tag{A.4}$$

Where:

$$\begin{split} A_1 &= 4.032219 \cdot G_1 + 0.115313 \cdot G_2 + 3.26 \cdot 10^{-4} \cdot G_3 \\ A_2 &= -0.108199 \cdot G_1 + 1.571 \times 10^{-3} \cdot G_2 - 4.23 \cdot 10^{-4} \cdot G_3 \\ A_3 &= -0.012247 \cdot G_1 + 1.74 \cdot 10^{-3} \times G_2 - 9 \cdot 10^{-6} \cdot G_3 \\ A_4 &= 6.92 \cdot 10^{-4} \cdot G_1 - 8.7 \cdot 10^{-5} \cdot G_2 - 5.3 \cdot 10^{-5} \cdot G_3 \\ G_1 &= 0.5 \end{split}$$

$$G_{2} = B$$

$$G_{3} = 2 \cdot B^{2} - 1$$

$$B = 2X \cdot 1000 - \frac{150}{150}$$

$$F_{1} = 0.5$$

$$F_{2} = A_{0}$$

$$F_{3} = 2 \cdot A_{0}^{2} - 1$$

$$F_{4} = 4 \cdot A_{0}^{3} - 3 \cdot A_{0}$$

$$A_{0} = (2 \cdot T - 200)/160$$

A.5. Overall heat transfer coefficient of the brine heater, U_{BH} (W/(m²·°C))

The overall heat transfer coefficient of the brine heater quantifies the heat exchange efficiency between the heating medium and seawater, as defined by Eq. (A.5).

$$U_{BH} = 1.7194 + 3.2063 \cdot 10^{-3} \cdot T + 1.5971 \cdot 10^{-5} \cdot T^2 - 1.9918 \cdot 10^{-7} \cdot T^3$$
 (A.5)

A.6. Boiling Temperature Elevation, BTE (°C)

Boiling temperature elevation is expressed as a third-degree polynomial function of salinity (W), valid for $1\% \le W \le 16\%$ and T_s ranging from 10° C to 180° C.

$$BTE = C_1 \cdot W + C_2 \cdot W^2 + C_3 \cdot W^3 \tag{A.6}$$

Where:

$$\begin{split} C_1 &= 8.325 \cdot 10^{-2} + 1.883 \cdot 10^{-4} \cdot T + 4.02 \cdot 10^{-6} \cdot T^2 \\ C_2 &= -7.625 \cdot 10^{-4} + 9.02 \cdot 10^{-5} \cdot T - 5.2 \cdot 10^{-7} \cdot T^2 \\ C_3 &= 1.522 \cdot 10^{-4} - 3 \cdot 10^{-6} \cdot T - 3 \cdot 10^{-8} \cdot T^2 \end{split}$$

A.7. Non-Equilibrium Allowance, NEA (°C)

Non-equilibrium allowance, determined by Eq. (A.7), depends on the temperature difference across the brine pool and its geometric properties. The dimensionless parameter NEA_{10} incorporates brine pool height in the stage H (m), stage length L_{st} (m), and brine flow rate per unit stage width V_b (kg/(m·s)).

$$NEA = (NEA_{10}/(0.5 \cdot \Delta T_{st} + NEA_{10})^{0.3281 \cdot L_{st}} \cdot (0.5 \cdot \Delta T_{st} + NEA_{10})$$
(A.7)

Where:

$$NEA_{10} = (0.9784)^{T_{b(i)}} \cdot (15.7378)^{H} \cdot (1.3777)^{V_b \cdot 10^{-6}}$$

A.8. Demister Pressure Drop, ΔP_{Dp} (Pa/m)

Eq. (A.8) expresses the pressure drop in the demister, incorporating demister density (ρ_p) , which denotes the material mass per unit volume, as well as vapor velocity (V_{ν}) and wire diameter (δ_w) .

$$\Delta P_{Dp} = 3.88178 \cdot (\rho_p)^{0.375798} \cdot (V_v)^{0.81317} \cdot (\delta_w)^{-1.56114147}$$
(A.8)

The equation is valid under these conditions:

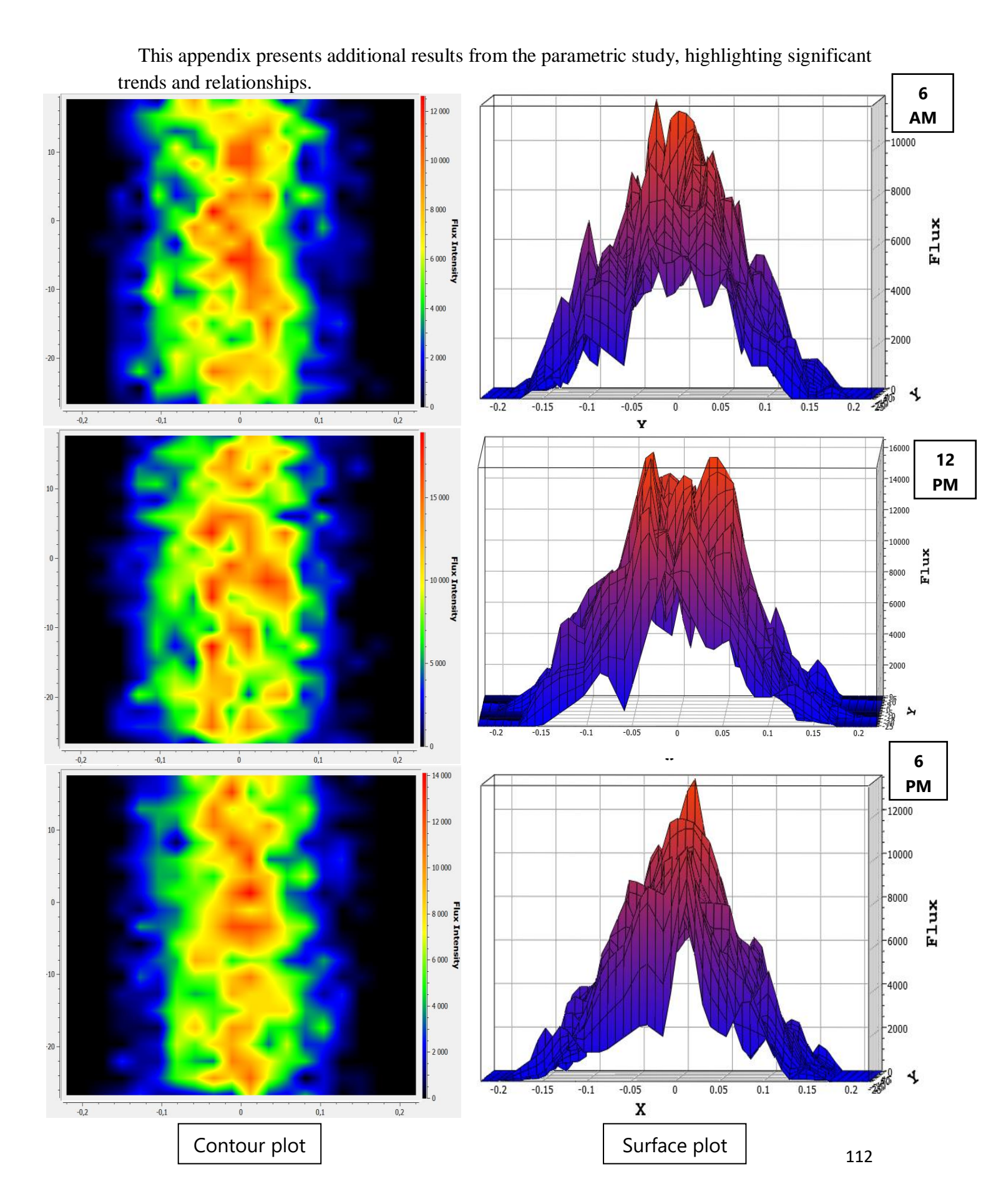
$$\checkmark 0.98 \frac{m}{s} < V_v < 7.5 \frac{m}{s}$$

✓
$$0.98 \frac{m}{s} < V_v < 7.5 \frac{m}{s}$$

✓ $80.31 \frac{kg}{m^3} < \rho_p < 208.16 \frac{kg}{m^3}$

$$\checkmark 0.2 \ mm < \delta_w < 0.32 \ mm$$

Appendix B: Results from the Parametric Study





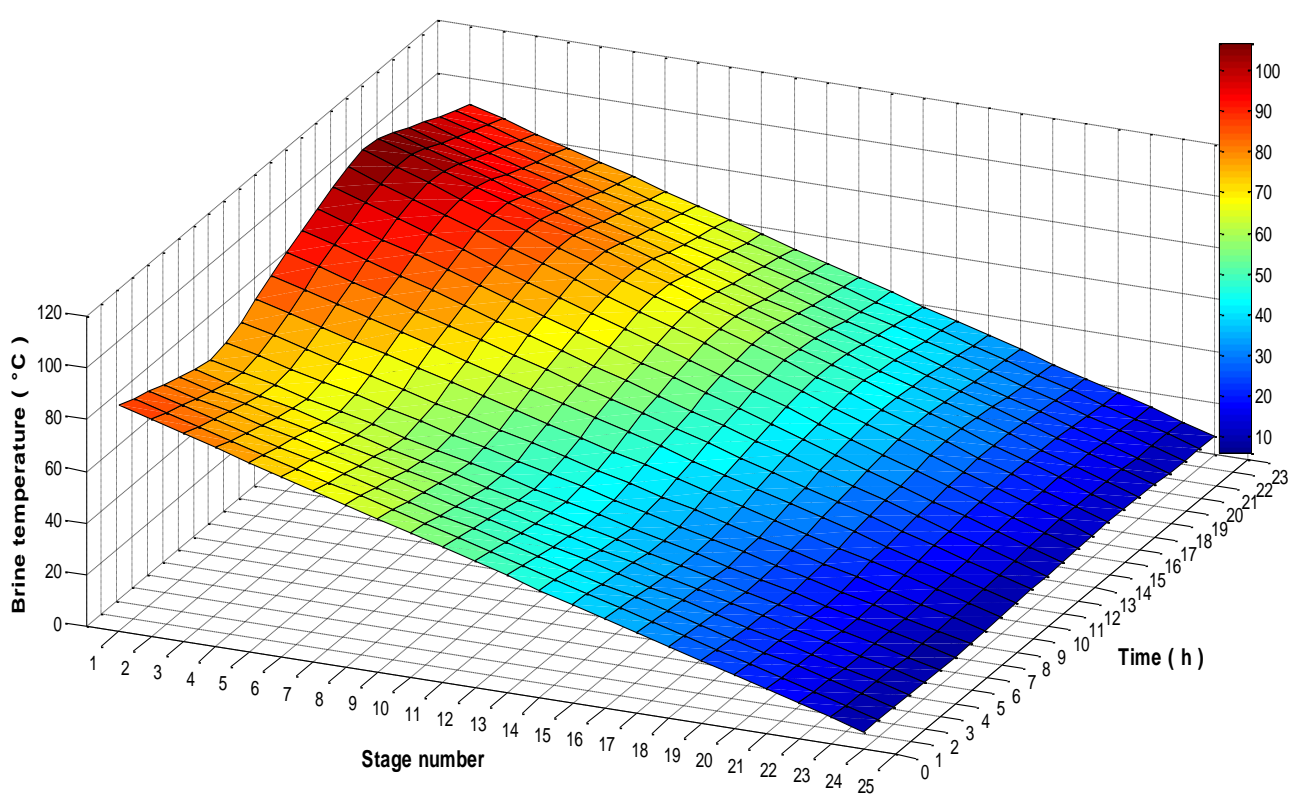


Fig.B. 2. Brine temperature evolution through the condenser tube across stages over 24-hours on an optimal day in Algiers.

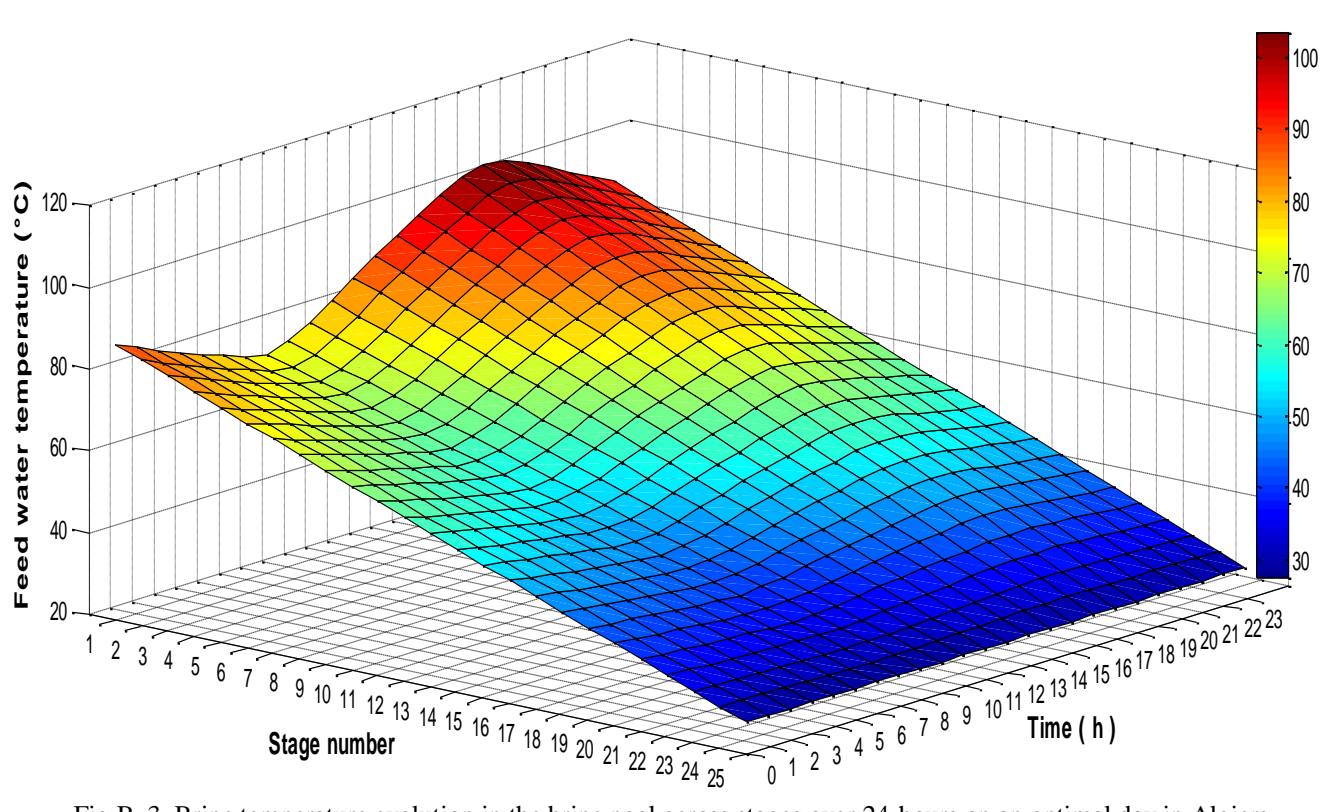


Fig.B. 3. Brine temperature evolution in the brine pool across stages over 24-hours on an optimal day in Algiers.

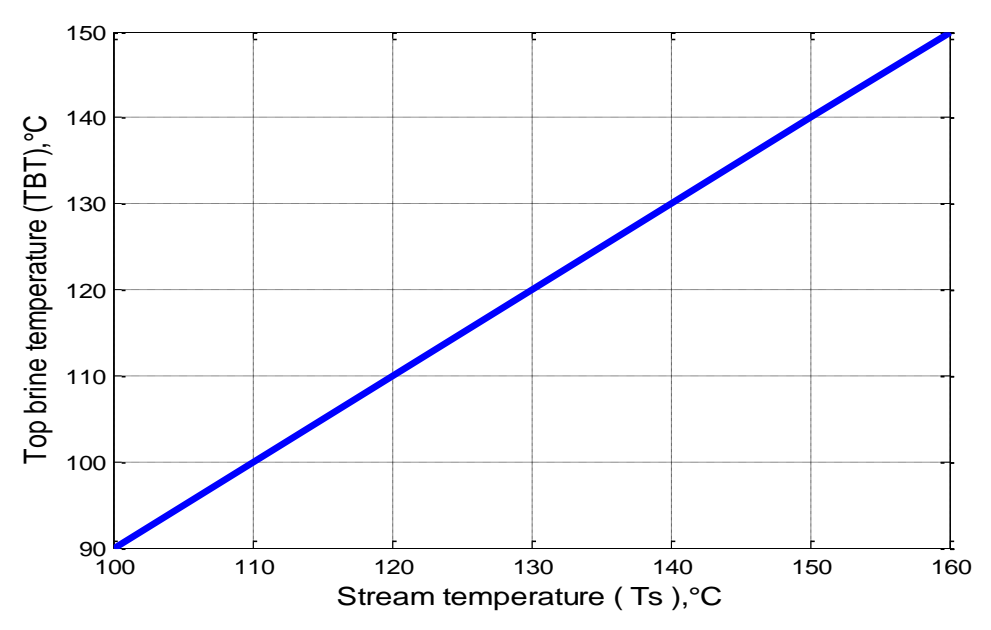
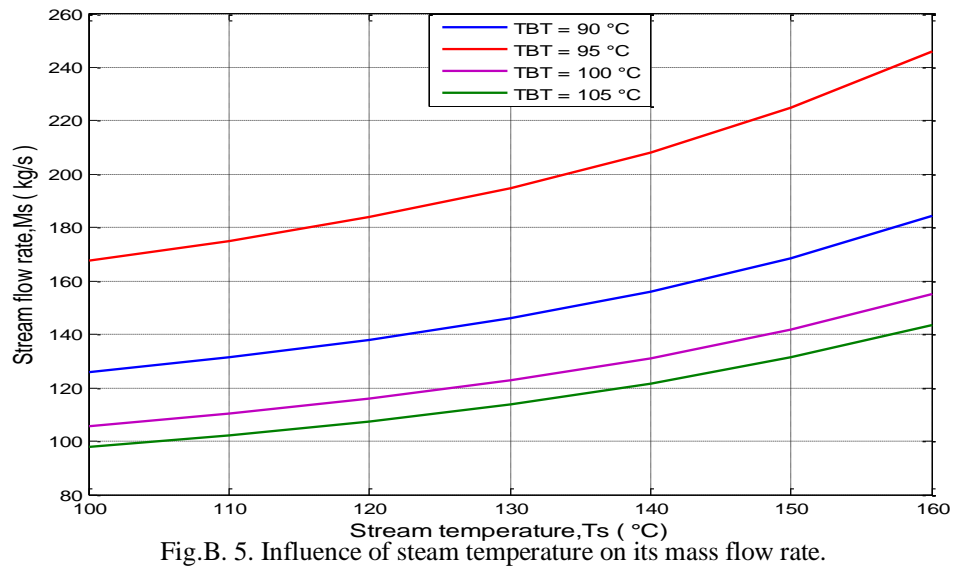


Fig.B. 4. Influence of steam temperature on top brine temperature.



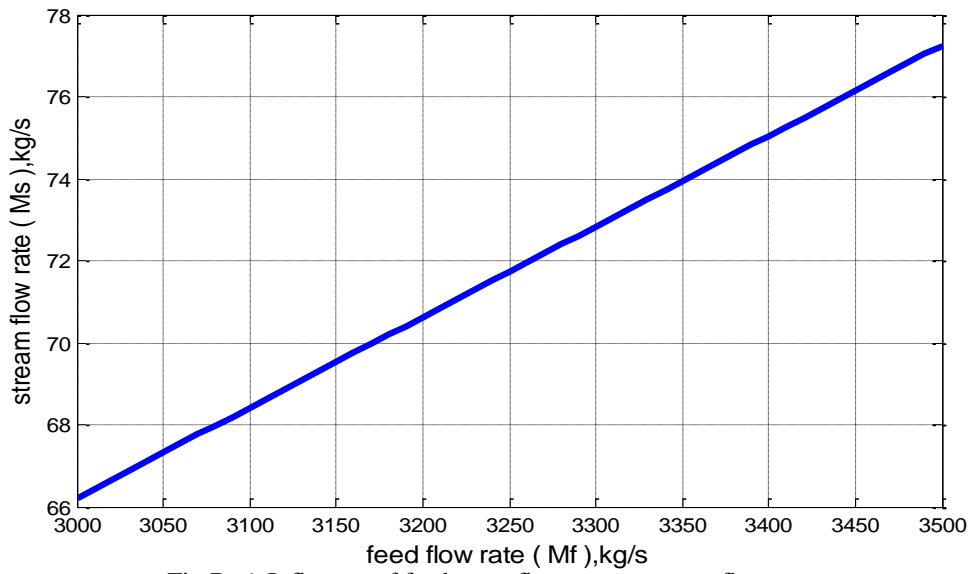
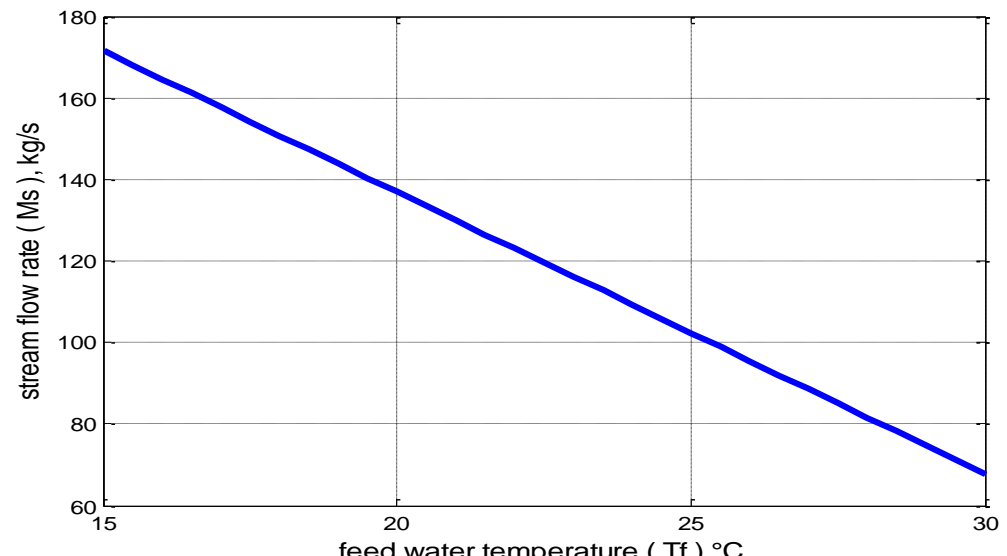


Fig.B. 6. Influence of feedwater flow rate on steam flow rate.



feed water temperature (Tf), $^{\circ}C$ Fig.B. 7. Influence of feed water temperature on steam flow rate.

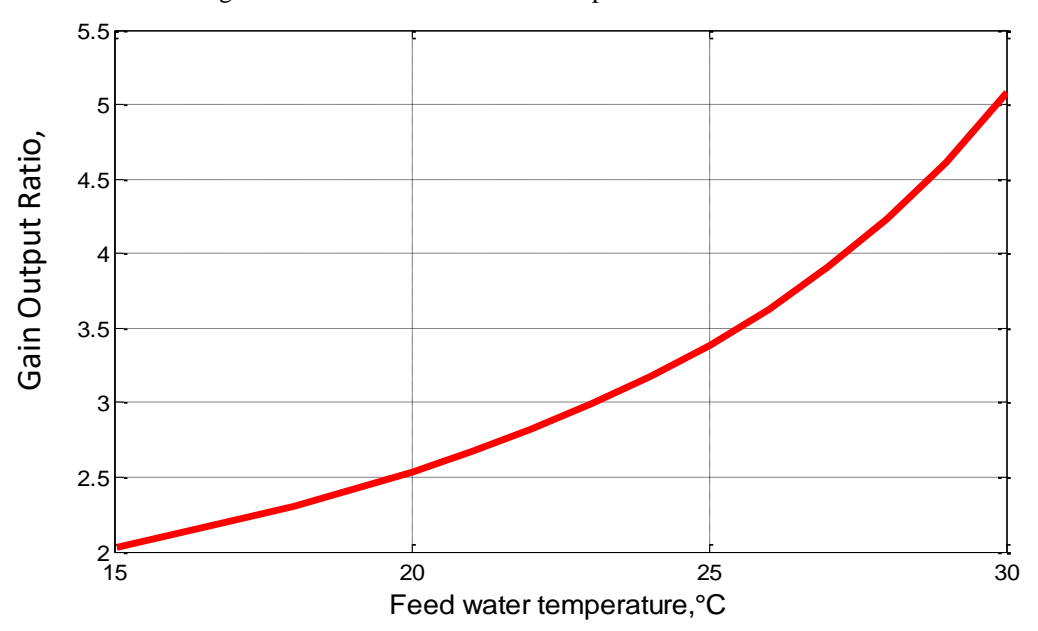


Fig.B. 8. Influence of feed water temperature on gain output ratio.

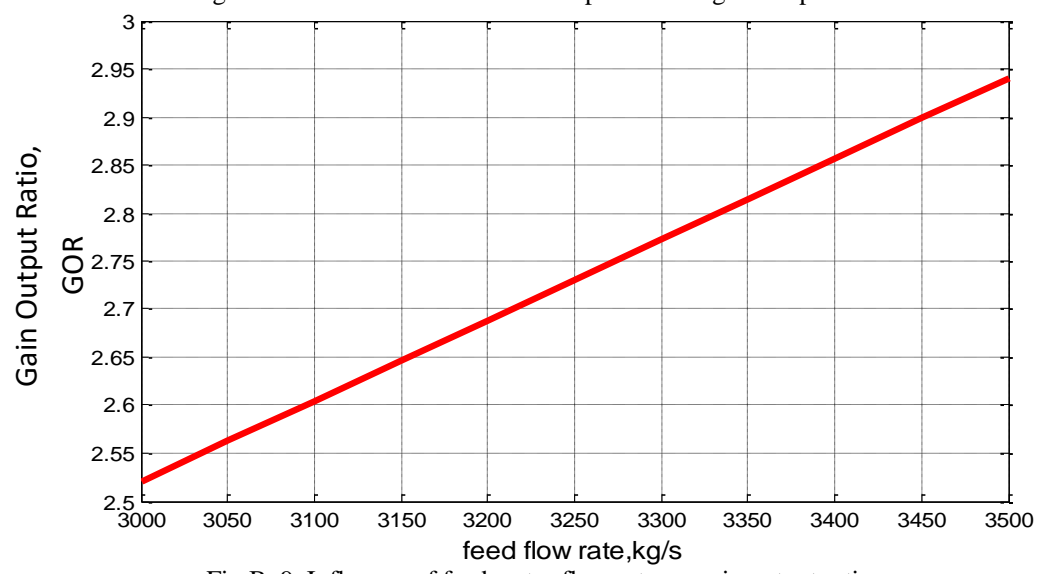


Fig.B. 9. Influence of feed water flow rate on gain output ratio.

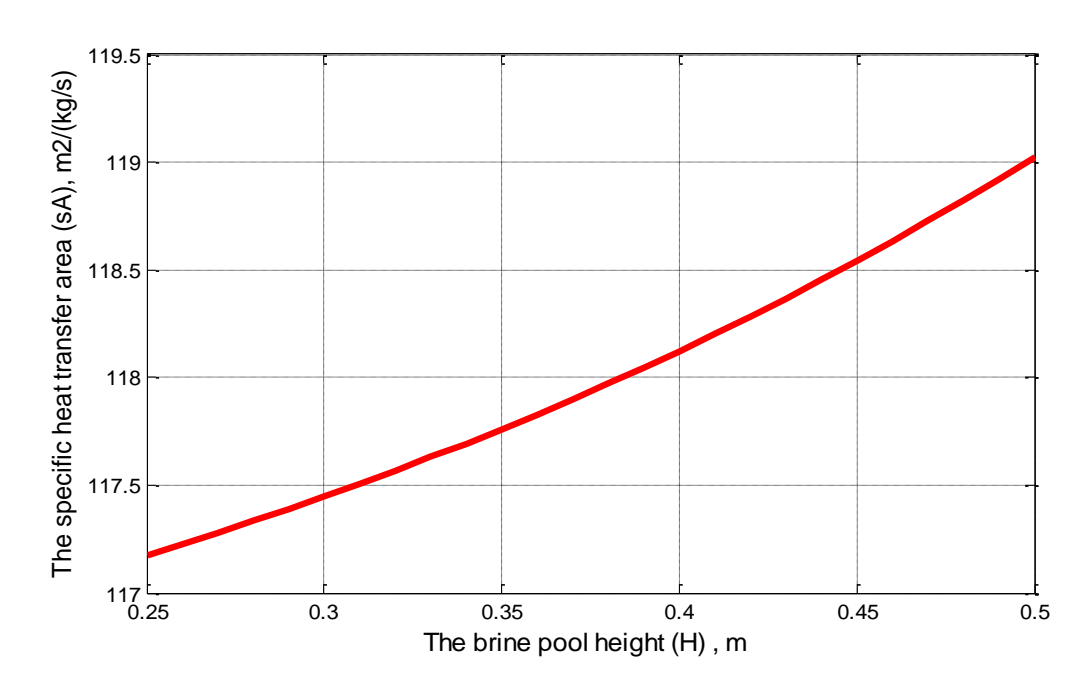


Fig.B. 10. Influence of brine pool height on specific heat transfer area.

Appendix C: Economic Calculation Procedure

This appendix presents a detailed step-by-step explanation of the economic calculations.

C.1. Levelized Cost of Water, LCOW (\$/year)

The total plant cost per year includes all expenses related to installation, operation, maintenance, and other associated costs. It is determined using the following equation.

$$LCOW = \frac{CAPEX \times CRF + OPEX}{Annual\ Water\ Production}$$
 (C.1)

C.1.1. Capital Expenditures, CAPEX (\$)

The capital expenditure represents the total initial investment required for the plant, covering both direct and indirect costs. The following equations define the components of CAPEX.

$$CAPEX = DC + IDC (C.2)$$

Where:

Direct Capital Cost (DC):
$$DC = DC_{col} + DC_{tank} + DC_{MSF} + DC_{build} + DC_{land}$$
 (C.3)

Indirect Capital Cost (IDC):
$$IDC = 0.25 \times DC$$
 (C.4)

The direct capital cost components are defined as follows:

- Solar array: $DC_{col} = \beta \times (A_{SF})^{0.95}$
- Storage Tank: $DC_{tank} = \alpha_{ST} \times V_{ST}$
- $Arr MSF: DC_{MSF} = 2867.7 \times M_D^{0.9878}$
- ► Building: $DC_{build} = 0.15 \times [DC_{col} + DC_{tank} + DC_{MSF}]$
- \triangleright Land: $DC_{land} = 0.1 \times [DC_{col} + DC_{tank} + DC_{MSF}]$

C.1.2. Operational Expenditures, OPEX (\$)

The operational expenditures include all recurring costs associated with the plant's operation and maintenance. These costs are categorized into energy consumption, labor, chemicals, and maintenance.

$$OPEX = E + C_{lab} + C_{chem} + MC (C.5)$$

C.1.2.1. Electrical Consumption, E (\$)

Energy consumption includes the power required for fluid circulation and desalination processes.

• Storage Tank Energy Consumption:

$$E_{tank} = E_c \times \left(\frac{\Delta P.V_{st}.t}{\eta_m.\eta_p}\right) \times f \times 365 \tag{C.6}$$

Where E_c is the unit electricity cost, ΔP is the pressure drop in the storage tank, V_{st} is the storage tank volume, t is the operational time per day, η_m and η_p are the mechanical and pump efficiencies, respectively, and f is the plant's availability factor.

• MSF Unit Energy Consumption:

$$E_{MSF} = SPC \times f \times M_D \times 365 \tag{C.7}$$

Here:

SPC is the specific power consumption of the MSF unit [kWh/m³].

 M_D is the daily freshwater production [m³/day].

C.1.2.2. Labor Cost, C_{lab} (\$)

Labor costs represent expenses associated with personnel responsible for system monitoring, operation, and maintenance, where L_c denotes the labor cost per unit of production.

$$C_{lab} = L_c \times f \times M_D \times 365 \tag{C.8}$$

C.1.2.3. Chemicals Cost, C_{chem} (\$)

Chemical costs cover the expenses for anti-scaling agents, corrosion inhibitors, and other essential treatment chemicals to maintain system performance and efficiency. Here, $chem_c$ represents the unit cost of chemicals.

$$C_{chem} = chem_c \times f \times M_D \times 365 \tag{C.9}$$

C.1.2.4. Maintenance Cost, MC (\$)

Maintenance costs ensure the durability and optimal performance of system components, including solar collectors, storage tanks, and the MSF unit.

$$MC = MC_{col} + MC_{tank} + MC_{MSF} (C.10)$$

Where:

- $MC_{col} = 0.0075 \times DC_{col}$
- $MC_{tank} = 0.008 \times DC_{tank}$
- $MC_{MSF} = 0.02 \times DC_{MSF}$

REFERENCES

- [1] T.E. Page, E. Capps, W.H.D. Rouse, L.A. Post, E.H. Warmington, Hippocrates, Vol. I, William Heinemann Ltd, London; Harvard University Press, Cambridge, MA, 1923.
- [2] F. Bacon, Sylva Sylvarum: Or a Natural History in Ten Centuries, 9th ed., J.R. for William Lee, London, 1670.
- [3] A.H. Khan, Desalination Processes and Multistage Flash Distillation Practice, Elsevier, Amsterdam, 1986.
- [4] H.T. El-Dessouky, H.M. Ettouney, Fundamentals of Salt Water Desalination, Elsevier, 2002.
- [5] F.W. Gilbert, An Experimental Investigation of Steady-State Characteristics of Flashing Salt Solution in Open Channel Flow Between Two Submerged Orifices at Low Pressures, PhD Thesis, University of Connecticut, USA, 1968.
- [6] R.S. Silver, British Patent No. 829,819, March 1960.
- [7] International Desalination Association (IDA), The 19th IDA Worldwide Desalting Plant Inventory, Topfield, MA, USA, 2006.
- [9] International Desalination Association (IDA), IDA Desalination Yearbook 2013–2014, Media Analytics Ltd, Oxford, United Kingdom, 2014.
- [8] M. Nair, D. Kumar, Water desalination and challenges: The Middle East perspective: a review, Desalination Water Treat. 51 (2013) 2030–2040.
- [10] J. Eke, A. Yusuf, A. Giwa, A. Sodiq, The global status of desalination: An assessment of current desalination technologies, plants, and capacity, Desalination 495 (2020) 114633. https://doi.org/10.1016/j.desal.2020.114633.
- [11] Plan Bleu, Desalination: State of play and prospects in the Mediterranean, 2024. https://planbleu.org/wp-content/uploads/2024/02/Notes-dessalement-EN.pdf. (accessed 15 March 2025).
- [12] United Nations, UN Water for Life Decade 2005–2015, (accessed 9 January 2025). Available at: http://www.un.org/waterforlifedecade/background.shtml.
- [13] M.A. Shannon, P.W. Bohn, M. Elimelech, J.G. Georgiadis, B.J. Marinas, A.M. Mayes, Science and technology for water purification in the coming decades, Nature 452 (2008) 301–310. https://doi.org/10.1038/nature06599.
- [14] World Water Council, The Use of Water Today, Chapter 2, Marseille, (accessed 31 March 2024). Available at: http://www.worldwatercouncil.org/fileadmin/world_water_council/documents_old/Library/W WVision/Chapter2.pdf.
- [15] L.K. Wang, J.P. Chen, Y. Hung, N. Shammas, Membrane and Desalination Technologies, Springer, London, 2011. https://doi.org/10.1007/978-1-59745-278-6_12.
- [16] Worldometers, Real-Time World Statistics, (accessed 31 March 2024). Available at: http://www.worldometers.info/world-population/.
- [17] Geohive, Global Population Statistics, (accessed 31 March 2024). Available at: http://www.geohive.com/earth/his_history3.aspx.

- [18] World Intellectual Property Organization (WIPO), International Renewable Energy Agency (IRENA), Global Institute for Water, Environment and Health (GIWEH), Patent Landscape Report on Desalination Technologies and the Use of Alternative Energies for Desalination, November 2011.
- [19] United Nations Environment Programme (UNEP), An Overview of the State of the World's Fresh and Marine Waters Report, 2nd Edition, 2008.
- [20] U.S. Geological Survey (USGS), The USGS Water Science School, (accessed 31 March 2024). Available at: http://water.usgs.gov/edu/gallery/global-water-volume.html.
- [21] S. Kalogirou, Seawater desalination using renewable energy sources, Prog. Energy Combust. Sci. 31 (2005) 242–281.
- [22] The Encyclopedia of Earth, Freshwater, (accessed 30 March 2024). Available at: http://www.eoearth.org/view/article/152861/.
- [23] J.L. Fuentes-Bargues, Analysis of the process of environmental impact assessment for seawater desalination plants in Spain, Desalination 347 (2014) 166–174.
- [24] The University of Illinois at Chicago, GlobalEd 2 Expanding the Science and Literacy Curricular Space, (accessed 31 June 2024). Available at: http://www.globaled.uconn.edu/student_water/simulation/simulation_introduction.html.
- [25] The National Academies Press (NAP), Global Issues in Water, Sanitation, and Health, (accessed 31 March 2014). Available at: www.nap.edu.
- [26] The National Academies Press (NAP), Dietary Reference Intakes for Energy, Carbohydrate, Fiber, Fat, Fatty Acids, Cholesterol, Protein, and Amino Acids (2002/2005) and Dietary Reference Intakes for Water, Potassium, Sodium, Chloride, and Sulfate (2005), (accessed 31 June 2024). Available at: www.nap.edu.
- [27] B.D. Negewo, Renewable Energy Desalination: An Emerging Solution to Close the Water Gap in the Middle East and North Africa, World Bank, 2012.
- [28] World Energy Council (WEC), The world energy demand in 2020, 2009.
- [29] BP P.I.C., Energy Outlook, 2016 edition, (accessed 18 January 2023). Available at: https://www.bp.com/content/dam/bp/pdf/energy-economics/energy-outlook-2016/bp-energy-outlook-2016.pdf.
- [30] I. Fechete, Y. Wang, J.C. Védrine, The past, present and future of heterogeneous catalysis, Catal. Today 189 (2012) 2–27.
- [31] A.B. Stambouli, E. Traversa, Solid oxide fuel cells (SOFCs): a review of an environmentally clean and efficient source of energy, Renew. Sustain. Energy Rev. 6 (2002) 433–455. https://doi.org/10.1016/S1364-0321(02)00014-X.
- [32] B. Metz, O. Davidson, P. Bosch, R. Dave, L. Meyer, Climate Change 2007: Mitigation of Climate Change, Cambridge University Press, Cambridge, 2007.
- [33] C.J. Schuster-Wallace, V.I. Grover, Z. Adeel, U. Confalonieri, S. Elliott, Safe Water as the Key to Global Health, The United Nations University International Network on Water, Environment and Health, 2008.
- [34] J.R. Stokes, A. Horvath, Energy and air emission effects of water supply, Environ. Sci. Technol. 43 (2009) 2680–2687. https://doi.org/10.1021/es801802h.
- [35] International Desalination Association (IDA), IDA Desalination Yearbook 2013–2014, Media Analytics Ltd, Oxford, United Kingdom, 2014.

- [36] International Renewable Energy Agency (IRENA), Water Desalination Using Renewable Energy Report, 2012. https://www.irena.org/DocumentDownloads/Publications/IRENA-ETSAP%20Tech%20Brief%20I12%20Water-Desalination.pdf (accessed 27 June 2024).
- [37] K. Feng, K. Hubacek, Y.L. Siu, X. Li, The energy and water nexus in Chinese electricity production: a hybrid life cycle analysis, Renew. Sustain. Energy Rev. 39 (2014) 342–355. https://doi.org/10.1016/j.rser.2014.07.080.
- [38] M. Sharifzadeh, R.K.T. Hien, N. Shah, China's roadmap to low-carbon electricity and water: disentangling greenhouse gas (GHG) emissions from electricity-water nexus via renewable wind and solar power generation, and carbon capture and storage, Appl. Energy 235 (2019) 31–42. https://doi.org/10.1016/j.apenergy.2018.10.087.
- [39] Y. Tokui, H. Moriguchi, Y. Nishi, Comprehensive environmental assessment of seawater desalination plants: multistage flash distillation and reverse osmosis membrane types in Saudi Arabia, Desalination 351 (2014) 145–150. https://doi.org/10.1016/j.desal.2014.07.034.
- [40] G. Micale, A. Cipollina, L. Rizzuti, Seawater Desalination: Conventional and Renewable Energy Processes, Green Energy and Technology, Springer, 2014.
- [41] N. Ghaffour, J. Bundschuh, H. Mahmoudi, M.F.A. Goosen, Renewable energy-driven desalination technologies: a comprehensive review on challenges and potential applications of integrated systems, Desalination 356 (2015) 94–114. https://doi.org/10.1016/j.desal.2014.10.024.
- [42] H. Nassrullah, S.F. Anis, R. Hashaikeh, N. Hilal, Energy for desalination: a state-of-the-art review, Desalination 491 (2020), 114569. https://doi.org/10.1016/j.desal.2020.114569.
- [43] B. Tomaszewska, L. Pająk, J. Bundschuh, W. Bujakowski, Low-enthalpy geothermal energy as a source of energy and integrated freshwater production in inland areas: technological and economic feasibility, Desalination 435 (2018) 35–44. https://doi.org/10.1016/j.desal.2017.10.041.
- [44] M. Paprapetrou, M. Wieghause, C. Biercamp (Eds.), Roadmap for development of desalination powered by renewable energy, PRODES, 2009. Available from: www.prodesproject.org (accessed 25 March 2025).
- [45] A.F. Abdul Fattah, Selection of a solar desalination system for supply water in arid zones, Desalination 60 (1986) 165–189. https://doi.org/10.1016/0011-9164(86)90007-X.
- [46] REN21, Available from: https://www.ren21.net (accessed 25 March 2025).
- [47] R. Meyer, S. Lohmann, C. Schillings, C. Hoyer, Climate statistics for planning and siting of solar energy systems: long-term variability of solar radiation derived from satellite data, 2006.
- [48] C.A. Gueymard, A review of validation methodologies and statistical performance indicators for modeled solar radiation data: towards a better bankability of solar projects, Renew. Sustain. Energy Rev. 39 (2014) 1024–1034. https://doi.org/10.1016/j.rser.2014.07.117.
- [49] S. Lohmann, C. Schillings, B. Mayer, R. Meyer, Long-term variability of solar direct and global radiation derived from ISCCP data and comparison with reanalysis data, Sol. Energy 80 (2006) 1390–1401. https://doi.org/10.1016/j.solener.2006.03.004.
- [50] J. Polo, S. Wilbert, J.A. Ruiz-Arias, R. Meyer, C. Gueymard, M. Súri, L. Martín, T. Mieslinger, P. Blanc, I. Grant, J. Boland, P. Ineichen, J. Remund, R. Escobar, A. Troccoli, M. Sengupta, K.P. Nielsen, D. Renne, N. Geuder, T. Cebecauer, Preliminary survey on site-

- adaptation techniques for satellite-derived and reanalysis solar radiation datasets, Sol. Energy 132 (2016) 25–37. https://doi.org/10.1016/j.solener.2016.03.001.
- [51] G. Bender, F. Davidson, F. Eichelberger, C.A. Gueymard, The road to bankability: improving assessments for more accurate financial planning, in: Solar 2011 Conference of the American Solar Energy Society, 2011.
- [52] F. Vignola, C. Grover, N. Lemon, A. McMahan, Building a bankable solar radiation dataset, Sol. Energy 86 (2012) 2218–2229. https://doi.org/10.1016/j.solener.2012.05.013.
- [53] Solargis, Solar resource maps and GIS data for 180+ countries. Available from: https://solargis.com/maps-and-gis-data/download/ (accessed 5 January 2022).
- [54] European Solar Thermal Electricity Association, Solar thermal electricity: global outlook 2016. Available from: www.estelasolar.org (accessed 2 March 2025).
- [55] International Energy Agency (IEA), Technology Roadmap: Solar Thermal Electricity, OECD Publishing, 2015.
- [56] F. Amrouche, A. Benzaoui, F. Harouadi, B. Mahmah, M. Belhamel, Compressed natural gas: the new alternative fuel for the Algerian transportation sector, Procedia Engineering 33 (2012) 102–110. https://doi.org/10.1016/j.proeng.2012.01.1180.
- [57] Office National des Statistiques (ONS), Retrieved from http://www.ons.dz, 2020.
- [58] United Nations, World Population Prospects, 28 pp. Available from: https://population.un.org/wpp/Publications/Files/WPP2019_DataBooklet.pdf (accessed 2 April 2022).
- [59] S. Noureddine, Potentiel solaire de l'Algérie : Photovoltaïque et CSP, Bulletin des Énergies Renouvelables, Centre de Développement des Énergies Renouvelables (CDER), Alger, Algérie. 2013.
- [60] Deutsches Zentrum für Luft- und Raumfahrt (DLR), Global Solar Atlas Direct Normal Irradiance (DNI) for Concentrated Solar Power (CSP) [dataset], 2023. Available at: https://www.dlr.de/eoc/en/desktopdefault.aspx/tabid-11958/ (accessed 6 April 2025).
- [61] ARENA, Atlas Solaire Méditerranéen, www.solar-med-atlas.org, (accessed 6 April 2025).
- [62] United Nations Environment Programme (UNEP), As shortages mount, countries hunt for novel sources of water. Available from: https://www.unep.org/news-and-stories/story/shortages-mount-countries-hunt-novel-sources-water (accessed 5 December 2024).
- [63] M. Shatat, M. Worall, S. Riffat, Opportunities for solar water desalination worldwide: review, Sustain. Cities Soc. 9 (2013) 67–80. https://doi.org/10.1016/j.scs.2013.03.004.
- [64] M.B. Mohamed, Low-Cost Nanomaterials for Water Desalination and Purification, United Nations UNSCO, 2011.
- [65] S. El-Manharawy, A. Hafez, Water type and guidelines for RO system design, Desalination 139 (2001) 97–113. https://doi.org/10.1016/S0011-9164(01)00298-3.
- [66] H. Al-Fulaij, Dynamic Modeling of Multi-Stage Flash (MSF) Desalination Plant, PhD thesis, University College London, 2011. https://discovery.ucl.ac.uk/id/eprint/1324506.
- [67] M. Schiffler, Perspectives and challenges for desalination in the 21st century, Desalination 165 (2004) 1–9. https://doi.org/10.1016/j.desal.2004.06.001.

- [68] International Desalination Association (IDA), International Desalination Association and Global Water Intelligence Release New Data in 30th Worldwide Desalting Inventory, Available from: https://idadesal.org/international-desalination-association-and-global-water-intelligence-release-newdata-in-30th-worldwide-desalting-inventory/ (accessed 18 April 2023).
- [69] International Water Association (IWA), Desalination past, present and future. Available from: https://iwa-network.org/desalination-past-present-future/ (accessed 18 April 2023).
- [70] S. Kehal, Retrospective et perspectives du dessalement en Algérie, Desalination 136 (2001) 35-42. https://doi.org/10.1016/S0011-9164(01)00162-X.
- [71] D.A. Baharoon, H.A. Rahman, W.Z.W. Omar, S.O. Fadhl, The historical development of concentrating solar power technologies to generate clean electricity efficiently A review, Renew. Sustain. Energy Rev. 41 (2015) 996–1027. https://doi.org/10.1016/j.rser.2014.09.008.
- [72] M.T. Islam, N. Huda, A.B. Abdullah, R. Saidur, A comprehensive review of state-of-the-art concentrating solar power (CSP) technologies: current status and research trends, Renew. Sustain. Energy Rev. 91 (2018) 987–1018. https://doi.org/10.1016/j.rser.2018.04.097.
- [73] J. Sun, Z. Zhang, L. Wang, Z. Zhang, J. Wei, Comprehensive review of line-focus concentrating solar thermal technologies: parabolic trough collector (PTC) vs linear Fresnel reflector (LFR), J. Therm. Sci. 29 (5) (2020) 1097–1124. https://doi.org/10.1007/s11630-020-1365-4.
- [74] P.D. Tagle-Salazar, K.D.P. Nigam, C.I. Rivera-Solorio, Parabolic trough solar collectors: A general overview of technology, industrial applications, energy market, modeling, and standards, Green Process. Synth. 9 (1) (2020) 595–649. https://doi.org/10.1515/gps-2020-0059.
- [75] A. Gil, et al., State of the art on high temperature thermal energy storage for power generation. Part 1 Concepts, materials and modellization, Renew. Sustain. Energy Rev. 14 (1) (2010) 31–55. https://doi.org/10.1016/j.rser.2009.07.035.
- [76] F.J. Santos-Alamillos, D. Pozo-Vázquez, J.A. Ruiz-Arias, L. Von Bremen, J. Tovar-Pescador, Combining wind farms with concentrating solar plants to provide stable renewable power, Renew. Energy 76 (2015) 539–550. https://doi.org/10.1016/j.renene.2014.11.055.
- [77] S.A. Kalogirou, Solar thermal collectors and applications, Prog. Energy Combust. Sci. 30 (2004) 231–295. https://doi.org/10.1016/j.pecs.2004.02.001.
- [78] A.E. Kabeel, E.M.S. El-Said, Applicability of flashing desalination technique for small-scale needs using a novel integrated system coupled with nanofluid-based solar collector, Desalination 333 (2014) 10–22. https://doi.org/10.1016/j.desal.2013.11.021.
- [79] R. Abbas, M.J. Montes, M. Piera, J.M. Martínez-Val, Solar radiation concentration features in Linear Fresnel Reflector arrays, Energy Convers. Manag. 54 (2012) 133–144. https://doi.org/10.1016/j.enconman.2011.10.010.
- [80] J.P. Chen, H. Mou, L.K. Wang, T. Matsuura, Y. Wei, Membrane Separation: Basics and Applications, in: L.K. Wang, T. Matsuura (Eds.), Handbook of Environmental Engineering: Membrane and Desalination Technologies, Springer, 2011.
- [81] M. Gunther, M. Joemann, S. Csambor, A. Guizani, D. Kruger, T. Hirsch, Linear Fresnel technology, Adv. CSP Teach. Mater. Enermena (2011). https://doi.org/10.4236/ajor.2021.113008.

- [82] C. Silvi, The pioneering work on linear Fresnel reflector concentrators (LFCs) in Italy, in: Proc. SolarPACES, 2009.
- [83] S. Benyakhlef, A. Al Mers, O. Merroun, A. Bouatem, N. Boutammachte, S. El Alj, et al., Impact of heliostat curvature on optical performance of Linear Fresnel solar concentrators, Renew. Energy 89 (2016) 463–474. https://doi.org/10.1016/j.renene.2015.12.018.
- [84] J.A. Duffie, W.A. Beckman, Solar Engineering of Thermal Processes, Wiley, Hoboken, 2013.
- [85] P.L. Singh, R.M. Sarviya, J.L. Bhagoria, Thermal performance of linear Fresnel reflecting solar concentrator with trapezoidal cavity absorbers, Appl. Energy 87 (2010) 541–550. https://doi.org/10.1016/j.apenergy.2009.08.019.
- [86] C. Choudhury, H.K. Sehgal, A Fresnel strip reflector-concentrator for tubular solar-energy collectors, Appl. Energy 23 (1986) 143–154. https://doi.org/10.1016/0306-2619(86)90036-X.
- [87] S.S. Sahoo, S. Singh, R. Banerjee, Analysis of heat losses from a trapezoidal cavity used for Linear Fresnel Reflector system, Sol. Energy 86 (2012) 1313–1322. https://doi.org/10.1016/j.solener.2012.01.023.
- [88] G. Zhu, T. Wendelin, M.J. Wagner, C. Kutscher, History, current state, and future of linear Fresnel concentrating solar collectors, Sol. Energy 103 (2014) 639–652. https://doi.org/10.1016/j.solener.2013.05.021.
- [89] B.S. Negi, T.C. Kandpal, S.S. Mathur, Designs and performance characteristics of a linear Fresnel reflector solar concentrator with a flat vertical absorber, Sol. Wind Technol. 7 (1990) 379–392. https://doi.org/10.1016/0741-983X(90)90023-U.
- [90] J.M. Gordon, H. Ries, Tailored edge-ray concentrators as ideal second stages for Fresnel reflectors, Appl. Opt. 32 (1993) 2243–2251. https://doi.org/10.1364/AO.32.002243.
- [91] D.R. Mills, Linear Fresnel reflector (LFR) technology, in: K. Lovegrove, W. Stein (Eds.), Concentrating Solar Power Technology, Woodhead Publishing, British Library, 2012, pp. 153–196.
- [92] E.Z. Moya, Parabolic-trough concentrating solar power (CSP) systems, in: K. Lovegrove, W. Stein (Eds.), Concentrating Solar Power Technology, Woodhead Publishing, 2012, pp. 197–239.
- [93] E. Bellos, Progress in the design and the applications of linear Fresnel reflectors A critical review, Therm. Sci. Eng. Prog. 10 (2019) 112–137. https://doi.org/10.1016/j.tsep.2019.01.014.
- [94] H. Beltagy, The effect of glass on the receiver and the use of two absorber tubes on optical performance of linear Fresnel solar concentrators, Energy 224 (2021) 120111. https://doi.org/10.1016/j.energy.2021.120111.
- [95] G. Morin, J. Dersch, W. Platzer, M. Eck, A. Häberle, Comparison of Linear Fresnel and Parabolic Trough Collector power plants, Sol. Energy 86 (2012) 1–12. https://doi.org/10.1016/j.solener.2011.06.020.
- [96] Y. Filali Baba, H. Ajdad, A. Al Mers, A. Bouatem, B.B. Idrissi, S. El Alj, Preliminary cost-effectiveness assessment of a Linear Fresnel Concentrator: Case studies, Case Stud. Therm. Eng. 22 (2020) 100730. https://doi.org/10.1016/j.csite.2020.100730.

- [97] J.F. Thye, Desalination: Can It Be Greenhouse Gas Free and Cost Competitive?, Report of MEM Masters Project, Yale School of Forestry and Environmental Studies, New Haven, CT, USA, 9 May 2010.
- [98] L. Garcia-Rodriguez, Renewable energy applications in desalination: state of the art, Sol. Energy 75 (2003) 381–393. https://doi.org/10.1016/j.solener.2003.08.005.
- [99] M. El-Bairouty, H. Fath, M. Saddiqi, O. El-Rabghy, Design, Construction and Testing of Experimental Education MSF Desalination Unit, in: Proc. IDA Congr. Desalin. Water Reuse, Singapore, 2005.
- [100] A.D. Khawaji, I.K. Kutubkhanah, J. Wie, Advances in seawater desalination technologies, Desalination 221 (2008) 47–69. https://doi.org/10.1016/j.desal.2007.01.067.
- [101] N. Hilal, G. J. Kim, C. Somerfield, Boron removal from saline water: A comprehensive review, Desalination 273 (2011) 23–35. https://doi.org/10.1016/j.desal.2010.05.012.
- [102] E. A. M. Hawaidi, I. M. Mujtaba, Simulation and optimization of MSF desalination process for fixed freshwater demand: Impact of brine heater fouling, Chem. Eng. J. 165 (2010) 545–553. https://doi.org/10.1016/j.cej.2010.09.071.
- [103] H. T. El-Dessouky, I. M. Alatiqi, H. M. Ettouney, N. S. Al-Deffeeri, Performance of wire mesh mist eliminator, Chem. Eng. Process. 39 (2000) 129–139. https://doi.org/10.1016/S0255-2701(99)00033-1.
- [104] N. Ghaffur, T. M. Missimer, G. L. Amy, Technical review and evaluation of the economics of water desalination: Current and future challenges for better water supply sustainability, Desalination 309 (2013) 197–207. https://doi.org/10.1016/j.desal.2012.10.015.
- [105] M. S. Mohsen, O. R. Al-Jayyousi, Brackish water desalination: An alternative for water supply enhancement in Jordan, Desalination 124 (1999) 163–174. https://doi.org/10.1016/S0011-9164(99)00101-0.
- [106] G. M. Marian, S. F. Mussati, P. A. Aguirre, N. J. Nicolás, N. J. Scenna, Optimization of hybrid desalination processes including multi-stage flash and reverse osmosis systems, Desalination 182 (2005) 111–122. https://doi.org/10.1016/j.desal.2005.03.011.
- [107] United Nations (UN), ESCWA Water Development Report 3, New York, 2009.
- [108] Fortune Business Insights, Desalination technologies market. https://www.fortunebusinessinsights.com/desalination-technologies-market-109806 (accessed 09 March 2025).
- [109] M. A. Darwish, A. Alsairafi, Technical comparison between TVC/MEB and MSF, Desalination 170 (2004) 223–239. https://doi.org/10.1016/j.desal.2004.01.006.
- [110] M. Al-Bahou, Z. Al-Rakaf, H. Zaki, H. Ettouney, Desalination experience in Kuwait, Desalination 204 (2007) 403–415. https://doi.org/10.1016/j.desal.2006.03.545.
- [111] R. Borsani, S. Rebagliati, Fundamentals and costing of MSF desalination plants and comparison with other technologies, Desalination 182 (2005) 29. https://doi.org/10.1016/j.desal.2005.03.007.
- [112] A. Hanafi, Design and performance of solar MSF desalination systems, Desalination 82 (1991) 175–185. https://doi.org/10.1016/0011-9164(91)85180-3.
- [113] A. S. Nafey, M. A. Mohamad, S. O. El-Helaby, M. A. Sharaf, Theoretical and experimental study of a small unit for solar desalination using flashing process, Energy Convers. Manag. 48 (2007) 528–538. https://doi.org/10.1016/j.enconman.2006.06.010.

- [114] K. S. Reddy, K. R. Kumar, T. S. O'Donovan, T. K. Mallick, Performance analysis of an evacuated multi-stage solar water desalination system, Desalination 288 (2012) 80–92. https://doi.org/10.1016/j.desal.2011.12.016.
- [115] A. E. Kabeel, E. M. S. El-Said, A hybrid solar desalination system of air humidification, dehumidification and water flashing evaporation: Part II. Experimental investigation, Desalination 341 (2014) 50–60. https://doi.org/10.1016/j.desal.2014.02.035.
- [116] I. Darawsheh, M. D. Islam, F. Banat, Experimental characterization of a solar powered MSF desalination process performance, Therm. Sci. Eng. Prog. 10 (2019) 154–162. https://doi.org/10.1016/j.tsep.2019.01.018.
- [117] T. Szacsvay, P. Hofer-Noser, M. Posnansky, Technical and economic aspects of small-scale solar-pond-powered seawater desalination systems, Desalination 122 (1999) 185–193. https://doi.org/10.1016/S0011-9164(99)00040-5.
- [118] G. Caruso, A. Naviglio, A desalination plant using solar heat as a heat supply, not affecting the environment with chemicals, Desalination 122 (1999) 225–234. https://doi.org/10.1016/S0011-9164(99)00043-0.
- [119] E. E. Delyannis, Status of solar assisted desalination: A review, Desalination 67 (1987) 3–19. https://doi.org/10.1016/0011-9164(87)90227-X.
- [120] European Commission, Desalination Guide Using Renewable Energies, European Commission, 1998.
- [121] A. A. Madani, Economics of Desalination for Three Plant Sizes, Desalination, 78 (1990) 187-200. https://doi.org/10.1016/0011-9164(90)80042-A.
- [122] A. M. El Nashar, K. Ishii, Abu Dhabi Solar Distillation Plant, Desalination 52 (1985) 217–234. https://doi.org/10.1016/0011-9164(85)80034-5.
- [123] F. Palma, Seminar on New Technologies for the Use of Renewable Energies in Water Desalination, Commission of the European Communities, DG XVII for Energy, Centre for Renewable Energy Sources, Athens, 1991.
- [124] V. Valverde Muela, Centro de Estudios de la Energía, Planta Desaladora con Energía Solar de Arinaga, Las Palmas de Gran Canaria, Departamento de Investigación y Nuevas Fuentes, 1982.
- [125] E. Zarza Moya, Solar Thermal Desalination Project: First Phase and Results & Second Phase Description, CIEMAT, Madrid, 1991.
- [126] F. Trieb, H. Müller-Steinhagen, J. Kern, J. Scharfe, M. Kabariti, A. Al Taher, Technologies for large-scale seawater desalination using concentrated solar radiation, Desalination 235 (2009) 33–43. https://doi.org/10.1016/j.desal.2007.04.098.
- [127] P. Palenzuela, D. C. Alarcón-Padilla, G. Zaragoza, Large-scale solar desalination by combination with CSP: Techno-economic analysis of different options for the Mediterranean Sea and the Arabian Gulf, Desalination 366 (2015) 130–138. https://doi.org/10.1016/j.desal.2014.12.037.
- [128] O. A. Hamed, H. Kosaka, K. H. Bamardouf, K. Al-Shail, A. S. Al-Ghamdi, Concentrating solar power for seawater thermal desalination, Desalination 396 (2016) 70–78. https://doi.org/10.1016/j.desal.2016.06.008.
- [129] A. Al-Othman, M. Tawalbeh, M. Assad, Novel multi-stage flash (MSF) desalination plant driven by parabolic trough collectors and a solar pond: A simulation study in UAE, Desalination 443 (2018) 237–244. https://doi.org/10.1016/j.desal.2018.06.005.

- [130] M. Alhaj, S. G. Al-Ghamdi, Reducing electric energy consumption in linear Fresnel collector solar fields coupled to thermal desalination plants by optimal mirror defocusing, Heliyon 4 (2018) e00813. https://doi.org/10.1016/j.heliyon.2018.e00813.
- [131] N. A. Moharram, S. Bayoumi, A. Hanafy, W. M. El-Maghlany, Hybrid desalination and power generation plant utilizing multi-stage flash and reverse osmosis driven by parabolic trough collectors, Case Stud. Therm. Eng. 23 (2021) 100807. https://doi.org/10.1016/j.csite.2020.100807.
- [132] A. Babaeebazaz, S. Gorjian, M. Amidpour, Integration of a Solar Parabolic Dish Collector with a Small-Scale Multi-Stage Flash Desalination Unit: Experimental Evaluation, Exergy and Economic Analyses, Sustainability 13 (2021) 11295. https://doi.org/10.3390/su132011295.
- [133] O. Behar, A. Khellaf, K. Mohammedi, A review of studies on central receiver solar thermal power plants, Renew. Sustain. Energy Rev. 23 (2013) 12–39. https://doi.org/10.1016/j.rser.2013.02.017.
- [134] D. R. Mills, G. L. Morrison, Compact linear Fresnel reflector solar thermal power plants, Sol. Energy 68 (2000) 263–283. https://doi.org/10.1016/S0038-092X(99)00068-7.
- [135] A. Häberle, C. Zahler, H. Lerchenmüller, M. Mertins, C. Wittwer, F. Trieb, et al., The Solarmundo line-focusing Fresnel collector: Optical and thermal performance and cost calculations, SolarPACES 2002.
- [136] Y.L. He, K. Wang, Y. Qiu, B.C. Du, Q. Liang, S. Du, Review of the solar flux distribution in concentrated solar power: Non-uniform features, challenges, and solutions, Appl. Therm. Eng. 149 (2019) 448–474. https://doi.org/10.1016/j.applthermaleng.2018.12.006.
- [137] R. Bernhard, H.G. Laabs, J. de Lalaing, M. Eck, M. Eickhoff, K. Pottler, et al., Linear Fresnel collector demonstration on the PSA Part I design, construction and quality control, in: Proceedings of the 15th SolarPACES International Symposium, Berlin, Germany, 2008.
- [138] Areva Solar, 2013. http://www.areva.com/EN/solar-220/arevasolar.html (accessed 9 October 2022).
- [139] Novatec Solar, 2013. http://www.novatecsolar.com/ (accessed 6 January 2022).
- [140] F. Veynandt, Cogénération héliothermodynamique avec concentrateur linéaire de Fresnel: modélisation de l'ensemble du procédé, PhD Thesis, Energétique et Transferts, under the supervision of J.-J. Bézian and P. Stouffs, 2011. https://doi.org/10.13140/RG.2.2.22567.39840.
- [141] A.E. Rungasamy, K.J. Craig, J.P. Meyer, 3-D CFD Modeling of a Slanted Receiver in a Compact Linear Fresnel Plant with Etendue-Matched Mirror Field, Energy Procedia 69 (2015) 188–197. https://doi.org/10.1016/j.egypro.2015.03.022.
- [142] J. Zhu, Z. Chen, Optical design of compact linear Fresnel reflector systems, Sol. Energy Mater. Sol. Cells 176 (2018) 239–250. https://doi.org/10.1016/j.solmat.2017.12.016.
- [143] M. Yang, Y. Zhu, R.A. Taylor, End losses minimization of linear Fresnel reflectors with a simple, two-axis mechanical tracking system, Energy Convers. Manag. 161 (2018) 284–293. https://doi.org/10.1016/j.enconman.2018.01.082.
- [144] M. Hongn, S.F. Larsen, Hydrothermal model for small-scale linear Fresnel absorbers with non-uniform stepwise solar distribution, Appl. Energy 223 (2018) 329–346. https://doi.org/10.1016/j.apenergy.2018.04.056.

- [145] D. Pulido-Iparraguirre, L. Valenzuela, J.-J. Serrano-Aguilera, A. Fernández-García, Optimized design of a Linear Fresnel reflector for solar process heat applications, Renew. Energy 131 (2019) 1089–1106. https://doi.org/10.1016/j.renene.2018.08.018.
- [146] J. Ma, Z. Chang, Understanding the effects of end-loss on linear Fresnel collectors, IOP Conf. Ser.: Earth Environ. Sci. 121 (2018) 052052. https://doi.org/10.1088/1755-1315/121/5/052052.
- [147] Y. Zhu, J. Shi, Y. Li, L. Wang, Q. Huang, G. Xu, Design and thermal performances of a scalable linear Fresnel reflector solar system, Energy Convers. Manag. 146 (2017) 174–181. https://doi.org/10.1016/j.enconman.2017.05.031.
- [148] Y. Zhu, J. Shi, Y. Li, L. Wang, Q. Huang, G. Xu, Design and experimental investigation of a stretched parabolic linear Fresnel reflector collecting system, Energy Convers. Manag. 126 (2016) 89–98. https://doi.org/10.1016/j.enconman.2016.07.073.
- [149] P. Tsekouras, C. Tzivanidis, K. Antonopoulos, Optical and thermal investigation of a linear Fresnel collector with trapezoidal cavity receiver, Appl. Therm. Eng. 135 (2018) 379–388. https://doi.org/10.1016/j.applthermaleng.2018.02.082.
- [150] M.J. Montes, R. Barbero, R. Abbas, A. Rovira, Performance model and thermal comparison of different alternatives for the Fresnel single-tube receiver, Appl. Therm. Eng. 104 (2016) 162–175. https://doi.org/10.1016/j.applthermaleng.2016.05.015.
- [151] H. Beltagy, D. Semmar, C. Lehaut, N. Said, Theoretical and experimental performance analysis of a Fresnel type solar concentrator, Renew. Energy 101 (2017) 782–793. https://doi.org/10.1016/j.renene.2016.09.038.
- [152] H. Ajdad, Y. Filali Baba, A. Al Mers, O. Merroun, A. Bouatem, N. Boutammachte, S. El Alj, S. Benyakhlef, Thermal and Optical Efficiency Analysis of the Linear Fresnel Concentrator Compound Parabolic Collector Receiver, ASME J. Sol. Energy Eng. 140 (2018) 051007. https://doi.org/10.1115/1.4040064.
- [153] G. Mokhtar, B. Boussad, S. Noureddine, A linear Fresnel reflector as a solar system for heating water: Theoretical and experimental study, Case Stud. Therm. Eng. 8 (2016) 176–186. https://doi.org/10.1016/j.csite.2016.06.006.
- [154] Y. Qiu, M.-J. Li, K. Wang, Z.-B. Liu, X.-D. Xue, Aiming strategy optimization for uniform flux distribution in the receiver of a linear Fresnel solar reflector using a multi-objective genetic algorithm, Appl. Energy 205 (2017) 1394–1407. https://doi.org/10.1016/j.apenergy.2017.09.092.
- [155] Y. Qiu, Y.-L. He, M. Wu, Z.-J. Zheng, A comprehensive model for optical and thermal characterization of a linear Fresnel solar reflector with a trapezoidal cavity receiver, Renew. Energy 97 (2016) 129–144. https://doi.org/10.1016/j.renene.2016.05.065.
- [156] S.S. Sahoo, S. Singh, R. Banerjee, Thermal hydraulic simulation of absorber tubes in linear Fresnel reflector solar thermal system using RELAP, Renew. Energy 86 (2016) 507–516. https://doi.org/10.1016/j.renene.2015.08.050.
- [157] E. Bellos, E. Mathioulakis, E. Papanicolaou, V. Belessiotis, Experimental investigation of the daily performance of an integrated linear Fresnel reflector system, Sol. Energy 167 (2018) 220–230. https://doi.org/10.1016/j.solener.2018.04.019.
- [158] S. Pauletta, A solar Fresnel collector based on an evacuated flat receiver, Energy Procedia 101 (2016) 480–487. https://doi.org/10.1016/j.egypro.2016.11.061.

- [159] R. Grena, Geometrical Aspects of the Optics of Linear Fresnel Concentrators: A Review, Energies 17 (2024) 3564. R. Grena, Geometrical Aspects of the Optics of Linear Fresnel Concentrators: A Review, Energies 17 (2024) 3564. https://doi.org/10.3390/en17143564.
- [160] Y. Qiu, Y.-L. He, Z.-D. Cheng, K. Wang, Study on optical and thermal performance of a linear Fresnel solar reflector using molten salt as HTF with MCRT and FVM methods, Appl. Energy 146 (2015) 162–173. https://doi.org/10.1016/j.apenergy.2015.01.135.
- [161] J. Ma, Z. Chang, S. Yan, R. Tian, Energy flux distribution and thermal performance of linear Fresnel collector system in cold region, Energy Power Eng. 9 (2017) 555–567. https://doi.org/10.4236/epe.2017.910039.
- [162] K.S. Reddy, S. Balaji, T. Sundararajan, Heat loss investigation of 125 kWth solar LFR pilot plant with parabolic secondary evacuated receiver for performance improvement, Int. J. Therm. Sci. 125 (2018) 324–341. https://doi.org/10.1016/j.ijthermalsci.2017.11.006.
- [163] M. Cagnoli, D. Mazzei, M. Procopio, V. Russo, L. Savoldi, R. Zanino, Analysis of the performance of linear Fresnel collectors: encapsulated vs. evacuated tubes, Sol. Energy 164 (2018) 119–138. https://doi.org/10.1016/j.solener.2018.02.037.
- [164] N.H. Aly, M.A. Marwan, Dynamic behaviour of MSF desalination plants, Desalination 101 (1994) 287–293. https://doi.org/10.1016/0011-9164(95)00032-W.
- [165] A.R. Glueck, R.W. Bradshaw, A mathematical model for a multistage flash distillation plant, in: Proc. 3rd Int. Symp. Fresh Water from the Sea, vol. 1, 1970, pp. 95–108.
- [166] E.A.M. Hawaidi, Simulation, optimization and flexible scheduling of MSF desalination process under fouling, PhD thesis, University of Bradford, 2011.
- [167] A.M. Omar, Simulation of MSF desalination plants, Desalination 45 (1983) 65–76. https://doi.org/10.1016/0011-9164(83)87009-X.
- [168] H.M. Ettouney, H.T. El-Dessouky, R. Faibish, P. Gowin, Evaluating the economics of desalination, CEP Mag. (2002).
- [169] A.M. Helal, M.S. Medani, M. Soliman, J. Flower, A TDM model for MSF desalination plants, Comput. Chem. Eng. 10 (1986) 327–342. https://doi.org/10.1016/0098-1354(86)87003-X.
- [170] M. Mazzotti, M. Rosso, A. Beltramini, M. Morbidelli, Dynamic Modeling multistage flash desalination plants, Desalination 127 (2000) 207–218. https://doi.org/10.1016/S0011-9164(00)00011-4.
- [171] H. El-Dessouky, I. Alatiqi, H. Ettouney, Process synthesis: the multi-stage flash desalination system, Desalination 115 (1998) 155–179. https://doi.org/10.1016/S0011-9164(98)00035-6.
- [172] M.S. Tanvir, I.M. Mujtaba, Modelling and simulation of MSF desalination process using gPROMS and neural network based physical property correlation, Comput. Aided Chem. Eng. 21 (2006) 315–320. https://doi.org/10.1016/S1570-7946(06)80065-9.
- [173] N.M. Abdel-Jabbar, H.M. Qiblawey, F.S. Mjalli, H. Ettouney, Simulation of large capacity MSF brine circulation plants, Desalination 204 (2007) 501–514. https://doi.org/10.1016/j.desal.2006.02.047.
- [174] C. Qi, M. Fan, F. Xie, et al., Numerical simulation of flash evaporation characteristics and optimization design of flash tank for seawater desalination, China Water Wastewater 25 (2009) 87–91.

- [175] S.A. Said, M. Emtir, I.M. Mujtaba, Flexible design and operation of multi-stage flash (MSF) desalination process subject to variable fouling and variable freshwater demand, Processes 1 (3) (2013) 279–295. https://doi.org/10.3390/pr1030279.
- [176] H. Al-Fulaij, A. Cipollina, G. Micale, H. Ettouney, D. Bogle, Eulerian–Lagrangian modeling and computational fluid dynamics simulation of wire mesh demisters in MSF plants, Desalination 385 (2016) 148–157. https://doi.org/10.1016/j.desal.2016.02.019.
- [177] H.F. Al-Fulaij, A. Cipollina, G. Micale, H. Ettouney, D. Bogle, Eulerian–Eulerian modelling and computational fluid dynamics simulation of wire mesh demisters in MSF plants, Eng. Comput. 31 (2014) 1242–1260. https://doi.org/10.1108/EC-03-2012-0063.
- [178] V.M. Maniar, P.B. Deshpande, Advanced controls for multi-stage flash (MSF) desalination plant optimization, J. Process Control 6 (1) (1996) 49–66. https://doi.org/10.1016/0959-1524(95)00030-5.
- [179] A. Gambler, E. Badreddin, Dynamic modelling of MSF plants for automatic control and simulation purposes: a survey, Desalination 166 (2004) 191–204. https://doi.org/10.1016/j.desal.2004.06.073.
- [180] M.T. Sowgath, Neural Network Based Hybrid Modelling and MINLP Based Optimisation of MSF Desalination Process Within gPROMS, PhD dissertation, University of Bradford, 2007.
- [181] S.M.M. Alsadaie, Design and Operation of Multistage Flash (MSF) Desalination: Advanced Control Strategies and Impact of Fouling, PhD dissertation, University of Bradford, 2017.
- [182] T.H. Nigim, J.A. Eaton, CFD prediction of the flashing processes in a MSF desalination chamber, Desalination 420 (2017) 258–272. https://doi.org/10.1016/j.desal.2017.06.026.
- [183] H. Hasan, S. Alsadaie, M.A. Al-Obaidi, I.M. Mujtaba, Dynamic modelling and simulation of industrial scale multistage flash desalination process, Desalination 553 (2023) 116453. https://doi.org/10.1016/j.desal.2023.116453.
- [184] D.-Y. Choi, C.-F. Jin, Y.-H. Song, S.-H. Choi, H.-S. Chung, P.-H. Kim, A study on the MED-TVC operating performance characteristics using the thermo-compressor, J. Korean Soc. Mar. Eng. 32 (2008) 1185–1191. https://doi.org/10.5916/jkosme.2008.32.8.1185.
- [185] I.S. Al-Mutaz, A comparative study of RO and MSF desalination plants, Desalination 106 (1996) 99–106. https://doi.org/10.1016/S0011-9164(96)00097-5.
- [186] K. Lovegrove, W. Stein, Concentrating Solar Power Technology: Principles, Developments and Applications, Woodhead Publishing, 2012.
- [187] Schott, Schott PTR70 Receivers, the 4th Generation. Available at: http://www.schott.com (Accessed 16 November 2023).
- [188] Eastman, Technical Data Sheet Therminol® 66 Heat Transfer Fluid. Available at: https://fr.scribd.com/document/387131153/TF-08-Therminol-66 (Accessed 28 November 2023).
- [189] T. Helsør, H. Svendsen, Experimental characterization of pressure drop in dry demisters at low and elevated pressures, Chem. Eng. Res. Des. 85 (2007) 377–385. https://doi.org/10.1205/cherd06048.
- [190] Joint Research Centre (JRC) of the European Commission, SARAH-2 Solar Radiation Data [Data set], 2024. Available at: https://re.jrc.ec.europa.eu/pvg_tools/fr/ (Accessed 20 September 2022).

- [191] F.J. Pino, R. Caro, F. Rosa, J. Guerra, Experimental validation of an optical and thermal model of a linear Fresnel collector system, Appl. Therm. Eng. 50 (2013) 1463–1471. https://doi.org/10.1016/j.applthermaleng.2011.12.020.
- [192] W.R. McIntire, Factored approximations for biaxial incident angle modifiers, Sol. Energy 29 (1982) 315–322. https://doi.org/10.1016/0038-092X(82)90246-8.
- [193] M.J. Wagner, Results and Comparison from the SAM Linear Fresnel Technology Performance Model, NREL/CP-5500-54758, National Renewable Energy Laboratory (NREL), 2012.
- [194] Novatec Solar, NOVA-1 brochure: "NOVA-1: Turnkey solar boiler, mass produced in industrial precision with performance guarantee", Germany. Available at: www.novatecsolar.com (Accessed 19 October 2023).
- [195] National Renewable Energy Laboratory (NREL), SolTrace (version 2013) [Software]. Available at: https://www.nrel.gov/csp/soltrace.html (Accessed 20 December 2023).
- [196] C.R. Steele, C.D. Balch, G.J. Jorgensen, T. Wendelin, A. Lewandowski, Membrane Dish Analysis: A Summary of Structural and Optical Analysis Capabilities, NREL/TP-253-3432, National Renewable Energy Laboratory, Golden, CO, 1991.
- [197] A.C. Ratzel, B.D. Boughton, CIRCE.001: A Computer Code for Analysis of Point-Focus Concentrators with Flat Targets, SAND86-1866, Sandia National Laboratories, Albuquerque, NM, 1987.
- [198] G.H. Spencer, M.V.R.K. Murty, General Ray Tracing Procedure, J. Opt. Soc. Am. 52 (1962) 672–678. https://opg.optica.org/josa/abstract.cfm?URI=josa-52-6-672.
- [199] C. Marugán-Cruz, D. Serrano, J. Gómez-Hernández, S. Sánchez-Delgado, Solar multiple optimization of a DSG linear Fresnel power plant, Energy Convers. Manag. 184 (2019) 571–580. https://doi.org/10.1016/j.enconman.2019.01.054.
- [200] M. Ghodbane, B. Boumeddane, Z. Said, E. Bellos, A numerical simulation of a linear Fresnel solar reflector directed to produce steam for the power plant, J. Clean. Prod. 231 (2019) 494–508. https://doi.org/10.1016/j.jclepro.2019.05.201.
- [201] M.J. Wagner, G. Zhu, A direct-steam linear Fresnel performance model for NREL's System Advisor Model, in: Proceedings of the ASME 2012 6th International Conference on Energy Sustainability & 10th Fuel Cell Science, Engineering and Technology Conference (ESFuelCell2012), San Diego, CA, USA, July 23–26, 2012.
- [202] A. Cipollina, G. Micale, L. Rizzuti, Investigation of flashing phenomena in MSF chambers, Desalination 216 (2007) 183–195. https://doi.org/10.1016/j.desal.2007.01.008.
- [203] Y. Wang, Q. He, Q. Yang, D. Zhang, M. Liu, J. Yan, Energy and exergy analyses of circulatory flash evaporation of aqueous NaCl solution, Desalination 436 (2018) 81–90. https://doi.org/10.1016/j.desal.2018.02.011.
- [204] M.A. Darwish, F. Al-Juwayhel, H.K. Abdulraheim, Multi-effect boiling systems from an energy viewpoint, Desalination 194 (2006) 22–39. https://doi.org/10.1016/j.desal.2005.08.029.
- [205] M.H. Sharqawy, M.A. Antar, S.M. Zubair, A.M. Elbashir, Optimum thermal design of humidification-dehumidification desalination systems, Desalination 349 (2014) 10–21. http://dx.doi.org/10.1016/j.desal.2014.06.016.

- [206] M.A. Darwish, F.A. Yousef, N.M. Al-Najem, Energy consumption and costs with a multi-stage flashing (MSF) desalting system, Desalination 109 (1997) 285–302. https://doi.org/10.1016/S0011-9164(97)00075-1.
- [207] C.P. Brichambaut, C. Vauge, Le Gisement Solaire Évaluation de la Ressource Énergétique, Éditions Lavoisier, Tec & Doc, Paris, 1982.
- [208] F. Kies, A. Kerfouf, Impact of climate change on the West coast of Algeria: Gulf of Oran, Arzew, and Mostaganem, Sustainability, Agri, Food and Environmental Research 2(3) (2014) 1–15. http://dx.doi.org/10.7770/safer-V2N3-art821.
- [209] M. Ghodbane, M. Majdak, B. Boumeddane, The efficiency of linear Fresnel reflectors in producing superheated steam for power plant drive, E3S Web of Conferences 323 (2021) 202132300011. https://doi.org/10.1051/e3sconf/202132300011.
- [210] F. Esmaeilion, M. Soltani, J. Nathwani, Assessment of a novel solar-powered polygeneration system highlighting efficiency, exergy, economic, and environmental factors, Desalination 540 (2022) 116004. https://doi.org/10.1016/j.desal.2022.116004.
- [211] People's Democratic Republic of Algeria, Ministry of Foreign Affairs and National Community Abroad. (Accessed 17 March 2025). https://www.mfa.gov.dz/discoveralgeria/about-algeria.
- [212] A.B. Stambouli, An overview of different energy sources in Algeria, United Nations, Index 382958, 2007.
- [213] O. Ketfi, M. Merzouk, N.M. Kasbadji, M. Bourouis, Feasibility study and performance evaluation of low-capacity water—LiBr absorption cooling systems functioning in different Algerian climate zones, International Journal of Refrigeration 82 (2017) 36–50. https://doi.org/10.1016/j.ijrefrig.2017.07.002.
- [214] M. Massimo, T. Franz, K. Jürgen, Combined water and electricity production on an industrial scale in MENA countries with concentrating solar power, EuroMed 2010. https://www.researchgate.net/publication/225020394.
- [215] A. Bendib, M.L. Boutrid, Assessment and prediction of land surface temperature effects on human thermal comfort in the city of Oran, Algeria, Theoretical and Applied Climatology 155(8) (2024) 1–19. https://doi.org/10.1007/s00704-024-05097-0.
- [216] C. Ouroua, S. Debache, M. Milardi, From nature to buildings: A biomimetic approach as an alternative against structures' humidity issues in Jijel, Algeria, Journal of Innovations and Sustainability 8(2) (2024) 7. https://doi.org/10.51599/is.2024.08.02.07.
- [217] Z. Lu, L. Zhao, H. Fu, E. Yeatman, H. Ding, L. Chen, Ocean wave energy harvesting with high energy density and self-powered monitoring system, Nature Communications 15(1) (2024) 6513. https://doi.org/10.1038/s41467-024-50926-5.
- [218] Algeria's Path to Sustainable Fleet Management: Navigating the Transition to Eco-Friendly Vehicles (Embracing Hybrid Electric Vehicles and Alternative Fuels for a Greener Corporate Fleet in Algeria), (Accessed 30 January 2025). https://scopesdata.com/sustainability-country-information/algeria-2023.
- [219] Y. Zheng, R.A.C. Gonzalez, K.B. Hatzell, M.C. Hatzell, Large-scale solar-thermal desalination, Joule 5 (2021) 1971–1986. https://doi.org/10.1016/j.joule.2021.07.005.

- [220] E. Ali, J. Orfi, H. AlAnsary, A.S. Alsaadi, N. Ghaffour, Novel multistage flash reversal concept: Modelling and analysis, Applied Thermal Engineering 217 (2022) 119223. https://doi.org/10.1016/j.applthermaleng.2022.119223.
- [221] S.I. Al-Mutaz, MSF challenges and survivals, Desalination and Water Treatment 177 (2020) 14–22. https://doi.org/10.5004/dwt.2020.24908.
- [222] H.T. Do Thi, A.J. Toth, Investigation of carbon footprints of three desalination technologies: Reverse osmosis (RO), multi-stage flash distillation (MSF) and multi-effect distillation (MED), Periodica Polytechnica Chemical Engineering 67 (2023) 41–48. https://doi.org/10.3311/PPch.20901.
- [223] R. Colciaghi, R. Simonetti, L. Molinaroli, M. Binotti, G. Manzolini, Levelized cost of water assessment for small-scale desalination plant based on forward osmosis process, Energy Conversion and Management 271 (2022) 116336. https://doi.org/10.1016/j.enconman.2022.116336.
- [224] B. Heidary, T.T. Hashjin, B. Ghobadian, R. Roshandel, Optimal integration of small-scale hybrid solar-wind RO-MSF desalination system, Renewable Energy Focus 27 (2018) 120–134. https://doi.org/10.1016/j.ref.2018.05.003.
- [225] Y. Zheng, K.B. Hatzell, Technoeconomic analysis of solar thermal desalination, Desalination 474 (2020) 114168. https://doi.org/10.1016/j.desal.2019.114168.
- [226] M. Alsehli, J.-K. Choi, M. Aljuhan, A novel design for a solar-powered multistage flash desalination, Solar Energy 153 (2017) 348–359. https://doi.org/10.1016/j.solener.2017.05.082.
- [227] I.B. Askari, M. Ameri, Techno-economic feasibility analysis of Linear Fresnel solar field as thermal source of the MED/TVC desalination system, Desalination 394 (2016) 1–17. https://doi.org/10.1016/j.desal.2016.04.022.